Modelling and Control of Biomass and Photovoltaic Distributed Generation Systems

by

Nabila Ahmed Rufa'I

Submitted in accordance with the requirements for the degree of

Doctor of Philosophy

The University of Leeds

School of Electronic and Electrical Engineering

February, 2019

The candidate confirms that the work submitted is her own and that appropriate credit has been given where reference has been made to the work of others.

The contribution of the candidate to this work has been indicated in the jointly authored publications below.

1. **N. A. Rufa'I**, L. Zhang, and B. Chong, "Performance analysis of adaptive notch filter active damping methods for grid-connected converters under a varying grid impedance," in *PowerTech, 2017 IEEE Manchester*, 2017.
2. **N. A. Rufa'I**, L. Zhang, and B. Chong, "Comparison of PI and PR Controllers with Adaptive Notch Filter for LCL Filtered Grid-Tie Converters under Weak Grid," in *PES PowerAfrica, 2019 IEEE Abuja*, 2019.

The work presented in the publications above were carried out by the candidate who is also the lead author. The supervisors, Dr. L. Zhang and Dr. B. Chong provided reviews and comments on the manuscripts. The publications have been reproduced in some aspects of chapters 3 and 4 of this thesis.

Dedication

This thesis is wholeheartedly dedicated to my loving parents, Dr. Ahmed Rufa'I Inuwa and Prof. (Mrs) Ruqayyatu Ahmed Rufa'I.

Acknowledgement

Firstly, I would like to express special appreciation to my primary supervisor, Dr. Li Zhang for her untiring support and encouragement throughout the duration of my studies. For her patience and immense knowledge. Her constructive critique and attention to detail has brought out the best in me. I would also like to thank my co-supervisor, Dr. Benjamin Chong for his continuous support and mentorship at every step of the way.

Sincere appreciation goes to my sponsors, the Tertiary Education Trust Fund (TETFund) for funding this study. I am also grateful to the Funds for Women Graduates (FfWG) for their financial aid in the final year of my PhD studentship.

I would like to acknowledge all staff, colleagues and friends from the School of Electronic and Electrical Engineering who have made my studies worthwhile. In particular, to my friends in iCapNet: Ogaga, John, Han, Sultan, Asi, Ify and Mohammed for their companionship and intellectual discussions.

My sincere gratitude and appreciation goes to my entire family, whose support has been a tremendous source of strength throughout this journey. To my parents, Dr. Ahmed Rufa'I Inuwa and Prof. (Mrs) Ruqayyatu Ahmed Rufa'I, for their unending encouragement and continuous prayers. To my grandparents, Alhaji Muhammadu Ibrahim, Hajiya Halima and Hajiya Fatima for their constant reassurance. To all my uncles and aunts, especially Uncle Ali, for the continuous support. To my siblings, Yaya Aisha, Yaya Bashir, Muhammad and Imran, who have always been there for me. And to my loving husband, Habeeb and my wonderful children, Abdurrahman and Ruqayya, whose presence has certainly made it easier to push on and work harder.

And finally, all thanks and praise to the Lord of the worlds, the most Beneficent, the most Merciful.

Abstract

Distributed generation units using various renewable energy sources are rapidly infiltrating traditional electric power networks. They bring the benefits of hugely increasing worldwide energy supplies and reducing greenhouse gas emissions. Several distributed generators (DGs) can be integrated to form a microgrid (MG) to supply the local power needs, hence curbing power transmission congestion and delivery costs. A MG can manage the transfer of electricity between regions, and improve the robustness of the electrical network and its resilience in times of disastrous events. However, renewable sourced DGs using voltage source inverters with LCL filters are sensitive to non-ideal grid conditions such as impedance variation, harmonic corruption, voltage dips or swells and imbalance. Control techniques capable of working against all abnormal grid conditions, hence ensuring robust and stable power flow in the network, are crucial.

One of the main contributions of this work is the development of a new adaptive notch filter for the control of grid connected DGs. Grid-side LCL power filters in the converter output, using small capacitors and inductors, are effective in attenuating the PWM carrier and side-band voltage harmonics, and are widely applied. However, they are characterised by a unique resonant frequency, at which the gain of the input current is magnified. This frequency must be removed from the converter output, and therefore from its current control loop. A notch filter (NF) in the DGs' current control loop can actively curb this resonant frequency problem, but only at the specific value determined by grid impedance and LCL parameters. With a dynamic grid having variable impedance and background harmonics, the NF parameters need to be adaptive. The new method detects the changes of the resonant frequency by analysing the grid-side measured current on-line in real-time using the fast Fourier transform (FFT) technique, and the resultant frequency value is then applied to adjust the parameters of the notch filter. The method is tested and found to be able to track the changes of resonant frequency quickly and accurately, hence allowing the converter to give high performance current control.

For testing and validating the control schemes, a DG system with two or more renewable sourced generators is required. A micro-grid consisting of a biomass generator and PV-plant jointly supplying the local load is therefore built in

simulation. Detailed models for the biomass-based thermal energy conversion plant driving a synchronous generator and a PV DG are developed. The robustness of the biomass DG (BDG) controller is investigated under load perturbations, and the relationship between the supply system and the inertia of the BDG system is analysed. The study includes the negative effects of unbalanced loads, and a proposed solution is to compensate the negative sequence component of the unbalanced load using the advanced decoupled double synchronous reference frame (DDSRF) technique.

Another contribution lies in the development of a new Optimised Flexible Power Control (OFPC) scheme for reference current generation for PV DGs operating under abnormal grid conditions. DGs are required to supply active and reactive power without tripping under low or unbalanced voltages, but suffer from high power ripples due to the effects of negative sequence current and voltage. Treating the suppression of real and reactive ripples under a specific unbalanced voltage condition as a constrained multi-objective optimisation problem, the proposed OFPC defines a cost function as the sum of weighted active and reactive power ripples with a control variable. A genetic algorithm is applied to search for the optimal variable value. With this scheme, the reference current for the DG current controller gives good power control, and the results compare favourably with conventional methods.

Table of Contents

List of Figures

List of Tables

List of Abbreviations

AC	Alternating Current
ANF	Adaptive Notch Filter
AVR	Automatic Voltage Regulator
BDG	Biomass Distributed Generator
BPSC	Balanced Positive-Sequence Control
CAPC	Constant Active Power Control
CRPC	Constant Reactive Power Control
CSI	Current Source Inverters
CT	Current Transformer
DC	Direct Current
DDSRF-PLL	Decoupled Double Synchronous Reference Frame-PLL
DERs	Distributed Energy Resources
DFT	Discrete Fourier Transform
DG	Distributed Generation
DSRF	Double Synchronous Reference Frame
ER	Equivalence Ratio
FFT	Fast Fourier Transform
FPC	Flexible Power Control
GA	Genetic Algorithm
GHG	Greenhouse Gas
HPF	High Pass Filter
IEA	International Energy Agency
LC	Local Controllers
LCL	Inductor-Capacitor-Inductor
LCOE	Levelised Cost of Energy

LPF	Low Pass Filter
MG	Microgrid
MGCC	Microgrid System Central Control
MOOP	Multi-Objective Optimisation Problem
MPPT	Maximum Power Point Tracking
NF	Notch Filter
NSC	Negative Sequence Components
OFPC	Optimised Flexible Power Control
PCC	Point of Common Coupling
PLL	Phase Locked Loop
PSC	Positive Sequence Components
PT	Power Transformer
PV	Photovoltaic
PVDG	PV Distributed Generator
RL	Resistor-Inductor
RMSE	Root Mean Square Error
SCR	Short Circuit Ratio
SRF-PLL	Synchronous Reference Frame-Phase Locked Loop
STATCOM	Static Synchronous Compensator
THD	Total Harmonic Distortion
VOC	Voltage Oriented Control
VSI	Voltage Source Inverters
VUF	Voltage Unbalance Factor
ZSC	Zero Sequence Components

Chapter 1 Introduction

1.1 Distributed Generation with Renewable Energy Sources

The organisational structure of the traditional power system follows a distinct hierarchy, commencing from the generation of electrical power, through its transmission along cables to distribution substations and finally terminating at the load centres. In terms of global electricity production, thermal and hydro power generators are the largest contributors, accounting for 76% of generated power in 2010 [1]. Environmental factors such as air pollution dictate the location of thermal power stations at a significant electrical distance from consumption sites. Hydro power generators must be strategically located near water resources with sufficient head for efficient electricity production. These factors contribute to large capital investments for power transmission line equipment.

According to the International Energy Agency (IEA), approximately 1.3 billion people lack access to electricity, with almost 97% of them living in sub-Saharan Africa and the developing parts of Asia [2].This may be attributed to a large percentage of people in such countries situated in regions far away from the main grid. With an increasing population in these regions, matching electricity demand and supply becomes a difficult task.

Figure 1.1 shows the projections for the population of sub-Saharan Africa without access to electricity, with Nigeria being one of the major contributors. The percentage is expected to rise further by the year 2020.Two solutions are viable: investing in more power generators with increased power delivery costs or incorporating generators at the distribution side of the power system proximal to the load centres. The latter approach gives rise to the concept of distributed generation (DG) and the energy resources employed are distributed energy resources (DERs). The advantages of DG are clear: when strategically sited, they ensure provision of electricity at reduced costs, with an overall reduction in power transmission losses [3]. Distributed generators have capacities ranging from less than 1 kW solar photovoltaic (PV) installations to several 100 MW combined cycle power plants [4] at distribution voltage levels of up to 33 kV [5].

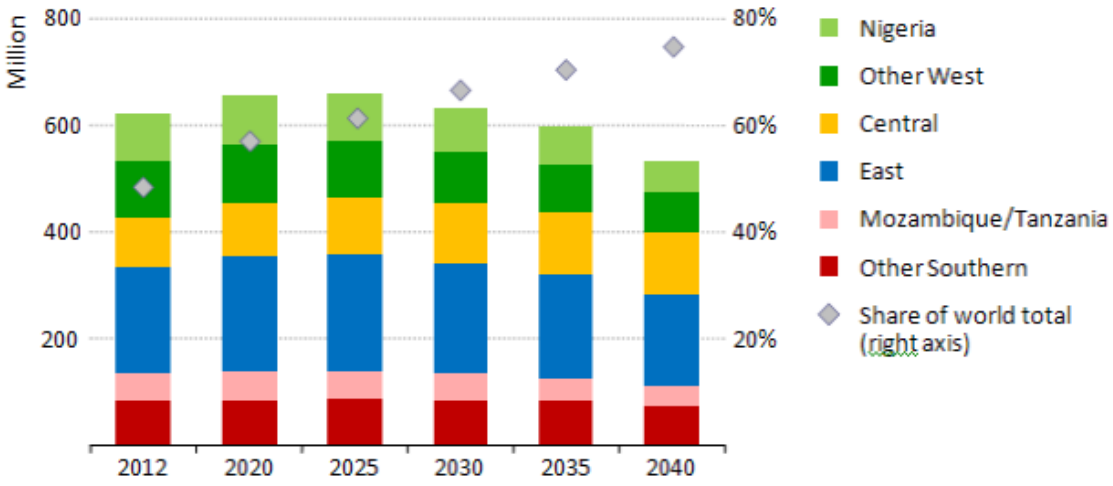

Figure 1:1: Population of sub-Saharan Africa without access to electricity [6]

There are primarily 9 sources of energy on earth: solar, biomass, wind, wave, hydro, tidal, geothermal, nuclear and fossils [6]. The first 6 are replenished by nature and are therefore considered to be renewable. Distributed generators utilising renewable forms of energy have the additional advantage of being environmentally friendly, as they do not lead to a net increase in atmospheric carbon dioxide, CO_2. For this reason, the presence of renewable sourced DGs connected to the grid is rapidly increasing [7].

On a global scale, several organisations have encouraged utilisation of renewable sources of energy. For example, the Kyoto Protocol established in 1997 has targeted a reduction in GHG emissions with emphasis on developed countries, where the level of industrial activity is high [8] . The Renewable Energy Directive for EU countries has encouraged the use of renewable sources to meet 20% of the energy demand by 2020 [9]. In view of this, the UK set up a policy to meet this target as outlined in The UK Renewable Energy Strategy [10].

1.2 Distributed Generators in Microgrids

Distributed energy resources (DERs) are important in ensuring continuous electricity supply. Integrating several DGs together and supplying a group of local loads forms a microgrid (MG). The Microgrid Exchange Group of the US Department of Energy defined the Microgrid as "*a group of interconnected loads*

and distributed energy resources within clearly defined electrical boundaries that act as a single controllable entity with respect to the grid. A Microgrid can connect and disconnect from the grid to enable it to operate in both grid-connected or island-mode" [11]. If grid connected, the MG requires an interface, which can be: a synchronous generator, asynchronous generator or power converter [4].

A MG has three unique features [12]:

1. The provision of an efficient means of integrating DERs with loads.
2. It is viewed by the main grid as a single autonomous entity.
3. It offers plug-and-play capabilities for the DERs, hence they can be added/removed without impacting the grid. This facilitates ease of installation of DERs without change in control strategy.

Renewable energy sources in MGs become a cost effective solution if the MG consists of hybrid energy sources [13]. This is specifically beneficial for solar and wind DERs, whose power generating capabilities are dependent on meteorological conditions. In order to ensure constant output power, it is common to find energy storage devices such as batteries and super capacitors within the MG. Generally, long term and short term energy storages with high energy and power densities respectively complement each other in the MG [14]. Long term storage systems (e.g. fuel cells and batteries) balance power supply and demand for extended periods while short term systems (e.g. super capacitors and flywheel) offer faster response speed for periods typically less than an hour [14, 15]. Incorporating energy storage in MGs is a fairly recent occurrence, as 90% of them have been included between 2011 and 2014 [16]. Energy storage devices are comparable to the spinning reserve of generators in the grid [17] and can offer short term voltage and frequency control.

Figure 1.2 shows DGs forming a MG consisting of both renewable (solar and wind) and non-renewable (diesel generator) DGs as well as connected loads. A battery and flywheel are used as energy storage devices. Both load and DGs are monitored by local controllers (LC) and microgeneration controllers (MC) respectively. The MG is connected to the main grid at the point of common coupling (PCC) with the connection controlled by the microgrid system central control (MGCC).

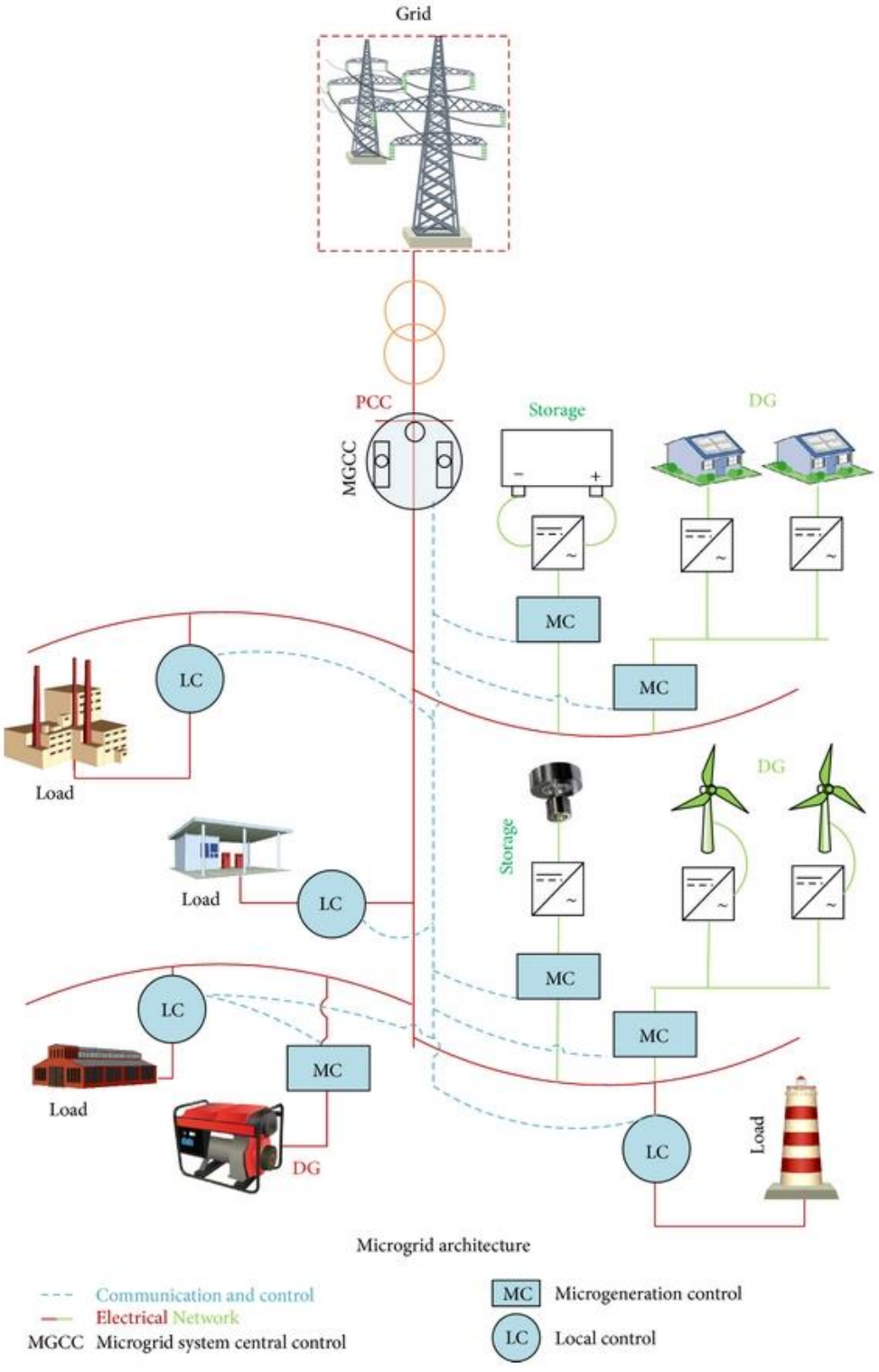

Figure 1:2: A typical microgrid with controllers and communication links [14]

1.3 Renewable Energy Sources for Distributed Generation

The renewable energy sources pertinent to this thesis are biomass and solar energies. These sources are described in the following sections.

1.3.1 Biomass Power Source

The word ‘biomass’ is the generic term that is used to describe all biological matter- living and non-living (for a short duration of time). It is therefore a vastly abundant renewable source of energy. According to Fischer and Schrattenholzer, the global biomass potential is estimated to be between 91 to 675 EJ/year for the years 1990 to 2060 [18]. Approximately 13.5 billion metric tons of available biomass (equivalent to 5%) can be used for producing energy [19]. With this amount, it is possible for biomass to provide roughly 26% of the world’s energy consumption [19].

Biomass comes from a vast number of sources including: forest residues, agricultural produce, sewage, industrial, animal and municipal solid wastes, as depicted in Fig. 1.3. These resources are abundant in virtually every developing country, therefore power generation from biomass can play a vital role in meeting the increasing load demand.

Figure 1:3: Sources of biomass [27]

Biomass is composed mostly of carbon, which was captured by plants in the form of carbon dioxide, CO_2 during photosynthesis producing carbohydrates in the form of glucose. This process can be expressed as [20]:

$$CO_2 + H_2O + hv\ (solar\ energy) \longrightarrow CH_2O\ (glucose) + O_2 \qquad (1.1)$$

When a plant is burnt, it returns to the atmosphere the carbon it had consumed in the process of growing. Biomass is therefore considered to be carbon neutral, as it does not increase the net amount of CO_2 in the atmosphere.

Plant-derived biomass is generally composed of cellulose, hemicellulose and lignin [21]. These are known as cell wall components and they protect the plant cells. Wood biomass can primarily be divided into: extractable (volatile oils, resin, wax, etc.), cell wall components and ash [21]. Extractables are derived from the living cell of a tree. Cell wall components form the major part of the wood and consist of lignin, cellulose and hemicellulose. Lignin binds the cellulose fibres together.

Recently, environmental concerns over greenhouse gas (GHG) emissions, coupled with the rising cost of fossil fuels have resulted in the need for exploring alternative sources of energy. As biomass can meet almost all demands currently met by fossil fuels [19], it is considered a viable option.

Despite its vast potential and availability, biomass is still underutilised. It has been estimated that biomass utilisation for electricity is less than 22% [19]. In view of this, investigation of biomass as a potential solution to power problems becomes an important area of research.

For any successful biomass power generation system, a number of factors must be considered. First, it must be ensured that the land used for growing biomass crops does not compete with that of growing food crops. Furthermore, the biomass power plant needs to be located near the source to reduce transportation costs, especially considering its low energy density [22].

1.3.1.1 Electricity Generation from Biomass

Biomass is effectively used for generating electricity through a process known as gasification, which involves heating the biomass in a limited supply of oxygen to produce synthesis gas. Biomass gasification is one of the most efficient means

of generating electric power in small scale power plants [23], with higher conversion efficiencies compared to combustion. However, the conventional fuel used in gasification to produce synthesis gas is coal [24], primarily due to its higher energy density and low moisture content compared to biomass [25]. The low energy density of biomass can be overcome through a process known as densification, which converts the biomass into pellets by reducing its moisture content and compressing it under high pressure [21]. The high moisture content of the biomass necessitates drying the feedstock prior to gasification.

Conversely, biomass gasification has the following merits compared to coal gasification [21]:

1. It has a higher percentage of volatile content (70-90%).
2. It contains water and oxygen, both of which help in the formation of gases from carbon rich feedstock.
3. It contains less than 2% ash as opposed to coal, with an ash content typically ranging between 5-20%.
4. The ash content may be used as fertiliser. Coal ash sometimes contains arsenic, which is a highly poisonous element.
5. The sulphur content is less than 0.1%, with coal having an amount ranging between 2-4%. High sulphur contents are associated with acid rain.

A biomass power plant typically consists of a biomass dryer, a gasifier, a gas clean-up system and a gas turbine-generator. Biomass drying reduces its moisture content though removal of water from its physical structure, leaving chemically bound water. For increase in system efficiency, it is possible to use the generated waste heat of gasifiers to dry the biomass feedstock [18].

In a gasifier, the biomass feedstock is heated in a restricted flow of oxygen with steam, producing synthesis gas (which predominantly comprises of carbon monoxide (CO) and hydrogen (H_2), with trace amounts of carbon dioxide (CO_2) and methane (CH_4)) as well as solid residues in the form of char and tar [26]. The chemical reaction for gasification can be expressed as [18]:

$$CH_xO_y(biomass) + O_2(21\%\ of\ air) + H_2O\ (steam) = CH_4 + CO + CO_2 + H_2$$

$$+ H_2O\ (unreacted\ steam) + C\ (char) + tar\ , \qquad (1.2)$$

where x, y respectively represent the hydrogen and oxygen content of the biomass uniquely dependent on its source.

In the gas clean-up system, impurities are removed from the synthesis gas prior to electricity production. The synthesis gas, at this point, has a calorific value ranging from 3- 5 MJ/m^3 [27]. It is then combined with air and combusted in the gas turbine, producing a mixture of hot gases. The expansion of these gases causes the rotation of the turbine. As the turbine is coupled to the shaft of a generator, the mechanical energy of the turbine is thereby converted to electricity by the generator.

1.3.2 Solar Photovoltaic (PV) Power Source

Unlike biomass which requires conversion into synthesis gas as a precursor to electricity generation, a solar PV array converts incident light directly into DC electricity. The greater the intensity of the solar energy, the higher the electric power produced. The basic building block of a PV array is a solar cell, which is a semiconductor p-n junction device that is most commonly made from silicon. Since solar cells produce approximately 0.5V [28], several such cells are connected together in series and/or parallel to form solar modules and arrays.

Figure 1.4 shows the one diode model representation of a solar cell. A photogenerated current, I_{PH} is produced by incident light falling on the surface of the solar cell. A parallel diode, *D* is used to represent the p-n junction [29] with current, I_D flowing through it. This current represents the diffusion of majority carriers across the p-n junction. Resistors, R_S and R_{SH} represent the internal

ohmic resistance and the leakage resistance of the semiconductor device respectively [29].

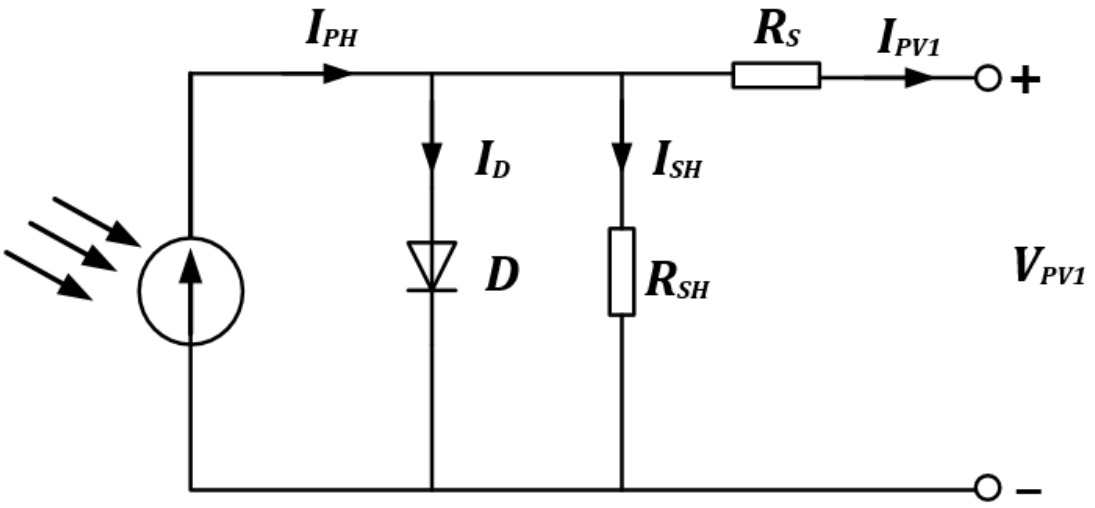

Figure 1:4: One diode equivalent circuit model of a solar cell

From Kirchhoff's current law, the PV cell current at the terminal of a solar cell, I_{PV1} is [30]:

$$I_{PV1} = I_{PH} - \underbrace{I_0 \exp\left(\frac{q(V_{PV1}+I_{PV1}R_S)}{AkT_C} - 1\right)}_{I_D} - \frac{(V_{PV1}+I_{PV1}R_S)}{R_{SH}}, \qquad (1.3)$$

where I_0 is the diode reverse saturation current,

q is the electron charge (1.602 × 10^{-19} *C*),

V_{PV1} is the PV cell voltage,

A is the diode ideality factor,

k is the Boltzmann's constant (1.38 × 10^{-23}*J/K*) and

T_C is the cell operating temperature.

PVs are capable of producing clean energy with the absence of any mechanical parts. However, silicon based solar cells have low conversion efficiencies of only about 23% [29].

1.3.2.1 PV Converters

The DC power generated by PV systems is converted to AC with DC-AC converters also known as inverters. At interfaces between the inverter and PV are DC-DC converters, which are primarily responsible for maintaining the PV output power at its maximum through control of the duty ratio, *d,* using maximum power point tracking (MPPT). DC-DC converter topologies may be classified according to their voltage level conversion as: step-down (buck) converter; step-up (boost) converter and a step-up-down (buck-boost) converter. The buck-boost converter is a cascaded combination of the step-down and step-up converter configurations, offering greater flexibility in the output voltage range. The inverting topology has the advantage of using a single switch compared to the non-inverting topology, resulting in reduced switching losses. The converter operates in step-down mode when *d* is less than 50%, and steps-up the input voltage when *d* is higher than 50%.

Inverters are classified according to the input power source as voltage source inverters (VSIs) or current source inverters (CSIs). VSIs require a large capacitor across the input of the inverter, which primarily consists of six switches, each of which is composed of a transistor and a free-wheeling diode for bidirectional current flow [31]. In CSIs, a DC current source supplies current to the inverter circuit through a large inductor. VSIs are the more common topology amongst the two and is employed in this thesis.

1.4 Benefits and Challenges of DG

Infiltration of DGs into the traditional electric power system has resulted in curbing power delivery costs through generation of power at distribution level. Consequently, transmission line losses are minimised. They are also capable of solving power outage issues, especially in developing countries [32-35]. Furthermore, DG plants running on RES are exempt from GHG emissions. Nevertheless, DGs are a fairly recent development [36] that face certain challenges as outlined below.

1. **High capital cost:** The price per kW of generators utilised in DGs are generally higher than centralised power plant generators [37]. Most renewable sourced DGs, except hydroelectricity, cannot compete

economically with the traditional generation techniques using fossil fuels. Some DG technologies, such as solar PV, gain economic benefits due to government incentives known as feed-in tariffs [38]. A levelised cost of energy (LCOE) comparison of power plant technologies by different resources has been done as shown in Table 1.1. From this, it is clear that costs of solar and wind powered DGs are reducing fast and possibly matching with the traditional gas powered generators.

Table 1.1: Estimated costs of power plant technologies [39, 40]

Power plant technologies	**2018 LCOE ($/MWh)**	**2015 LCOE ($/MWh)**	**Difference (%)**
Advanced coal with 30% CCS*	106.5	139.5	-24
Natural Gas-fired Conventional CC**	55	58.1	-5
Advanced Nuclear	73.5	102.8	-29
Geothermal	40.5	45	-10
Biomass	85.1	96.1	-11
Onshore Wind	51.3	64.5	-20
Offshore Wind	110.4	158.1	-30
Solar Thermal	137.5	235.9	-42
Solar PV	52.7	84.7	-38
Hydroelectric	49.6	67.8	-27

*CCS –Carbon capture sequestration
*CC –Combined cycle

2. Control complexity: Most DGs use power electronic inverters with pulse-width modulation techniques for DC-AC power conversion. To comply with the IEEE standard 519 for harmonic control, signal filtering is required to limit the total harmonic distortion (THD) in the output voltages and currents to the 5% maximum [41]. Inductor-capacitor-inductor (LCL) filters employed for this purpose offer good harmonic elimination, but at the expense of increased controller complexity

required to curb the resonance associated with the filter. Left undamped, LCL filter resonance may lead to system instability.

Controller complexity may increase even further due to the changes of resonant frequencies caused by the unpredictable nature of the renewable energy sources, and non-ideal grid conditions such as variable grid impedance and background harmonics.

3. Operation under unbalanced conditions: A power network is a complex and dynamic system. It is affected by continuous variations of loads, increasing interconnection and the unpredictable generating nature of renewable energy sources, disturbances and harmonics flowing along the lines. There are also occurrences of unbalanced voltage dips due to faults and current imbalance caused by unequal phase current drawing and feeding. In order to ensure stability in power supply, DGs are now required to remain connected to the grid for temporary faults [42]. Unbalanced grid faults have the effect of altering the symmetrical pattern of the voltage at the PCC through the production of a negative sequence voltage. Single-phase loads draw current in only one-phase, and the unbalance across the three-phases produces a negative sequence current in the power system. Negative sequence voltages and currents rotate in opposing directions to the conventional positive sequence voltages and currents. For single-phase loads, the interconnected DGs at the PCC supply the negative sequence currents of the load. The effect on synchronous generator-based DGs is the production of negative sequence electromagnetic torque, which causes rotor acceleration and excessive heating. For power electronic-based DGs, oscillations occur in the terminal active and reactive powers due to the opposing directions of the positive and negative sequence currents. The oscillations in the active power upset the power balance of the DC link voltage, leading to oscillations appearing in the voltage, which may exceed the maximum ripple voltage tolerance.

4. Protection Issues: Conventional protection schemes are not directly applicable to DGs forming a MG [7], as traditional power systems are not normally built with the intention of integration with DGs [43]. The presence of various DGs in the MG causes current flow to be multidirectional and protective relays must be adapted such that the MG can operate properly in both island and grid

connected modes [44-46]. Some DGs use an inverter interface for either power conversion or for maximum power extraction (e.g. solar modules) [45]. As the inverter switches are made of silicon, their current carrying capability cannot exceed twice their rated current [46-49]. On the other hand, machine based DGs can provide fault currents between 5-10 times their rated currents [50]. As such, MGs containing a combination of these DGs would need to have a wider range of fault current levels. At certain times, either due to planned activities such as MG maintenance, or unplanned activities such as faults, the MG may need to be disconnected from the main grid to form an island. When the MG shifts to island mode, it is required that there be a sufficient number of DGs that can offer high levels of fault currents. In the absence of these, there will be a significant change in short circuit current magnitude, rendering conventional protection schemes inadequate [44, 45]. Clearly, protection devices that operate based on fault current level only cannot be directly applied. Furthermore, some MGs consist of renewable sources that are intermittent in nature, and the short circuit current capacity is thereby subject to change. Thus, there is need for intelligent protection systems that consider the state of the current in the event of faults [42].

1.5 Techniques for Unbalanced Power System Analysis

Unbalanced voltages and currents can be analysed with Fortescue's theorem. The theory states that any set of unbalanced three-phase quantities may be converted into a set of three balanced phasors. These are: positive sequence components (PSC), negative sequence components (NSC) and zero sequence components (ZSC). According to this theory:

- PSC comprise of three phasors of the same magnitude and displaced 120^{o} apart with the same phase sequence as the original phasors i.e. abc phase sequence.
- NSC comprise of three phasors of the same magnitude and displaced 120^{o} apart with the opposite phase sequence as the original phasors i.e. acb phase sequence.
- ZSC comprise of three phasors of the same magnitude with no phase displacement between the phasors.

With PSC denoted by '+', NSC denoted as '-' and ZSC denoted by '0', an unbalanced voltage represented by phasors V_a, V_b and V_c can be written as:

$$V_a = V_a{}^0 + V_a{}^+ + V_a{}^- \quad (1.4)$$

$$V_b = V_b{}^0 + V_b{}^+ + V_b{}^- \quad (1.5)$$

$$V_c = V_c{}^0 + V_c{}^+ + V_c{}^-. \quad (1.6)$$

The symmetrical sequence components described by Equs. (1.4) - (1.6) are shown in Fig. 1.5.

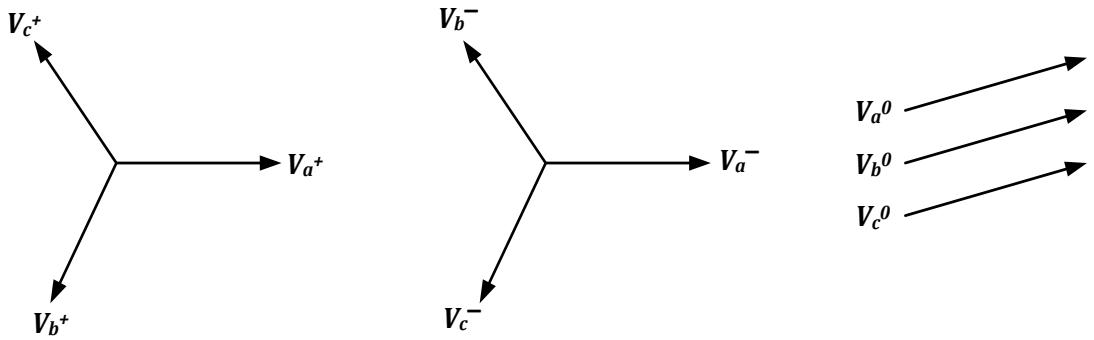

(a) (b) (c)

Figure 1:5: Three phase voltage symmetrical sequence components (a) positive sequence (b) negative sequence (c) zero sequence

Analysis can be further simplified by defining phase voltages V_b and V_c in terms of V_a using a phase operator, α given by:

$$\alpha = 1\angle 120° \quad (1.7)$$

and

$$\alpha^2 = 1\angle 240°. \quad (1.8)$$

In terms of α, Equs. (1.4) - (1.6) can be re-written as:

$$V_a = V_a{}^0 + V_a{}^+ + V_a{}^- \quad (1.9)$$

$$V_b = V_a{}^0 + \alpha^2 V_a{}^+ + \alpha V_a{}^- \quad (1.10)$$

$$V_c = V_a{}^0 + \alpha V_a{}^+ + \alpha^2 V_a{}^-. \quad (1.11)$$

And in matrix form:

$$\begin{bmatrix} V_a \\ V_b \\ V_c \end{bmatrix} = \begin{bmatrix} 1 & 1 & 1 \\ 1 & \alpha^2 & \alpha \\ 1 & \alpha & \alpha^2 \end{bmatrix} \begin{bmatrix} {V_a}^0 \\ {V_a}^+ \\ {V_a}^- \end{bmatrix}. \quad (1.12)$$

The sequence components ${V_a}^0, {V_a}^+$and ${V_a}^-$ can be obtained from Equ. (1.12) by taking the inverse of the matrix, resulting in:

$$\begin{bmatrix} {V_a}^0 \\ {V_a}^+ \\ {V_a}^- \end{bmatrix} = \frac{1}{3} \begin{bmatrix} 1 & 1 & 1 \\ 1 & \alpha & \alpha^2 \\ 1 & \alpha^2 & \alpha \end{bmatrix} \begin{bmatrix} V_a \\ V_b \\ V_c \end{bmatrix}. \quad (1.13)$$

In a three-phase three-wire system, the sequence components of the abc voltages and currents sum up to zero, indicating there are no zero sequence components. A three-phase four wire system, on the other hand, has a neutral wire which carries three-times the zero sequence current.

1.6 Grid Synchronisation Techniques Under Balanced and Unbalanced Conditions

Interconnection of power electronic DGs with the electric power grid require synchronisation through precise estimation of the grid phase angle. Grid synchronisation under balanced conditions is most commonly achieved through the synchronous reference frame - phase locked loop (SRF-PLL), described in section 1.6.1.

1.6.1 The Synchronous Reference Frame-Phase Locked Loop (SRF-PLL)

The basic principle of a PLL technique according to the SRF is illustrated in the block diagram of Fig. 1.6. The technique is used to track the phase angle, $\theta\ (\omega t)$ of the grid voltage vector, V_{gabc} and consists of the following basic parts [31]; a phase detector (represented by a simple multiplier), a loop filter (represented by a proportional-integral, PI controller) and a voltage controlled oscillator (represented by a linear integrator).

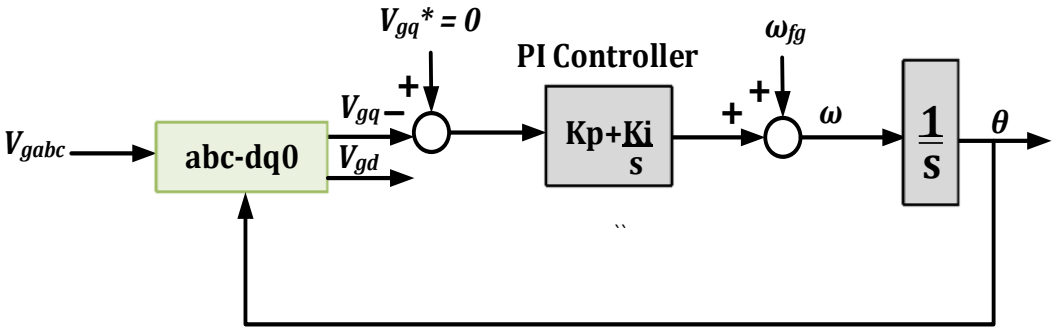

Figure 1:6: Block diagram for SRF-PLL system

According to Fig. 1.6, the PLL operates using a closed-loop control scheme which converts the grid voltage vector, V_{gabc} into SRF, with either the d or q element of the vector (V_{gd} or V_{gq}) as feedback variable. Assuming an arbitrary initial voltage phase angle value, θ the measured grid three-phase voltage, V_{gabc} can be transformed to its equivalent SRF d-q frame by aligning the d-axis voltage, V_{gd} with phase A of the grid voltage, V_{ga} using the following Park's transform equation:

$$\begin{bmatrix} V_{gd} \\ V_{gq} \end{bmatrix} = \frac{2}{3} \begin{bmatrix} \cos\theta & \cos\left(\theta - \frac{2\pi}{3}\right) & \cos\left(\theta + \frac{2\pi}{3}\right) \\ -\sin\theta & -\sin\left(\theta - \frac{2\pi}{3}\right) & -\sin\left(\theta + \frac{2\pi}{3}\right) \end{bmatrix} \begin{bmatrix} V_{ga} \\ V_{gb} \\ V_{gc} \end{bmatrix}. \quad (1.14)$$

Taking the q-element as the feedback variable, V_{gq} is controlled by the loop PI controller to zero while the d-component voltage, V_{gd} becomes the magnitude of the positive-sequence input voltage [31].The grid phase angle, θ is obtained by integrating the estimated frequency, ω which is the sum of the PI-controller output and the feedforward grid frequency, ω_{fg}. As the PI controller regulates V_{gq} to 0, ω is equivalent to ω_{fg} and its integral value will therefore be the grid phase angle, θ. Figure 1.7 depicts phase angle estimation using the SRF-PLL scheme. Figure 1.7 (a) is the grid voltage and the estimated phase angle, θ is shown in Fig. 1.7 (b). As observed, the SRF-PLL has accurately detected the sinusoidal phase angle, θ with a fundamental frequency of 50 *Hz* (equivalent to *0.02 seconds*).

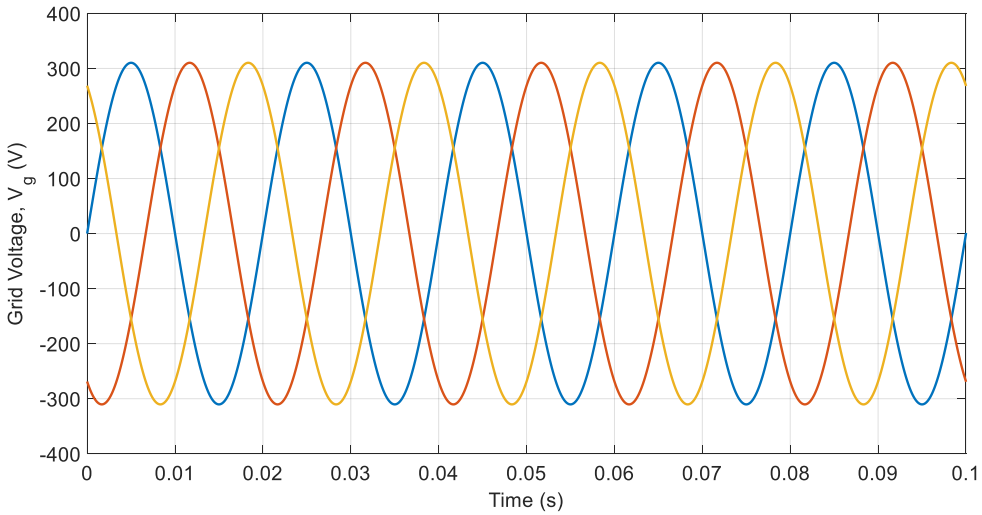

(a)

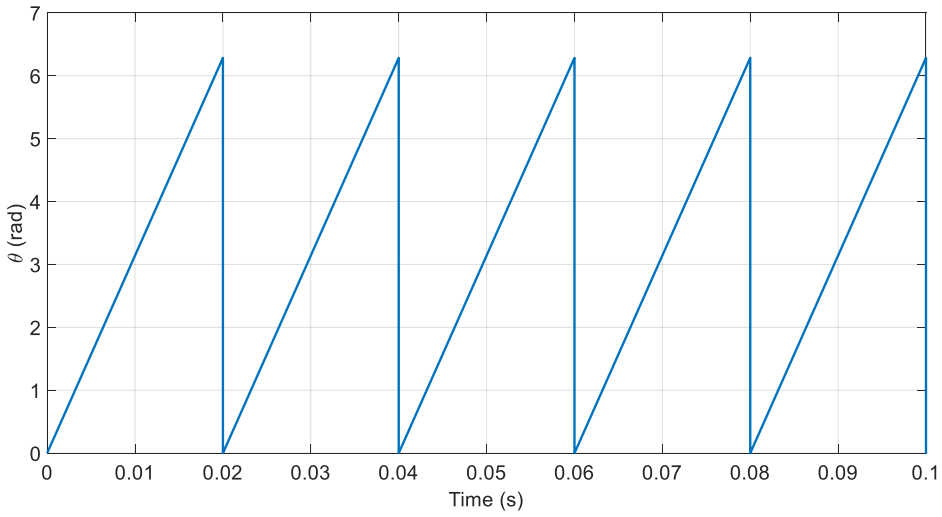

(b)

Figure 1:7: SRF-PLL (a) Grid voltage (b) SRF-PLL angle tracking

For an ideal grid free from harmonic distortion or unbalance, phase angle can easily be detected using the SRF-PLL of Fig. 1.6. In cases where harmonics are the cause of grid distortion, a reduction in PLL bandwidth has proven to be an effective method of extracting pure sinusoidal signals [31]. However, in an unbalanced voltage situation, imposing a limitation on the PLL bandwidth alone is not an effective method of phase angle tracking [31]. Figures 1.8 (a) and (b) show ineffective tracking of the grid phase angle, θ with SRF-PLL under unbalanced grid voltages. Clearly, advanced techniques are required to

accurately detect the grid voltage phase angle in the presence of voltage unbalance.

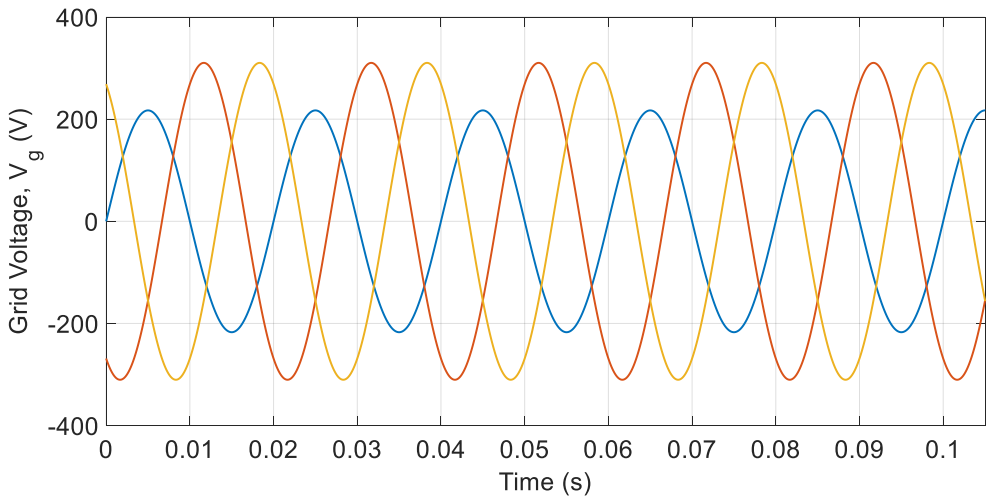

(a)

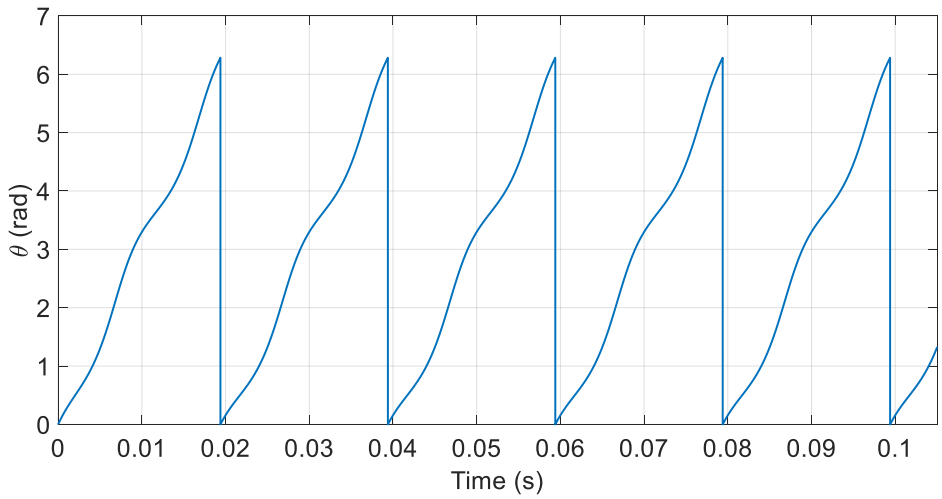

(b)

Figure 1:8: SRF-PLL with voltage unbalance (a) Grid voltage (b) SRF-PLL phase angle tracking

1.6.2 Decoupled Double Synchronous Reference Frame-PLL (DDSRF-PLL)

Figure 1.9 depicts an unbalanced voltage vector, *V* transformed into its equivalent positive (dq^+) and negative (dq^-) sequence components in the double SRF (DSRF). The positive sequence component of the voltage, denoted as V^+ rotates with speed, ω while the negative sequence component of the voltage,

represented by V^-, rotates with speed, $-\omega$.When projected onto the DSRF, the vectors rotate with a speed of ω' and $-\omega'$ in the dq^+ and dq^- frames respectively.

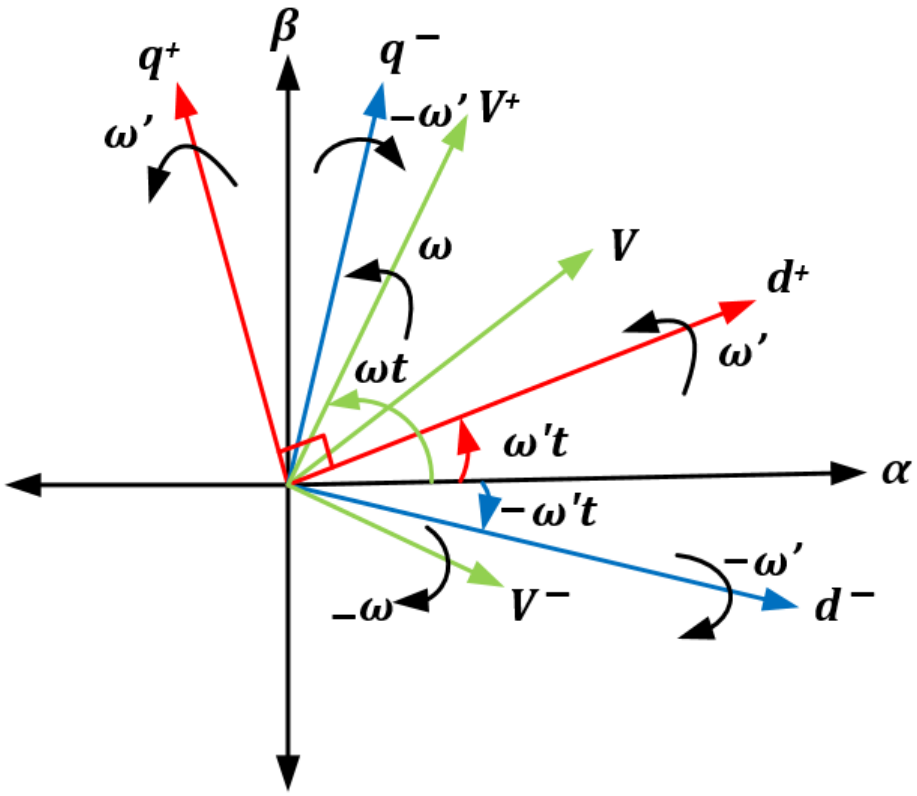

Figure 1:9: Voltage vectors in the DSRF

In the *αβ*-frame, V may be expressed using Clarke's transformation as:

$$V_\alpha = V^+ \cos \omega t + V^- \cos(-\omega t) \tag{1.15}$$

and

$$V_\beta = V^+ \sin \omega t + V^- \sin(-\omega t). \tag{1.16}$$

Assuming the d-axis position is perfectly aligned to the positive sequence component of the input voltage (i.e. $\omega' t = \omega t$), applying Park's transform to Equs. (1.15) and (1.16) and simplifying using trigonometric identities will yield:

$$\begin{bmatrix} V_d{}^+ \\ V_q{}^+ \end{bmatrix} = [T_{dq}{}^+] \begin{bmatrix} V_\alpha \\ V_\beta \end{bmatrix} = V^+ \begin{bmatrix} 1 \\ 0 \end{bmatrix} + V^- \begin{bmatrix} \cos(2\omega t) & \sin(2\omega t) \\ -\sin(2\omega t) & \cos(2\omega t) \end{bmatrix} \tag{1.17}$$

and

$$\begin{bmatrix} V_d{}^- \\ V_q{}^- \end{bmatrix} = [T_{dq}{}^-] \begin{bmatrix} V_\alpha \\ V_\beta \end{bmatrix} = V^+ \begin{bmatrix} \cos(2\omega t) & -\sin(2\omega t) \\ \sin(2\omega t) & \cos(2\omega t) \end{bmatrix} + V^- \begin{bmatrix} 1 \\ 0 \end{bmatrix}, \tag{1.18}$$

where $\left[T_{dq}{}^{+}\right] = \left[T_{dq}{}^{-}\right]^{T} = \begin{bmatrix} \cos(2\omega t) & \sin(2\omega t) \\ -\sin(2\omega t) & \cos(2\omega t) \end{bmatrix}$.

It is clear from Equs. (1.17) and (1.18) that transforming an unbalanced three-phase voltage signal to its equivalent dq-components results in cross coupling terms that rotate at twice the fundamental frequency, 2ω. As these AC terms cannot be tracked by a PI controller without steady state errors, they must be eliminated. A low pass filter could be used, but the challenge is ensuring that the filter is perfectly capable of attenuating the 2ω frequency, especially in the case of a frequency sensitive grid. To address this issue, the DDSRF method in [31] is employed to ensure perfect cancellation of the unwanted frequencies through implementation of a decoupling network based on Equs. (1.17) and (1.18) as seen in Fig. 1.10 (a) and (b). Both positive and negative decoupling cells take as inputs the voltage components, $V_d{}^{+}, V_q{}^{+}, V_d{}^{-}$ and $V_q{}^{-}$ to produce intermediate terms $V_d{}^{+*}, V_q{}^{+*}, V_d{}^{-*}$ and $V_q{}^{-*}$. These terms are further processed by a low pass filter (LPF) to ensure effective cancellation of the 2ω harmonics.

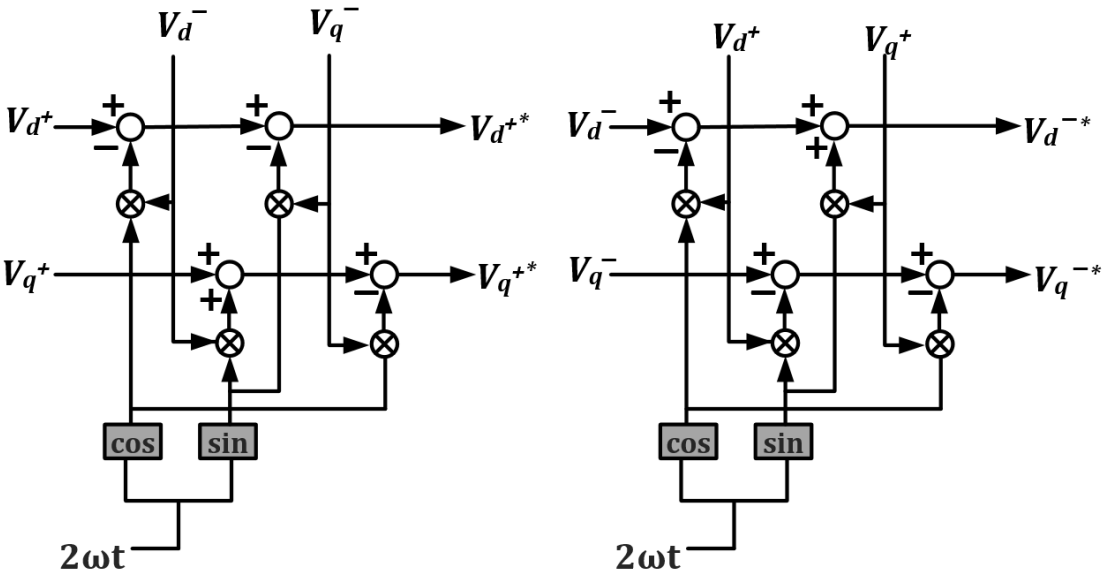

(a) (b)

Figure 1:10: DDSRF decoupling cells (a) positive and (b) negative decoupling cells

The DDSRF-PLL schematic is illustrated in Fig. 1.11. The unbalanced grid voltage, V_{gabc} is transformed into the DSRF with the positive and negative components of the detected phase angle, θ ($\theta^{+}$and θ^{-}). The components

V_d^+, V_q^+, V_d^- and V_q^- are decoupled with the cells in Fig.1.10. The outputs from the decoupling block, $V_d^{+*}, V_q^{+*}, V_d^{-*}$ and V_q^{-*} are passed through a LPF of cut-off frequency, ω_f with transfer function:

$$G_{LPF}(s) = \frac{\omega_f}{s+\omega_f}, \tag{1.19}$$

finally producing the harmonic-free output terms $\overline{V_d}^{+*}$, $\overline{V_q}^{+*}, \overline{V_d}^{-*}$ and $\overline{V_q}^{-*}$.

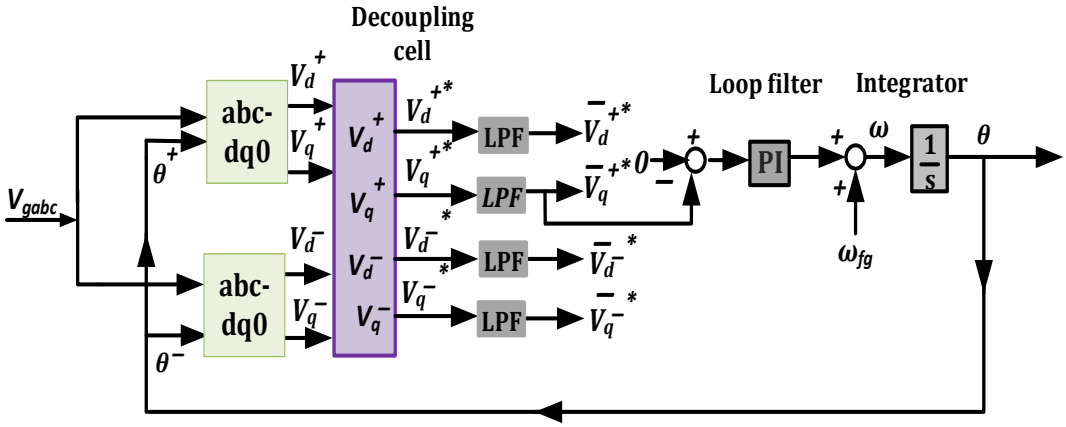

Figure 1:11: DDSRF-PLL with decoupling cell

With the implementation of the DDSRF-PLL, the grid phase angle, θ of the unbalanced grid voltage in Fig. 1.8 (a) is accurately detected as 50 Hz (*0.02 seconds*) as seen in Fig. 1.12.

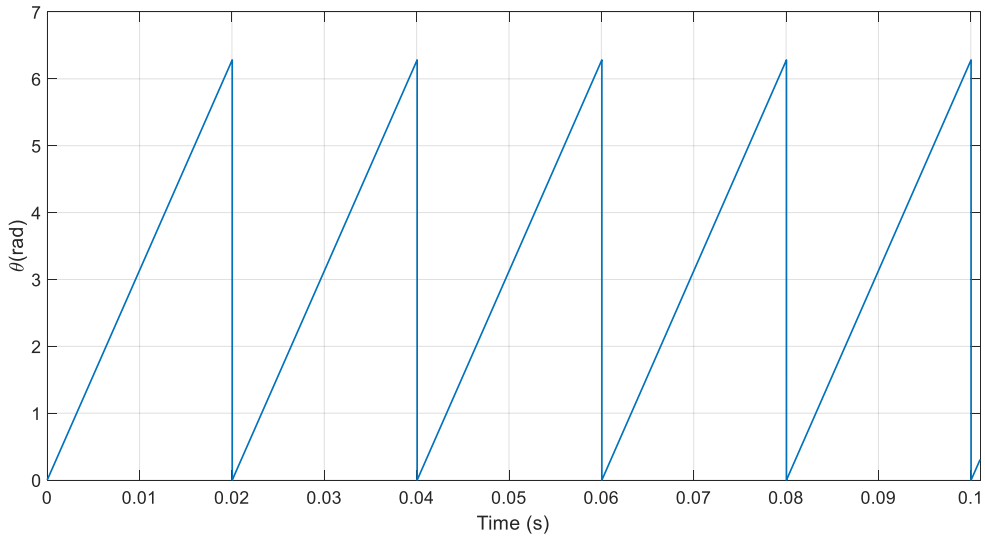

Figure 1:12: DDSRF-PLL phase angle tracking under voltage unbalance

1.7 Problem Statement, Aims and Objectives

The ever increasing penetration of DGs into the electric power grid can cause severe impacts on the operational performance and stability of the grid, unless they fulfil some strict requirements. One of these is the compliance with the stringent limitations for frequencies above a certain threshold set by the grid code. This can be achieved since most DGs with VSI-based converters are equipped with carefully tuned LCL filters. However, the resonances created by these high order filters in response to the grid background harmonics are a serious issue for grid-tie inverter stability. Worse still, the resonant frequencies may change due to grid impedance variation. Advanced control schemes able to track and eliminate the variable frequency harmonics are the key to coping with the condition. Another requirement is DGs being able to ride-through voltage dips due to transient grid faults without interruption in order to maintain power delivery, hence supporting the grid [31]. The proper control strategy for DGs under such conditions may result in unbalanced and distorted current injection to attenuate power oscillations and boost the instantaneous active and reactive powers.

The main aim of this thesis, therefore, is to develop advanced control schemes for distributed generation systems for robust operation under unbalanced and distorted grid conditions. The analysis, design and verification of the control schemes need to be performed on renewable sourced DGs, thus another aim is to develop computer models for a biomass synchronous generator-based DG and a PV power electronic-based DG. A hybrid DG system is also considered, comprising of the biomass DG and the PVDG with line impedances and connected loads as shown in Fig. 1.13.

The following specific objectives are defined to achieve the above project aims:

1. To study the composition viability of biomass as a valuable energy source, its energy conversion process and electricity generation technique. Hence to develop a computer model of a biomass powered turbine driving a synchronous generator and assessing its operational performance in response to load perturbations.
2. To design and develop a computer model of an LCL filter for PV grid-connected inverters and investigate passive and active damping schemes for resonance suppression.

3. To investigate and design a novel adaptive notch filter technique for active harmonic suppression under variable grid impedance.
4. To simulate a grid-connected hybrid DG system consisting of a biomass sourced generator and a PV-power plant supplying multiple loads and to investigate and develop current control strategy for DG inverters which are able to alleviate the adverse effects of unbalanced loads on the hybrid biomass-PV DG system.
5. To analyse the existing techniques and propose novel reference current generation and control schemes which can enhance fault ride through capabilities of the PVDG system under unbalanced grid faults.

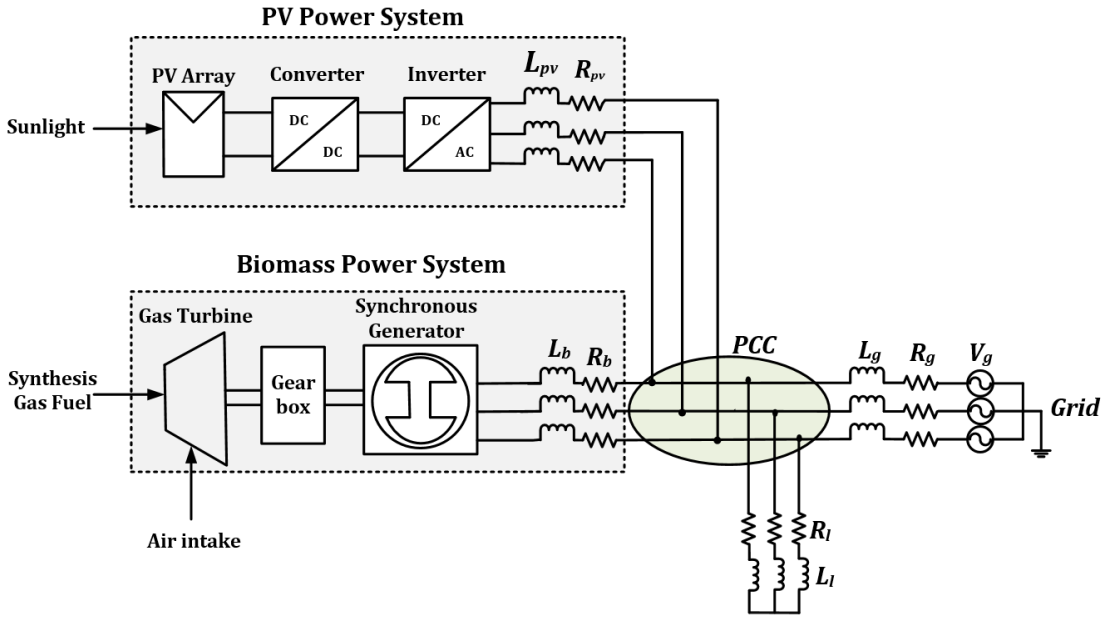

Figure 1:13: Schematic diagram of proposed hybrid biomass-PV DG system

1.7.1 Thesis Contributions

The major contributions of this thesis are as follows:

- A detailed model for the BDG is built in simulation consisting of a gas turbine and synchronous generator with associated control systems. The main control variable in the gas turbine is its speed, which is regulated with the General Electric Mark IV Speedtronic Turbine Control System. The generator excitation is controlled with the IEEE AC5A brushless excitation system which ensures the terminal voltage of the generator is maintained within pre-defined limits. The operational responses of the BDG model

are analysed when subjected to load variations. Transient stability studies performed on the BDG with varying levels of the system inertia constant shows the system stability is enhanced with higher levels of the inertia constant.

- A novel ANF for actively damping the resonance effect of the grid converter's LCL filter under dynamic grid conditions such as line impedance variations. The adaptive feature of the NF is realised using the FFT method which analyses the spectrum of the measured grid current and determines the highest frequency present within the signal as the resonant frequency. The NF center frequency is tuned to the resonant frequency, thereby ensuring effective damping. A variation in grid impedance further perturbs the resonant frequency, prompting the activation of FFT spectrum analysis in determining the new resonant frequency and correspondingly retuning the NF frequency. This method ensures injection of harmonic-free current to the grid in compliance with grid codes.
- A novel optimised flexible power control (OFPC) method of generating reference currents for a PVDG under unbalanced grid voltages. The effect of the unbalanced voltages are the generation of negative sequence components in the grid voltages and currents, resulting in ripples in both the active and reactive powers generated by the PVDG. Through constrained multi-objective optimisation implemented using the genetic algorithm, both active and reactive power ripples are minimised by defining a cost function as the weighted sum of the two power ripples. The control variable providing the optimal solution to the genetic algorithm is utilised to compute the reference currents for the PVDG. Simulation results comparing the OFPC with conventional methods proves its advantages with regards to simultaneous suppression of active and reactive powers, reduction of DC link fluctuations as well as ensuring the maximum PV inverter current is not exceeded.

1.8 Thesis Organisation

Chapter 2 provides a detailed mathematical model for the biomass DG with the control systems for the gas turbine and synchronous generator. Simulation

studies for system responses and transient stability are performed under load disturbances.

Chapter 3 describes the design and control process for a grid connected PVDG system using LCL- filters. Notch filter-based active damping is proposed for the LCL filter and analysis of the notch filter in terms of control system stability is performed.

Chapter 4 presents a new adaptive notch filter scheme for grid impedance variations based on the advanced fast Fourier transform (FFT) signal processing technique.

Chapter 5 investigates the hybrid biomass-PV DG responses to an unbalanced load and proposes an unbalanced load compensation scheme utilising the PV inverter control system, to mitigate the negative effects of the unbalanced load currents.

Chapter 6 describes a novel optimised flexible power control (OFPC) scheme for simultaneous suppression of active and reactive power generated by the PVDG under unbalanced grid voltages. The scheme is based on the principle of constrained multi-objective optimisation using Genetic Algorithms.

Chapter 7 concludes the thesis and provides recommendations for future work.

Chapter 2 Biomass Distributed Generator Modelling

2.1 Introduction

Biomass distributed generators (BDGs) are gradually gaining prominence, owing to the diverse and renewable nature of biomass sources as described in Chapter 1 [51]. For electricity production, biomass may be converted to synthesis gas through an efficient thermochemical process known as gasification [52, 53]. The synthesis gas is utilised in a gas turbine, where the chemical energy of the gas is converted into rotational mechanical energy in the turbine shaft. The mechanical energy is further transformed into electrical energy by a generator coupled to the turbine shaft.

Gas turbines may be classified according to their generating capacity, the smallest of which are known as micro-turbines [54]. Micro-turbines generate up to 500 kW and are most widely used in distributed generation [54, 55]. Rotational speeds are in the range of 50,000 to 120,000 revolutions per minute (rpm) [56]. As generators rotate at a slower speed, a speed reduction gearbox must be incorporated in the biomass distributed generator to act as an interface between the gas turbine and the generator.

Virtually all power system generators are of the synchronous type [57]. Synchronous generators run at a speed synchronised with the frequency of the utility grid. Through modification of their field excitation, synchronous generators are able to supply reactive power for connected inductive and capacitive loads [58]. Alternatively, they can source or sink reactive power for line voltage support [59]. For this purpose, they are known as synchronous condensers.

Crucial to the satisfactory performance of any synchronous generator-based power system is its ability to remain in synchronous operation after a transient disturbance [60]. This is known as the rotor angle stability, which together with frequency and voltage stability [61] form the main stability indicators of a synchronous machine.

This chapter presents a systematic approach to the modelling of a grid connected BDG. The developed model is used to study the dynamics of the system and the control responses to typical disturbances such as load variations. The chapter is divided into four main parts. In the first part, the energy conversion process of

biomass is presented. In part two, detailed mathematical models are presented for the gas turbine and synchronous generator, which collectively form a biomass distributed generation unit suitable for grid connected operation. The third part describes the control systems for the turbine and generator models. Finally, the fourth part focuses on testing the transient stability of the system under a sudden change in electrical power modelled as a load disturbance.

2.2 Energy Conversion of Biomass

Stored energy in biomass fuels can be released by converting the biomass into gaseous or liquid forms. There are typically two major conversion processes for biomass: thermochemical and biochemical processes [18]. The selection of the conversion process depends on a number of factors, including the moisture content of the biomass feedstock, as well as its chemical composition. Feedstock with a high moisture content is usually converted using biochemical processes, whereas feedstock with less moisture (less than 40%) are more suited for thermochemical conversion [20].

Plant biomass such as wood comprises of up to 50% cellulose and 30% lignin [62]. While cellulose is insoluble in aqueous solutions, lignin is indigestible by enzymes [62]. Consequently, high proportions of cellulose and lignin within biomass feedstock indicates that thermochemical conversion process is desirable.

The biochemical and thermochemical biomass conversion processes and their main classifications with associated products are shown in Fig. 2.1. The products of the conversion depend on the content of the biomass itself. Biochemical conversion consists of: anaerobic digestion, aerobic digestion and fermentation. Thermochemical conversion is classified into: combustion, gasification and pyrolysis. Brief descriptions of the processes are outlined below.

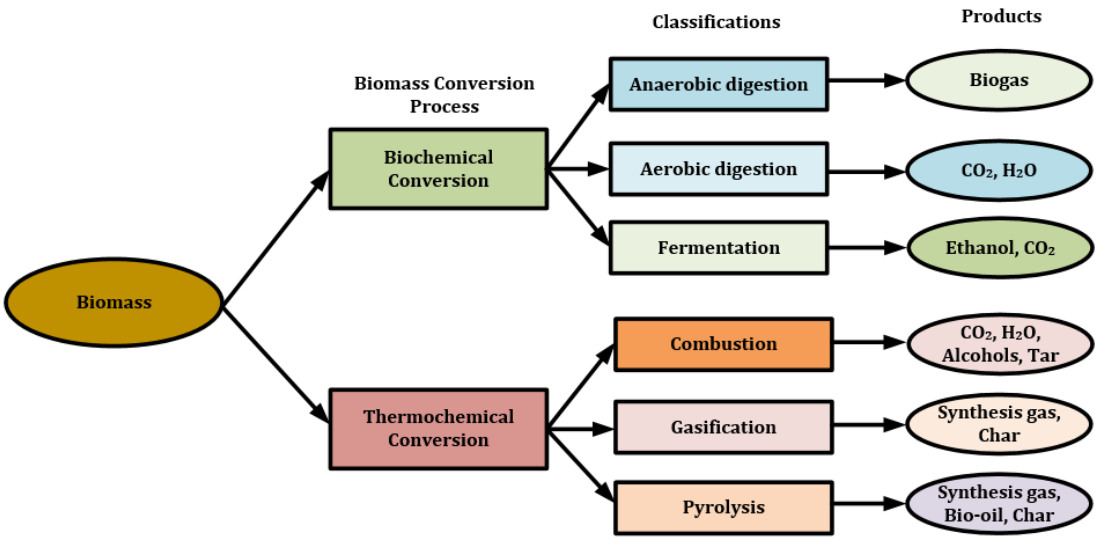

Figure 2:1: Biomass conversion processes

2.2.1 Biochemical conversion

This involves the use of micro-organisms to breakdown biomass into biofuel, mostly liquids and gases. The main disadvantage of biochemical conversion is that the process is relatively slow, with lower conversion efficiencies compared to thermochemical conversion [63]. It is classified into:

- **Anaerobic digestion:** This is the most common method of biochemical conversion. It involves the breakdown of biomass by micro-organisms in the absence of oxygen to produce biogas, which is a mixture of methane and carbon dioxide. As the main product of the process is methane, anaerobic digestion is also known as biomethanation [63]. It produces 65-70% methane (CH_4), 30-35% carbon dioxide (CO_2), with small amounts of hydrogen sulphide (H_2S) and hydrogen (H_2) [63, 64]. As a by-product, a solid residue known as 'digestate' is produced, which can be used as fertilizer for soil conditioning [26, 65]. Anaerobic digestion is most suitable for wet biomass such as sewage, high moisture agricultural biomass, animal and human wastes [26, 65]. Depending on the temperature range, three basic anaerobic digestion processes can take place [23, 26]:

  Psychrophilic digestion: This takes place at temperatures less than $30^{O}C$ and is very slow. In some cases, external heating may be required to speed up the conversion process.

Mesophilic digestion: This occurs between 30^{O}C and 40^{O}C, with a slow completion time of up to 2 months.

Thermophilic digestion: This takes place at higher temperatures of between 40^{O}C to 55^{O}C, resulting in a faster conversion process compared to psychrophilic and mesophilic digestion**.**

- **Aerobic digestion:** Aerobic digestion, as the name implies, occurs in the presence of air, producing heat, carbon dioxide and water. As no amount of methane is produced, it is unsuitable for bioenergy production [64, 66].
- **Fermentation:** This is the anaerobic breakdown of biomass by yeast to produce ethanol and carbon dioxide. Ethanol is currently being used as a transport fuel, where it is blended with either gasoline or diesel. This use of ethanol helps to reduce air pollution. However, bio-fuels tend to be more expensive compared to using petroleum fuels alone [67].

2.2.2 Thermochemical conversion

In this conversion process, heat energy is used to breakdown the biomass material to release bioenergy. Thermochemical conversion has an advantage over biochemical conversion as it may be used for a wider range of biomass, including agricultural and municipal solid wastes [18]. The disadvantage, however, is that the synthesis gas produced requires extra cleaning equipment to purify the gas from char, tar and other contaminants [18]. The major classifications of thermochemical processes are: direct combustion, gasification and pyrolysis.

- **Combustion:** This is the oldest method of obtaining energy from biomass and it involves burning the organic material in the presence of air to release heat. It accounts for 97% of the world's bioenergy production [63]. It is the most common method of extracting power from agricultural products. The products of combustion consist of CO_2, H_2O, alcohols and tar [63].

  However, direct combustion is an inefficient process owing to the amount of energy wasted in the process (between 20-40%) [18, 20]. Further reductions in efficiency occur due to high moisture content of feedstock and incomplete combustion [63]. Biomass conversion through combustion

is most suitable for feedstock with a moisture content less than 50%, as anything higher is more suitable for biochemical conversion [63].

Gasification: This involves heating biomass in a limited supply of oxygen, producing a mixture of gases commonly referred to as producer gas. The biomass feedstock may be pre-heated to reduce the moisture content to about 25%, before further drying occurs in the gasifier [63]. If the process occurs at a low temperature range of between $700^{O}C$ to $1000^{O}C$,the producer gas will comprise higher levels of hydrocarbons as compared to high temperature gasification. High temperature gasification, which occurs between $1200^{O}C$ and $1600^{O}C$, produces fewer hydrocarbons, with higher proportions of *CO* and H_2, forming synthesis gas (syngas). Syngas predominantly comprises of hydrogen and carbon monoxide [26].

Both air and oxygen may be used as gasifying agents. Air gasification is the simplest and cheapest form of gasification, producing a low energy syngas less than 150 Btu/SCF due to dilution of air with nitrogen [21]. Oxygen gasification, on the other hand, produces syngas with a higher calorific value ≥300 Btu/SCF [21]. For complete combustion, the equivalence ratio (ER), which is oxidant to fuel ratio divided by the stoichiometric ratio, is greater than or equal to 1. Both oxygen and air gasification occur with low equivalence ratios of between 0.25 to 0.3 (since little air is used), leading to the production of small portions of methane [21].

The nature of the biomass feedstock determines the type of gasifier used. For information on gasifier classifications, see Appendix A.

A sample computation of syngas composition from wood biomass using the thermodynamic equilibrium model is described in Appendix B.

- **Pyrolysis:** Similar to gasification, pyrolysis involves heating the biomass feedstock to very high temperatures to produce synthesis gas. The major difference between pyrolysis and gasification is that pyrolysis involves anaerobic heating of the biomass feedstock. Other products of pyrolysis include bio-oil and solid char. When the process occurs at lower

temperatures of about 400^{O}C, more solid char is produced. Higher temperatures of around 500^{O}C favour more bio-oil production [26].

From the economic point of view, the cost of electricity production from biomass is lower for combustion compared to gasification. If biogas from anaerobic digestion is combusted, cost is further reduced due to the absence of gas clean-up equipment. However, combustion requires larger portions of biomass feedstock for the same electrical output as the gasification process [68]. Although gasification has a higher conversion efficiency, the capital cost required for the gasifier and gas cleaning equipment is high.

2.3 Biomass Distributed Generator Configuration

The biomass distributed generator (BDG) shown in Fig. 2.2 consists of a gas turbine driving a synchronous generator. The two components are interfaced by a speed reducing gear box. The BDG connects to the main grid at the PCC via the line resistance, R_b and line inductance, L_b. The grid is represented by its Thevenin equivalent voltage, V_g, in series with the grid resistance (R_g) and inductance (L_g). A load represented by resistance, R_l and inductance, L_l connected at the PCC represents the load supplied by the BDG.

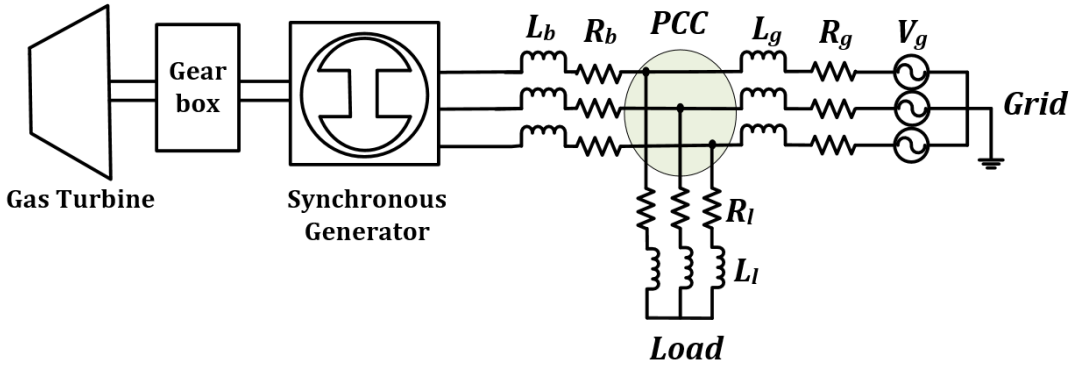

Figure 2:2: Biomass distributed generator connected to the grid

The operating principles of the gas turbine and synchronous generator are briefly described in the following sections.

2.3.1 Gas Turbine

A gas turbine is an internal combustion engine which utilises the energy in air to convert the chemical energy in a fuel into mechanical energy. Its major parts are: the axial flow compressor, combustion chamber and multistage expansion turbine mounted on a single-shaft as seen in Fig. 2.3. Both the turbine and compressor consist of alternate rows of stationary and rotating blades. The gas turbine takes in air and fuel as its primary input variables to produce the output mechanical power required to drive the connected generator.

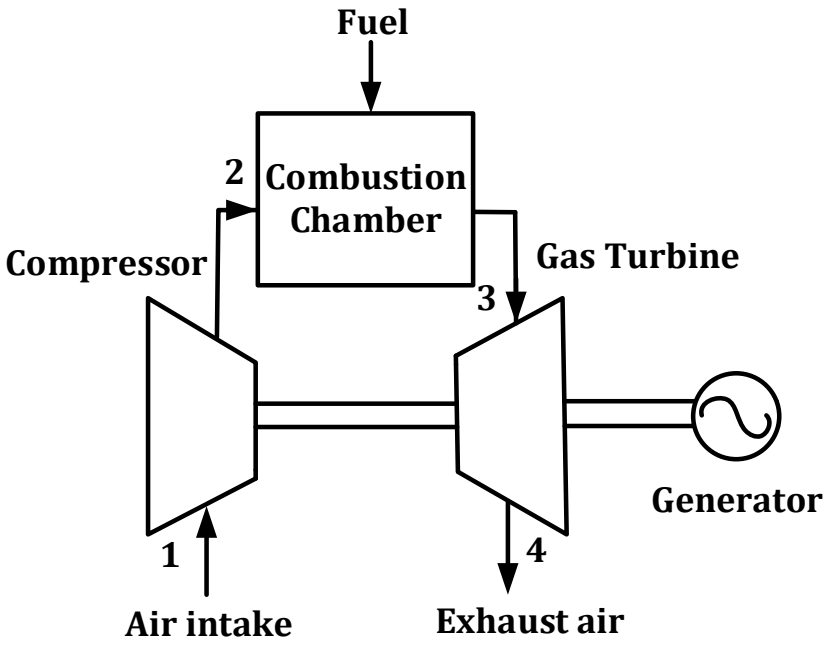

Figure 2:3: Single-shaft gas turbine

The operating principle of the gas turbine in Fig. 2.3 is based on the Brayton cycle, with air as the working fluid. The heat transfer occurring in Fig. 2.3 at points 1, 2, 3 and 4 can be visualised on the temperature-entropy (T-S) axis of Fig. 2.4. The points represent reversible stages in the heat transfer process of the Brayton cycle. Points 2s and 4s in the T-S axis represent ideal isentropic processes, which are both reversible and adiabatic (i.e. no transfer of heat to the surrounding) [69]. The 4 stages of the cycle are described as follows:

1-2 isentropic compression: Air at ambient conditions (temperature and pressure) is drawn from point 1 into the compressor through the inlet guide vanes

(IGVs). The air is compressed into a high temperature and pressure gas at point 2 before being passed to the combustor.

2-3 isobaric combustion: Compressed air in the combustion chamber is mixed with the fuel and ignited, raising the temperature of the air-fuel mixture up to point 3.

3-4 isentropic expansion: The heated gases move from the combustor to the turbine, where they are expanded to point 4 with a drop in temperature, causing the rotation of the shaft, which in turn drives the connected generator. The total power generated by the turbine is therefore used to drive the compressor, with residual energy for powering the rotating shaft.

4-1 isobaric expulsion: expelled air at point 4 loses energy and falls back to initial temperature at point 1.

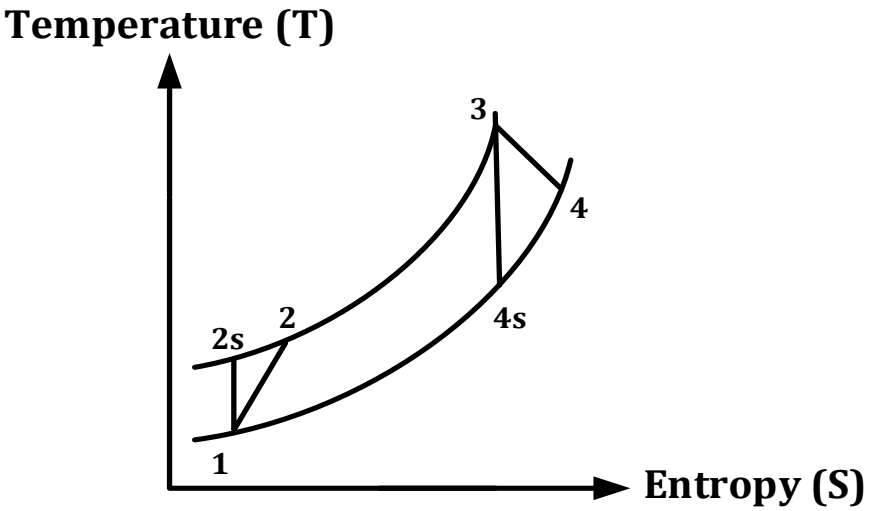

Figure 2:4: Brayton cycle in temperature-entropy axis

2.3.2 Synchronous Generator

The synchronous generator at the terminal of the gas turbine produces an AC voltage through the interaction of its rotor (field) windings and stator (armature) windings as shown in Fig. 2.5. As the 2-pole rotor is connected to a gas turbine, the rotation of its field windings produces a rotating magnetic field which in turn induces an AC voltage in the three-phases of the armature windings separated 120 electrical degrees. The rotor mechanical speed, ω_s (in rpm) is synchronised with the frequency, f (in Hz) of the induced stator voltages through Equ. (2.1):

$$\omega_s = \frac{120f}{p}, \tag{2.1}$$

where *p* is the number of poles.

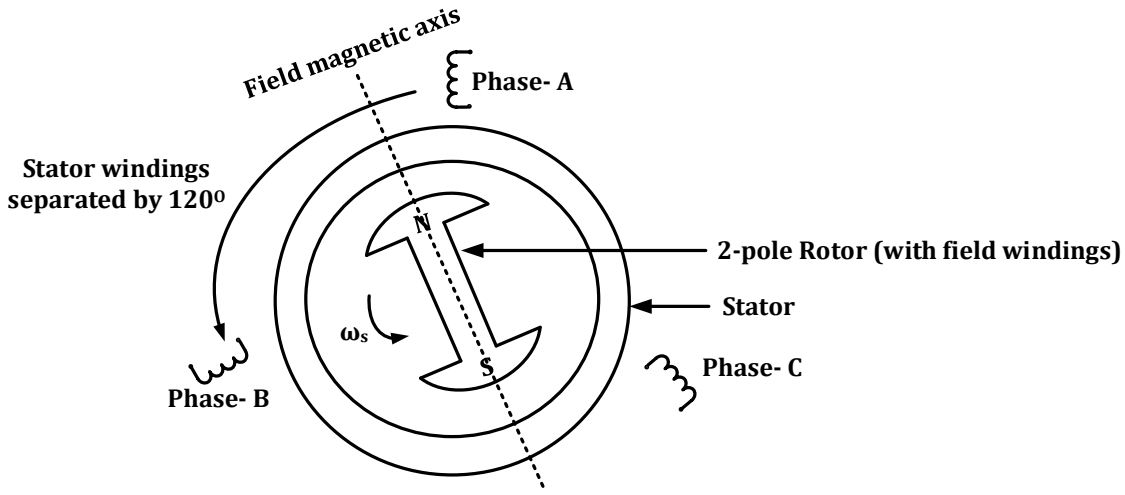

Figure 2:5: Synchronous generator principle of operation

The equation of motion for the synchronous generator and the connecting gas turbine is described through the swing equation, expressed as:

$$J\frac{d\omega_s}{dt} = T_a = T_m - T_e, \tag{2.2}$$

where J is the combined moment of inertia of the turbine, generator and gearbox,

T_a is the accelerating torque,

T_m is the mechanical torque of the turbine and

T_e is the electromagnetic torque of the generator.

According to Equ. (2.2), the electromagnetic torque matches the mechanical torque at steady state, leading to a net accelerating torque of zero. The generator and turbine therefore rotate at the constant synchronous speed of the generator. Any sudden increase in electrical load increases the electromagnetic torque above the mechanical torque. This causes the generator-turbine to decelerate with a rate of change of speed proportional to the amplitude of the electromagnetic torque. Equilibrium is restored by the speed control system of the turbine through an increase in mechanical torque to match the new set point of the electrical load.

2.4 Biomass Distributed Generator Models

2.4.1 Gas Turbine Dynamic Model

Gas turbine models can largely be classified into the thermodynamic model and the generic transfer function model. The thermodynamic model utilises fundamental mass, momentum and heat balance equations for individual components of the gas turbine [55]. Central to this modelling approach is the detailed thermodynamic analysis of the turbine, which may be unnecessarily cumbersome for the study of power system dynamics. Conversely, the generic transfer function model represents the gas turbine dynamic process with gains and time constants determined through actual performance data [70, 71]. One of the most common generic gas turbine models is the empirical model developed by W.I. Rowen in 1983 [70]. The model is considered to capture the most important dynamic characteristics of a gas turbine and is therefore suitable for use in power system analysis [70]. Though initially developed for heavy duty gas turbine (HDGTs), the model is also considered applicable to micro-turbines as described in [55, 72-74].

Rowen's model for a single-shaft gas turbine is seen in Fig. 2.6, with all parameters in per unit (pu). The model controllers are:

- The speed governor, which adjusts fuel flow to achieve a desired turbine speed.
- The temperature controller, which adjusts fuel flow to maintain exhaust gas temperature of the turbine at the required value.
- The acceleration controller, which adjusts fuel flow to prevent the turbine from over speeding.

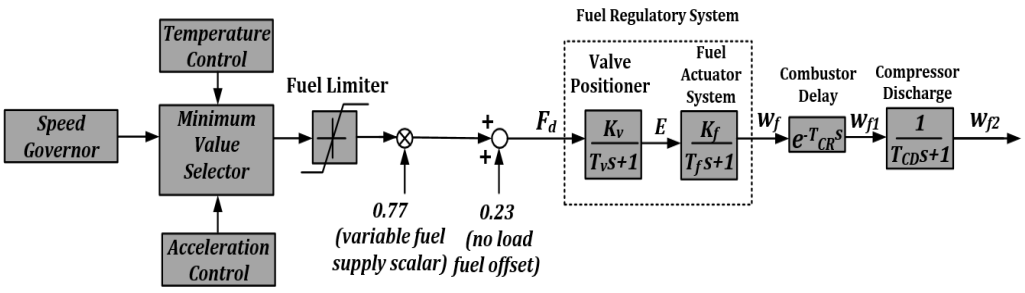

Figure 2:6: Single shaft gas turbine model

The operation of the three controllers are not concurrent: the prevailing control action for any given situation is determined by the minimum value selector. The minimum value selector adopts the control action requiring the least amount of fuel. The speed governor is the main controller, dictating the amount of fuel, F_d required for maintaining the speed of the turbine. Under normal conditions, the reference exhaust temperature exceeds the measured temperature, setting the temperature control output to a maximum value. When the turbine exhaust temperature exceeds the specified limits, the temperature control output falls below the speed governor output. Temperature control is therefore activated by the minimum value selector, reducing the output power of the turbine by modifying the amount of fuel flowing into the combustion chamber. Switching from one controller to the other occurs without time delays [70]. The acceleration control is only active at turbine start-up to maintain turbine acceleration within limits [70]. Hence, the acceleration control may be eliminated for nominal operating conditions.

The fuel limiter imposes constraints on the amount of fuel that can flow into the combustor. The upper limit augments the temperature controller by imposing a maximum limit on fuel flow [70]. The lower limit set at -0.1 represents a negative torque [70], indicating that the gas turbine is capable of absorbing transient power due to its inertia [75].

One fundamental difference between a gas and steam turbine is the requirement for 23% of the rated fuel by a gas turbine, under no load conditions [75]. This is implemented in Rowen's model by separating the fuel signal into the no load fuel offset (0.23) and the variable fuel supply scalar (0.77). The fuel signal from the minimum selector only affects the variable fuel supply, as the no load fuel requirement remains fixed [76].

Under no load conditions, the fuel demand signal, F_d may be determined from the no load fuel offset (0.23), the variable fuel supply scalar (0.77) and the lower fuel limit of -0.1 as:

$$Fuel\ demand,\ F_d = 0.23 + 0.77(-0.1) = 0.16, \tag{2.3}$$

corresponding to a fuel flow of 16% [75] which ensures that the fuel supply to the combustor is capable of maintaining flames for combustion activities [77].

The fuel regulatory system in Fig. 2.6 consists of 2 parts: the first part is the valve positioner and its position determines the rate of fuel flow to the combustor [70, 78]. The second part is the fuel actuator system, which supplies fuel to the combustor according to the fuel demand signal, E from the valve positioner. The valve positioner transfer function is:

$$E = \frac{K_v}{\tau_v s+1} F_d, \tag{2.4}$$

and the fuel flow, w_f to the combustor is determined from the fuel actuator system as:

$$w_f = \frac{K_f}{\tau_f s+1} E \tag{2.5}$$

where:

K_v is the valve positioner gain,

τ_v is the valve positioner time constant,

w_f is the per unit fuel flow to the combustor,

K_f is the fuel actuator gain and

τ_f is the fuel actuator time constant.

A delay due to fuel injection and release of heated gases to the turbine is accounted for in the combustion delay block with the following equation [75]:

$$w_{f1} = e^{-T_{CR}s} w_f, \tag{2.6}$$

where w_{f1} is per unit fuel flow with combustor delay and

T_{CR} is the combustor time constant.

The time lag before compressor discharge gases are supplied to the combustor is represented by a time constant in the compressor discharge block as:

$$w_{f2} = \frac{1}{T_{CD}s+1} w_{f1} \tag{2.7}$$

where w_{f2} is per unit fuel flow with compressor discharge dynamics and

T_{CD} is the compressor time constant.

Finally, the mechanical torque, T_m is determined from Equ. (2.8) as [79, 80]:

$$T_m = 1.3\left(w_{f2} - 0.23\right) + C(1 - N), \tag{2.8}$$

where C is the speed sensitivity coefficient generally taken as 0.5 [70, 75] and N is the per unit rotor speed.

The output mechanical power, P_m is linearly dependent on rotor speed, N and mechanical torque, T_m as described by Equ. (2.9):

$$P_m = NT_m. \tag{2.9}$$

Figure 2.7 illustrates the computation of the mechanical torque, T_m and mechanical power, P_m according to Equs. (2.8) and (2.9) respectively. Note that for per unit computations, the nominal rotor speed is 1 pu, therefore P_m and T_m are equivalent.

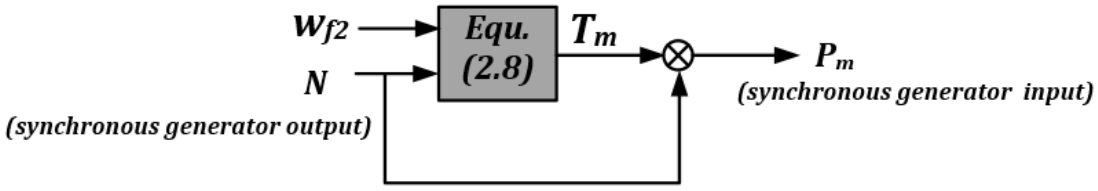

Figure 2:7: Determination of mechanical torque and mechanical power

Some assumptions made in Rowen's model are that the IGVs are fully open and that the same pressure ratio exists across both the compressor and the turbine. Additionally, a speed limit in the range of 95-107% is imposed on the system. Within this range, both the torque and temperature have a linear relationship with fuel flow [70].

2.4.2 Synchronous Generator Model

The synchronous generator is modelled in the synchronous reference frame (SRF) with the equivalent circuit for the stator and rotor shown in Fig 2.8. The stator and rotor parameters are represented as follows:

V_{ds} and V_{qs} are the stator voltages in the dq-axes,

V'_{fd} is the rotor field voltage in the d-axis,

V'_{kd}, V'_{kq1} and V'_{kq2} are the rotor damper voltages in the dq-axes,

I_{ds} and I_{qs} are the stator currents in the dq-axes,

I'_{fd} is the rotor field current in the d-axis,

I'_{kd}, I'_{kq1} and I'_{kq2} are the rotor damper currents in the dq-axes,

R_s is the stator resistance,

R'_{fd} is the rotor field resistance in the d-axis,

R'_{kd}, R'_{kq1} and R'_{kq2} are the damper field resistances in the dq-axes,

L_l is the leakage inductance,

L_{md} and L_{mq} are the mutual inductances between the stator and rotor in the dq-axes,

L'_{fd} is the rotor field inductance in the d-axis,

L'_{kd}, L'_{kq1} and L'_{kq2} are the damper field inductances in the dq-axes and

ϕ_d and ϕ_q are the dq-axes stator flux linkages.

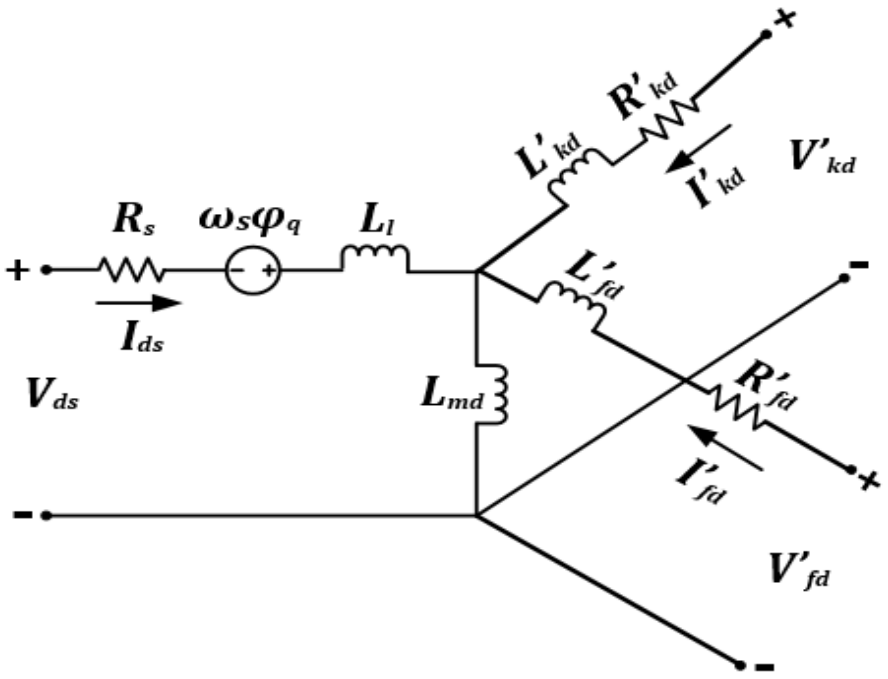

(a)

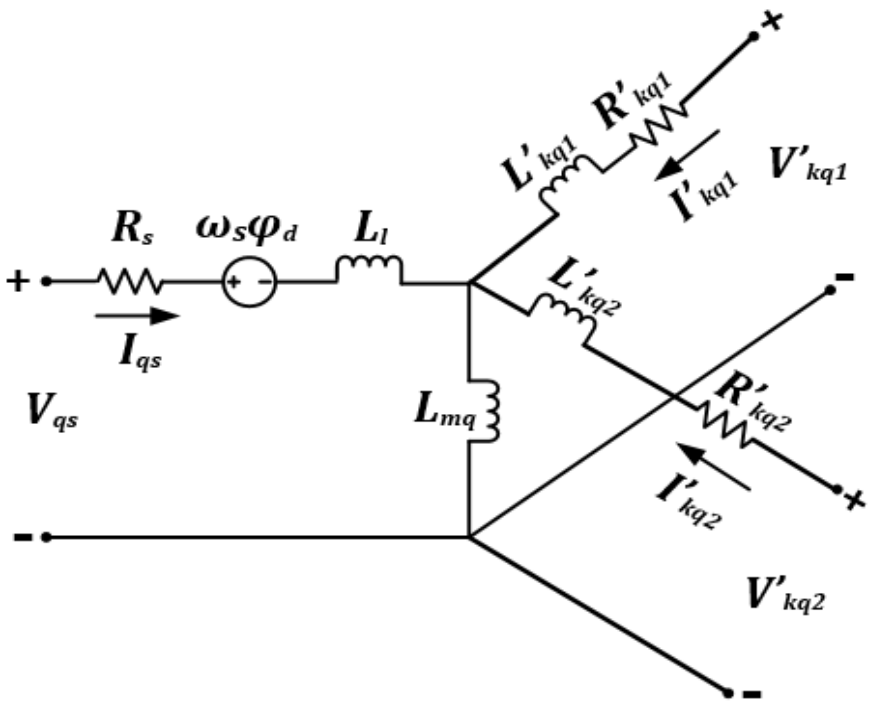

(b)

Figure 2:8: Equivalent circuit of a synchronous generator in SRF (a) d-axis (b) q-axis

The dynamic equations describing the stator and rotor voltages of the synchronous generator according to Fig. 2.8 are [81]:

$$V_{ds} = R_s I_{ds} + \frac{d}{dt}\phi_d - \omega_s \phi_q \tag{2.10}$$

$$V_{qs} = R_s I_{qs} + \frac{d}{dt}\phi_q + \omega_s \phi_d \tag{2.11}$$

$$V'_{fd} = R'_{fd} I'_{fd} + \frac{d}{dt}\phi'_{fd} \tag{2.12}$$

$$V'_{kd} = R'_{kd}\, I'_{kd} + \frac{d}{dt}\phi'_{kd} \tag{2.13}$$

$$V'_{kq1} = R'_{kq1}\, I'_{kq1} + \frac{d}{dt}\phi'_{kq1} \tag{2.14}$$

$$V'_{kq2} = R'_{kq2}\, I'_{kq2} + \frac{d}{dt}\phi'_{kq2} \tag{2.15}$$

The terms '$\omega_s\phi_q$' in Equ. (2.10) and '$\omega_s\phi_d$' in Equ. (2.11) are the speed voltages and are a consequence of transforming the stator quantities from stationary reference frame to synchronous reference frame.

The flux linkage equations are:

$$\phi_d = L_l I_{ds} + L_{md}\,(I'_{fd} + I'_{kd}) \tag{2.16}$$

$$\phi_q = L_l I_{qs} + L_{mq} I'_{kq} \tag{2.17}$$

$$\phi'_{fd} = L'_{fd} I'_{fd} + L_{md}\,(I_{ds} + I'_{kd}) \tag{2.18}$$

$$\phi'_{kd} = L'_{kd}\, I'_{kd} + L_{md}\left(I_{ds} + I'_{fd}\right) \tag{2.19}$$

$$\phi'_{kq1} = L'_{kq1}\, I'_{kq1} + L_{mq} I_{qs} \tag{2.20}$$

$$\phi'_{kq2} = L'_{kq2}\, I'_{kq2} + L_{mq} I_{qs} \tag{2.21}$$

where ϕ'_{fd} is the d-axis rotor field flux linkage,

ϕ'_{kd}, ϕ'_{kq1} and ϕ'_{kq2} are the dq-axes rotor damper flux linkages.

2.4.3 Excitation System Model

The primary function of the excitation system is to provide the synchronous generator rotor field windings with a DC current. By controlling the DC current, the excitation system is capable of regulating the generator terminal voltage. Depending on the nature of the excitation power source, excitation systems may be classified into [60]:

- DC excitation systems- These excitation systems source their energy from DC generators and provide the DC field current to the generator through slip rings. The problems associated with this particular class of excitation systems are brush wearing and voltage drops, leading to increase in losses incurred by the system.
- AC excitation systems- These excitation systems source their energy from alternators. The exciter output is an AC voltage which must be rectified to supply the DC field current. The rectifier can either be stationary or rotating. With rotating rectifiers, slip rings and brushes are not required.
- Static excitation systems- These are stationary exciters, and they supply DC current to the generator field windings through slip rings with the use of static rectifiers.

The excitation system shown in Fig. 2.9 is a brushless excitation system [60, 82]. It consists of a pilot exciter and an AC exciter, which regulate the terminal voltage

of the main generator. The pilot exciter is a permanent magnet generator which functions as an excitation system to the stationary field of the AC exciter. The AC exciter rotor is stationary with its armature rotating with the rotor of the main generator.

Measurements from a current transformer (CT) and power transformer (PT) at the terminal of the main generator are supplied to the voltage regulator as inputs, in conjunction with the voltage reference. The regulator output adjusts the field current of the AC exciter. The AC exciter thereafter supplies an AC current which is rectified to a DC current prior to application to the rotor windings of the main generator. Through this control action, the excitation system is capable of controlling the main generator voltage.

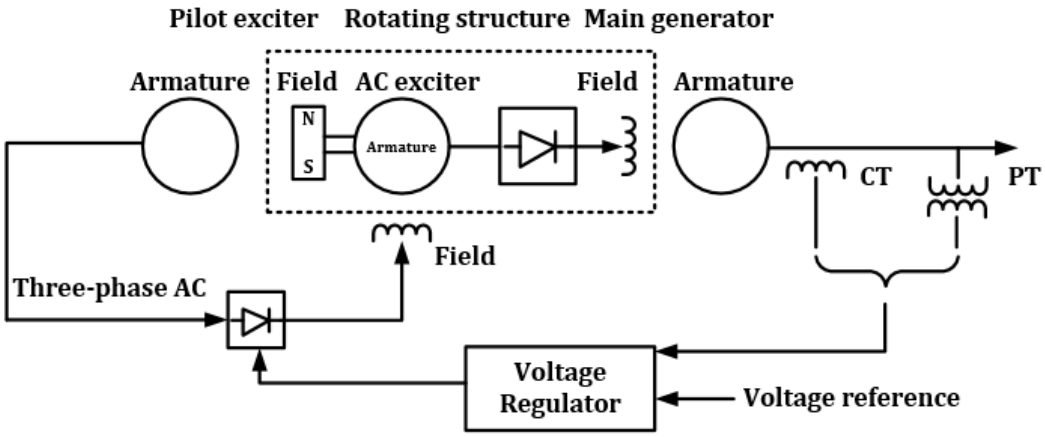

Figure 2:9: Brushless excitation system

2.4.4 Gearbox Model

For system simplification, the gearbox is modelled as a dimensionless scalar quantity known as the gearbox ratio, k_{gear} which relates the turbine speed, *N* and the generator speed, ω_s through Equ. (2.22):

$$k_{gear} = \frac{N}{\omega_s}. \tag{2.22}$$

For per unit (pu) operation, the value of k_{gear} is unitised.

2.5 Control Principle of the Biomass Distributed Generator

Maintaining a stable voltage and frequency is a major concern in any power system, as deviations from the set values may cause significant deterioration of

the system. In the BDG, the speed governor of the gas turbine regulates the turbine speed. The operation mode of the speed governor varies according to the status of the BDG: a grid connected BDG has its frequency fixed by the grid and therefore operates in droop control mode. For islanded operation, the speed governor indirectly controls the frequency of the BDG through speed regulation in isochronous mode.

As the speed governor controls turbine speed by regulating the fuel flow within the turbine, it is imperative that the gas turbine does not operate beyond its temperature limit, thus necessitating the inclusion of the temperature controller. Both speed and temperature controllers regulate fuel flow to ensure that the speed and temperature of the gas turbine are maintained within permissible limits.

The stator terminal voltage of the generator is regulated at a consistent level by the automatic voltage regulator (AVR) of the generator excitation system.

The complete BDG with the control systems are shown in Fig. 2.10. The gas turbine control block regulates the generator synchronous speed, ω_s to the reference value, $\omega_s{}^*$ to produce the mechanical power, P_m . The generator stator voltage, V_{Sabc} is transformed from the stationary reference frame to the synchronous reference frame as V_{DS} and V_{QS}, using Park's transformation described in Chapter 1. The excitation block regulates the magnitude of the stator d-q voltages, V_{DS} and V_{QS}, to the reference terminal voltage, V^* to produce the excitation voltage, E_{FD}. The operating principles of the control systems are detailed in the following sections.

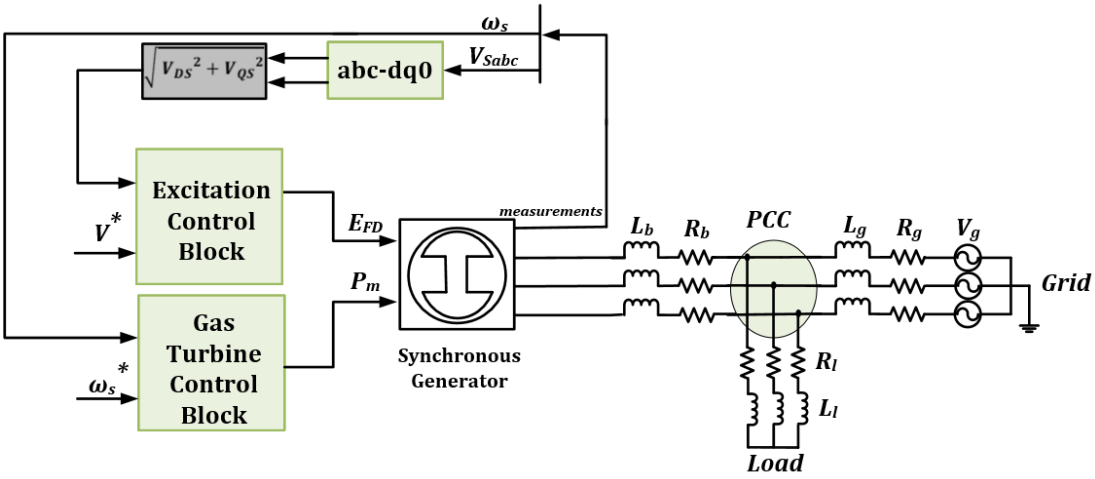

Figure 2:10: Biomass distributed generator with excitation and gas turbine control

2.5.1 Gas Turbine Control System

The gas turbine control system consists of the speed governor and the temperature controller. The controllers are described in sections 2.5.1.1 and 2.5.1.2 respectively.

2.5.1.1 Speed Governor Control

The speed governor control in Fig. 2.11 is a General Electric Mark IV Speedtronic Turbine Control System [70]. The controller is a lead-lag compensator that can operate either in droop control mode for load sharing among parallel generators in grid connected operation, or isochronous mode for isolated operation. A droop governor produces an output proportional to the input speed error, while an isochronous controller has an output whose rate of change is proportional to the speed error [70]. The transfer function of the speed governor, $G_s(s)$ is given as:

$$G_s(s) = \frac{W(Xs+1)}{(Ys+Z)} \tag{2.23}$$

where:

W is the governor gain (1/droop control setting),

X is the governor lead time constant,

Y is the governor lag time constant and

Z is the governor operation mode (1 for droop control mode, 0 for isochronous control mode).

The droop control setting is typically within the 2%-10% range, corresponding to governor gain values of 50-10 respectively [78, 79].

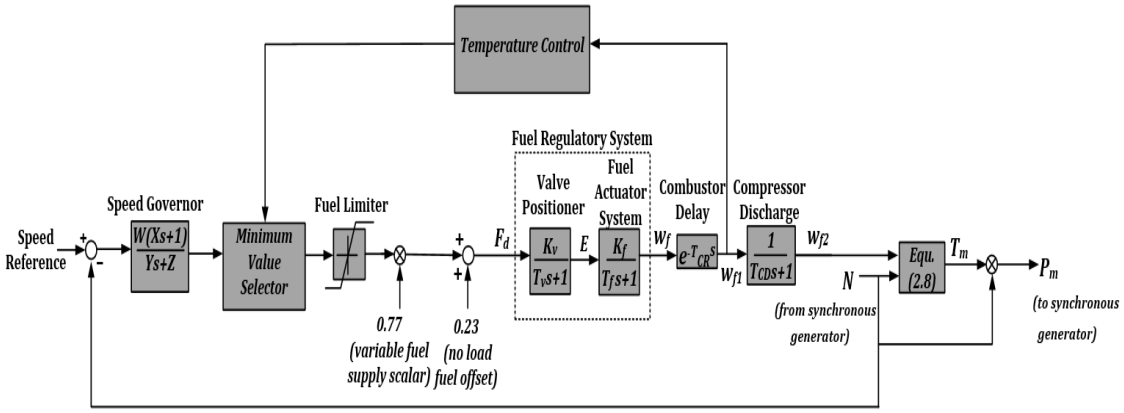

Figure 2:11: Speed control of a gas turbine

The operating principle of the speed control system in Fig. 2.11 is described as follows: when there is a reduction in system frequency due to an increase in load, the system will offer an inertial response and the speed of the compressor will reduce [76]. As output power, P_m depends on turbine speed, N the turbine output power will also reduce. The pressure ratio across the turbine falls, leading to a decrease in air flow from the turbine [83]. A rise in temperature will ensue as a result of the decrease in air flow. To mitigate this problem, the speed governor reacts by increasing the fuel flow to the combustor, w_f. This results in a higher fuel flow, w_{f2} according to Equ. (2.7). The linear relationship between fuel flow, w_{f2} and turbine mechanical torque, T_m in Equ. (2.8) translates into an increased mechanical torque, T_m and hence output mechanical power, P_m.

The action of increasing w_f causes the temperature to increase. If the system is operating at partial load, the IGVs may be opened further to allow more airflow into the compressor. This keeps the fuel/air ratio consistent and the exhaust temperature within limits. However, during base load operation, IGVs are completely open and airflow cannot be increased further. The exhaust temperature therefore rises until it exceeds its reference value. At this point, the temperature control output starts to decrease until it becomes lower than the output from the speed governor, taking over the fuel system control. The temperature controller thus reduces the fuel flow, and hence the fuel/air ratio, restoring the exhaust temperature to the desired value.

2.5.1.2 Temperature Control

The temperature controller is a proportional-integral (PI)-controller and its function is to limit fuel flow when the exhaust temperature exceeds the reference value. The exhaust temperature, T_{ex} computations incorporate a delay time in transporting the exhaust gases to the temperature measurement system, expressed in Equ. (2.24) as:

$$w_{f3} = e^{-T_{TD}S} w_{f1}, \tag{2.24}$$

where w_{f3} is per unit fuel flow with turbine and exhaust delay and

T_{TD} is the turbine and exhaust system time constant.

The exhaust temperature, T_{ex} is calculated using fuel flow, w_{f3} according to the following formula [70]:

$$T_{ex} = T_r - 390 * (1 - w_{f3}) + 306 * (1 - N), \tag{2.25}$$

where T_r is the rated exhaust temperature (^{O}C).

The temperature control system of the gas turbine is shown in Fig. 2.12.

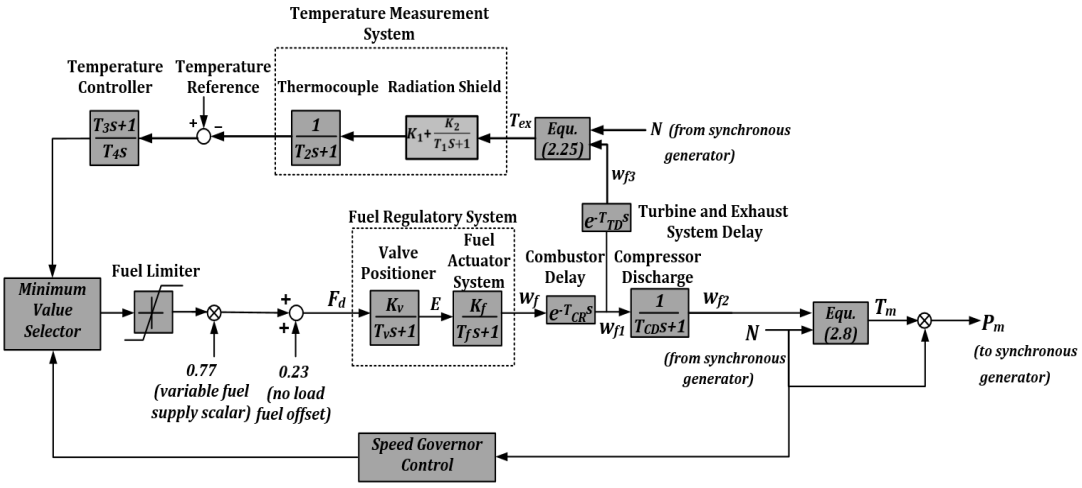

Figure 2:12: Temperature control of a gas turbine

The temperature measurement system consists of a radiation shield and thermocouple. The radiation shield prevents turbine radiation from affecting the temperature measurement [75]. The transfer functions for the radiation shield, $R(s)$ and the thermocouple, $TH(s)$ are respectively given as:

$$R(s) = K_1 + \frac{K_2}{T_1 s + 1} \tag{2.26}$$

and

$$TH(s) = \frac{1}{T_2 s+1}\,, \tag{2.27}$$

where K_1, K_2 are the radiation shield gains,

T_1 is the radiation shield time constant and

T_2 is the thermocouple time constant.

The time constants, T_1 and T_2 determine how fast the change in exhaust temperature will reflect in the measurement.

The measured temperature at the thermocouple output is compared with a reference temperature, which is normally at a higher value. In this case, the output from the temperature controller remains higher than the speed governor control output and fuel flow is determined by the speed governor. If, however, the measured temperature is higher than the reference value, a negative output is obtained, causing the temperature controller output value to start decreasing. At a certain point, this value becomes lower than the output from the speed governor control. The temperature controller output will therefore pass through the minimum value selector and temperature control dictates fuel flow [80], determining the fuel demand signal, F_d. This determines the new value of the per unit fuel flow, w_{f2} which is utilised to re-compute the mechanical torque and power according to Equs. (2.8) and (2.9) respectively. The temperature control transfer function, $T(s)$ is expressed in Equ. (2.28) as:

$$T(s) = \frac{T_3 s+1}{T_4 s}, \tag{2.28}$$

where T_3 and T_4 are the temperature controller time constants.

2.5.2 Excitation Control System

In the synchronous generator, the terminal voltage is controlled through the automatic voltage regulation (AVR) of the excitation system. By varying the field current in the rotor windings at a given speed, the generator terminal voltage can be varied according to the equation:

$$E_A = K\phi\omega_s, \tag{2.29}$$

where E_A is the induced voltage in the stator windings,

K is a constant dependent on machine construction,

ϕ is the field flux and

ω_s is the synchronous speed.

Figure 2.13 shows the block diagram for the IEEE AC5A brushless excitation system [82]. It consists of 2 parts: the voltage regulator and the exciter. The voltage regulator inputs are: the reference stator voltage, V^*, the magnitude of the measured stator d-q voltages: V_{DS} and V_{QS}, and a damping filter feedback for power system oscillation damping [60]. The damping filter gain is represented by K_F, with time constants T_{F1}, T_{F2} and T_{F3}. The voltage error between the regulator inputs is amplified by the voltage regulator gain, K_A with T_A as the regulator time constant. Anti-windup limits imposed on the regulator set upper and lower boundaries on the output as V_{RMAX} and V_{RMIN} respectively.

The voltage regulator output provides reference to the exciter, represented by gain, K_E and time constant, T_E. The exciter output voltage, E_{FD} is the excitation field voltage of the synchronous generator. A non-linear function, V_X, which is a product of the exciter output voltage, E_{FD} and a saturation function, $S_E(E_{FD})$ prevents saturation of E_{FD}.

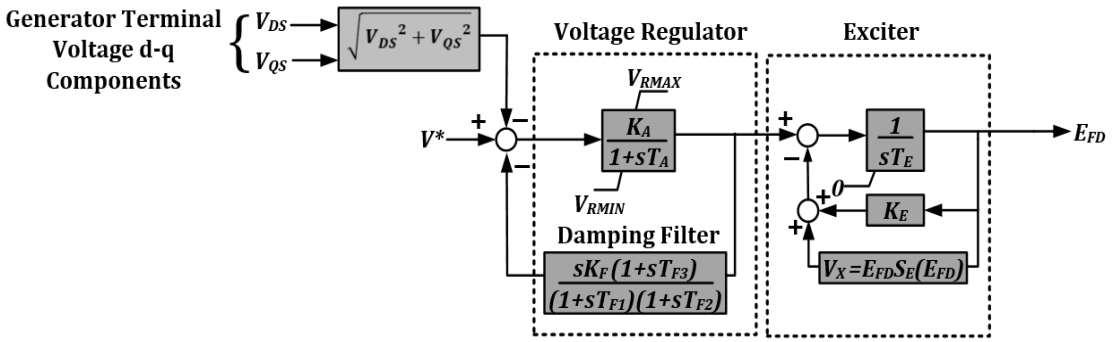

Figure 2:13: Functional block of IEEE AC5A excitation system

2.6 Simulation Studies for the Biomass Distributed Generator

The BDG is modelled using Simulink/MATLAB software. The gas turbine has a 400 kW capacity and is connected to a 490 kVA, 4-pole, 1500 rpm, salient pole synchronous generator. The generator model is an inbuilt model in the Simulink library. Identical distribution line parameters are employed for the BDG and grid, with resistances, R_b and R_g as *1 Ω* and inductances, L_b and L_g as *2.5 mH*.

Table 2.1 provides the gas turbine system parameters obtained from [70, 72]. The synchronous generator parameters specified in Table 2.2 are based on the Marelli generators from FKI Energy Technology [84]. Table 2.3 provides the excitation model parameters obtained from [82].

Table 2.1: Gas turbine parameters

Parameter	Value
Speed reference (pu)	1
Speed governor gain and time constants (*W/X/Y/Z*)	10/0/0.05/1
Valve positioner gain and time constant (K_v/T_v)	1/0.05
Fuel actuator system gain and time constant (K_f/T_f)	1/0.4
Combustor delay time constant (T_{CR})	0.01
Compressor discharge time constant (T_{CD})	0.1
Turbine and exhaust system time constant (T_{TD})	0.02
Radiation shield gains and time constant ($K_1/ K_2/T_1$)	0.8/0.2/15
Thermocouple time constant (T_2)	2.5
Temperature controller time constants (T_3/ T_4)	3.3/250
Temperature reference (^{O}C)	510

Table 2.2: Synchronous generator parameters

Parameter	Value
Number of poles, *p*	4
Power Output, *S* (kVA)	490
Voltage Rating, V_n (V)	380
Active power, P_n (kW)	392
Power Factor	0.8
Speed, *N* (rpm)	1500
Frequency, *f* (Hz)	50
Moment of Inertia, *J* (kgm^2)	7.97
Stator winding resistance, R_s (mΩ)	8.6

Table 2.3: Excitation system parameters

Parameter	Value
Voltage regulator gain and time constant (K_A/ T_A)	400/0.02
Voltage regulator output limits (V_{RMIN} (pu)/V_{RMAX} (pu))	-7.3/7.3
Damping filter gain and time constants (K_F /T_{F1}/T_{F2} /T_{F3})	0.03/1/ 0/ 0
Exciter gain and time constant (K_E/T_E)	1.0 /0.8
Field voltage values (E_{FD1} (pu)/E_{FD2} (pu))	5.6 / 0.75*5.6
Exciter saturation function values (S_EE_{FD1} (pu) /S_EE_{FD2} (pu))	0.86 / 0.5

2.6.1 Preliminary Computations

Two important parameters of the synchronous generator that require computation based on Table 2.2 are: the inertia constant and the per unit stator winding resistance.

2.6.1.1 Inertia Constant

The Inertia constant, *H*, defined as the ratio of energy stored in the rotor at synchronous speed to the nominal power rating of the synchronous generator is expressed as:

$$H = {}^{\frac{1}{2} M\omega_s}\Big/_{G}, \tag{2.30}$$

where:

M is the moment of inertia in MJs/electrical radians and

G is the MVA rating of the generator.

The moment of inertia, M is expressed as:

$$M = J\left(\frac{2}{p}\right)^2 \omega_s \times 10^{-6}, \tag{2.31}$$

where *J* is the combined rotor moment of inertia for the turbine, generator and gearbox and

p is the number of poles.

Based on the moment of inertia, *J* of the synchronous machine specified in Table 2.2, the inertia constant, *H* computed according to Equ. (2.30) is *0.19*. Higher values are expected when the moments of inertias of the turbine and gearbox are incorporated. Typical values of *H* generally range from 4 to 10 [60].

2.6.1.2 Per Unit Stator Winding Resistance

The per phase stator winding resistance, R_s according to Table 2.2 is *8.6 mΩ*. To convert to per unit values, the per unit stator winding resistance, $R_s(pu)$ is expressed as:

$$R_s(pu) = \frac{R_s}{Z_{sbase}}, \tag{2.32}$$

where Z_{sbase} is the base value for the generator impedance. The value of Z_{sbase} may be determined from the ratings of the generator voltage, V_n and active power, P_n in Table 2.2 as:

$$Z_{sbase} = \frac{{V_n}^2}{P_n}. \tag{2.33}$$

Inserting Equ. (2.33) into Equ. (2.32) and substituting R_s, V_n and P_n with the specified values in Table 2.2, the per unit stator winding resistance, $R_s(pu)$ is computed as 0.029.

2.6.2 Simulation Results

Two cases of simulation results are presented. In case 1, the system response to a step change in electrical power demand, P_e is presented. In case 2, the transient stability of the system is investigated for different inertia constants, *H* of the BDG.

2.6.2.1 Case 1: BDG response to a step change in load

An inertia coefficient of 4 is assumed in this simulation. The BDG system initially supplies a load of *0.48 pu*. A step change in load from *0.48 pu* to *0.81 pu* occurs at time, *t=10 seconds,* as seen in the electrical and mechanical powers of Fig. 2.14 (a). At time *t=10 seconds*, the electrical power demand increases sharply, leading to an unbalance between the electrical power demanded by the additional load and the mechanical power supplied by the BDG. The fuel regulatory system

of the gas turbine responds appropriately by increasing the fuel flow to the combustor at time, *t = 10 seconds* as shown in Fig. 2.14 (b).

The inertial response of the BDG due to unbalance between the electrical and mechanical powers at time, *t > 10 seconds* is shown in the rotor speed response of Fig. 2.14 (c). The rotor responds by decelerating according to Equ. (2.2). As the rotor speed, *N* is synchronised with the generator speed, ω_s, the generator frequency, *f* responds in proportion to the rotor speed as seen in Fig. 2.14 (d).

The unbalanced powers in Fig. 2.14 (a) cause oscillations in the rotor angle of Fig. 2.14 (e). The electrical and mechanical powers both reach a steady state value of *0.81 pu* at time, *t≅16 seconds,* indicating a balance between the electromagnetic and the mechanical torques in Equ. (2.2). Consequently, the fuel flow, rotor speed, generator frequency and rotor angle in Figs. 2.14 (b) - (e) reach steady state. The rotor speed and hence generator frequency return to their initial unperturbed values of *1 pu* and *50 Hz* respectively, due to the action of the speed governor regulating fuel flow in the turbine combustor.

According to Equ. (2.29), the stator terminal voltage in Fig. 2.14 (f) depends directly on the generator synchronous speed, ω_s and hence the generator frequency in Fig. 2.14 (d). Thus, the voltage drops at time, *t=10 seconds.* The AVR responds accordingly through adjustment of the exciter voltage in Fig. 2.14 (g). The exciter voltage increases until the stator voltage settles at *≅ 1 pu* at time*, t = 14 seconds.*

The exhaust temperature of the gas turbine, initially at *335^{O}C* for a load of *0.48 pu*, rises by *100 ^{O}C* for a load of *0.81 pu* as shown in Fig. 2.14 (h). The exhaust temperature remains below the reference value of *510^{O}C*. As a result, the flow of fuel in the gas turbine combustor is solely controlled by the speed governor. This is further verified by Fig. 2.14 (i), where the speed governor control output is less than the temperature controller output for the entire duration of time, *t > 0 seconds*. The minimum value selector therefore chooses the speed governor for gas turbine fuel flow control.

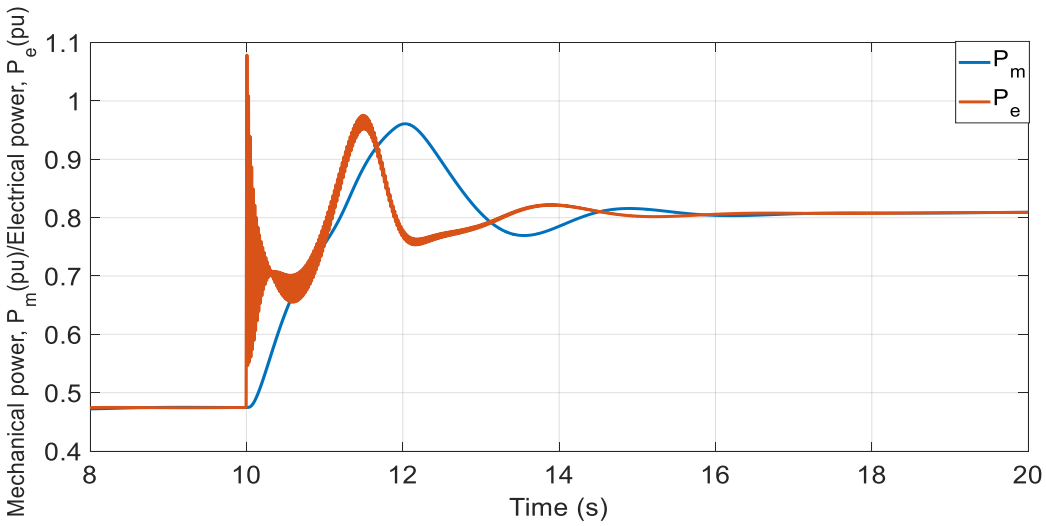
Mechanical power, P_m (pu)/Electrical power, P_e (pu)
1.1
1
0.9
0.8
0.7
0.6
0.5
0.4
8
10
12
14
16
18
20
Time (s)
P_m
P_e

(a)

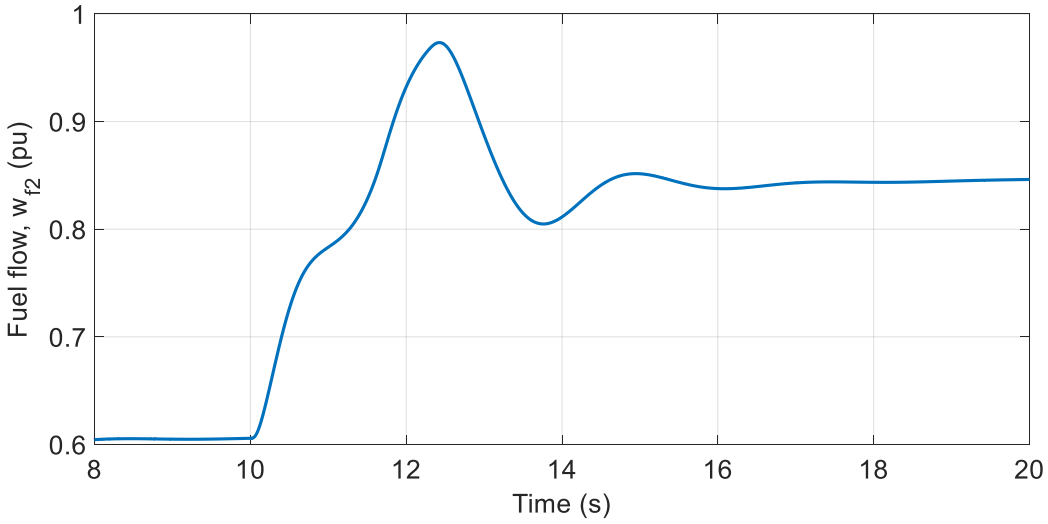
Fuel flow, w_{f2} (pu)
1
0.9
0.8
0.7
0.6
8
10
12
14
16
18
20
Time (s)

(b)

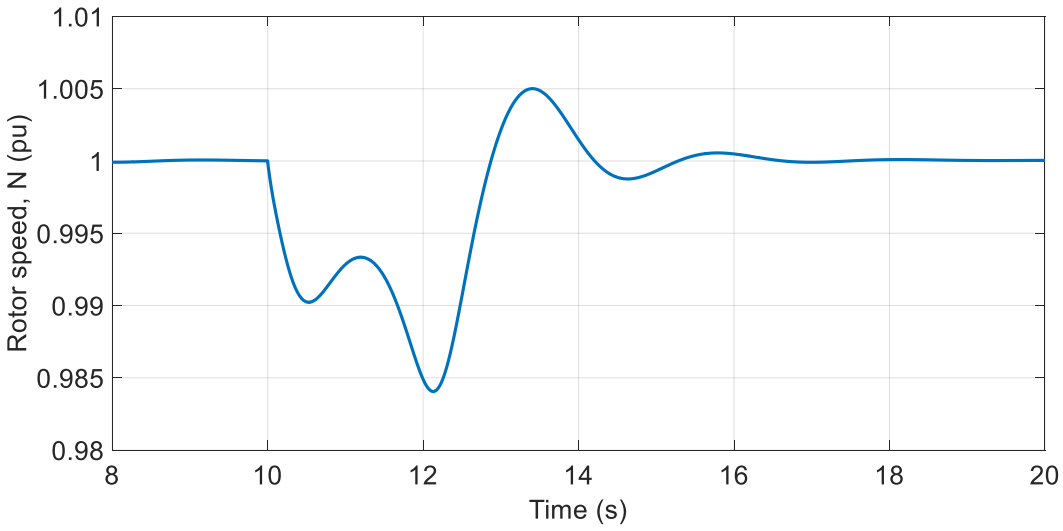
Rotor speed, N (pu)
1.01
1.005
1
0.995
0.99
0.985
0.98
8
10
12
14
16
18
20
Time (s)

(c)

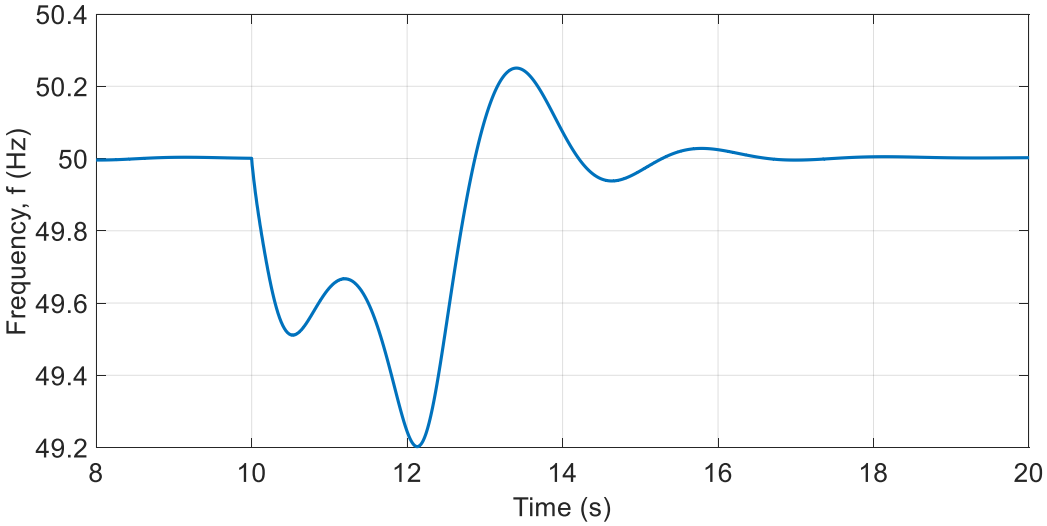
50.4
50.2
50
49.8
49.6
49.4
49.2
Frequency, f (Hz)
8
10
12
14
16
18
20
Time (s)

(d)

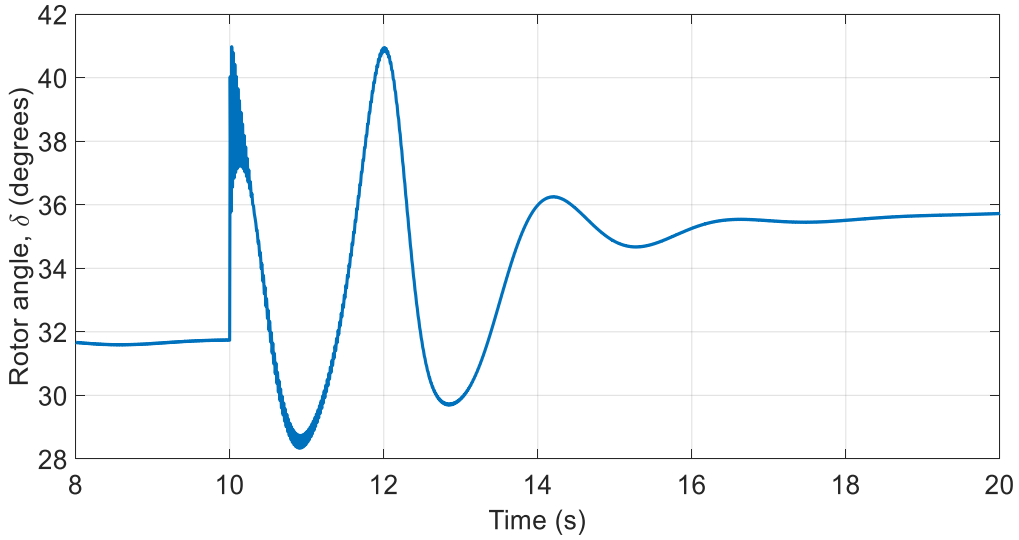
42
40
38
36
34
32
30
28
Rotor angle, δ (degrees)
8
10
12
14
16
18
20
Time (s)

(e)

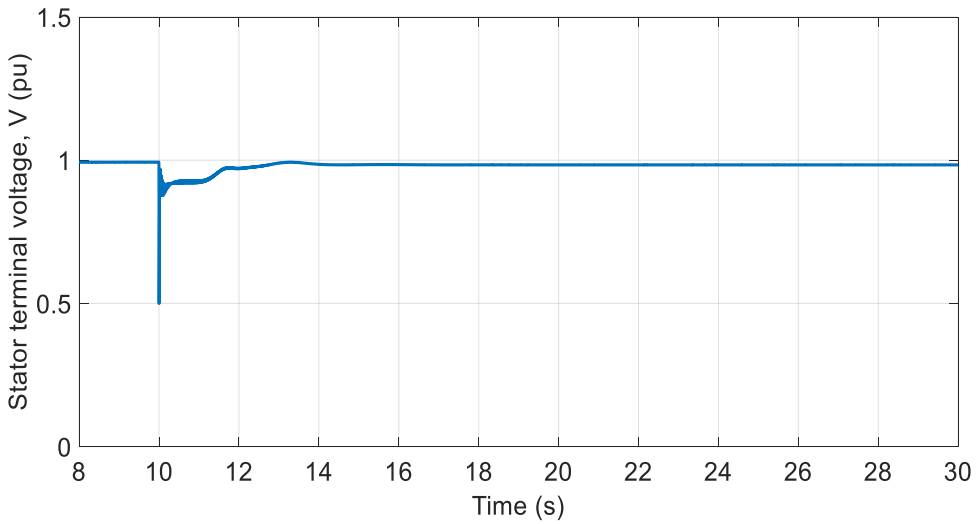
1.5
1
0.5
0
Stator terminal voltage, V (pu)
8
10
12
14
16
18
20
22
24
26
28
30
Time (s)

(f)

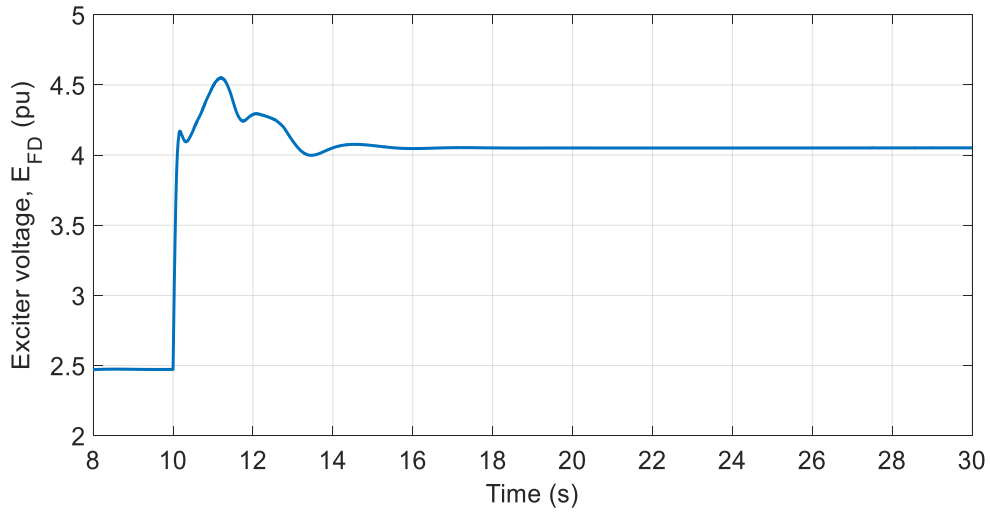
Exciter voltage, E_{FD} (pu)
5
4.5
4
3.5
3
2.5
2
8
10
12
14
16
18
20
22
24
26
28
30
Time (s)

(g)

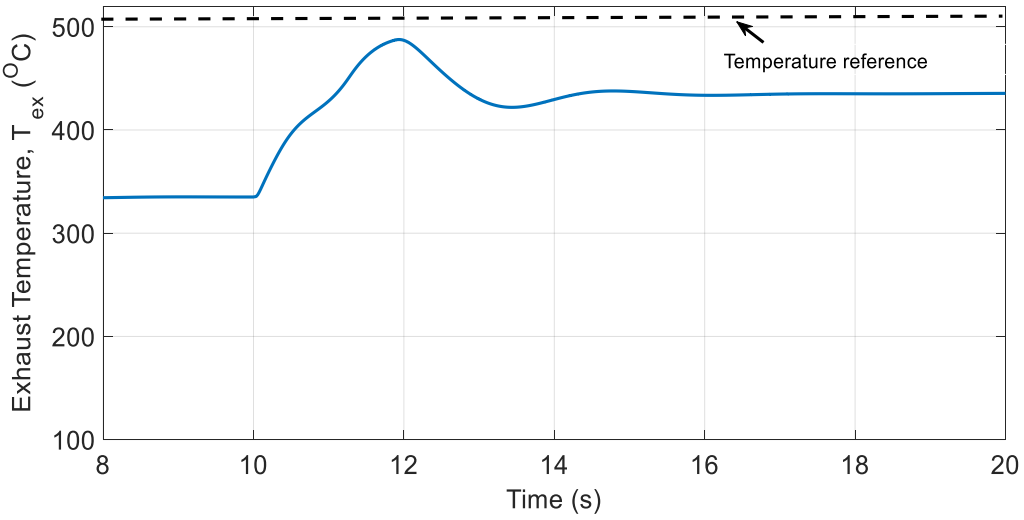
Exhaust Temperature, T_{ex} (^{O}C)
500
400
300
200
100
8
10
12
14
16
18
20
Time (s)
Temperature reference

(h)

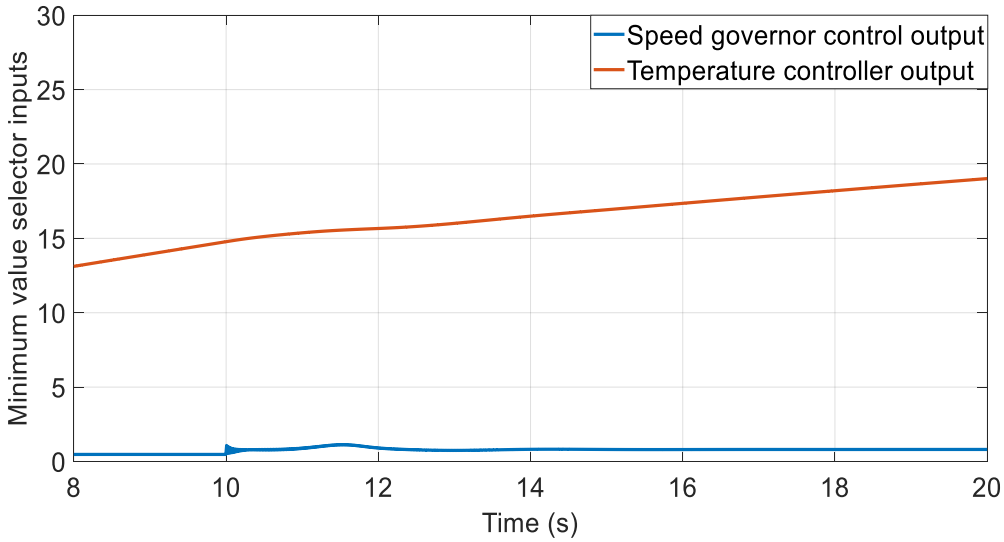

(i)

Figure 2:14: Biomass distributed generator responses for a step increase in load (a) Electrical and mechanical powers (b) Per unit fuel flow (c) Rotor speed (d) Generator frequency (e) Rotor angle (f) Stator terminal voltage (g) Exciter voltage (h) Exhaust temperature (i) Minimum value selector inputs from controllers

2.6.2.2 Case 2: Transient Stability of BDGs with Different Inertia Constants

The stability of the BDG is tested under sudden load changes with inertia constants, *H=4, 7, 10* and *12*. Fixed parameters have been used for all values of the inertia constant, although in reality, speed governor parameters may be altered to increase system response speed. As seen in Fig. 2.15 (a), the step increase in load from *0.48 pu* to *0.81 pu* occurs at time, *t = 10 seconds*. The transient stability of the system is compared for different values of the inertia constant, *H*. The stability indicators of the BDG system in the form of the rotor angle, *δ* and the generator frequency, *f* are shown in Figs. 2.15 (b) and 2.15 (c) respectively.

The time domain transient response of the rotor angle following a load disturbance in Fig. 2.15 (b) reveals faster dynamics for the BDG with *H=4,* settling within *2%* of the final steady state value in *3.4 seconds*. This is followed by BDG with *H=7,* settling in *4.9 seconds.* The BDG with *H=10* reaches steady state in *6.3 seconds.* The slowest response is for BDG with *H=12,* with a settling time of

7.2 seconds, more than twice as slow as the BDG with *H=4*. The overshoot is approximately 12.8% for all values of the inertia constant.

The generator frequency transient response for different values of inertia constant, *H* reveals variation in terms of overshoot and settling time, as seen in Fig. 2.15 (c). The maximum overshoot, in descending order of magnitude, is as follows: 0.4% (*H=4*), 0.16% (*H=7*), 0.08% (*H=10*) and 0.06% (*H=12*). The ascending order for the settling time within which the responses reach 0.5% of the final steady state frequency of 50 Hz are: *2.3 seconds* (*H=4*), *3.2 seconds* (*H=7*), *3.9 seconds* (*H=10*) and *4.3 seconds* (*H=12*). Comparing the highest and lowest inertias, the BDG with *H=4* has a maximum overshoot of more than six times the BDG with *H=12,* and settles at 50 Hz with a leading 2 second time margin.

From the analysis above, it is indicative that the BDG system with the least inertia constant offers a faster settling time. However, the faster dynamics may inadvertently lead to tripping of over-frequency protection devices of a generator. Conversely, the BDG system with the highest inertia constant has the highest damping. This indicates that from the point of view of stability, employing machines with higher inertias alone can improve the transient stability of the BDG system, albeit at the expense of a slower response time.

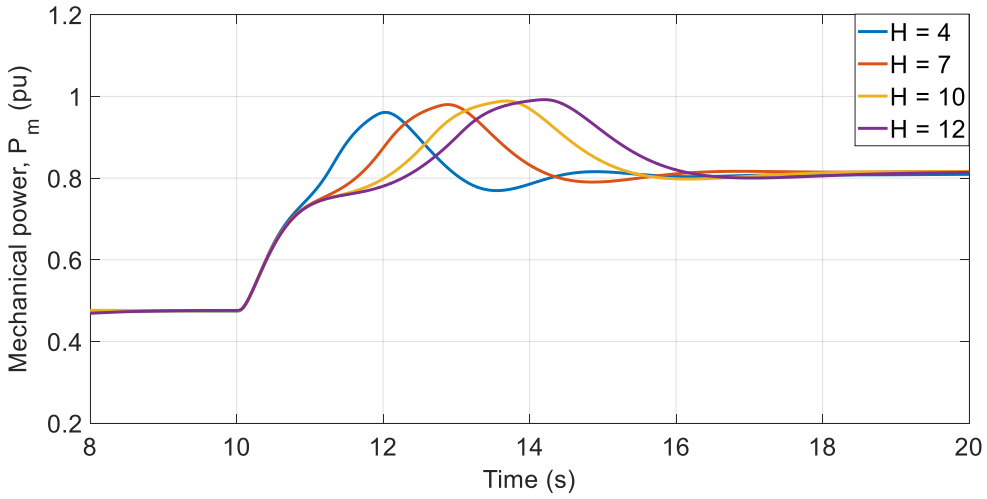

(a)

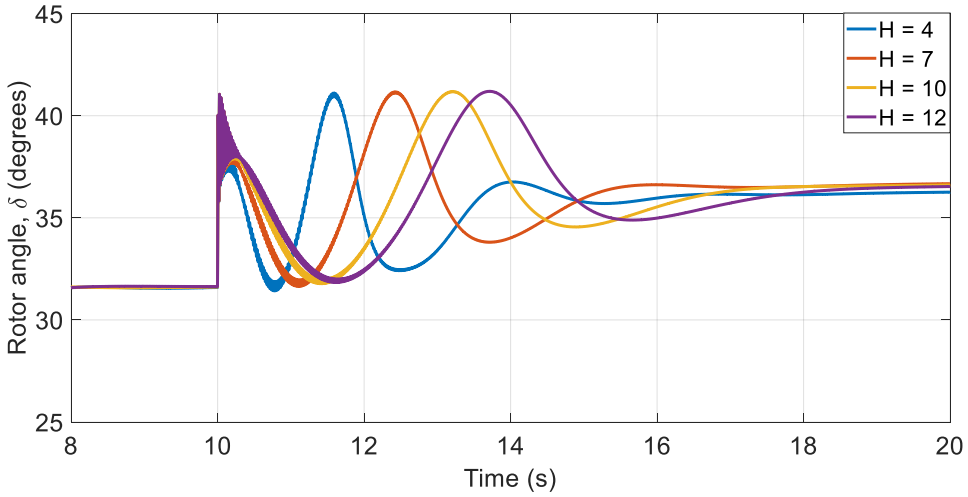

(b)

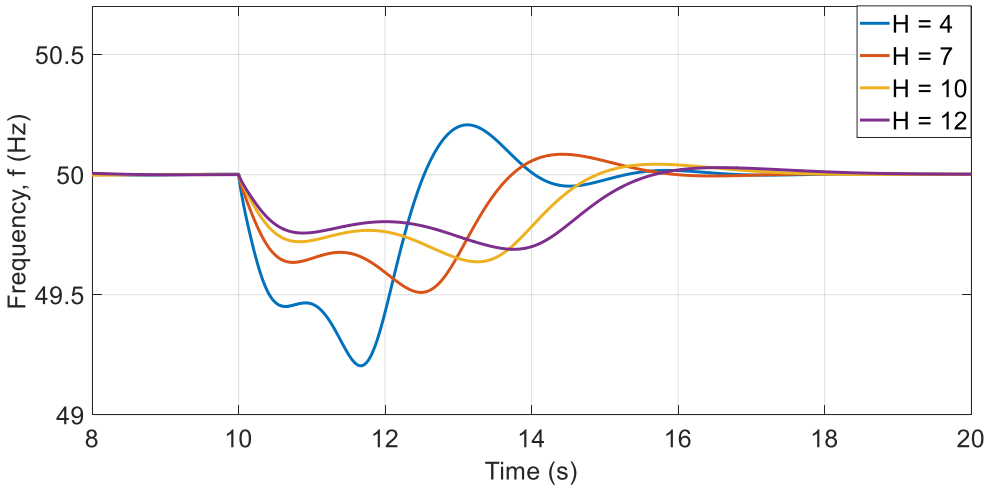

(c)

Figure 2:15: Biomass distributed generator transient stability (a) Mechanical power (b) Rotor angle (c) Generator frequency

2.7 Conclusion

The chapter has presented biomass conversion processes, working principles and detailed mathematical models for a gas turbine and synchronous generator, constituting the biomass distributed generator. Additionally, the models and control principles of the speed and temperature controls of the gas turbine and the excitation control system of the synchronous generator have been described. A simulation study revealing the characteristics of the BDG in the event of a sudden increase in electrical load demand has been presented, reflecting the response of the speed control governor in maintaing the rotor speed

synchronised with the generator frequency and the excitation system in regulating the stator voltage to the nominal value. Transient stability analysis performed on the BDG shows the relationship between stability and inertia constant of the BDG, following a large load disturbance. Higher inertias for the BDG resulted in a more stable system with slower dynamics compared to BDGs with lower inertias, offering faster dynamics with more rigorous deviations from the nominal system frequency.

Chapter 3 Grid Connected PV Distributed Generation with Inductor-Capacitor-Inductor (LCL) Filters

3.1 Introduction

PV generators are the most common renewable sourced generators in DG systems and are studied in this work as the second type of power source apart from the biomass distributed generator (BDG) presented in Chapter 2. The main components in a PV distributed generator (PVDG) are naturally the PV module/array itself, possibly with an associated DC-DC converter–based power conditioner for power tracking and voltage conversion, and most importantly, a DC-AC voltage source inverter (VSI) to convert the DC power generated into AC power suitable for connection with the power grid. Many types of PV inverters are applied for grid connections, but the majority are still based on the transformerless topology. Two design issues are important for PV-grid inverters: maintaining high efficiency active and reactive power supply to the grid, and minimising current harmonics generated by using PWM schemes for inverter switch control. The former depends on applying high performance power control strategies and the most common and effective one is based on the grid voltage oriented control scheme. The latter relies on adequate VSI filter design and currently, low-pass inductor-capacitor-inductor (LCL) filters have been favoured as opposed to a simple resistor- inductor (RL) filter. The advantages provided by an LCL filter are clear: better harmonic elimination with smaller inductor size [85], making it possible for lower inverter switching frequencies to be used. This leads to an overall reduction in converter switching losses. Also, being of third order, the LCL filter offers a better harmonic attenuation capability compared to the RL-filter, the amplitude of which is of -60 dB/decade above the LCL resonant frequency. However, a complexity attributed to an LCL filter is the infinite gain at that particular frequency, which occurs when the magnitude of the inductive reactance equals and thereby cancels the capacitive reactance, rendering the filter input impedance negligible. This leads to amplification of unwanted noise around the LCL resonant frequency, hence preventing the converters' controller from accurately tracking its reference value.

Passive and active damping methods have been proposed to curb the above described LCL filter resonance [31, 86]. While passive damping uses additional passive elements in the LCL filter structure, active damping is achieved through modification of the control system. The downside of utilising passive elements are the power losses, which lead to a reduction in overall system efficiency, particularly in high power applications.

Active damping techniques are generally classified into single loop filter based methods and multi-loop methods [87]. Multi loop methods can be implemented with a virtual resistor [86, 88-93] by means of either a capacitor current or voltage feedback. The requirement for an additional sensor increases the overall cost of implementation. Single loop methods achieve damping via supplementary filters e.g. low pass, lead-lag and notch filters (NFs) [86, 94] cascaded with the main controller. The performance of such filters have been analysed in detail in [94], where the NF has shown superior performance in terms of flexibility and robustness to gain variations in the low frequency region.

This chapter discusses a notch filter (NF)-based active damping scheme to overcome the LCL filter resonance problem. The investigation is based on a PV-grid inverter with a power rating in the range of a hundred kW and connected to a balanced three-phase grid. The inverter is a three- phase type connected to the grid via an LCL filter. It also employs independent active and reactive power regulators combined with a grid voltage oriented control (VOC) scheme. The model of the PVDG system and its control scheme will be detailed in the chapter. The design procedure for the PVDG system and hence control structure in this particular application will be described, and the performance of three LCL filter damping methods will be analysed in the frequency domain. Finally, the NF effect on PVDG control system stability will be studied in the frequency domain, along with further validation through time domain simulations.

3.2 Configuration of the Grid Connected PVDG System

The grid connected PVDG system studied here is shown in Fig.3.1. It consists of a solar PV array connected to a DC-DC converter, a DC link capacitor, C_{DC}, a DC-AC voltage source inverter (VSI) and an LCL filter connected at the inverter AC side to the 3-phase grid. The DC-DC converter shown is an inverting buck-

boost converter. The VSI is a three-phase, two-level inverter. The grid is represented by its Thevenin equivalent voltage, V_{grid} in series with the grid resistance, R_g and inductance, L_g. The topology offers no galvanic isolation between the PV and the grid due to the absence of a transformer.

The power generated by the PV is maintained at its maximum by controlling the duty ratio of the DC-DC converter through maximum power point tracking (MPPT). Acting as an interface between the PV DC source and the AC grid, the VSI switches are controlled by a sine-triangle PWM scheme to convert the DC generated power into AC power. The spectral output of the VSI consists of harmonics at various frequencies due to combinations of the grid frequency and the inverter switching frequency. These harmonics are attenuated to insignificant levels by the LCL filter prior to injection into the AC power grid.

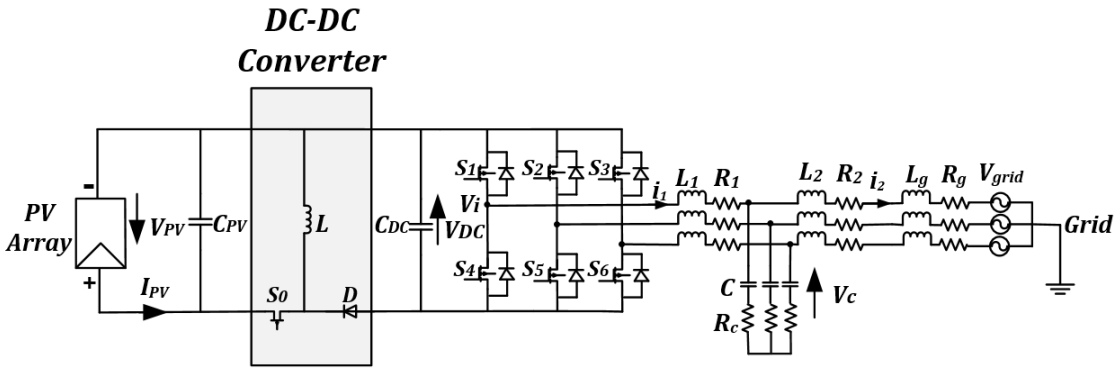

Figure 3:1: Configuration of a transformerless PV-grid connected distributed generation system with LCL filter

3.2.1 LCL Filter Model

The LCL filter for eliminating the harmonics due to inverter switching consists of the inverter side inductor and resistor L_1–R_1, grid side inductor and resistor, L_2–R_2 and a capacitor, C connected between them. A resistor, R_c cascaded with the capacitor, C represents its internal series resistance. Through careful selection of $R_{c,}$ the oscillation effect caused by zero impedance of the LCL filter at its resonant frequency can be curtailed [95]. Using vector representations for all three phase variables in this system, the time domain equations describing the inductor current and capacitor voltage variations according to Kirchhoff's voltage law are given as:

$$L_1 \frac{di_1}{dt} = V_i - V_c - i_1 R_1 - (i_1 - i_2) R_c, \quad (3.1)$$

$$L_2 \frac{di_2}{dt} = V_c - V_g - i_2 R_2 + (i_1 - i_2) R_c \quad (3.2)$$

and

$$\frac{dV_c}{dt} = \frac{i_1 - i_2}{C}, \quad (3.3)$$

where V_i, V_c are the voltage vectors across the terminals of the inverter and filter capacitor,

V_g is the PCC voltage and

i_1, i_2 are the inverter and grid side current vectors respectively.

Applying voltage oriented analysis by defining a d-q frame rotating in synchronism with the angular grid frequency, ω and aligning the d-axis with the grid voltage vector, V_{gd}, all vectors in the equations above are converted into their equivalent d-q forms in synchronous reference frame (SRF). Taking the Laplace and d-q transforms of Equs (3.1) - (3.3) gives:

$$I_{1dq}(s) = \left(V_{idq}(s) - V_{cdq}(s) \underline{+} \omega L_1 I_{1qd}(s) + R_c I_{2dq}(s)\right)\left(\frac{1}{sL_1 + R_1 + R_c}\right), \quad (3.4)$$

$$I_{2dq}(s) = \left(V_{cdq}(s) - V_{gdq}(s) \underline{+} \omega L_2 I_{2qd}(s) + R_c I_{1dq}(s)\right)\left(\frac{1}{sL_2 + R_2 + R_c}\right) \quad (3.5)$$

and

$$V_{cdq}(s) = \frac{1}{sC}\left(I_{1dq}(s) - I_{2dq}(s) \underline{+} \omega C V_{cqd}(s)\right). \quad (3.6)$$

Note that a natural consequence of SRF transformation manifests itself in an introduction of cross coupling speed terms of $\underline{+}\,\omega L_1 I_{1qd}(s)$, $\underline{+}\,\omega L_2 I_{2qd}(s)$ and $\underline{+}\omega C V_{cqd}(s)$ due to the presence of inductors L_1 , L_2 and capacitor, C respectively.

The LCL filter block diagram is shown in Fig. 3.2. The diagram assumes an ideal system, where the magnitudes of resistors, R_1, R_2 and R_c are insignificant. The inverter terminal voltage vector components, $V_{idq}(s)$ are the inputs of the system and the output vector components are either the inverter current, $I_{1dq}(s)$ or the grid side current, $I_{2dq}(s)$. Based on these outputs, two distinct LCL filter transfer

functions can be derived. By also setting the grid voltage disturbance, $V_{gdq}(s)$ to zero and implementing block diagram reduction techniques, the transfer functions, $G_{LCL1}(s)$ and $G_{LCL2}(s)$ from the inverter current, $I_{1dq}(s)$ and the grid current, $I_{2dq}(s)$ to the inverter voltage, $V_{idq}(s)$ are respectively given as:

$$G_{LCL1}(s) = \frac{I_{1dq}(s)}{V_{idq}(s)} = \frac{s^2+\omega_{LC}{}^2}{sL_1\,(s^2+\omega_{res}{}^2)} \tag{3.7}$$

and

$$G_{LCL2}(s) = \frac{I_{2dq}(s)}{V_{idq}(s)} = \frac{\omega_{LC}{}^2}{sL_1\,(s^2+\omega_{res}{}^2)}, \tag{3.8}$$

where $\omega_{LC} = \sqrt{1/(L_2C)}$ and $\omega_{res} = \sqrt{(L_1+L_2)/L_1L_2\,C}$, with $\omega_{LC} < \omega_{res}$.

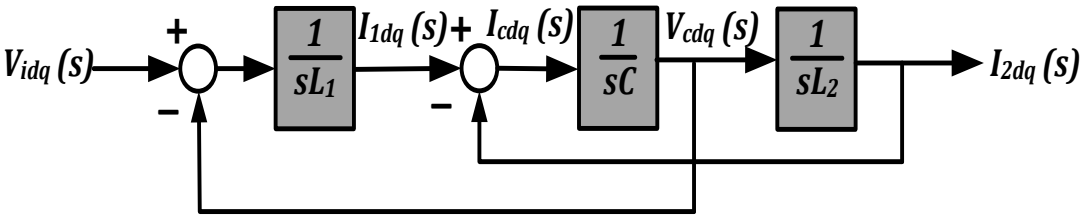

Figure 3:2: Block diagram for the LCL Filter

3.3 Control Principles of the Grid Connected PVDG System

The control structure for the grid connected PVDG system can be seen in Fig. 3.3. Power flow from PV-VSI to the grid is controlled using the voltage oriented control (VOC) technique [96]. The VSI control is implemented with proportional-integral (PI) controllers. PI controllers offer an infinite gain at zero frequency (due to the presence of the integrator pole at origin), hence their control action favours time invariant DC signals. Therefore, all three-phase voltage and current variables are transformed according to the rotating reference d-q frame, thus their fundamental equivalent dq-values are DC quantities. The transformation to the SRF dq-frame is based on the grid voltage phase angle, ωt which is identified through a phase locked loop (PLL) technique described in chapter 1. On the PV power generation side, the maximum power extraction from the PV array is achieved using the perturb and observe (P & O) MPPT method.

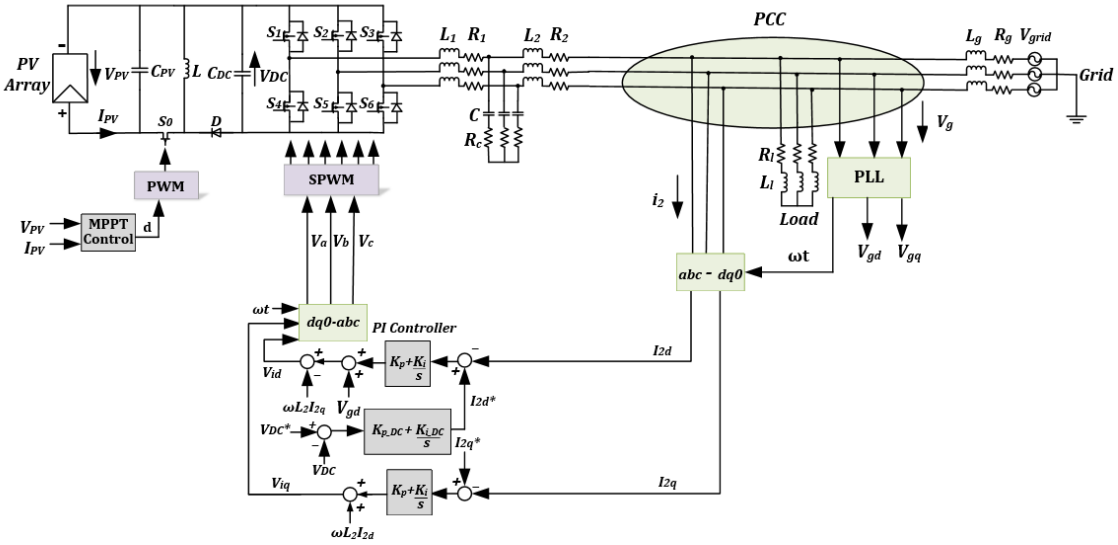

Figure 3:3: Control of a PV-grid connected distributed generation system with LCL filter (using grid current feedback control)

3.3.1 Voltage Oriented Power Flow Control

The basic principle of VOC involves aligning the d-q axis of the controlled variable rotating at the angular grid frequency, ω with the grid voltage vector, V_g. From Fig. 3.3, the controlled variable is the grid current, $i_{2.}$ It is measured from the point of common coupling (PCC) and decomposed into its d-q elements as I_{2d} and I_{2q} using Park's transformation presented in chapter 1.

The reference d-q current values for the PI controllers may be determined by the active *(P)* and reactive *(Q)* powers required to flow from the VSI to the grid, which are given by:

$$P = \frac{3}{2}(V_{gd}{I_{2d}}^* + V_{gq}{I_{2q}}^*) \tag{3.9}$$

and

$$Q = \frac{3}{2}\left(V_{gq}{I_{2d}}^* - V_{gd}{I_{2q}}^*\right). \tag{3.10}$$

Decoupled control of real and reactive powers (P and Q) in Equs. (3.9) - (3.10) is possible, since the q-axis component of grid voltage, V_{gq} has been controlled to zero in the PLL controller. The reference currents in Equs. (3.9) - (3.10) may therefore be re-written as:

$$I_{2d}{}^{*} = \frac{2}{3}\frac{P}{V_{gd}} \tag{3.11}$$

and

$$I_{2q}{}^{*} = -\frac{2}{3}\frac{Q}{V_{gd}}. \tag{3.12}$$

From Equs. (3.11) - (3.12), $I_{2d}{}^{*}$ can be used to regulate the flow of active power in the system, while $I_{2q}{}^{*}$ is generally used for unity power factor regulation.

The control system for the PVDG has two important functions: maintaining the DC link voltage at a fixed value and adjusting the PV generated power supplied to the grid. This leads to the realisation of a cascaded control loop structure: an outer loop for controlling the DC link voltage and inner control loops for regulating the dq-currents. The DC link voltage control loop may therefore provide the reference for the d-axis grid current, $I_{2d}{}^{*}$ which in turn maintains the DC link voltage at a constant value by controlling the magnitude of the current delivered to the grid. Note that the outer DC voltage control loop is decoupled from the inverter d-axis current loop by choosing a sufficiently narrow bandwidth for the former compared to the latter.

From Fig. 3.3, the d-q elements of the measured grid side current, I_{2d} and I_{2q} are compared to their references, $I_{2d}{}^{*}$ and $I_{2q}{}^{*}$ and the errors are applied to their respective PI controllers with identical parameters, K_p and K_i. For the d-element current, the output of this control process is summed with the grid voltage term, V_{gd}, which offers faster speed response for the current controller, consequently improving the current reference tracking performance [96, 97]. The cross coupling term $-\omega L_2 I_{2q}(s)$ must also be added. For q-current element, since q-element of grid voltage, $V_{gq}(s)$ is zero, only $\omega L_2 I_{2d}(s)$ is added. The current control loop generates the reference d-q voltages for the inverter Sine PWM controller, V_{id} and V_{iq}, which generate the VSI switching pulses.

The complete block diagrams of the closed-loop d-q current controllers for grid current ($I_{2d}(s)$ and $I_{2q}(s)$) considering the PWM delay transfer function, $G_D(s)$ and the PWM controller gain, K_{pwm} are implemented in Figs. 3.4 (a) and (b)

respectively. The PI controller and PWM delay transfer functions, $G_{PI}(s)$ and $G_D(s)$ are respectively given as:

$$G_{PI}(s) = K_p + \frac{K_i}{s} \tag{3.13}$$

and

$$G_D(s) = \frac{1}{1+sT_d(s)}, \tag{3.14}$$

where T_d is the time delay due to PWM control and is generally approximated as 1.5 times the switching period [96, 98].

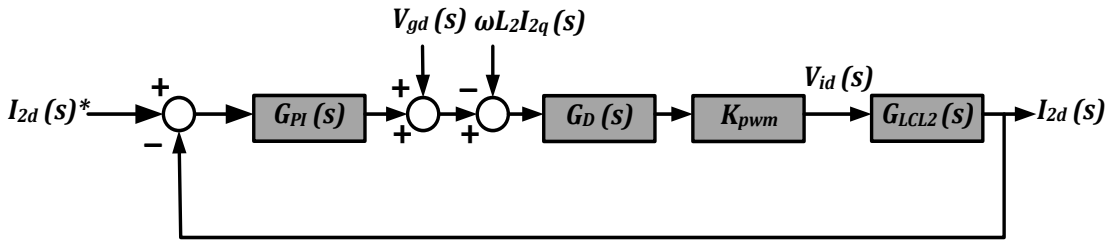

(a)

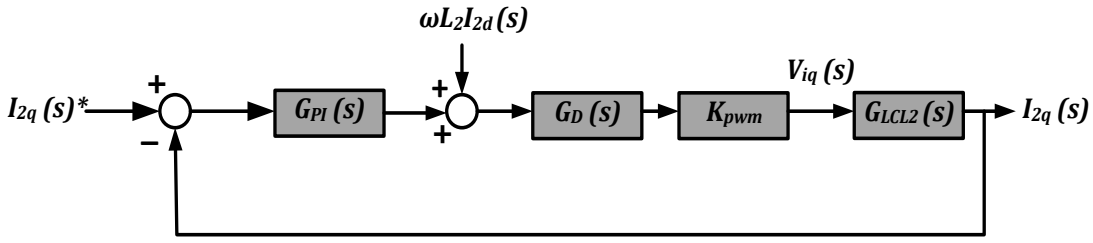

(b)

Figure 3:4: Block diagram for cascaded dq-axis grid current control with an LCL filter (a) d-axis control (b) q-axis control

The above described scheme can also be applied to control the inverter side current, $I_{1dq}(s)$ with the LCL filter transfer function, $G_{LCL1}(s)$ as derived from Equ. (3.7).

3.3.2 Sine PWM Control

The sine PWM technique is used to control the VSI switches by comparing a modulating reference sinusoidal signal with a high frequency triangular carrier signal. Intersections of the two signals generate pulses for the VSI switches. The width of a pulse is directly dependent on the amplitude of the reference sine wave.

Additionally, the reference signal determines the frequency of the synthesised AC voltage while the triangular signal determines the VSI switching frequency. From Fig. 3.3, the reference signals at the output of the PI controllers, V_{id} and V_{iq} are converted into three-phase stationary reference frame signals V_a, V_b and V_c with the grid phase angle, ωt. Each of the three sinusoidal signals is compared with a triangular carrier wave, generating pulse signals for the six VSI switches. Fig. 3.5 (a) illustrates the process of generating PWM pulses by comparing phase A reference sine wave, V_a with a 5 kHz triangular signal. The intersections of the two signals generate the gating pulses for the inverter as shown in Fig. 3.5 (b).

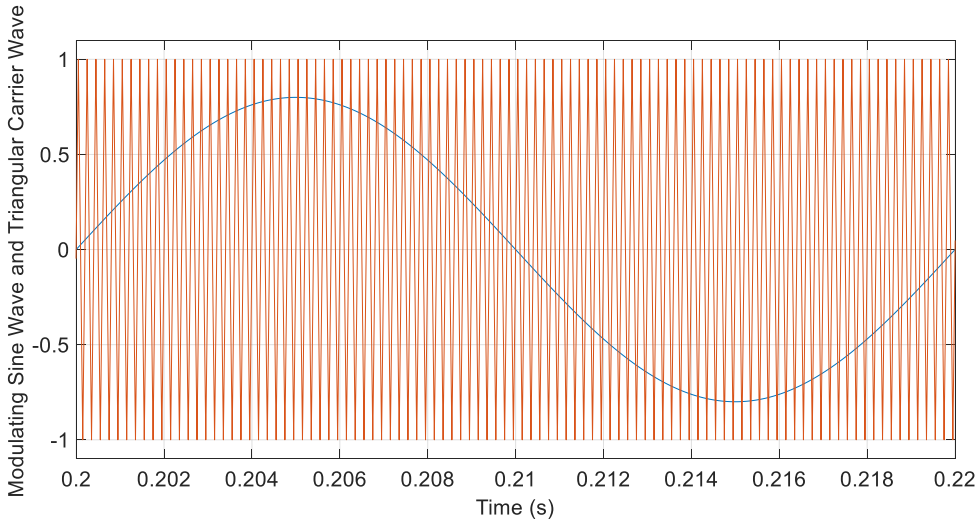

(a)

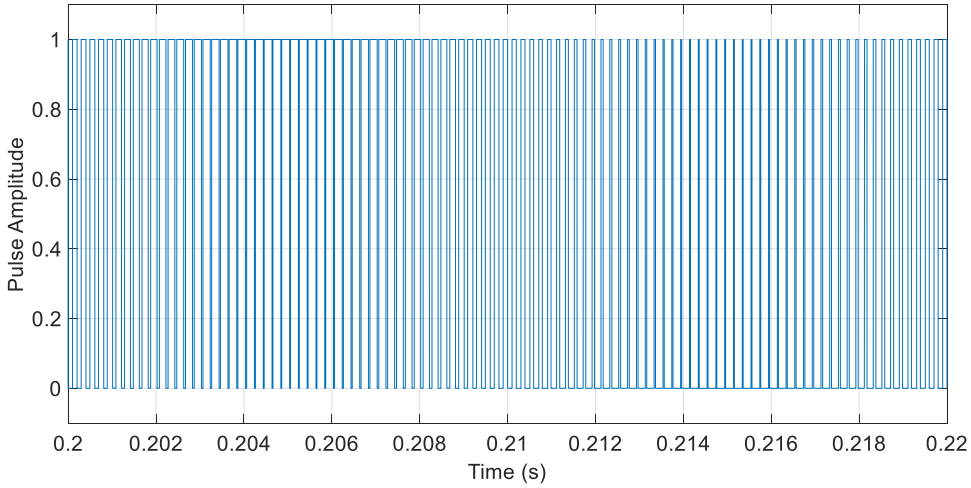

(b)

Figure 3:5: Sine PWM pulse generation (a) Sine-triangle comparison (b) switching pulses

3.4 PV Distributed Generation System Design

3.4.1 Solar PV Array

The solar PV array is designed using the SunPower SPR-305-WHT model from MATLAB/Simulink Software. Based on the atmospheric conditions of 1 *kW/m²* solar irradiance at a temperature of 25^{O}C, the number of series modules per string, n_s and the number of parallel connected strings, n_p can be deduced from the following:

$$n_s = \frac{V_{PV}}{V_{mp}} \tag{3.15}$$

and

$$n_p = \frac{P_{max}/V_{PV}}{I_{mp}}, \tag{3.16}$$

where V_{PV} is the DC voltage across the terminals of the PV array,

P_{max} is the maximum power generated by the array at 1 *kW/m²* solar irradiance and nominal operating cell temperature (NOTC) of 25^{O}C,

V_{mp} is the voltage at the maximum power point and

I_{mp} is the current at the maximum power point.

The design specifications for the PV array are detailed in Table 3.1.

Table 3.1: PV array design specifications

Parameter	**Value**
PV maximum power (P_{max})	100 kW
PV terminal Voltage (V_{PV})	600 V
Voltage at P_{max} (V_{mp})	54.7 V
Current at P_{max} (I_{mp})	5.58 A

Based on the values in Table 3.1, Equs. (3.15) and (3.16), $n_s = 11$ and $n_p = 30$. The current-voltage (I-V) and power-voltage (P-V) characteristics of the PV array at varying levels of solar irradiance are shown in Fig. 3.6. It can be observed that the PV generated current and hence power are strongly dependent on the value of the solar irradiance. The characteristics also portray the non-linear relationship the PV current and PV generated power have with the terminal PV voltage. Determining the magnitudes of both the voltage and current that provide the maximum power from the PV array at different levels of light intensity is therefore crucial for efficient operation of the PV grid tie-system. Maximum power point tracking (MPPT) algorithms have therefore been proposed as a solution.

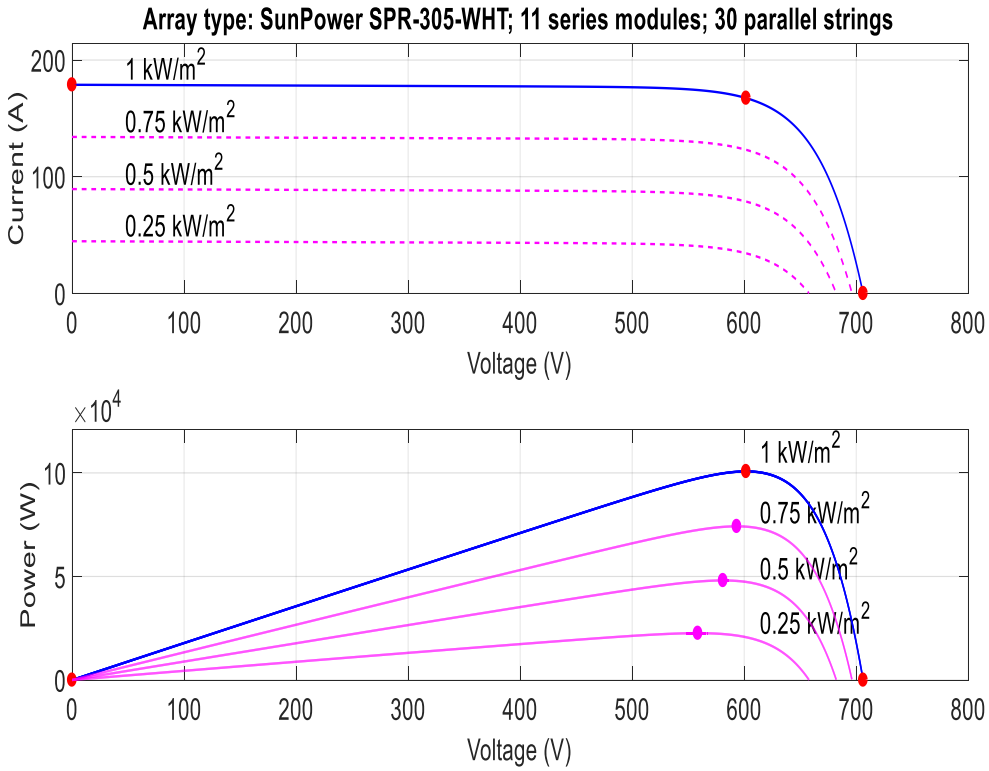

Figure 3:6: IV and PV characteristics of SunPower SPR-305-WHT PV array with varying solar irradiance

MPPT algorithms are generally based on variation of the PV operating point in the direction of increasing output power [99]. One of the simplest methods is the perturb and observe algorithm, which is implemented according to the flowchart in Fig. 3.7. The algorithm uses the present sampled values of the measured PV current and voltage ($I_{PV}(n)$ and $V_{PV}(n)$) to compute the present PV power ($P_{PV}(n)$).Depending on the difference between the present and previous samples of the power ($P_{PV}(n)$ and $P_{PV}(n-1)$) and voltage($V_{PV}(n)$ and $V_{PV}(n-1)$), the DC-DC converter duty ratio, d is perturbed in a particular direction by a small quantity, Δd. If the PV power increases, i.e. $\Delta P_{PV}(n)>0$, d is perturbed further in the same direction until MPP is reached. For a decrease in power (i.e. $\Delta P_{PV}(n)<0$), the direction of perturbation of d is reversed.

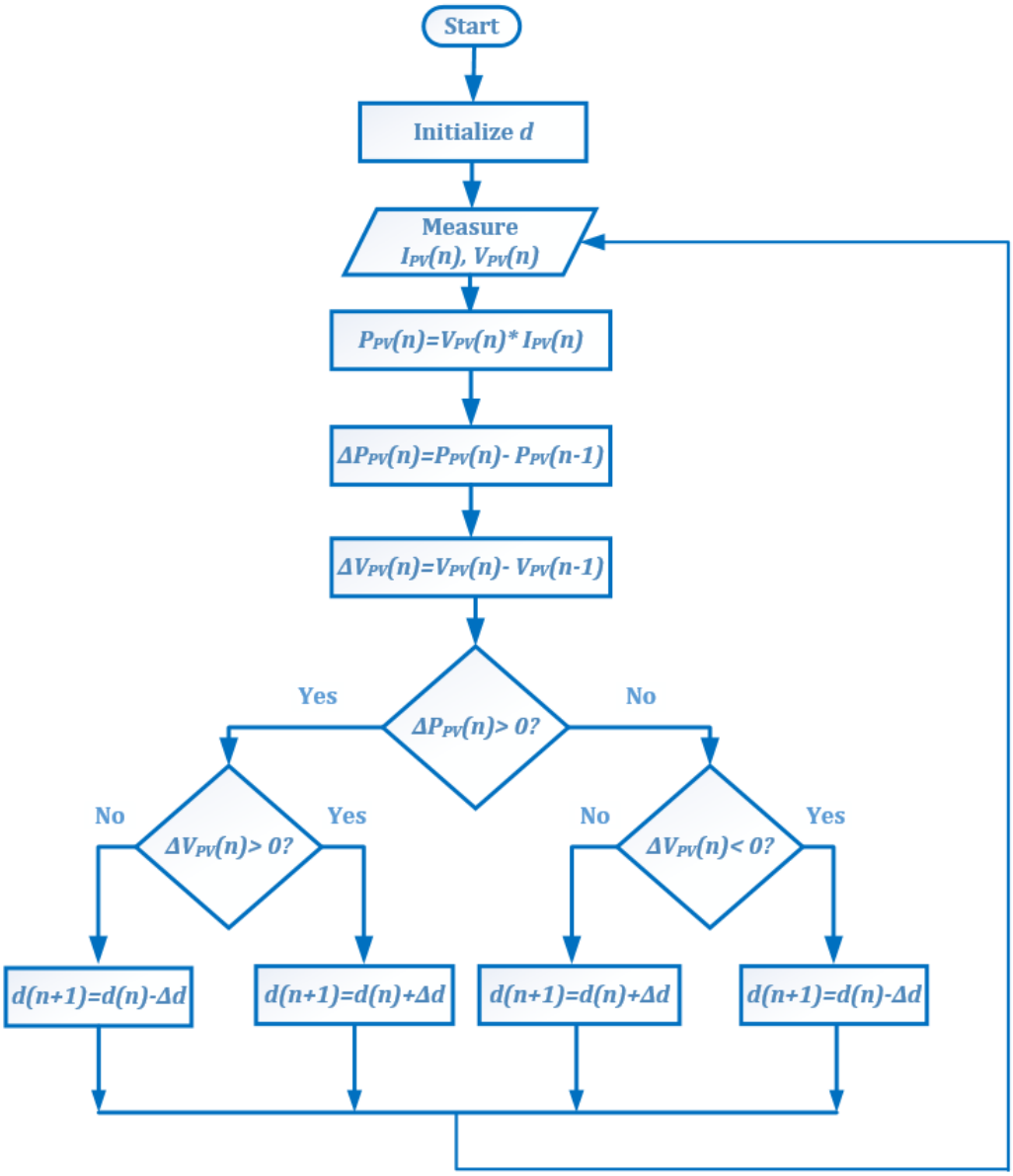

Figure 3:7: Perturb and Observe MPPT algorithm

3.4.2 The DC-DC converter

The DC-DC converter is designed with the parameters specified in Table 3.2.

Table 3.2: DC-DC converter design parameters

Parameter	Rating
PV terminal Voltage (V_{PV})	600 V
Converter switching frequency ($f_{s(DC)}$)	10 kHz
Maximum PV current (I_{mp_array})	167 A
DC link Voltage (V_{DC})	620 V

3.4.2.1 Inductor

The converter inductor, L may be selected using the ripple current specification as a trade-off between inductor sizes and switching losses. At the expense of cost, a large inductor would reduce the ripple current and switching losses. The inductor ripple current is commonly assumed to be 10% of the rated current [31], which in this case is the maximum current generated by the PV array, I_{mp_array}. From the parameters specified in Table 3.2, the inductor is therefore determined from:

$$L = \frac{V_{PV}}{0.1 f_{s(DC)} I_{mp\_array}} \tag{3.17}$$

as

$$L \cong 3.6\, mH. \tag{3.18}$$

3.4.2.2 DC Link Capacitor

The duty cycle of the buck-boost converter, *d* relates to the converter input PV voltage,V_{PV} and the DC link voltage, V_{DC} through Equ. (3.19):

$$d = \frac{V_{DC}}{V_{DC} - V_{PV}}. \tag{3.19}$$

Clearly, the maximum duty cycle occurs when V_{PV} is minimum. Assuming the minimum solar irradiance for PV generation is 100 *W/m²*, the corresponding voltage at maximum power is found to be 347 *V* through simulations. From the specifications in Table 3.2, the maximum duty cycle, d_{max} is therefore:

$$d_{max} = 0.64. \tag{3.20}$$

The DC link capacitor is designed with a maximum 1% ripple tolerance for the DC link voltage [100] according to Equ. (3.21) [101]:

$$C_{DC} = \frac{I_{mp\_array} d_{max}}{f_{s(DC)} \Delta V_{DC}}. \tag{3.21}$$

Substituting for the parameters in Equ. (3.21) from Table 3.2:

$$C_{DC} = 2000\, \mu F. \tag{3.22}$$

The voltage and current levels at the input and output of the DC-DC converter are similar (since the inductor does not consume power), hence the value of C_{PV} is also taken as:

$$C_{PV} = 2000\ \mu F. \tag{3.23}$$

3.4.3 Grid-tie Voltage Source Inverter

The inverter in the simulated system is a two-level, three-phase converter. The switching devices used are assumed ideal, though in practice, they need to be selected according to the inverter power, voltage and current ratings. The specifications are given in Table 3.3.

Table 3.3: Voltage source inverter design parameters

Parameter	Rating
Inverter rated power (P)	100 kW
Grid frequency (f)	50 Hz
Switching frequency (f_s)	5 kHz
DC link voltage (V_{DC})	620 V
RMS Inverter line voltage (V_n)	$220\sqrt{3}$ V
RMS Inverter phase voltage (V_{ph})	220 V

The modulation index, m for a sine PWM controlled VSI is defined as the ratio of the amplitudes of the sinusoidal modulating signal, A_M and the triangular carrier signal, A_C:

$$m = \frac{A_M}{A_C}. \tag{3.24}$$

Operating the VSI within the linear region requires that $A_M \leq A_C$. In the linear region, the RMS value of the fundamental component of the inverter phase voltage, V_{ph} is [102]:

$$V_{ph} = \frac{mV_{DC}}{2\sqrt{2}}. \tag{3.25}$$

If the sine PWM VSI is controlled to maintain a modulation index of unity, the inverter phase voltage magnitude will entirely depend on the DC link voltage. In transformerless grid-tie inverter topology, the inverter phase voltage magnitude should be at least equal to the phase voltage of the grid. From the nominal value of 220 V for V_{ph} in Table 3.3, Equ. (3.25) was used to determine V_{DC} as 620 V.

3.4.4 LCL Filter Parameters

The prime factor to consider when designing an LCL filter is the amount of ripple current on the inverter side [95]. Inductor, L_1 must limit the amount of ripple in the inverter current before grid injection. Inductor, L_2 on the other hand, is designed on the basis of current harmonic contents according to the standard recommendations and utility codes and is therefore designed in the frequency domain [31]. The capacitor selection is based on the constraint of reactive power generation. The specifications of the LCL filter are listed in Table 3.3.

1. **Inverter side inductor, L_1:** The inductor, L_1 is evaluated based on the constraint of maximum ripple current amplitude. Assuming the allowance for current ripple magnitude is 10% of the maximum inverter phase current [103], L_1 is computed thus:

$$L_1 = \frac{V_{DC}}{0.1 n f_s I_{max}}, \tag{3.26}$$

where n is a coefficient depending on the inverter output voltage levels (in this case 2) [31] and I_{max} is the maximum inverter current, given as:

$$I_{max} = \frac{P\sqrt{2}}{3V_{ph}}. \tag{3.27}$$

Upon substitution for V_{DC}, n, f_s, P and V_{ph} from Table 3.3:

$$L_1 \cong 3\ mH. \tag{3.28}$$

2. **Filter Capacitor, C:** The maximum value of the filter capacitor,C is designed to limit the amount of reactive power it produces. A high capacitance results in a higher current flow through inductor, L_1 and the VSI switches, resulting in a lower LCL filter efficiency. The ratio of the reactive power produced by capacitor, C to the rated active power of the VSI, P is defined as λ and is generally restricted to a maximum of 5% [97, 103]. Hence, filter capacitor may be determined form Equ. (3.29) as:

$$C = \lambda \frac{P}{2\pi f {V_n}^2}. \quad (3.29)$$

Considering λ as 5% and substituting for P, f and V_n from Table 3.3:

$$C \cong 118\ \mu F. \quad (3.30)$$

3. **Grid side inductor, L_2**: An attenuation factor, k_a is defined for supressing the amplitude of the harmonic current supplied to the grid, $i_2(h)$. It is commonly limited to 20% of the harmonic current on the inverter side, $i_1(h)$ [87, 103] and is expressed as:

$$k_a = \frac{i_2(h)}{i_1(h)}. \quad (3.31)$$

The value of inductor, L_2 is related to k_a from Equ. (3.31) through Equ. (3.32) [87]:

$$L_2 = \frac{\sqrt{\frac{1}{{k_a}^2}+1}}{C(2\pi f_s)^2}. \quad (3.32)$$

Setting k_a to 20% and substituting for capacitor, C from Equ. (3.30) and f_s from Table 3.3:

$$L_2 \cong 51\ \mu H. \quad (3.33)$$

4. **The resonant frequency, f_{res}**: This occurs when the impedance of the inductors, L_1 and L_2 match and cancel the impedance of the capacitor, C. It is defined as:

$$f_{res} = \frac{\omega_{res}}{2\pi} = \frac{1}{2\pi}\sqrt{\frac{L_1+L_2}{L_1 L_2 C}}. \quad (3.34)$$

Substituting the filter values L_1, C and L_2 given in Equs. (3.28), (3.30) and (3.33) respectively gives a value of approximately 2.1 *kHz*. This satisfies the requirement for the LCL filter resonant frequency, which is set to lie in the range:

$$10f < f_{res} < 0.5f_s. \quad (3.35)$$

The reason for this is to prevent the filter resonance from appearing near the grid and VSI switching frequencies, as this would lead to amplification and propagation of unwanted harmonics in the control systems.

5. **The damping resistor, R_d**: If passive damping is to be employed to curb the resonant frequency, a damping resistor, R_d cascaded with the

capacitor, C is calculated as 1/3 of the impedance of the capacitor at the resonant frequency [103]. Therefore:

$$R_d = \frac{1}{3\omega_{res}C}. \tag{3.36}$$

Substituting for C from Equ. (3.30):

$$R_d \cong 0.22\ \Omega \tag{3.37}$$

6. **LCL series resistors**: To confirm with practical analysis, the effect of parasitic resistance on the LCL filter components must be considered, and this is known as the equivalent series resistance (ESR). With a known quality factor (Q) and reactance (X), the ESR of the individual LCL components can be determined from Equ. (3.38):

$$ESR = \frac{X}{Q}, \tag{3.38}$$

where

$$X = \omega L \text{ for an inductive reactance and} \tag{3.39}$$

$$X = \frac{1}{\omega C} \text{ for a capacitive reactance.} \tag{3.40}$$

The larger the quality factor, the closer the component is to ideal. The typical value of *Q* for ferrite pot cored inductors used in filters is 40 [25], with capacitors typically having higher quality factors [104, 105]. For the purpose of LCL resonant frequency analysis, a large quality factor of 2000 is assumed for L_1, L_2 and C. This correspondingly gives the ESR values as:

$$R_1 = 4.7 \times 10^{-4}\Omega; \tag{3.41}$$

$$R_2 = 0.8 \times 10^{-5}\Omega \tag{3.42}$$

and

$$R_c = 0.015\ \Omega. \tag{3.43}$$

3.4.5 Control systems Design

3.4.5.1 Current Control

A simplification in designing the control parameters for the PVDG system is that the dynamics of the LCL filter capacitor play a minimal role in the low frequency spectrum in which the control system operates. The LCL filter thus approximates to an RL- filter, with currents, $i_1 = i_2$. Equ. (3.1) may be re-written as:

$$L \frac{di_2}{dt} = V_i - V_g - i_2 R, \tag{3.44}$$

where L is the sum of inductors, L_1 and L_2 and

R is the sum of resistors, R_1 and R_2.

Taking the Laplace and d-q transform of Equ. (3.44) gives:

$$I_{2dq}(s) = \left(V_{idq}(s) - V_{gdq}(s) \pm \omega L I_{2qd}(s)\right)\left(\frac{1}{sL+R}\right) \tag{3.45}$$

The simplified block diagram for control of d-axis and q-axis currents, $I_{2d}\ (s)$ and $I_{2q}\ (s)$ is seen in Figs. 3.8 (a) and (b) respectively, with the cross coupling and feedforward terms eliminated, and the RL-filter transfer function represented as $G_{RL}(s)$.

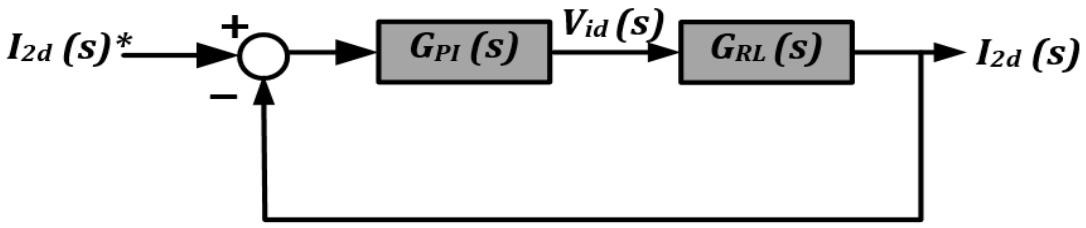

(a)

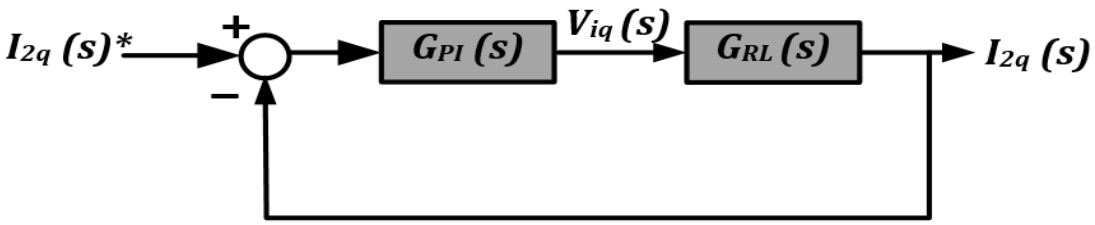

(b)

Figure 3:8: Simplified block diagram for cascaded dq-axis grid current control with an RL- filter (a) d-axis control (b) q-axis control

The closed loop transfer function from Fig. 3.8, considering the PI-controller and the RL-filter transfer functions is given as:

$$\frac{I_{2dq}(s)}{I_{2dq}(s)^*} = \frac{\frac{K_p}{L}s+\frac{K_i}{L}}{s^2+\left(\frac{R+K_p}{L}\right)s+\frac{K_i}{L}}. \tag{3.46}$$

The PI controller parameters are determined using the pole-assignment design technique [106], where the parameter values are tuned according to the desired closed loop characteristics of the system in terms of bandwidth and damping ratio.

The standard second order transfer function, $G(s)$ in terms of the natural frequency, ω_o and the damping ratio, ζ is:

$$G(s) = \frac{{\omega_o}^2}{s^2+2\zeta\omega_o s+{\omega_o}^2}. \tag{3.47}$$

Comparing Equ. (3.46) with the transfer function in Equ. (3.47):

$$K_p = 2\zeta\omega_o L - R \tag{3.48}$$

and

$$K_i = L{\omega_o}^2. \tag{3.49}$$

A trade-off between response speed and noise sensitivity in the current control loop is applied in selecting the closed loop bandwidth. A value of ω_o set to $100\ Hz$ and ζ set to 1 [106] were used to determine K_p as 4 and K_i as 1200 from Equs. (3.48) and (3.49) respectively.

3.4.5.2 DC Link Voltage Control

The DC link voltage magnitude is determined by the instantaneous power balance at the input and output of the VSI. Assuming a scenario where switching losses are negligible, the DC link capacitor is ideal and unity power factor control is employed, the power balance equation may be expressed as:

$$V_{DC}I_{DC} = \frac{3}{2} V_{gd}I_{2d}, \tag{3.50}$$

where I_{DC} is the DC current flowing through the capacitor and is given as:

$$I_{DC} = C\frac{dV_{DC}}{dt}. \tag{3.51}$$

The amplitude of the d-component of the voltage, V_{gd} with respect to the DC link voltage, V_{DC} can be established from Equ. (3.25), since V_{gd} is equivalent to the maximum value of the RMS phase voltage, V_{ph}. Thus:

$$V_{gd} = \frac{mV_{DC}}{2}. \tag{3.52}$$

Substituting Equs. (3.51) and (3.52) into Equ. (3.50):

$$C\frac{dV_{DC}}{dt} = \frac{3m}{4} I_{2d}. \tag{3.53}$$

Taking the Laplace transform of Equ. (3.53) and re-arranging:

$$\frac{V_{DC}(s)}{I_{2d}(s)} = \frac{3m}{4Cs}. \tag{3.54}$$

The DC link voltage control loop is shown in Fig. 3.9, with the transfer function of Equ. (3.54) represented as $G_{DC}(s)$.

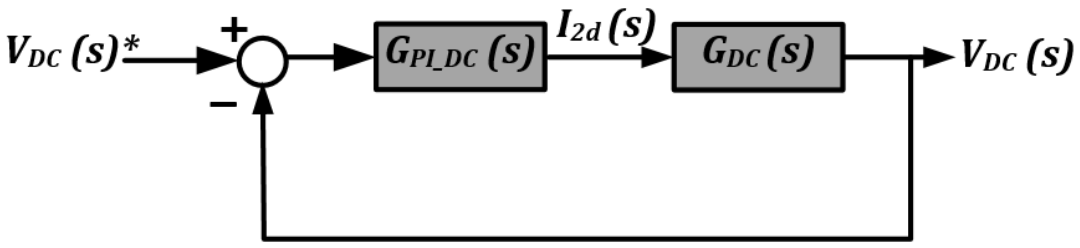

Figure 3:9: DC link voltage control

The DC link voltage controller, $G_{PI\_DC}(s)$ is designed using the same technique as the dq-current controllers. The closed loop transfer function according to Fig. 3.9 is:

$$\frac{V_{DC}(s)}{V_{DC}(s)^*} = \frac{\frac{3mK_{p\_DC}}{4C}s+\frac{3mK_{i\_DC}}{4C}}{s^2+\frac{3mK_{p\_DC}}{4C}s+\frac{3mK_{i\_DC}}{4C}}. \quad (3.55)$$

Comparing Equ. (3.55) to Equ. (3.47), the PI control parameters, K_{p_DC} and K_{i_DC} are computed. The closed loop bandwidth for the outer DC voltage control loop is set to be 10 times smaller than the inner d-axis current control loop, thereby ensuring decoupling between the two controllers. Assigning ω_o to be $10\,rad/s$ and ζ to be 0.7, [106] K_{p_DC} was determined as 0.23 and K_{i_DC} as 11.

3.5 Undamped LCL Filter Analysis

In the absence of damping, the Bode plot for the LCL filter designed in section 3.4.4 can be seen in Fig. 3.10. The open loop gain rises around the resonant frequency, ω_{res} corresponding to the frequency at which the impedances of the inductors and capacitor of the LCL filter cancel out, offering negligible resistance to the flow of current. According to the Nyquist stability criterion, a system is considered unstable if there is a negative crossing of -180^O in the phase plot, where the magnitude of the transfer function,

$$|G(j\omega)| > 0. \quad (3.56)$$

From Fig.3.10,$|G(j\omega_{res})| > 0$ at the negative crossing of -180^O, resulting in a negative phase margin of -21.5^O at ω_{res}. This clearly indicates instability in the undamped LCL filter.

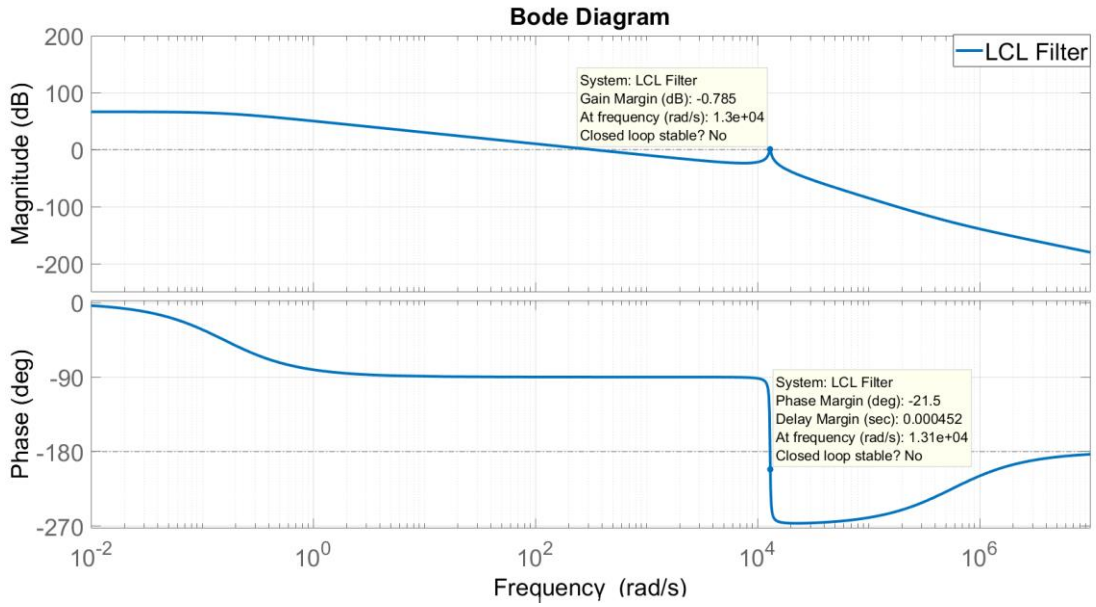

Figure 3:10 Bode plot for undamped LCL filter

The roots of the LCL filter can be visualised more clearly with the root locus diagram in Fig. 3.11. It shows the high frequency resonant poles of the filter lying close to the imaginary axis, an indication that the they are lightly damped. The pole pair have their root loci located almost entirely in the unstable region of the s-plane for all values of the loop gain, $K > 0.9$. The third pole, located at the origin, is critically damped with a damping ratio of unity. The control aim is therefore to explore techniques that can improve the stability range of the LCL filter.

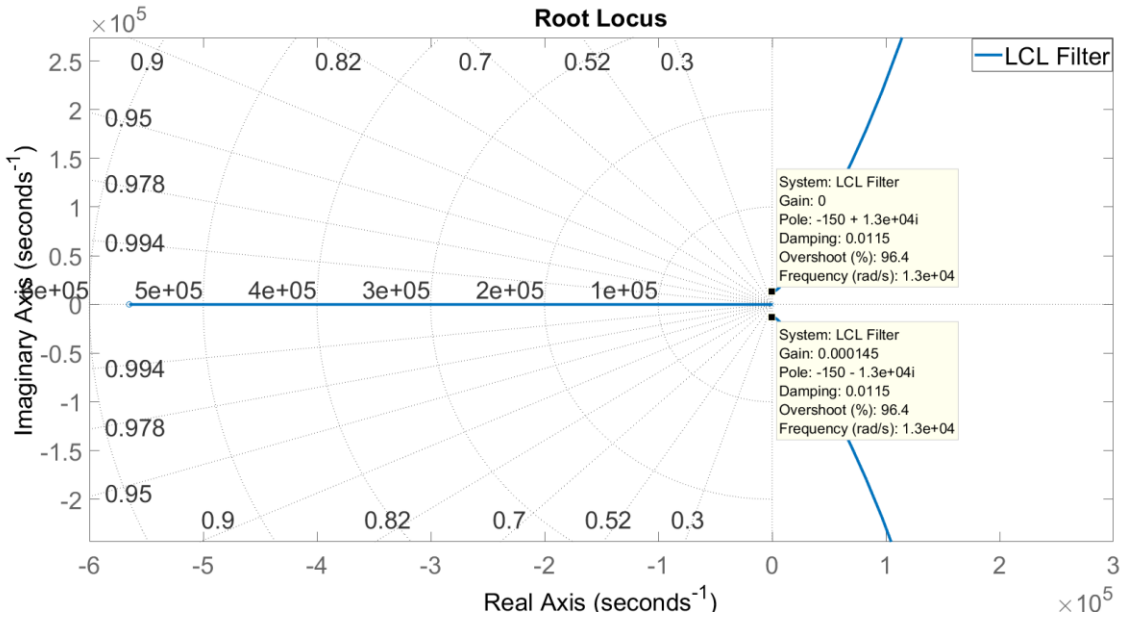

Figure 3:11: Root locus for undamped LCL filter

3.6 LCL Filter Resonance Damping Methods

The unstable dynamics of the LCL filter due to its resonance result in perturbation of the control system. Consequently, LCL filter damping methods have been developed and can be broadly classified into: passive and active damping.

3.6.1 Passive damping

This is the most simplistic method, as it employs a resistor, R_d providing a resistive element to the flow of current at the resonant frequency, ω_{res} of the LCL filter. The resistor can be placed in series or parallel with the capacitor [86]. The control realisation for the grid current, $I_{2dq}(s)$ incorporating a series connected damping resistor, R_d is shown in Fig. 3.12 (a) and (b) for the d-axis and q-axis current controls respectively.

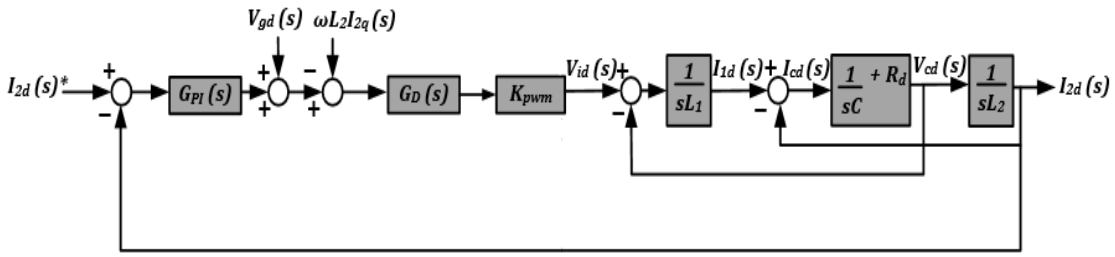

(a)

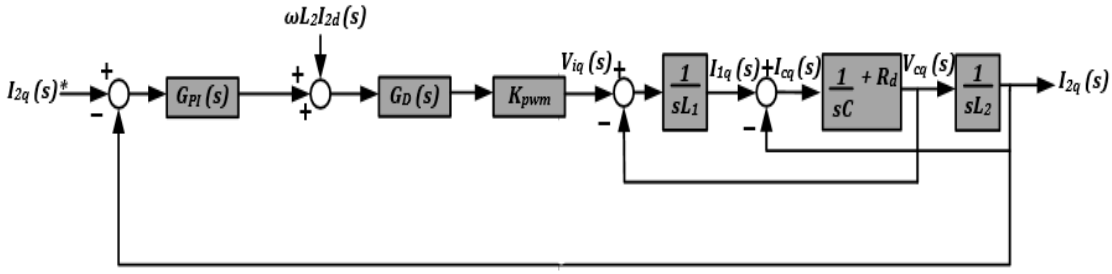

(b)

Figure 3:12: Passive damping of an LCL filter (a) d-axis control (b) q-axis control

The transfer function from the grid current, $I_{2dq}(s)$ to the inverter voltage, $V_{idq}(s)$ with the damping resistor, R_d is:

$$\frac{I_{2dq}(s)}{V_{idq}(s)} = \frac{sR_dC+1}{s^3L_1\,L_2\,C+s^2CR_d(L_1+L_2\,)+s(L_1+L_2\,)}. \quad (3.57)$$

Figure 3.13 compares the Bode plots of the undamped LCL filter with that employing passive damping. The gain and phase margins have improved with passive damping, having values of 26.9 and 90^O respectively. In the high frequency region above the resonant frequency, the slope of the LCL filter plot changes from -60 *dB/decade* for the undamped case to -40 *dB/decade* when passive damping is introduced. This is due to the additional zero in Equ. (3.57). As a result, the attenuation capacity for high frequency components has been reduced in the system and this is one of the major disadvantages of passive damping [86].

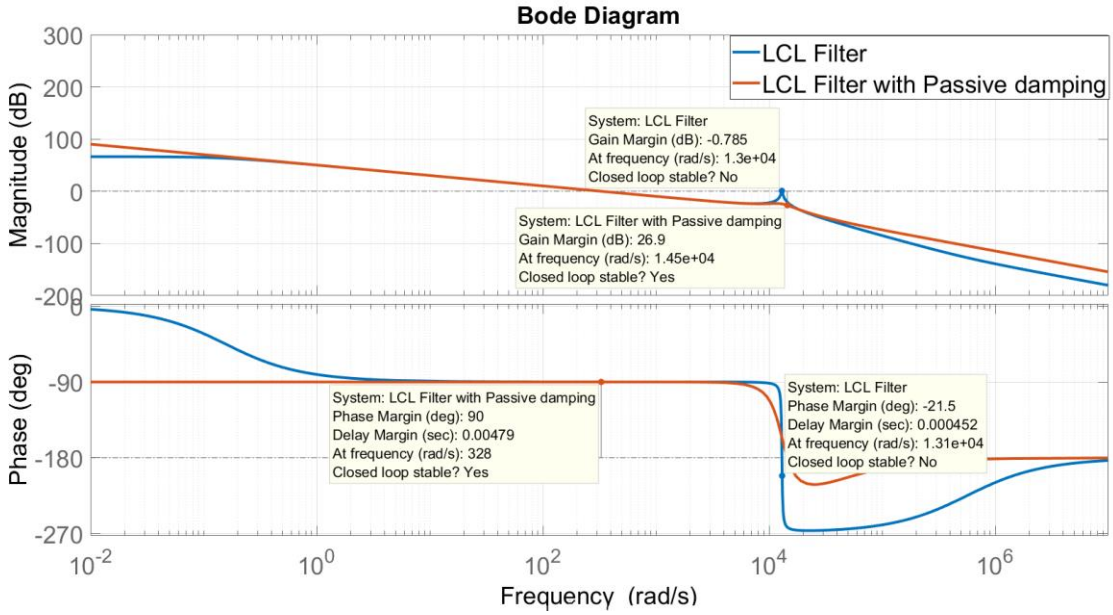

Figure 3:13: Open loop Bode plot comparing passive damping with an undamped LCL filter

The power loss due to passive damping, P_{PD} may be computed as:

$$P_{PD} = 3R_d\left(i_1{}^2 - i_2{}^2\right). \quad (3.58)$$

It is apparent from Equ. (3.58) that when this form of damping is used, significant power loss incurs hence impairing efficiency, particularly in the case of large power applications, where sufficiently large current flows into the LCL filter circuit.

In a bid to reduce the losses caused by R_d, passive components such as capacitors and inductors may be used [88]. These methods, however, increase

filter complexity and cost, with further reductions in filter performance in the high frequency range [86]. Furthermore, introduction of more capacitors into the filter damping circuit produces additional resonant peaks [86].

3.6.2 Active Damping

These methods aim to tackle filter resonance through modification of the control algorithm, reducing the chances of instability. Compared to the passive method, active damping increases the complexity of the control loop [107]. They are classified as single loop filter-based and multi-loop active damping methods. While the former uses a filter such as a notch filter to eliminate the resonance, the latter involves an additional feedback loop for damping [108]. Some common methods of active damping discussed below are: the virtual resistance method and the notch filter method.

3.6.2.1 Virtual resistance

Virtual resistance active damping can be implemented by means of adding a capacitor current feedback [86, 88-93]. The block diagram for the grid current control loop with virtual resistance active damping is as shown in Fig. 3.14 (a) and (b). The d-q current elements through the capacitor branch, $I_{cdq}(s)$ after multiplying a gain factor, *k* are used as feedback to reduce the inverter voltage, $V_{idq}(s)$. It is termed 'virtual resistance' because it emulates a real resistance, with the exception of the losses. The effect on the LCL filter is the reduction of the voltage across the capacitor by a value proportional to its current. Both the capacitor voltage or current may be used in the feedback loop [109].

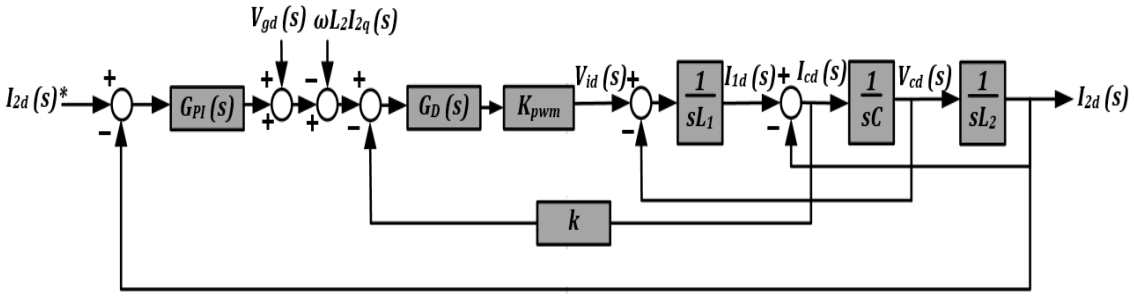

(a)

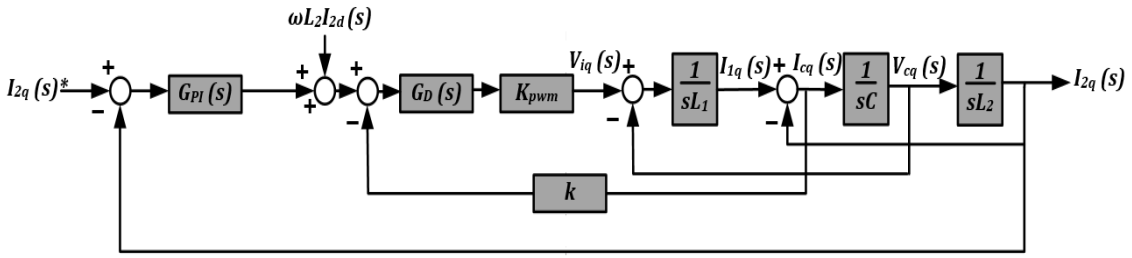

(b)

Figure 3:14: Virtual resistance damping of an LCL filter (a) d-axis control

(b) q-axis control

The transfer function between the grid side current, $I_{2dq}(s)$ and the inverter voltage, $V_{idq}(s)$ with the virtual resistance, *k* is:

$$\frac{I_{2dq}(s)}{V_{idq}(s)} = \frac{1}{s^3 L_1 L_2 C + s^2 C k L_2 + s(L_1 + L_2)}. \quad (3.59)$$

Figure 3.15 compares the performance of two virtual resistors (*k* = *10* and *100*) in attenuating the gain at the resonant frequency. The virtual resistance is capable of eliminating resonance while simultaneously maintaining the same attenuation level of -60dB/decade for high frequency components, as in the case of the undamped filter. As the value of *k* increased from 10 to 100, the gain margin improved by 20 dB. On the other hand, the phase margin reduced from 89.6^{O} to 86.3^{O} due to the increased negative phase shift before the resonant frequency, a typical characteristic of overdamped systems. As this negatively affects the system phase margin, careful selection of the virtual resistance value, *k* is required in damping the LCL filter.

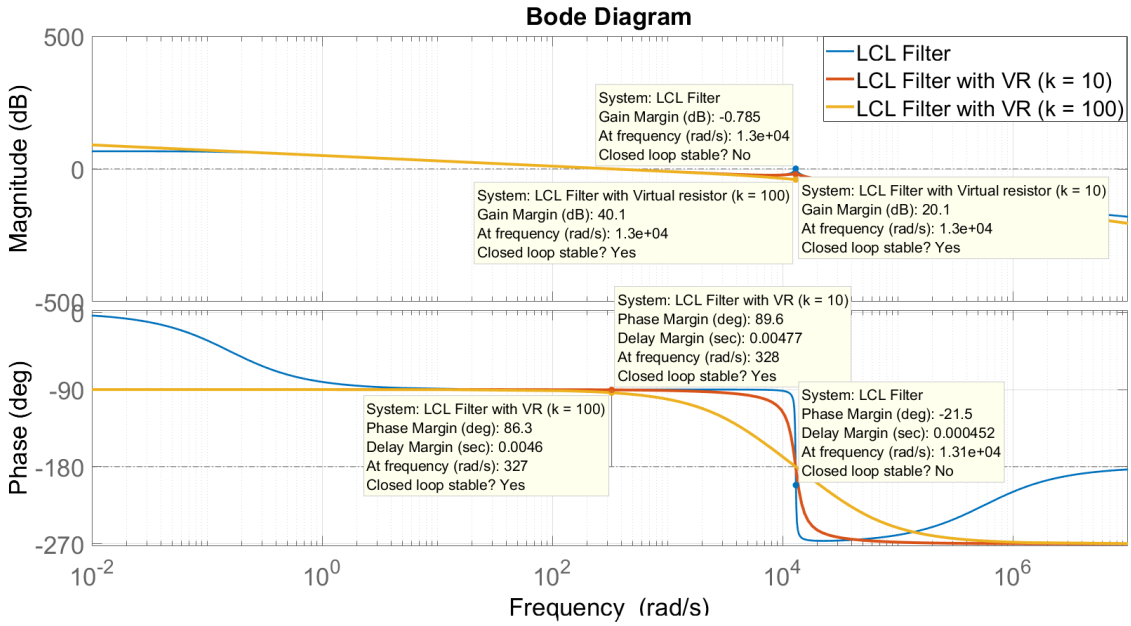

Figure 3:15: Open loop Bode plot comparing virtual resistances (*k = 10* and *100*) with an undamped LCL filter

The drawbacks with this technique are the requirement for extra sensors and in some cases a differentiator, as differentiators are associated with amplification of high frequency signals [109].

3.6.2.2 Notch filter

The notch filter (NF), also known as a band stop filter, may be used to attenuate frequencies within a certain band, by producing a notch at a specific frequency, as seen from the Bode plot frequency response in Fig. 3.16. An ideal notch filter offers an infinite gain at the notch frequency, ω_n with a transition from 90^O phase lagging to leading. It is considered a very good active damping option, as it does not require extra sensors for capacitor current measurement, as in the case of using a virtual resistance [107].The transfer function of a notch filter, $G_{NF}(s)$ is given as:

$$G_{NF}(s) = \frac{s^2+2\zeta_1\omega_n s+{\omega_n}^2}{s^2+2\zeta_2\omega_n s+ {\omega_n}^2}, \qquad \zeta_2 > \zeta_1 \tag{3.60}$$

where ζ_1 is the damping ratio of the NF zeros

and ζ_2 is the damping ratio of the NF poles.

For a given frequency, ζ_1 and ζ_2 are responsible for setting the magnitude of the NF gain.

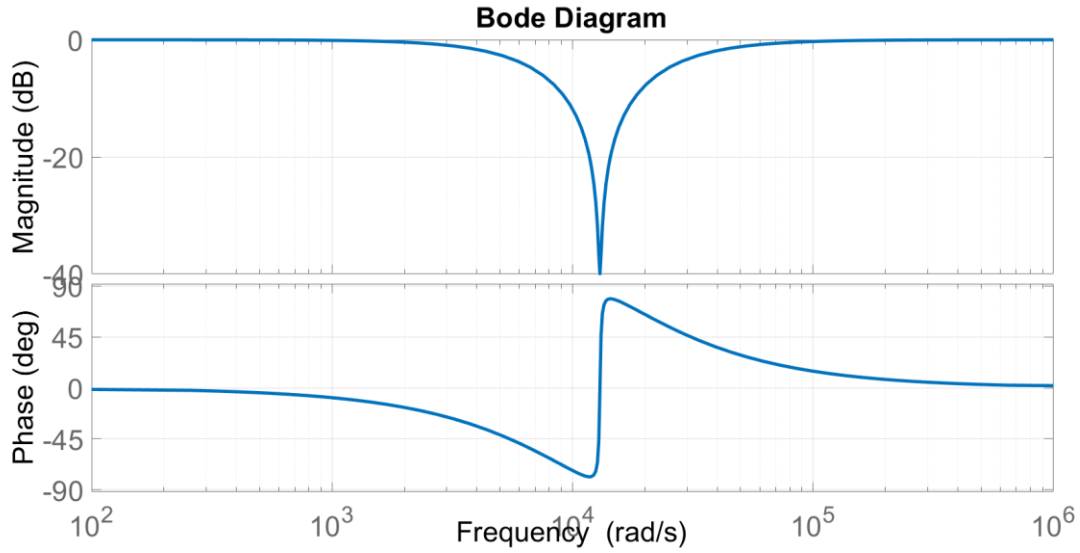

Figure 3:16: Bode plot for notch filter

For LCL filter resonant frequency suppression, the notch filter, with transfer function, $G_{NF}\ (s)$ is cascaded with the d-q grid current controllers, as shown in Fig. 3.17 (a) and (b) respectively. Through this arrangement, the NF produces a high negative gain at the resonant frequency, thereby suppressing the LCL filter's resonance to insignificant levels. The NF introduces a pair of complex zeros (Equ. (3.60)), which if tuned to ω_{res}, can cancel the effect of the LCL filter poles. To prevent the NF poles form affecting the system dynamics and cancellation of NF zeros, they are situated well into the left of the imaginary axis [109]. This results in an improved stability margin for the entire system.

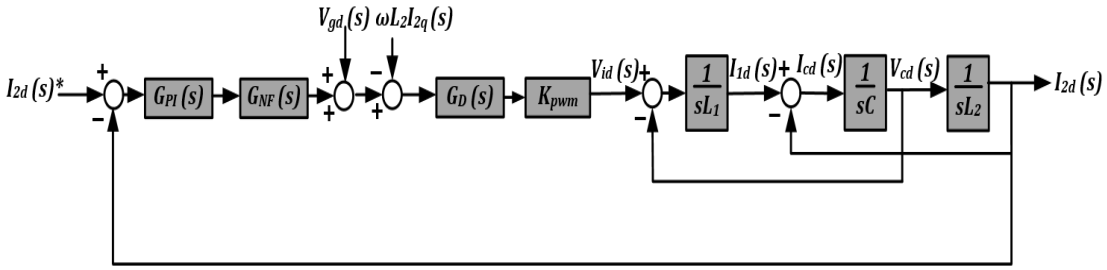

(a)

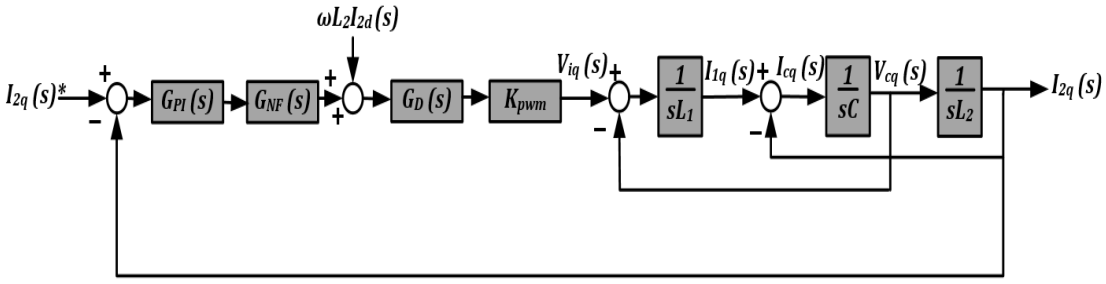

(b)

Figure 3:17: Current control loop for grid connected LCL filter with notch filter active damping (a) d-axis (b) q-axis

The Bode plot frequency response for the NF connected in series with the LCL filter is depicted in Fig. 3.18 and contrasted with that without the NF. By introducing a NF with a negative gain at the LCL resonant frequency, the magnitude of the combined gain, $|G_{LCL2}(j\omega_{res})G_{NF}(j\omega_{res})| < 0$ at the negative crossing of -180^{O}, satisfying the requirement for stability. The gain margin and phase margin improve to 37.7 and 87.2^{O} respectively. Additionally, the attenuation of the high frequency components by the LCL filter remain unchanged at -60 *dB/decade* after it is cascaded with the NF. The NF, however, produces a negative phase shift before the resonant frequency. If this produces an unacceptable phase margin, a lead compensator may be required.

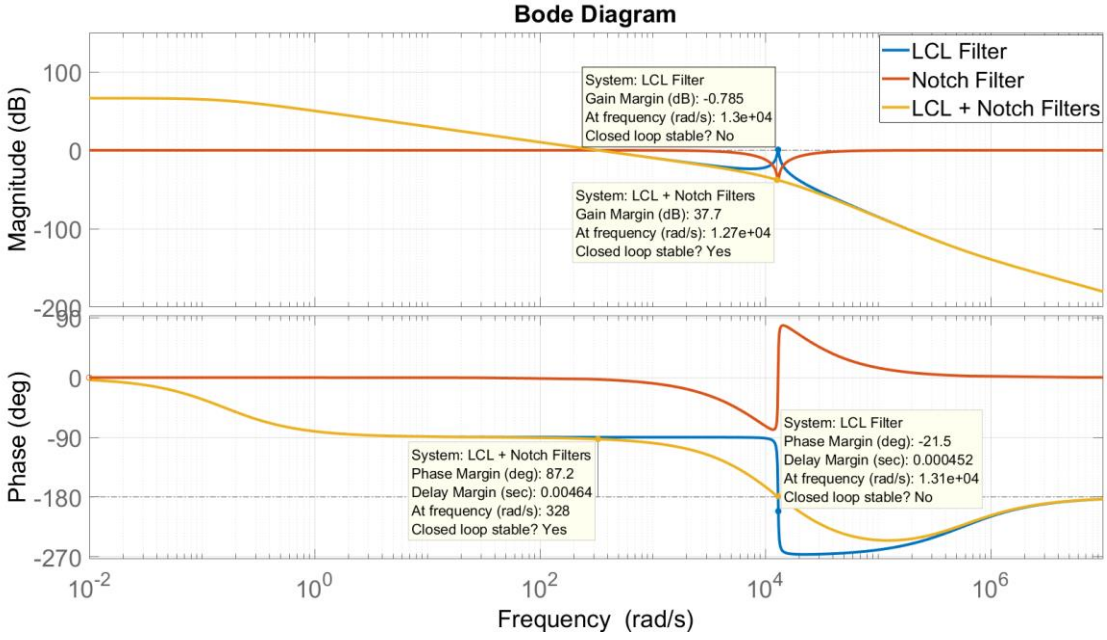

Figure 3:18: Open loop Bode plot comparing an undamped LCL filter with a cascaded LCL and notch filter

Fig 3.19 shows the root locus for the cascaded NF and LCL filters. Compared to the undamped LCL filter root locus in Fig. 3.11, the stability range of the system for finite values of gain, *K* has increased by 98%, from 0.9 to 77. This, coupled with the improved gain and phase margins of Fig. 3.18 ,verify that the NF has positive effects on the stability of the system.

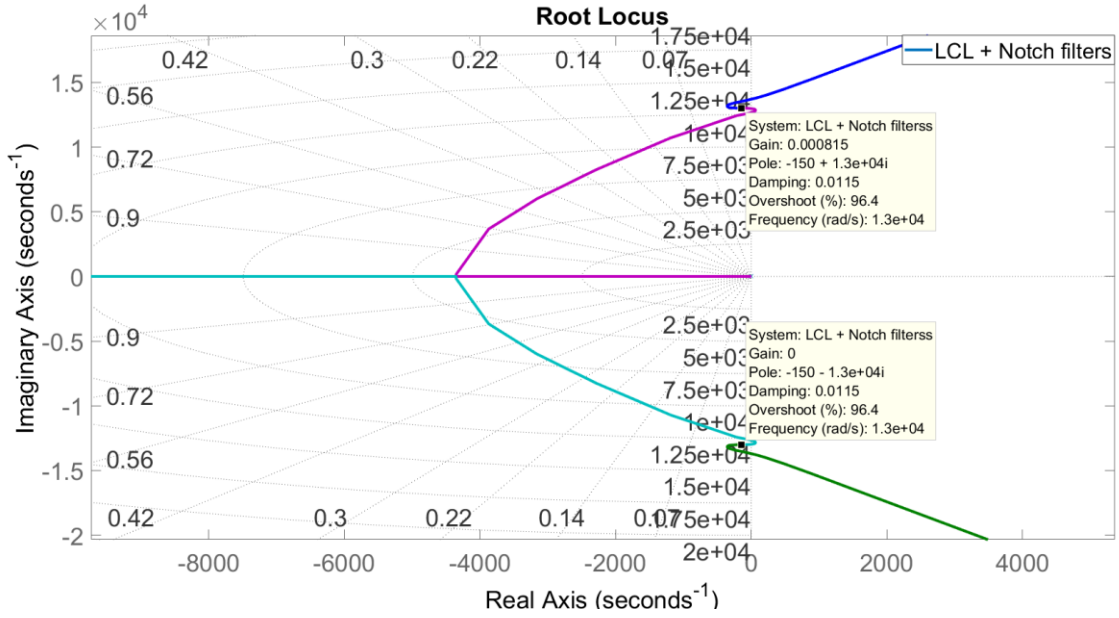

Figure 3:19: Root locus for cascaded LCL and notch filters

3.7 Notch Filter Frequency Analysis

3.7.1 Effect of Varying Notch Filter Damping Ratios

From Equ. (3.60), if ω_n is equivalent to the LCL filter resonant frequency, ω_{res}:

$$G_{NF}(j\omega_{res}) = \frac{\zeta_1}{\zeta_2}. \tag{3.61}$$

Equ. (3.61) indicates that the amplitude of the NF gain at the resonant frequency depends on the ratio of the damping of zeros and poles respectively. Figure 3.20 shows the Bode plots for a notch filter with a centre frequency, ω_n of $100\ rad/s$,while ζ_2 is varied between 0.5, 1 and 2. ζ_1 is maintained at 0.01.

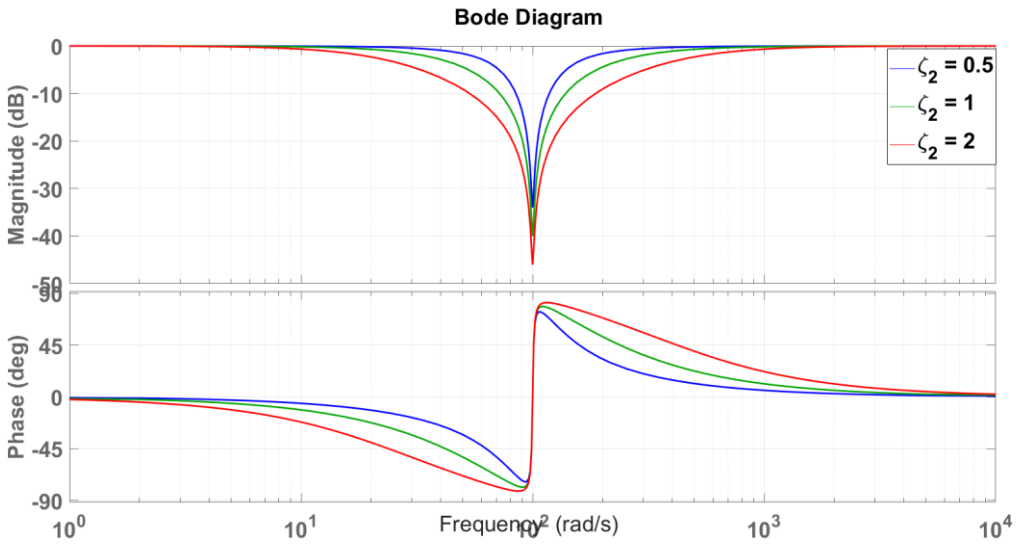

Figure 3:20: Bode plot showing the effect of increasing ζ_2 in a NF

The effect of increasing the value of ζ_2 is a wider width around the NF centre frequency. The increase in width causes higher low frequency phase lag with reduced phase margin.

From Equ. (3.61), a fixed value for ζ_2 renders ζ_1 responsible for setting the desired depth at the NF gain. This has a direct effect on the attenuation level at the LCL resonant frequency, as seen in Fig. 3.21, where ζ_1 is varied between 0.001, 0.01 and 0.1, while ζ_2 remains fixed at unity. A shallow notch amplitude at ω_{res} increases phase margin with reduced attenuation capabilities whereas a deeper notch gain provides better attenuation of the LCL resonant frequency with a reduced phase margin. Since the control aim is to reduce the resonant frequency significantly, ζ_2 should be made sufficiently higher than ζ_1 in order to suppress the gain at the LCL resonant frequency.

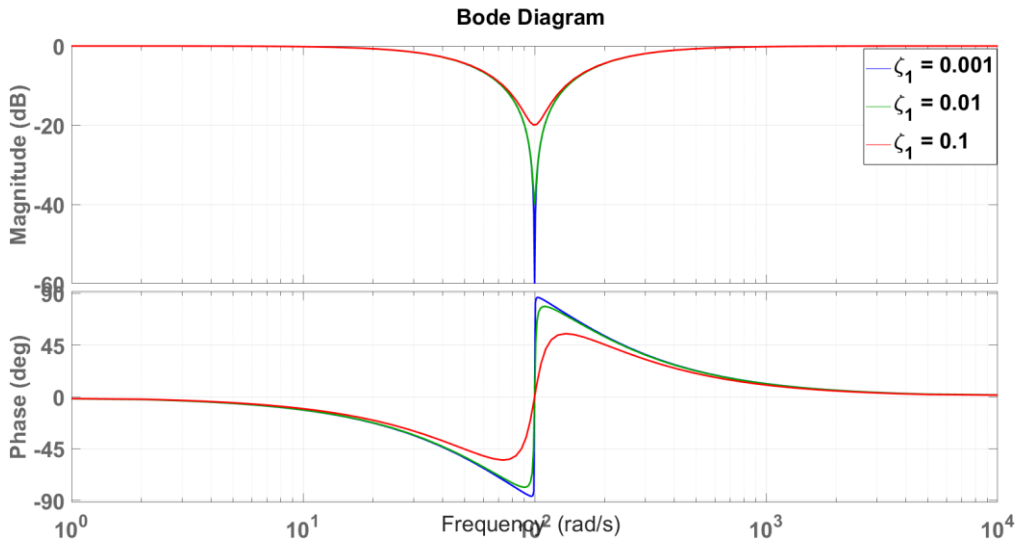

Figure 3:21: Bode plot showing the effect of increasing ζ_1 in a NF

3.7.1.1 Effect on Control System Stability

The notch filter effect on the closed loop system stability is studied through variation of the NF gain at the resonant frequency, $G_{NF}(j\omega_{res})$, represented by α. The effect can be seen in the Bode plot of Fig. 3.22 (a). The increase in α has opposite effects on the gain and phase margins: higher values for α result in better system phase margin, as seen in Fig. 3.22 (b). From the two extreme magnitudes of α, i.e. 0.01 and 0.1, the phase margin of the closed loop system has improved by 1.7%. Conversely, increasing α from 0.01 to 0.1 has resulted in a 72% decrease in gain margin in Fig. 3.22 (c). This is expected, since increasing α is tantamount to reducing the NF gain at the resonant frequency.

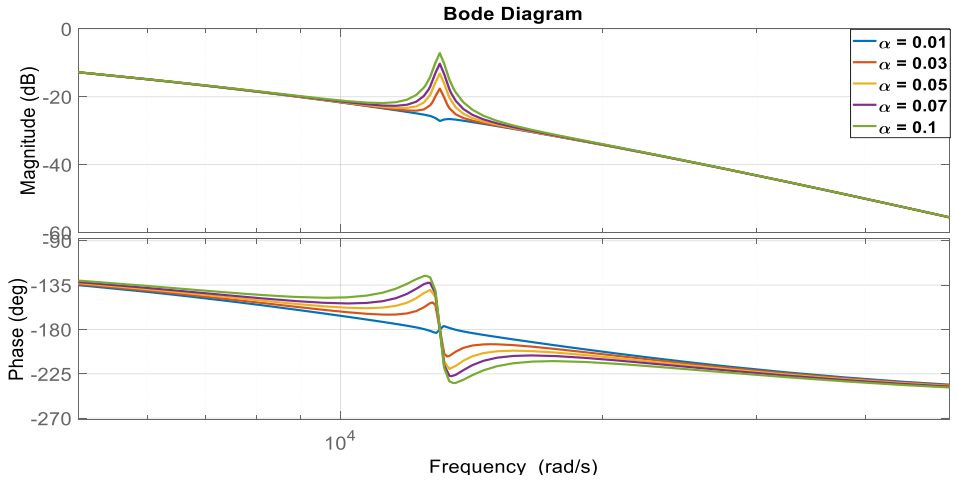

(a)

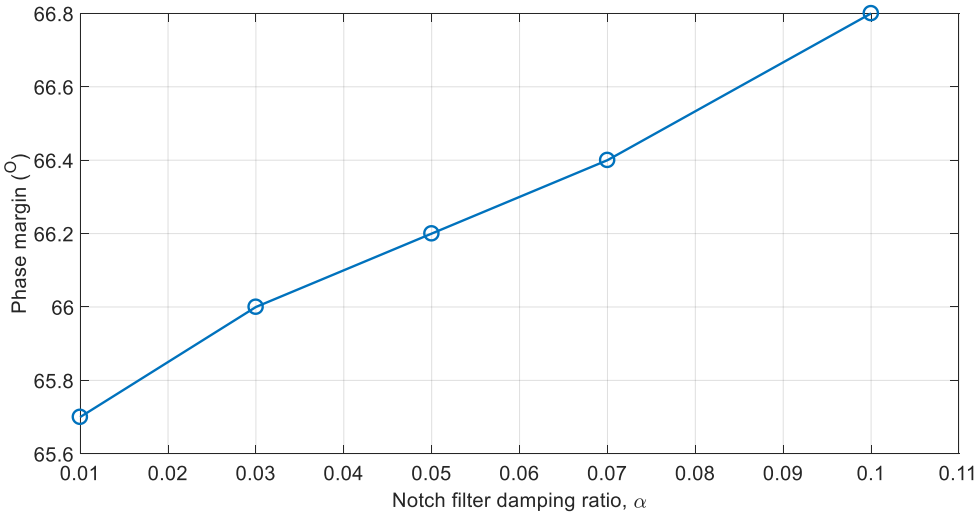

(b)

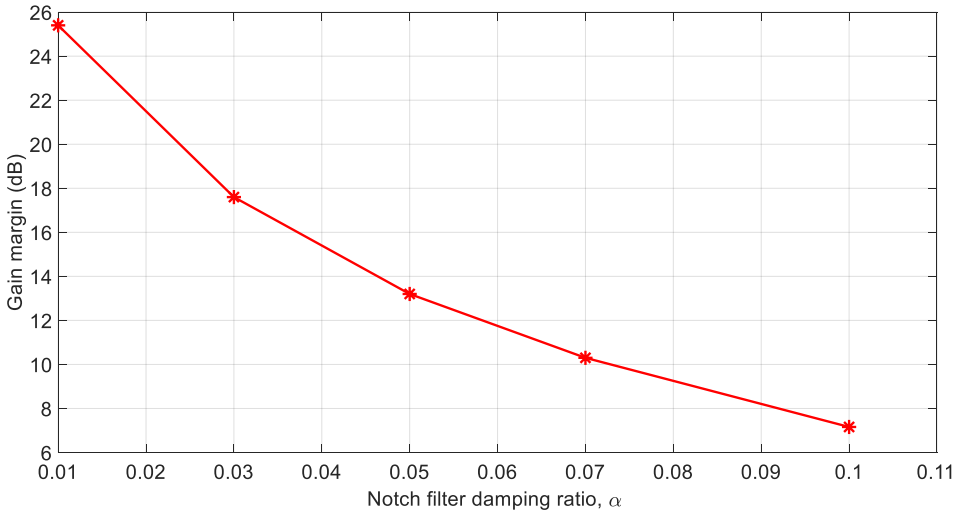

(c)

Figure 3:22: Notch filter damping ratio effect on stability margins (a) open loop Bode plot of cascaded PI controller, LCL filter and notch filter (b) phase margin variations with *α* (c) gain margin variations with *α*

3.8 Simulation Studies for LCL Filter Active Damping with Notch Filter

The simulations presented in this section were performed using MATLAB/Simulink software simulation tool. The system parameters have been specified in Tables 3.1, 3.2 and 3.3, with the designed parameters of section 3.4.

A purely active load of 100 kW is connected at the PCC. The grid is considered ideal, with negligible resistance, R_g and inductance, L_g.

In order to prevent proliferation of harmonic frequencies in the control loops, the lower boundary of the PWM switching frequency, f_{sw} must be at least twice the largest frequency, f_{max}, which in this case is the LCL filter resonant frequency. Selecting high values for f_{sw} produce waveforms with negligible harmonic content. The trade-off in selecting a high switching frequency is, however, the power losses incurred in the switches. Furthermore, the PWM time delay, T_d is decreased, securing a better phase margin for the control loop. This is illustrated in the open loop Bode plot of Fig. 3.23, which displays the inverter current controller in series with the LCL filter, notch filter and PWM time delay. The closed

loop controller operating at a PWM switching frequency of 20 *kHz* has a gain margin of 10.3 dB and phase margin of 41.5^{O}. This is followed by a gain margin of 8.12 and phase margin of 31.8 ^{O} when the switching frequency falls to 10 kHz. With the least gain and phase margins of 5.97 and 19.5^{O} respectively is the controller with PWM switching frequency of 5 kHz. It can therefore be inferred that form a stability point of view, a higher switching frequency is required to attain better stability margins. For this reason, a switching frequency of 20 *kHz* is selected.

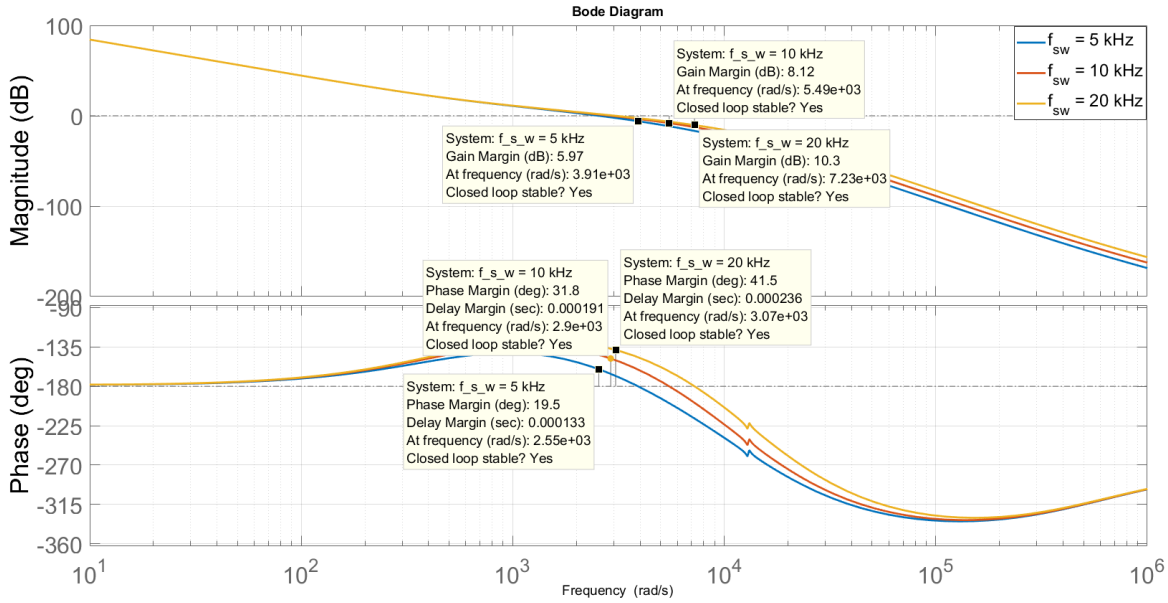

Figure 3:23: Open loop Bode plot for inverter control at different switching frequencies

3.8.1 Simulation Results

Figure 3.24 shows the maximum PV power of 100 kW extracted using the P&O algorithm described in section 3.4.1 by adjusting the DC-DC converter duty cycle in Fig. 3.25. This action regulates the PV terminal voltage to 600 V as seen in Fig. 3.26. The power generated by the PV is supplied to the grid by controlling the DC link voltage, V_{DC} and the d-q components of the grid current, I_{2d} and I_{2q}. In this simulation, the inverter operates in unity power factor mode, hence ${I_{2q}}^{*} = 0$. For a grid line voltage of 380 V, the minimum DC link voltage as stated in section 3.4.3 is 620 V and is shown in Fig. 3.27. In practice, to maintain power flow from the PV to the grid, higher values for the DC link voltage will be required, especially when the line impedance is increased. The exact magnitude of the DC link voltage is directly dependent on the line impedance values.

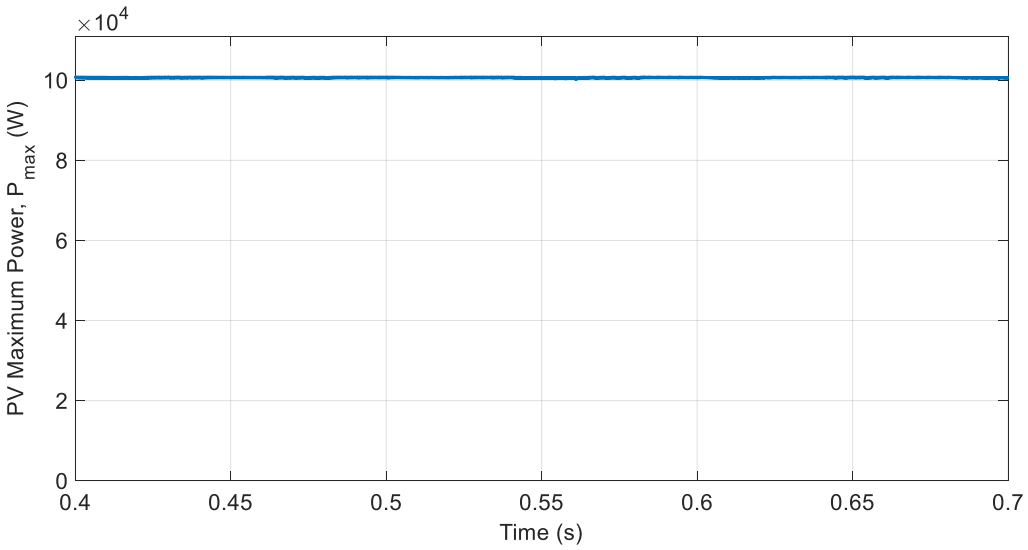

Figure 3:24: PV Maximum Power

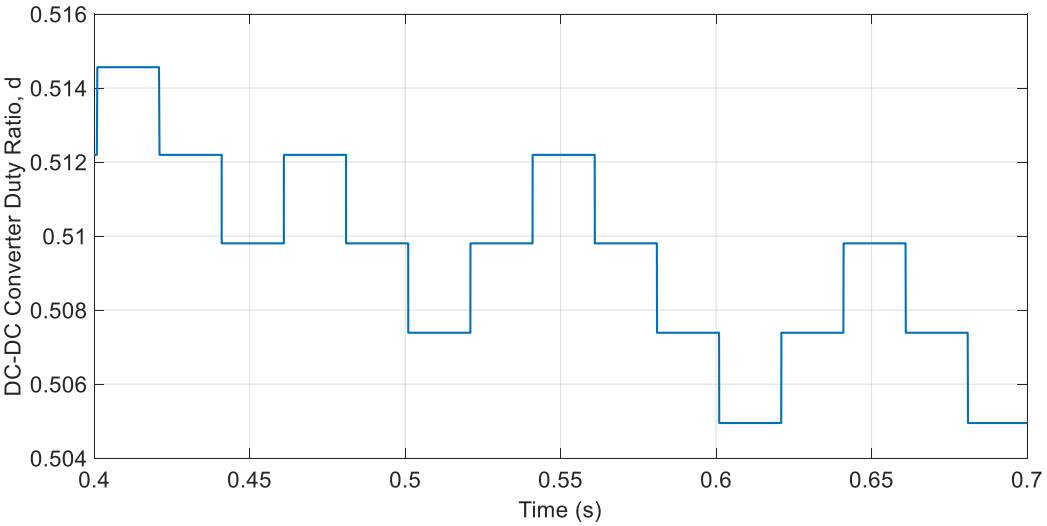

Figure 3:25: Duty Cycle determined from P&O

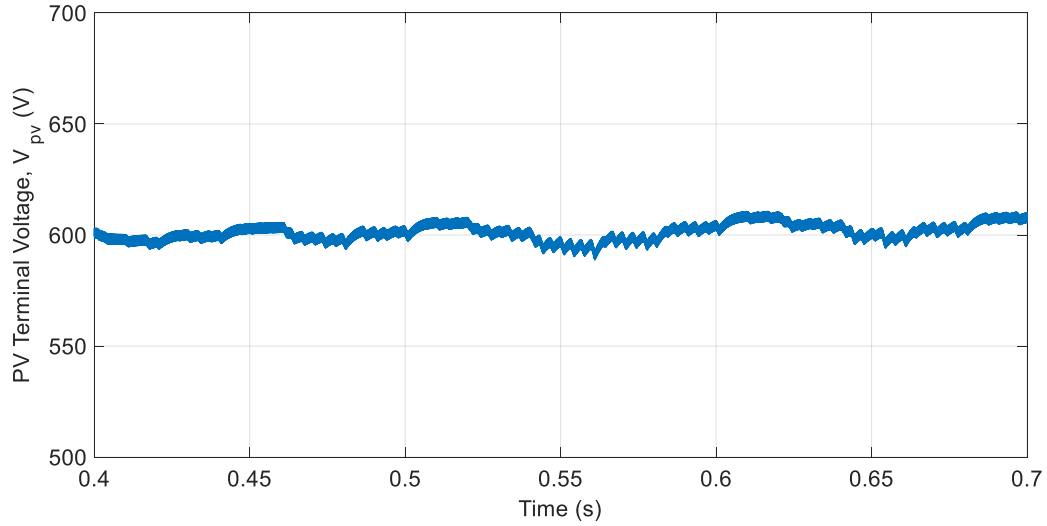

Figure 3:26: PV terminal voltage

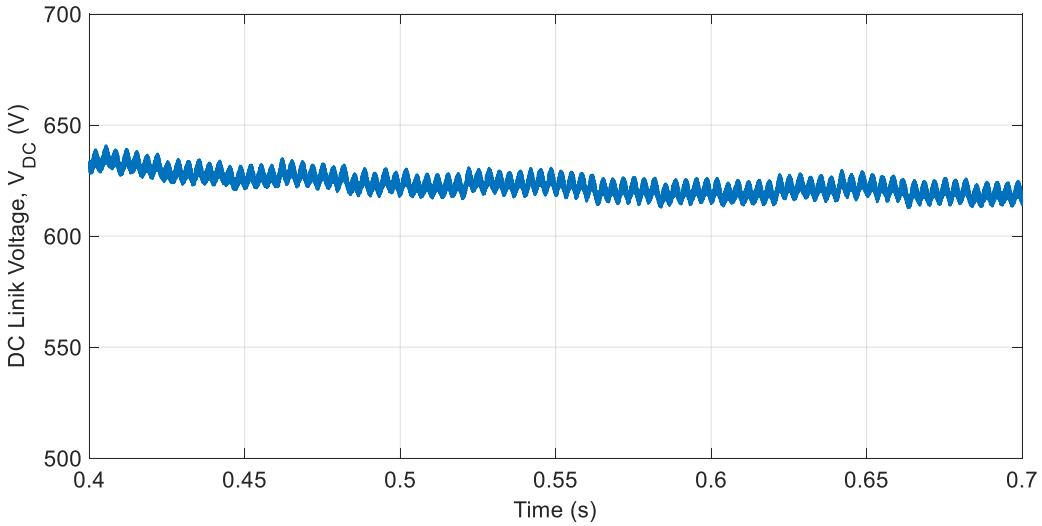

Figure 3:27: DC link voltage

The effect of the NF on the grid current waveform can be visualised by initially leaving the LCL filter undamped for time, *t <0.5 seconds*. The notch filter is activated at time, *t ≥ 0.5 seconds.* The effect of different NF gains on the resonant frequency are studied, by maintaining the damping ratio ζ_2 at 1 while ζ_1 is varied. Three different cases are considered: $\zeta_1 = 0.01, 0.2$ and 0.5. Correspondingly, the NF gain at the resonant frequency, $G_{NF}(j\omega_{res}) = 0.01, 0.2$ and 0.5 respectively, according to Equ. (3.61). The resulting grid current waveforms are discussed in the following sections.

3.8.1.1 Case 1: $G_{NF}(j\omega_{res}) = 0.01$

The grid current waveform is seen in Fig. 3.28 (a).Due to the absence of damping, a highly distorted grid current is observed between time, *t = 0.4* and *t = 0.5 seconds.* Fig. 3.28 (b) shows the frequency spectrum of the current, where the LCL resonant frequency of 2.06 *kHz* is clearly observed, leading to a total harmonic distortion (THD) of 65.16%. This high level of distortion may prevent the current controllers from performing accurate reference tracking.

When the NF is activated at time, *t = 0.5 seconds*, Fig. 3.28 (a) shows the response improving significantly, with pure sinusoidal waveforms supplying the grid with the PV generated power. The resonant frequency harmonic is significantly attenuated and a THD of less than 1% is seen in Fig. 3.28 (c). This satisfies the requirement for grid current, which must be maintained less than 5% [31].

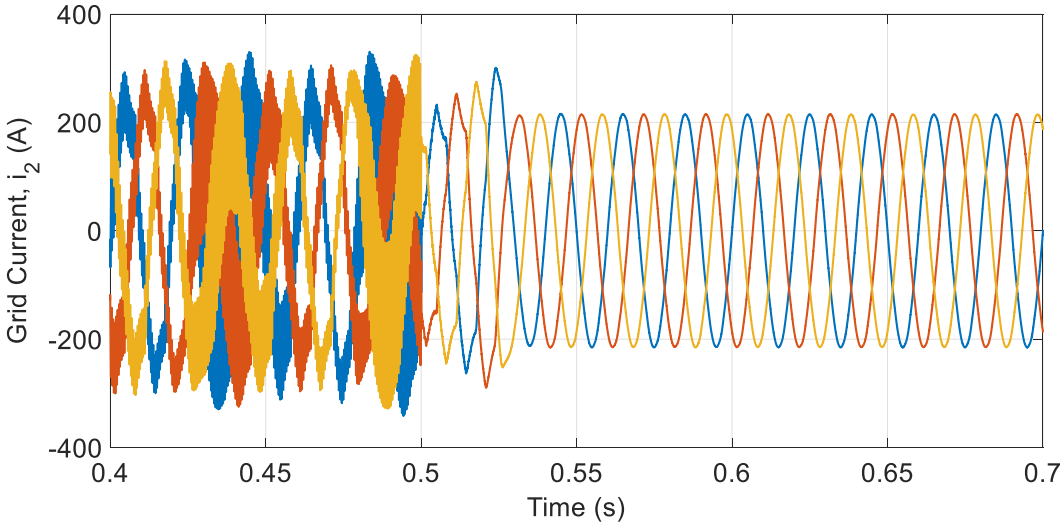
400
200
0
-200
-400
Grid Current, i_2 (A)
0.4
0.45
0.5
0.55
0.6
0.65
0.7
Time (s)

(a)

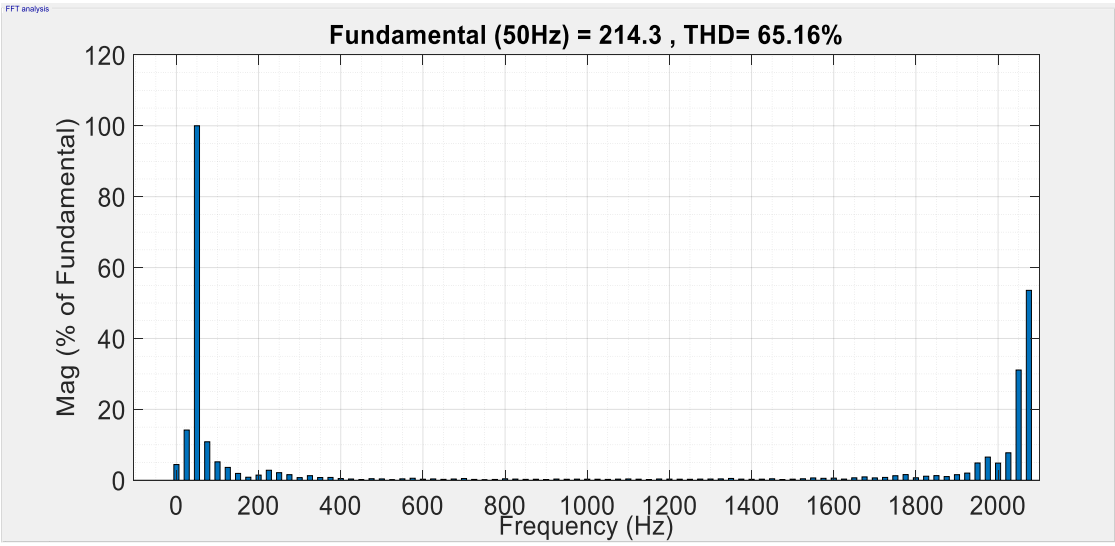
FFT analysis
Fundamental (50Hz) = 214.3 , THD= 65.16%
120
100
80
60
40
20
0
Mag (% of Fundamental)
0
200
400
600
800
1000
1200
1400
1600
1800
2000
Frequency (Hz)

(b)

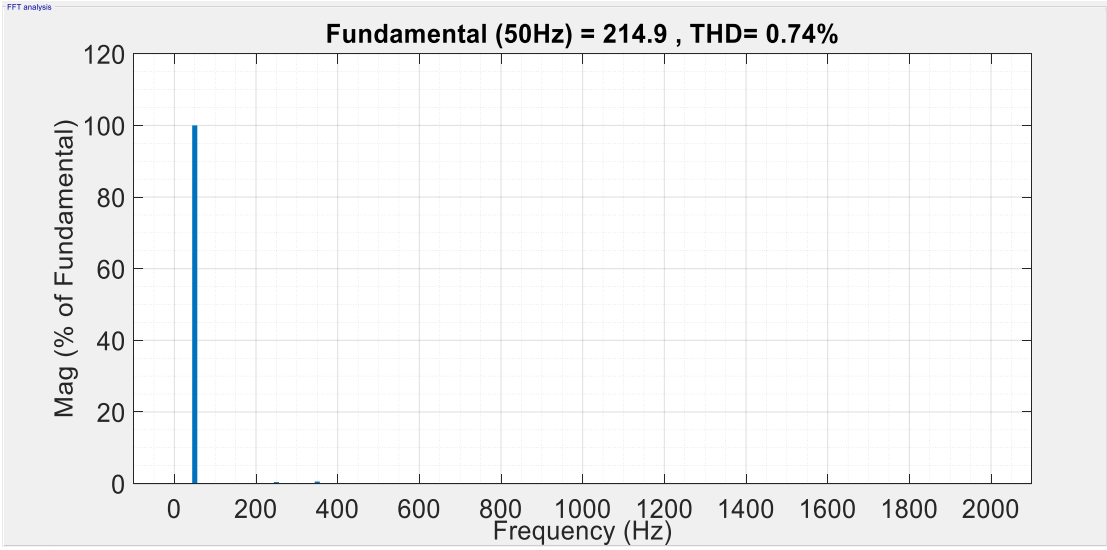

(c)

Figure 3:28: Notch filter active damping with a 0.01 gain at the resonant frequency (a) Grid current waveform (b) Frequency spectrum of grid current at *t < 0.5 seconds* (c) Frequency spectrum of grid current at *t > 0.5 seconds*

3.8.1.2 Case 2: $G_{NF}(j\omega_{res}) = 0.2$

For a NF gain of 0.2, the grid current waveform in seen in Fig. 3.29 (a). The waveform clearly has lesser harmonic distortions when NF is activated at time, *t = 0.5 seconds*. However, the THD is 8.33% as shown in Fig. 3.29 (b). This is greater than the 5% maximum limit for grid current harmonic distortions. Theoretically, the LCL filter gain at the resonant frequency, according to Equ. (3.8) is:

$$G_{LCL2}(j\omega_{res}) = \infty. \tag{3.62}$$

The amplitude of $G_{NF}(j\omega_{res})$ set to 0.2 is clearly not sufficiently small as to attenuate the LCL gain in Equ. (3.62) to insignificant levels, leading to high harmonic content in the grid current signal.

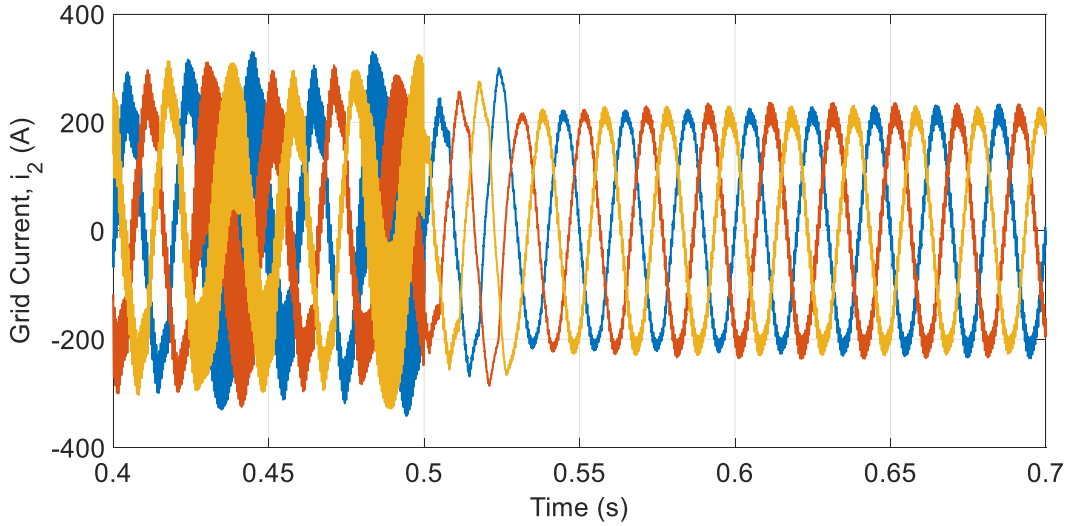

(a)

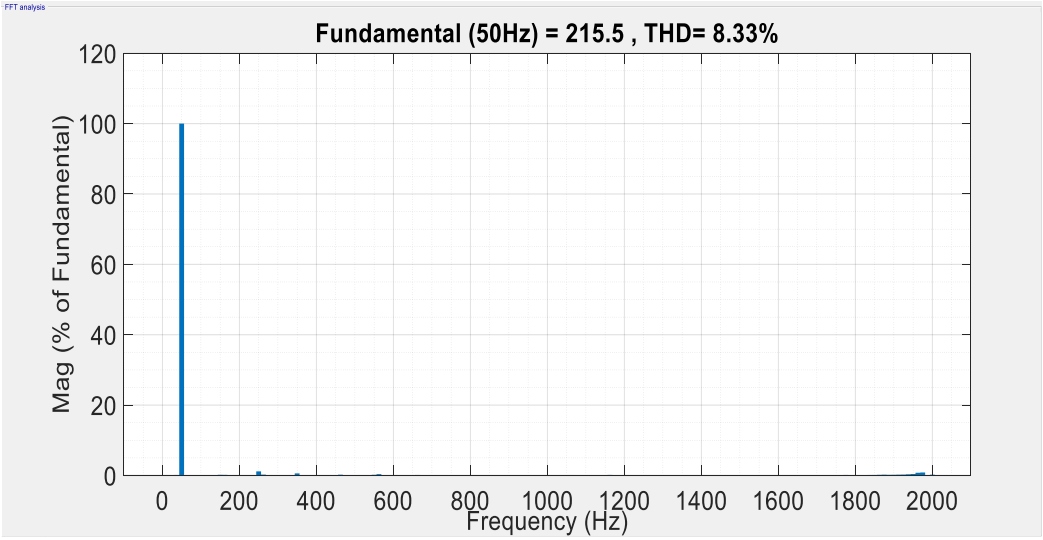

(b)

Figure 3:29: Notch filter active damping with a 0.2 gain at the resonant frequency (a) Grid current waveform (b) Frequency spectrum of grid current at *t > 0.5 seconds*

3.8.1.3 Case 3: $G_{NF}(j\omega_{res}) = 0.5$

The grid current waveform when $G_{NF}(j\omega_{res})$ is 0.5 is seen in Fig. 3.30 (a). The level of harmonic distortion is significant, even with the NF active at time, *t = 0.5 seconds*. Figure 3.30 (b) shows the THD in the grid current as 31.84%. This can be explained from Equ. (3.62), which signifies that an infinitesimal value of $G_{NF}(j\omega_{res})$ is required to reduce the LCL resonant frequency gain to insignificant levels. Consequently, this necessitates a careful selection for damping ratios, ζ_1

and ζ_2 which can produce a negligible gain at ω_{res} while simultaneously ensuring adequate stability margins, as discussed in section 3.7.

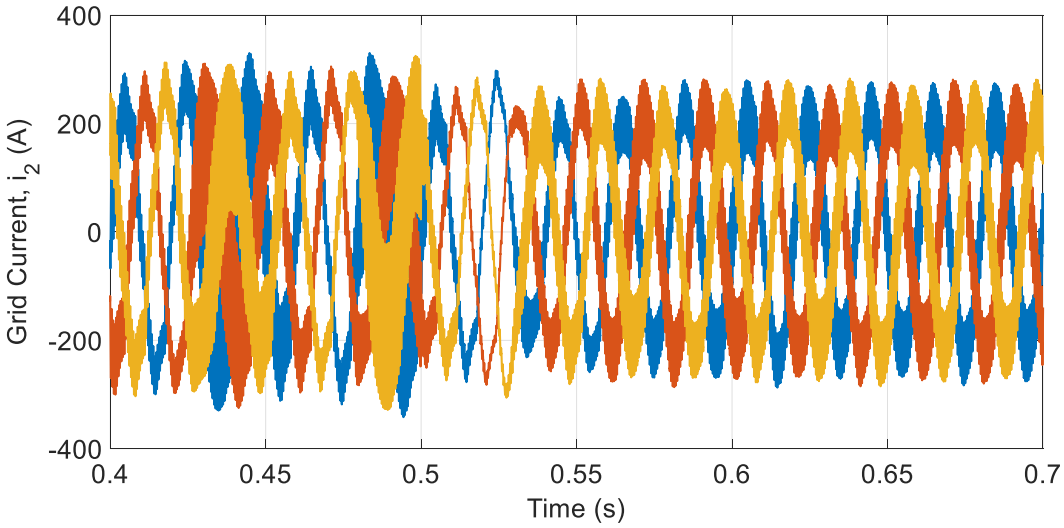

(a)

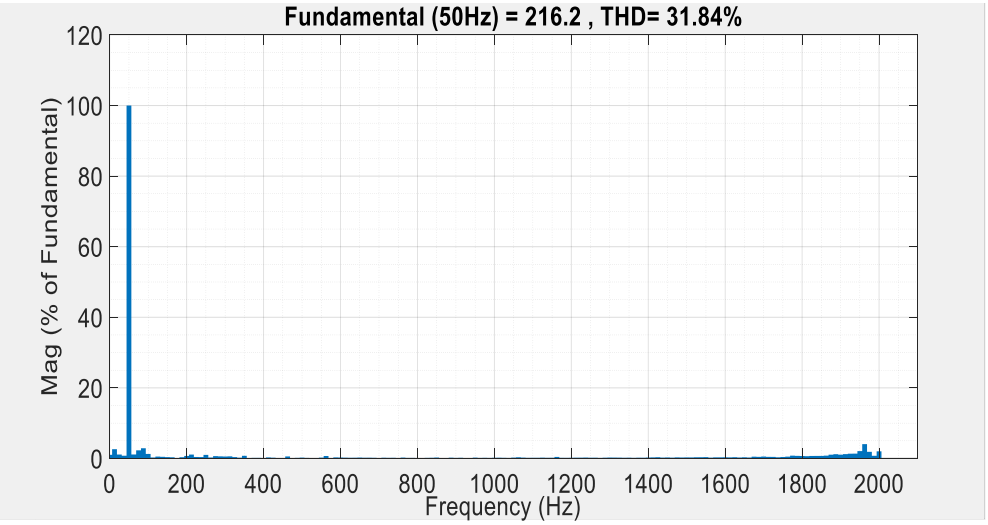

(b)

Figure 3:30: Notch filter active damping with a 0.5 gain at the resonant frequency (a) Grid current waveform (b) Frequency spectrum of grid current at *t > 0.5 seconds*

As previously mentioned in section 3.6.2.2, the notch filter method of LCL filter damping has a significant advantage over passive damping, as it does not incur power losses. Furthermore, it does not need additional current sensors, which is a major drawback of the virtual resistance technique. The main challenge lies in choosing the damping coefficients, ζ_1 and ζ_2 for high sensitivity and stability.

Also, due to the possible variations of grid impedance, the resonant frequency may vary and correspondingly the notch frequency must be re-set. This relies on accurate identification of the resonant frequency, which will be the theme of the next chapter.

3.9 Conclusion

The chapter has discussed the detailed design of a grid connected PVDG system with emphasis on the LCL filter resonance issue and offered a systematic theoretical analysis based on the frequency domain methods. The proposed notch filter has been shown to be capable of attenuating the gain at the resonant frequency of the LCL filter by introducing an opposing notch at the resonant frequency. Simulation results show the efficient resonant frequency attenuation offered by the notch filter, which will be used further in this work. Further analysis has been presented for selecting the appropriate damping coefficients of the notch filter.

Chapter 4 Active Damping for LCL Filter-based Grid Connected Inverters with Adaptive Notch Filters

4.1 Introduction

It is clear from Chapter 3 that a notch filter whose centre frequency corresponds to the LCL resonant frequency is capable of neutralising the resonance effect. However, the resonant frequency may not be static, as it can vary with a changing line impedance or LCL filter parameters. It may also change due to non-linearity of inductors, where inductance magnitude varies with the applied current [94, 110, 111]. A change in the resonant frequency may cause harmonic distortions in the voltage and current signals of a power system. Harmonic distortions affect the performance of components such as transmission lines and transformers, as well as the accuracy of measuring instruments [112]. To avoid compromising the robustness and stability of the LCL filter, resonant frequency estimation is unavoidable. A possible method of dealing with a changing resonant frequency is to incorporate a number of controllers or filters tuned to various frequencies, as in [113]. However, to cover a wide range of frequencies, a very large number of such controllers and filters would be required, deeming it an impractical solution. It is therefore indicative that any robust LCL filter damping technique should incorporate an adaptive feature, capable of modifying the controller parameters based on the on-site estimated resonant frequency.

Some of the most prominent research on this topic fall into the following categories: filter-based single loop methods and multi - loop control methods. The multi - loop control methods provide damping through modification of the current control loop. The virtual resistance and capacitor current feedback methods in [91] provide system robustness against varying grid impedance by increasing the phase and gain margins through rigorous controller parameter tuning. References [92, 93, 114] proved the robustness of their adaptive control against grid impedance variations, but the control complexities were further increased [115] with the use of multi-loop current control strategy. However, digital implementation of the multi-loop control method causes the system to lose its stability when the resonant frequency is 1/6 of the switching frequency [116].

Consequently, a lag-compensator was incorporated in the control loop to improve stability at the resonant frequency.

Owing to their simplicity and ease of implementation, single loop filter-based methods are generally preferred, as they do not require additional sensors [107]. The notch filter (NF) studied in Chapter 3 belongs to this category. They are, however, sensitive to grid impedance variations and a number of techniques have been developed to enable the NF adapt to the grid changes. The NF centre frequency in [108] was adapted to the resonant frequency by estimating the grid impedance according to variations in the reactive power at the PCC. The limitation for this technique lies in its insensitivity to LCL parameter variations, which have been shown to affect the resonant frequency [111]. The estimation further neglects grid resistance, R_g making it inapplicable in low voltage distribution networks where the line resistance is generally significant.

Careful selection of the LCL resonant frequency under the Nyquist limit ensured robustness of notch and lag filters in [117]. A consequence of this process is that a greater tolerance to a changing grid inductance, L_g is achieved at the expense of a reduced system bandwidth. Furthermore, the lag filters proved more advantageous compared to the notch filters, as the latter required a priori knowledge of the grid resistance.

The authors in [111] proposed a discrete NF whose centre frequency and bandwidth can be altered in real time to suit the application. The digital ANFs in [115, 118] were designed with the NF frequency smaller than f_{res}, thus improving the system stability margins. For sufficient phase lag compensation, the NF centre frequency must be situated close to f_{res} [118], limiting its effectiveness for large deviations in L_g. Although effective damping was achieved for large L_g variations in [115], it was ineffective for reduced filter capacitor values, which caused f_{res} to increase beyond the point where the NF could not prevent the system frequency response from a negative crossing of -180^{O} at $f_{res.}$

Spectrum analysis using the Goertzel algorithm for resonant frequency estimation was presented in [107]. While the algorithm generally requires less memory than the fast Fourier transform (FFT) due to its sequential processing of data [119], it is limited to a small bandwidth. For larger bandwidths, the

computational complexity is increased, resulting in a slow speed of frequency estimation.

This chapter proposes an adaptive notch filter (ANF) for active damping of the resonant frequency using discrete Fourier transform (DFT) analysis [120]. The DFT algorithm, implemented with the more efficient FFT, identifies the resonant frequency on-line in real time based on the grid current and updates the notch filter centre frequency accordingly, based on the transmission line impedance variations. The technique does not require prior knowledge of the system, particularly in terms of grid resistance. The accuracy of the resonant frequency estimation makes it possible to design a narrow NF, improving the phase margin of the control system. The chapter describes the principles and implementation of the method. The accuracies and data processing speed of the technique and their effects on the stability of the system are theoretically analysed. Simulation results under various grid operational conditions are presented in time domain. Finally, frequency estimation using FFT and the Goertzel algorithm are compared in terms of ANF robustness.

4.2 Effect of Grid Impedance Variation on LCL Filter Resonant Frequency

The power grid can be represented by a voltage source, V_g with a variable impedance, Z_g having resistive and inductive elements of R_g *and* L_g respectively. The per-phase equivalent circuit model for a VSI connected to the grid via an LCL filter and the grid impedance, Z_g is shown in Fig. 4.1. For simplified analysis, the grid line resistance, R_g may be considered negligible. Hence, the inductive element, L_g needs to be considered in the analysis of an LCL filter. The resonant frequency, f_{res} of the LCL filter presented in Chapter 3 is thus modified as:

$$f_{res} = \frac{\omega_{res}}{2\pi} = \frac{1}{2\pi}\sqrt{\frac{L_1+(L_2+L_g)}{L_1(L_2+L_g)C}}. \quad (4.1)$$

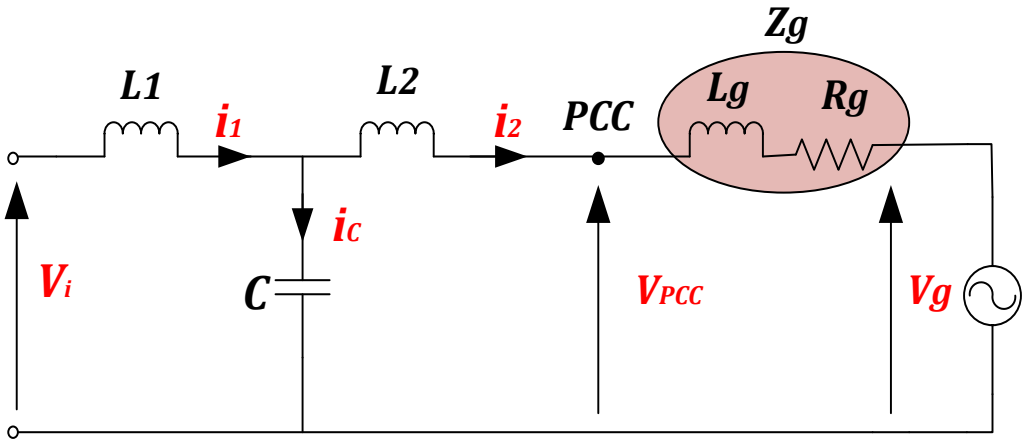

Figure 4:1: Per-phase equivalent circuit for LCL grid connected inverter with grid impedance

Equ. (4.1) shows the effect of the grid inductance on the resonant frequency: the higher the value for L_g, the lower the resonant frequency. Since the variations in grid inductance may cause a shift in resonant frequency, the notch filter damping method must be able to detect L_g variations and adjust the NF centre frequency accordingly, lest the damping becomes ineffective. Hence, an adaptive control scheme is required. If this can detect variations in ω_{res} due to changes in L_g and correspondingly retune the NF centre frequency by re-setting ω_n in Equ. (4.2)

$$G_{notch}(s) = \frac{s^2+2\zeta_1\omega_n s+{\omega_n}^2}{s^2+2\zeta_2\omega_n s+ {\omega_n}^2}, \tag{4.2}$$

to ω_{res} in Equ. (4.1), stable operation of the VSI may be attained.

When R_g is considered in Equ. (4.1), a more complex relationship is established with the resonant frequency, as illustrated in Fig. 4.2.

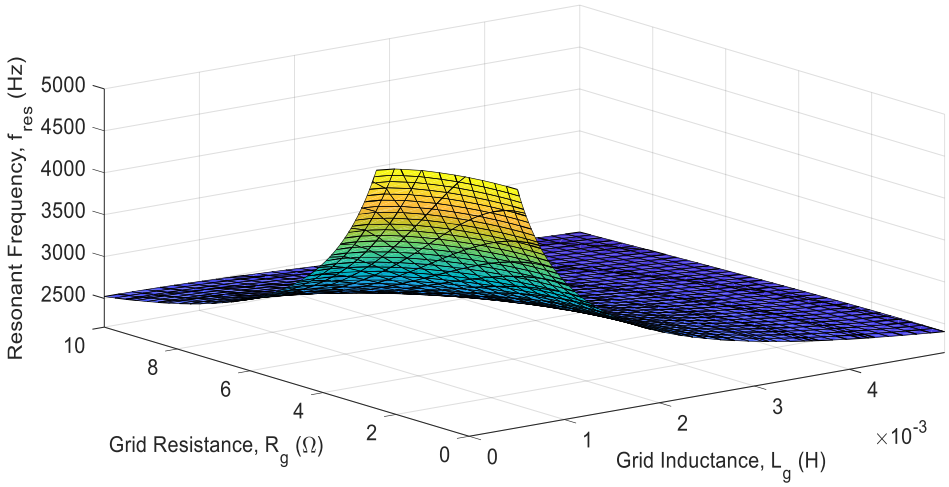

Figure 4:2: Variation of f_{res} with L_g and R_g

As with L_g, the resonant frequency exhibits an inverse relationship with the grid resistance, R_g. In distribution systems, the magnitude of R_g is comparable to L_g. Consequently, the accuracy of active damping techniques that rely solely on determining the value of L_g, cannot be guaranteed. This points to an advantage of signal processing techniques, where the resonant frequency is directly determined from the current signals, as opposed to impedance estimation methods, where the grid resistance is generally ignored [108]. In order to study the effect of variation of the grid parameters on the resonant frequency, it is essential that one parameter be varied while the other remains fixed. Since inductors have a higher chance of change in value due to their non-linear nature [94, 110, 111] caused by core saturation, the grid inductance variation effect on the LCL filter resonance will be considered with a stable grid resistance.

4.2.1 Grid Short Circuit Ratio (SCR)

When initially designing the LCL filter in Chapter 3, the grid was modelled as an infinite bus-bar, hence Z_g =0. However, an AC grid is a dynamic system and its impedance varies continuously. An AC system is considered weak if it has a high impedance or low mechanical inertia [60]. An important factor to consider is the grid short circuit ratio (*SCR*), which gives a measure for the strength of an AC system [60]:

$$SCR = \frac{P_{AC}}{P_{DC}}, \tag{4.3}$$

where P_{AC} is the short circuit MVA rating of the AC system and

P_{DC} is the DC inverter MW rating.

The MVA rating of the grid is given by:

$$P_{AC} = \frac{{V_{ac}}^2}{Z_g}, \tag{4.4}$$

where V_{ac} is the bus voltage at the PCC and Z_g is the equivalent Thevenin impedance of the AC network, expressed as:

$$|Z_g| = \sqrt{{R_g}^2 + \omega^2 {L_g}^2}. \tag{4.5}$$

Substituting Equs. (4.4) and (4.5) into Equ. (4.3), the relationship between the SCR and L_g is:

$$SCR = \frac{{V_{ac}}^2}{P_{DC}\sqrt{{R_g}^2+\omega^2 {L_g}^2}}. \tag{4.6}$$

From Equ. (4.6), the grid impedance has a negative impact on the SCR of the AC system. As they are directly proportional, a large grid impedance increases the systems' susceptibility to a large change in voltage in the event of a disturbance [121, 122]. The increased impedance also affects the position of the LCL resonant frequency by shifting it to the lower end of the spectrum.

Table 4.1 shows grid classification in terms of SCR values, with SCR values > 5 attributed to strong grids. High impedance grids with SCR values < 3 are considered weak and therefore easily affected by disturbances.

Table 4.1: Grid classification based on SCR values

SCR	**Grid Classification**
SCR>5	Strong
3<SCR<5	Medium
SCR<3	Weak

Figure 4.3 illustrates the inverse relationship between an increasing grid inductance, L_g with *SCR* and f_{res}. Both SCR and f_{res} decrease with higher values of L_g, with the rate of change decreasing at higher L_g values.

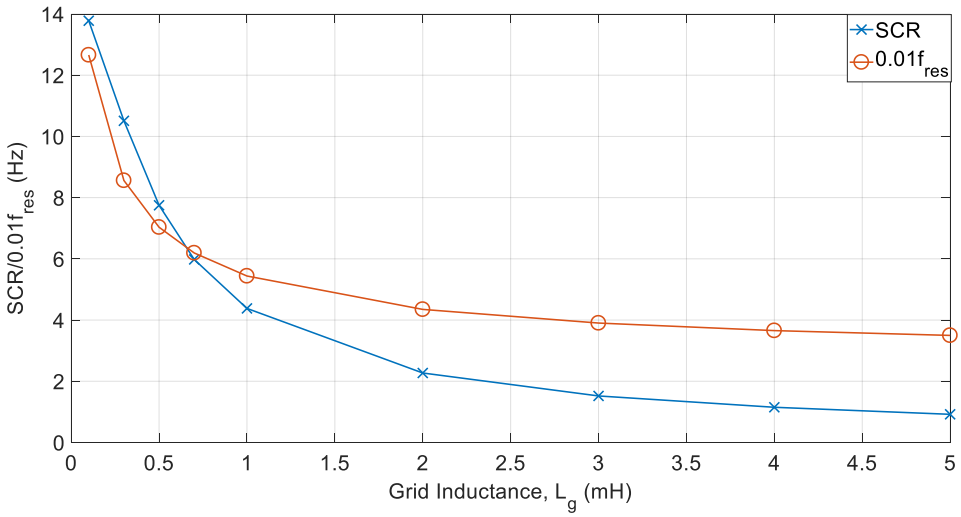

Figure 4.3: Variation of SCR and f_{res} with L_g

Figure 4.4 shows the effect of increasing resonance due to the SCR changing from infinitely high, where $L_g = 0$ *mH* to as low as 0.92 with $L_g = 5$ *mH*, at time, t = *0.5 seconds*. The NF is tuned to the resonant frequency corresponding to $L_g = 0$ *mH*. For a change in L_g and hence SCR, the current containing high order harmonics cannot follow the desired reference and the stability of the system will therefore be compromised. This is attributed to a significant deviation from the tuned NF frequency. To overcome this limitation, the NF centre frequency can be reduced to cope with the grid impedance fluctuations [118]. However, this cannot guarantee stability for a wide range of grid impedance variation. Hence, an adaptive scheme for changing the NF centre frequency through estimation of the actual resonant frequency is proposed to overcome the challenge of LCL resonant damping in the event of a varying grid impedance.

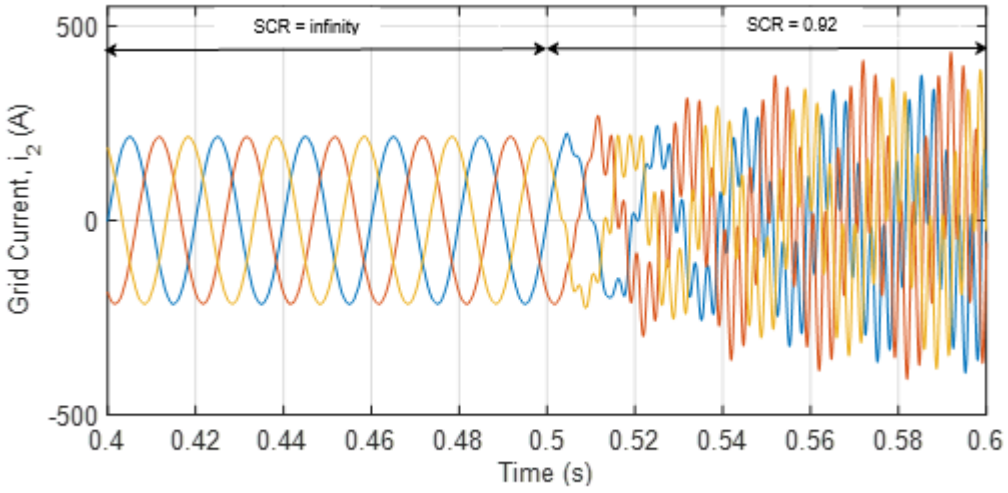

Figure 4:4: Grid impedance variation effect on grid current with non-adaptive notch filter

4.3 Adaptive Notch Filter (ANF) by DFT

A viable approach to the LCL resonance problem is to identify the frequency component with the largest amplitude in the output current waveform and reset the notch filter centre frequency to this identified value. This forms the basis for this method whereby the frequency of the notch filter is changed according to the spectral measurement results whenever a grid impedance variation occurs. An effective spectrum measurement algorithm is the discrete Fourier transform (DFT).

The DFT is a conventional means of identifying harmonics within the voltages and currents of a power system, for the purpose of assessing the power quality indices. In this case, it can be applied to analyse the spectrum of the output current of the LCL filter to seek the resonant frequency.

With negligible values of R_g, the system in Fig. 4.1 is undamped and f_{res} becomes the largest frequency component present in the current signal. However, R_g is non-negligible in distribution systems, and may therefore offer an intrinsic damping effect. Depending on the magnitude of R_g, the fundamental frequency component in the current signal may become larger than f_{res}, therefore affecting the accuracy in detecting f_{res}. To overcome this issue, the current signal at the output of the LCL filter is passed through a high pass filter (HPF) to eliminate the

fundamental frequency component, making f_{res} the largest frequency component within the signal. The ANF centre frequency may therefore be re-tuned to the detected value of f_{res}.The HPF can be a hardware filter or, conveniently, realised in software by discarding the lower frequencies in the output current of the LCL filter.

4.3.1 Principles of the Discrete Fourier Transform (DFT)

The discrete Fourier transform (DFT) is a power signal processing tool that can be used to determine the spectral strength of a finite periodic signal. For a signal sampled over a given time window, the DFT of the signal is defined as:

$$F[k] = \sum_{n=0}^{N-1} f[n] e^{-j\frac{2\pi nk}{N}},\ 0 < k < N-1 \qquad (4.7)$$

where N is the total number of samples which are equally spaced in the time domain, and $f[n]$ is the $n'th$ sample of the input continuous time signal. In this discrete signal, the product of N and the sample time interval, T_s set the duration of the sampled time window.

For accurate resonant frequency extraction, both T_s and N should be chosen carefully. For T_s, this should be based on some prior knowledge of the possible range of the resonant frequency, f_{res} and should satisfy the Nyquist criterion. Thus, if a maximum frequency, f_{max} can be chosen slightly above the highest expected f_{res}, the sampling frequency,

$$f_{samp} > 2f_{max}. \qquad (4.8)$$

This enables all significant components in the resonant peak to be displayed, i.e. the peak is completely within the measured spectrum. Still, higher frequencies may be present at a lower level, due to mixing products of the grid frequency and the inverter switching frequency, and possibly also generated in loads connected to the grid. Desirably, frequencies above f_{res} should be filtered out before computing the DFT, otherwise oversampling may be used.

Selection of N should ensure a wide enough data window to give a sufficiently high frequency resolution, FR. Note that the frequency resolution of a DFT is the distance between two adjacent frequencies, given as:

$$FR = \frac{f_{samp}}{N}. \qquad (4.9)$$

Clearly, both DFT window size, *N* and the sampling frequency, f_{samp} influence *FR*. *FR* may be improved by increasing the DFT window size or reducing the sampling frequency. In any case, a better *FR* leads to increased DFT sampling time, t_{samp} according to Equ. (4.10):

$$t_{samp} = N \times T_s. \tag{4.10}$$

DFT is usually implemented with the computationally efficient fast Fourier transform (FFT) [123]. The FFT offers a faster execution time for the DFT in Equ. (4.7). According to this equation, the number of operations required to determine the DFT of the spectrum of interest is N^2 operations, i.e. each $F[k]$ has N outputs, each requiring the summation on N terms. The FFT algorithm reduces the number of arithmetic operations to $Nlog_2N$. The most commonly implemented FFT algorithm is the Cooley-Tukey algorithm [124], which recursively decomposes the DFT for N data samples into smaller samples and the DFT is applied to the smaller samples.

4.3.2 FFT-based Resonant Frequency Estimation

Implementation of FFT for resonant frequency identification in the voltage oriented current control loop of the grid-connected PVDG in Chapter 3 is shown in Fig. 4.5.

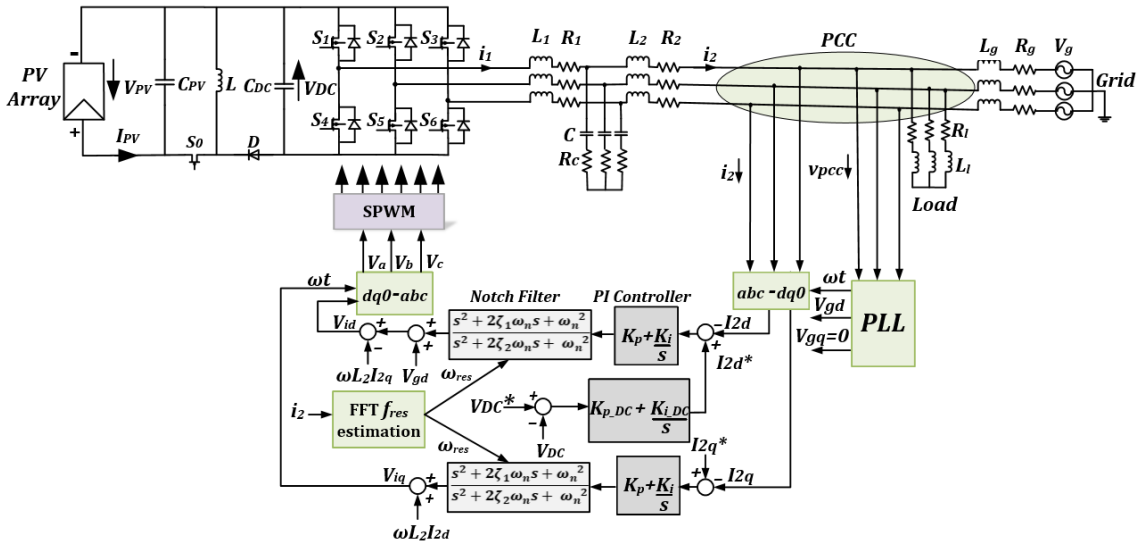

Figure 4:5: Voltage oriented control of grid connected PVDG inverter with adaptive notch filters

The FFT estimation process is triggered when the THD of the grid-side measured current, i_2 is higher than 5%, according to the IEEE standard [43]. Once activated,

the estimation process collects *N* grid current samples, $i_2[n]$ one by one, at a sampling rate, f_{samp} (10 kHz) and stores them in a buffer. The FFT algorithm is then called to process these data as a batch. It evaluates the current components according to the spectral power of the constituent frequencies, $I_2[k]$ using Equ. (4.7). The resonant frequency, f_{res} is then identified as the one having the highest magnitude, f_{max} and this value is set as the NF centre frequency, f_n. The flowchart for the estimation process and ANF re-tuning is detailed in Fig. 4.6.

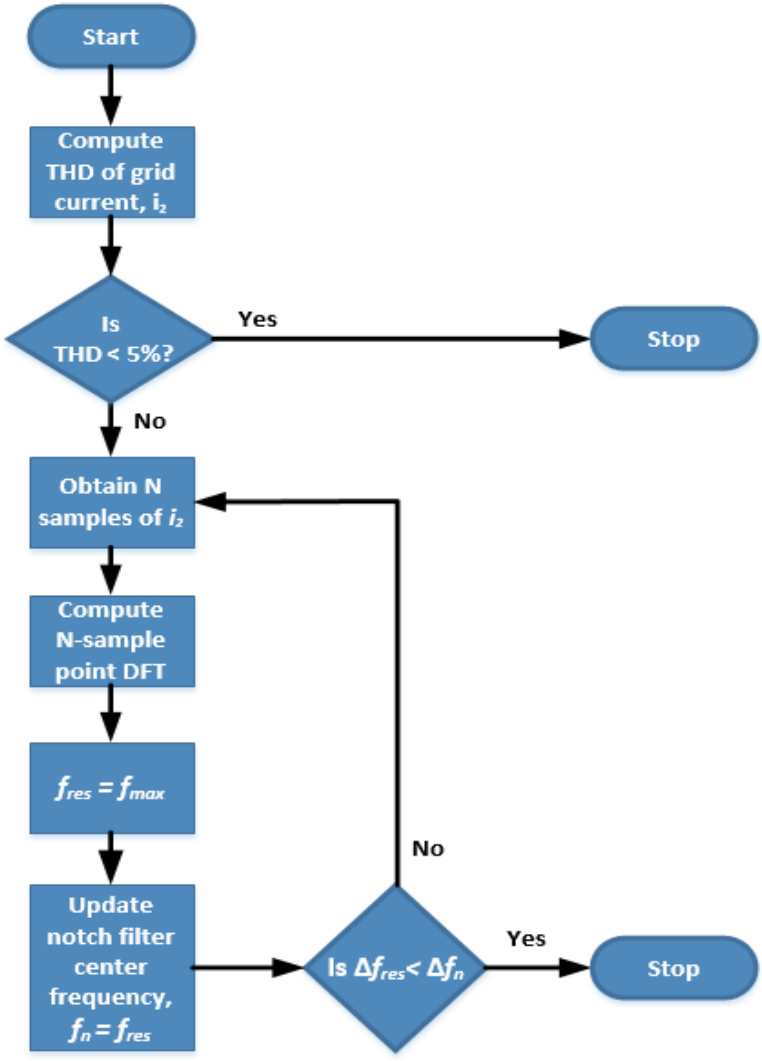

Figure 4:6: Flow chart for adaptive notch filter tuning using FFT

In situations where the estimation process may be triggered by a cause other than a deviation in f_{res}, computational burden on the processor is minimised by terminating the resonant frequency estimation process when the difference

between two consecutive frequencies, Δf_{res} is less than the set frequency range of the NF, Δf_n. Although additional memory is required to store estimated values of f_{res}, it is still considered an improvement compared to continuous frequency estimation of the grid current, i_2 using the FFT algorithm.

As described in the previous sub-section, implementation of FFT results in an inherent sampling delay time, t_{samp}. The computational complexity of the actual FFT involves the execution time required to complete $Nlog_2N$ operations, t_{exe}. Thus, the time for the entire FFT is:

$$t_{FFT} = t_{samp} + t_{exe}. \tag{4.11}$$

Figure 4.7 compares the execution and sampling times for various *N*-sample point FFTs. Clearly from the figure, the sampling time is larger than the execution time by an average factor of 1.7×10^4. Consequently, Equ. (4.11) approximates as:

$$t_{FFT} \cong t_{samp}. \tag{4.12}$$

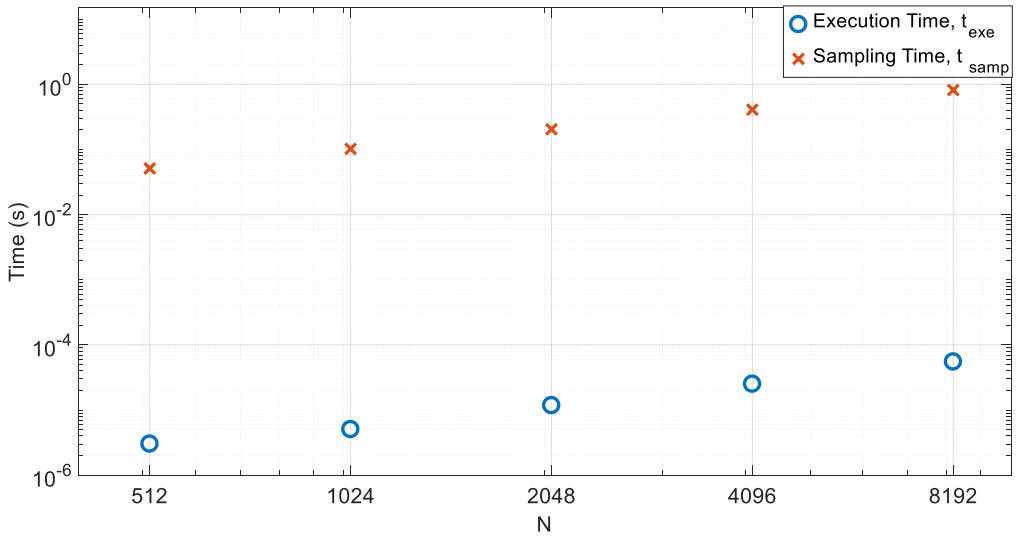

Figure 4:7: FFT sampling and execution times for different N-point FFTs

As stated above, with the same sampling frequency, a larger *N* value gives higher *FR*, however requiring longer FFT processing time. This may delay updating the notch filter frequency, e.g. in the case when *N*=8192, the time delay is about *1 second*. Thus, a compromise needs to be made between *FR* requirement and FFT execution speed. It is important to note that the FFT computational time, t_{FFT}

does not impose a time delay on the control system. Rather, the delay is in updating the NF frequency, ω_n which is independent of the current control loops in Fig. 4. 5. From the cascaded LCL and notch filter Bode plots of Fig. 3.18 in Chapter 3, the delay margin of the system is *0.0046 seconds*, thus inferring that any time delay greater than *0.0046 seconds* in the current control loop would cause the system to lose its stability.

4.3.3 Accuracy Analysis in Resonant Frequency Estimation

Selecting the number of samples, *N* in the FFT affects the accuracy of estimation of the LCL filter resonant frequency. From the Bode plot in Fig. 4.8, the frequency range of the NF, Δf_n within which the grid current at the resonant frequency, ω_{res} can be suppressed by a factor of 100 (i.e. $\zeta_1/\zeta_2 = 0.01$) lies between *12.8* and *13 krad/s*. This corresponds to a frequency band of *31.83 Hz*. Thus, the desired N sample FFT must provide a *FR* such that:

$$FR < \Delta f_n. \tag{4.13}$$

Note that for a *512-point* FFT, the *FR* is:

$$FR = \frac{10\,000}{512} = 19.53\ Hz. \tag{4.14}$$

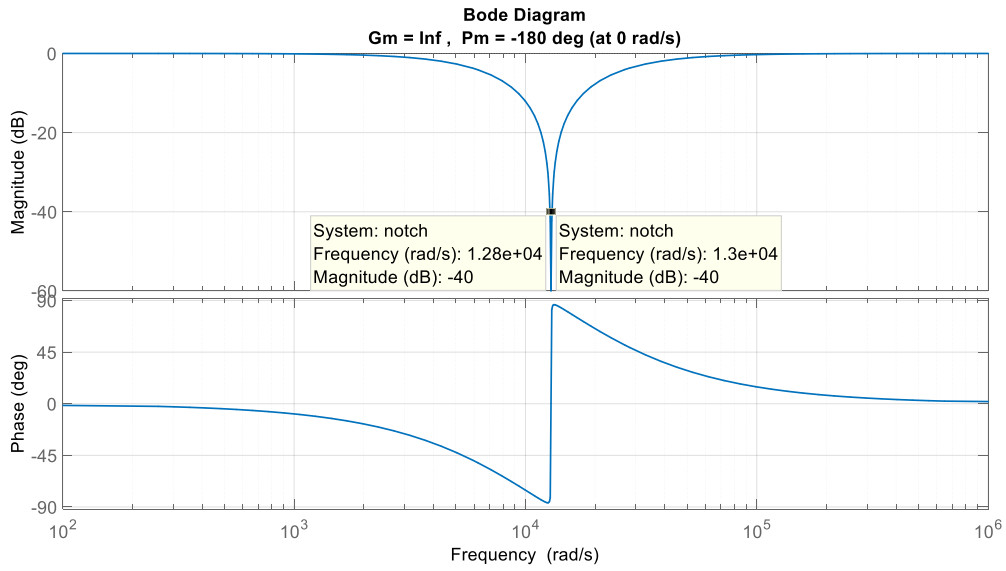

Figure 4:8: Notch filter Bode plot

Figure 4.9 compares the magnitude of frequency deviations from the actual resonant frequency, f_{res} for different number of samples and for different SCRs. As expected, the accuracy in estimating f_{res} is higher for larger values of *N*. The

deviations from f_{res}, particularly noticeable at higher SCRs, may be attributed to the approximations in Equ. (4.1), which do not consider the effect of grid resistance, R_g. Therefore, since the *FR* in Equ (4.14) is less than the value of Δf_n specified earlier, i.e. 31.83Hz, the width of the notch filter is therefore considered adequate in suppressing the resonance even for *N* set to 512, which gives the shortest execution time.

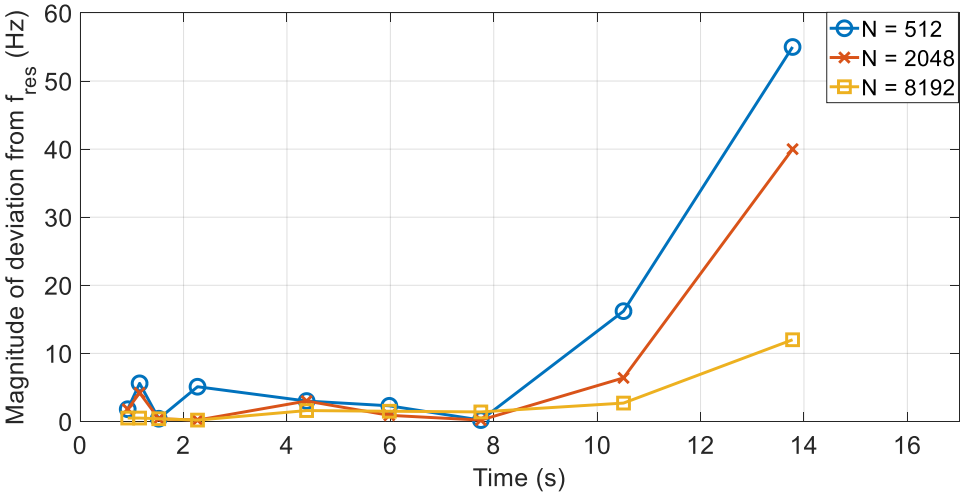

Figure 4:9: Comparing resonant frequency estimation accuracy for different N-point FFTs

4.4 Simulation Studies for Adaptive Notch Filter

The simulations in this chapter were performed using MATLAB/Simulink software. The DG system parameters are specified in Table 4.2, with VSI power switches considered ideal. The FFT function in MATLAB is based on an adaptive and improved Cooley-Tukey algorithm known as the FFTW algorithm [125]. The reference for the current control loops were determined using Equs. (3.11) and (3.12).

Table 4.2: Grid connected DG system parameters

Parameter	Rating
Inverter Rated Power (P)	100 kW
DC Link Voltage (V_{DC})	800 V
Grid phase voltage (V_{ph})	220 V
Grid frequency (f)	50 Hz
LCL filter parameters: $L_1/C/L_2$	3 mH / 110 μF / 51 μH
LCL resonant frequency (f_{res})	2.05 kHz (13 krad/s)
Grid Impedance (R_g/ L_g)	0.1 Ω/ 0.1-5mH
Grid SCR	0.92-13.78
Inverter switching frequency (f_{sw})	20 kHz
Notch Filter damping ratios (ζ_1/ζ_2)	0.01/1

As mentioned previously, the accuracy of resonant frequency estimation is improved by using a high pass filter (HPF) to eliminate frequencies below 100 Hz, so that the fundamental frequency does not affect the resonant frequency tracking. The magnitude –frequency response for the HPF is seen in Fig. 4.10.

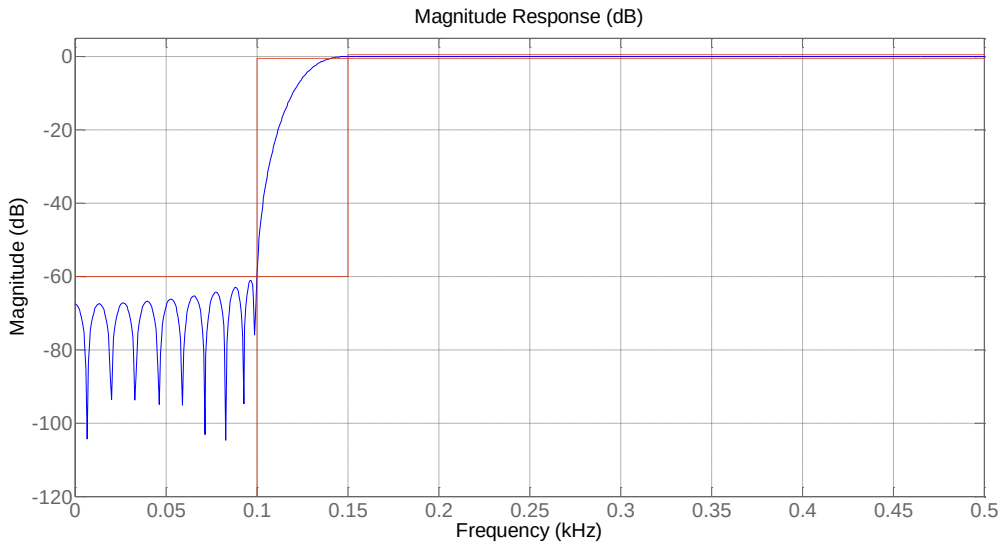

Figure 4:10: Frequency response of a high pass filter

4.4.1 Results for Adaptive Notch Filter

The performance of the Adaptive Notch Filter (ANF) is analysed for two situations with different grid inductance values. Each illustrates the effect of using FFT resonant frequency estimation on the stability of the system.

Case 1: Figure 4.11 shows the grid current responses when the ANF is used to determine the resonant frequency due to a grid inductance of 1 *mH* (SCR = 4.38) introduced at *t =0 seconds,* to a strong grid with negligible impedance. As seen in Fig. 4.11 (a), the NF is initially untuned to the new resonant frequency of 543.9 Hz, leading to a THD of 134.60% as seen in Fig. 4.11 (b). Once the FFT estimates f_{res} as 546.9 Hz as seen in the power spectrum of Fig. 4.11 (c), the notch filter is tuned accordingly, thereby reducing the THD to 0.37% as seen in Fig.4.11 (d).

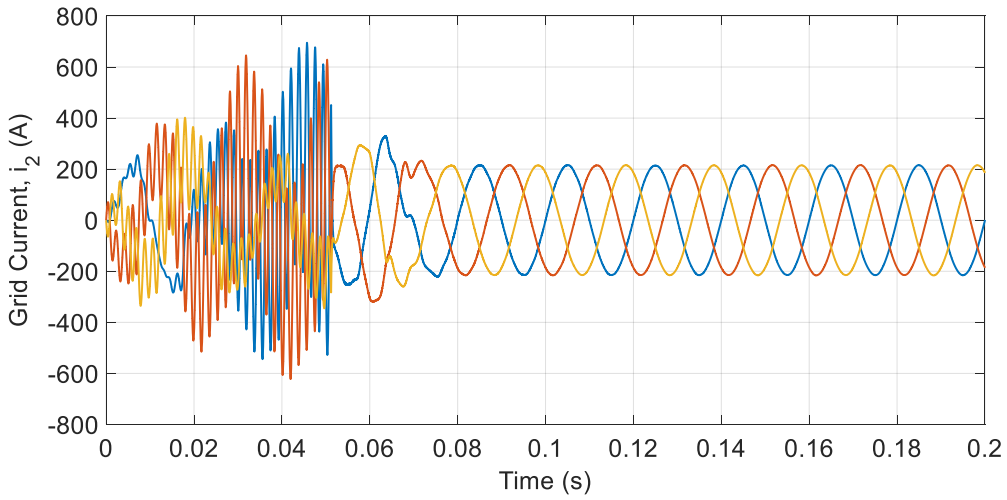

(a)

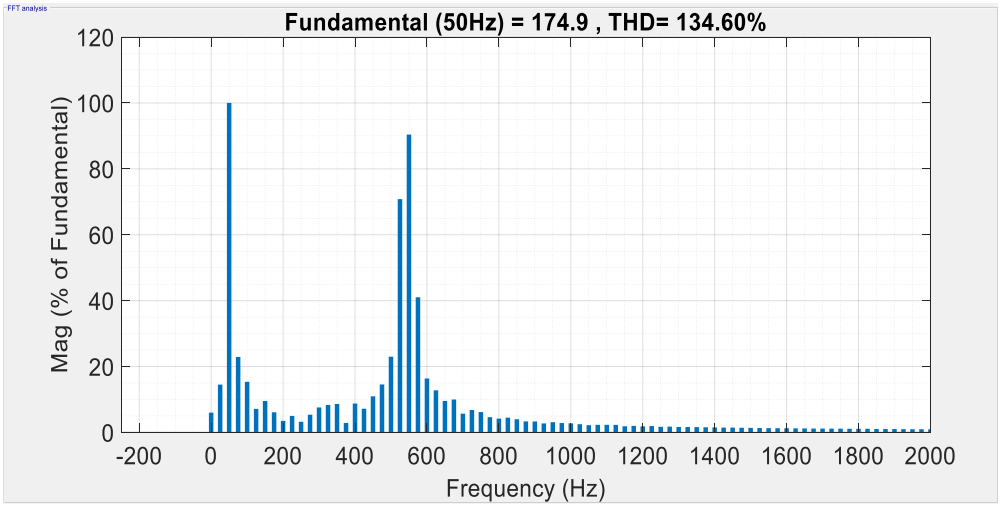

(b)

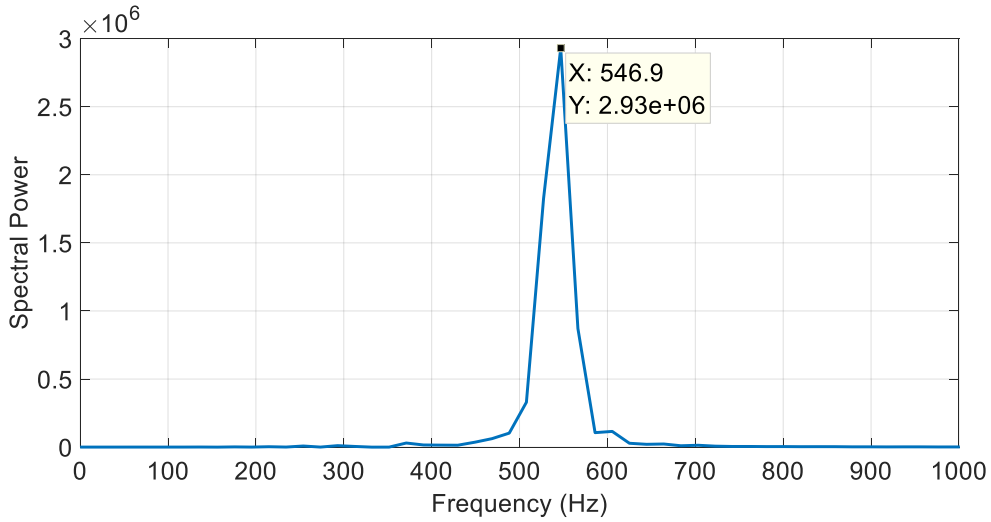

(c)

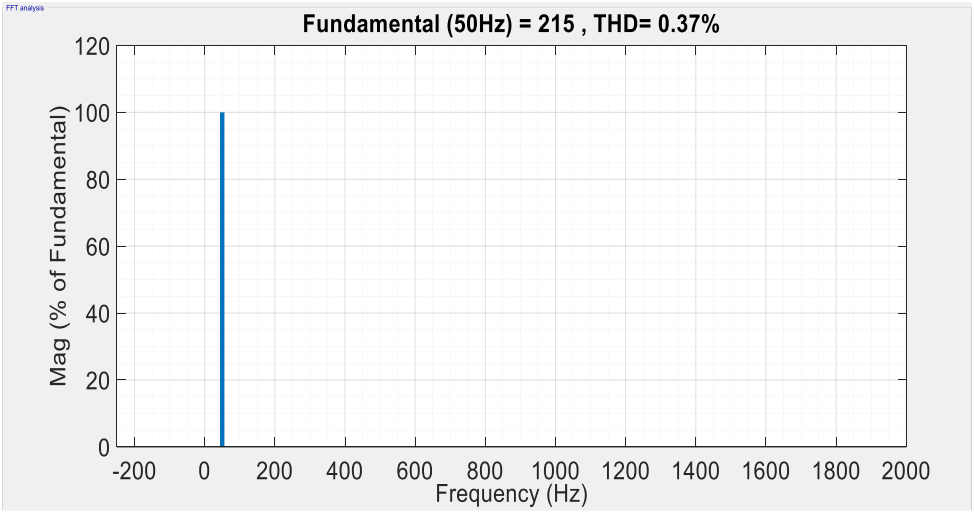

(d)

Figure 4:11: Performance of ANF with 1 mH grid inductance (a) Grid current (b) Harmonic spectrum before 0.05 s (c) Resonant frequency estimation (d) Harmonic spectrum after 0.05 s

Case 2: Figure 4.12 shows the grid current responses when the FFT-based ANF is used to detect a shift in grid impedance from an initial value of 0.1*mH* (SCR = 13.78) to 4*mH* (SCR = 1.15). At time, *t=0.5 seconds*, the change in inductance occurs as seen in Fig. 4.12 (a). The grid current THD therefore rises to 32.50% as seen in Fig. 4.12 (b). At time, *t = 0.55 seconds,* the FFT estimated frequency is 371.1 *Hz* as shown in the power spectrum of Fig. 4.12 (c). Adapting the NF frequency to this value, the current can be controlled properly with a THD factor as low as just 1.54% as shown in Fig. 4.12 (d). Clearly using the adaptive notch

filter, all cases tested give good current waveforms with THDs < 5%, which is in line with the limit set by the IEEE standard 519 [41].

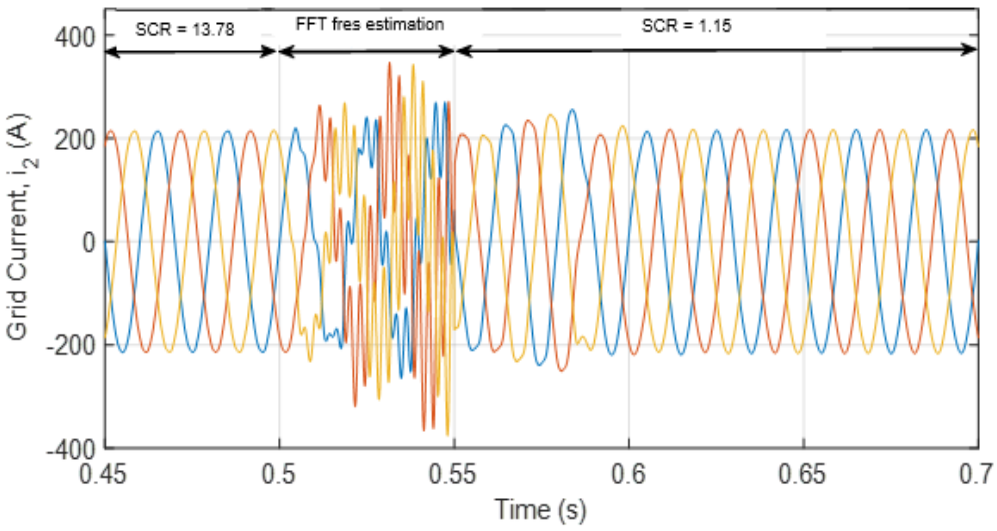

(a)

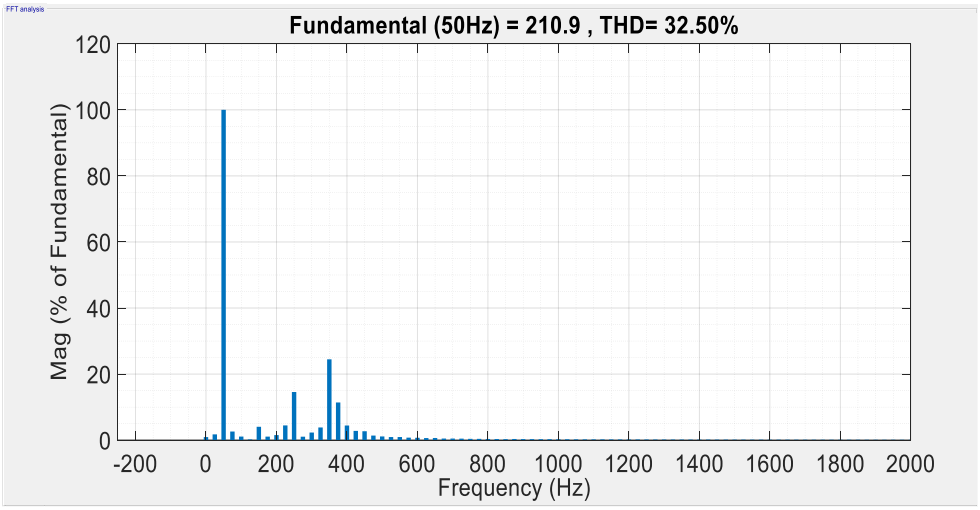

(b)

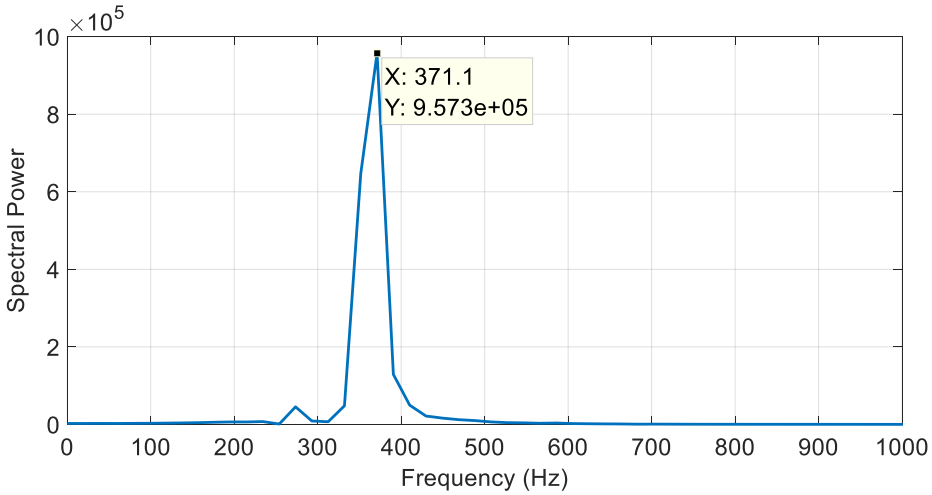

(c)

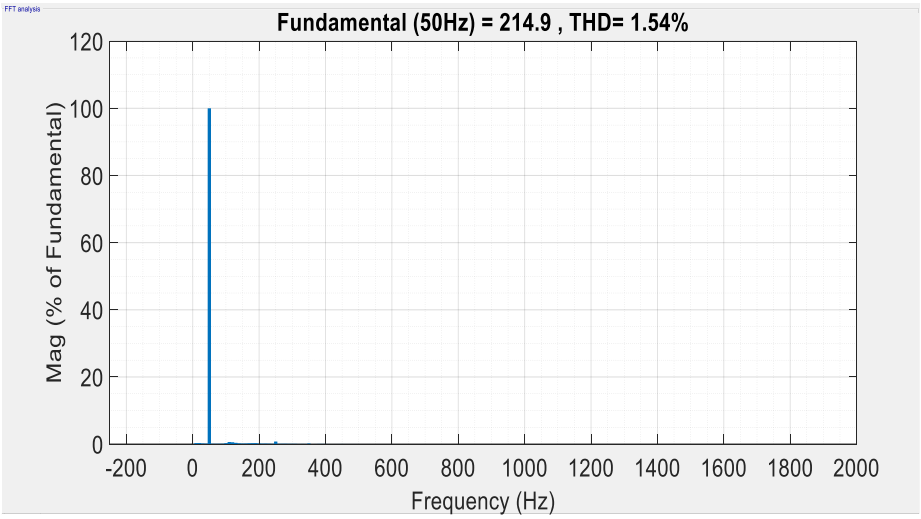

(d)

Figure 4:12: Performance of ANF with grid inductance changing from 0.1 mH to 4 mH (a) Grid current (b) Harmonic spectrum at 0.5 s (c) Resonant frequency estimation (d) Harmonic spectrum after 0.55 s

Table 4.3 summarises the resonant frequencies estimated by the FFT method with 512 samples.

Table 4.3:Estimation of resonant frequencies with FFT algorithm (N = 512)

SCR	**L_g (mH)**	**Actual f_{res} (Hz)**	**f_{res} (Hz) (512- Point FFT)**
13.78	0.1	1266	1211
10.51	0.3	856	839.8
7.75	0.5	703.3	703.1
5.98	0.7	619.2	625
4.38	1	543.9	546.9
2.27	2	434.8	429.7
1.52	3	390.2	390.6
1.15	4	365.5	371.1
0.92	5	349.8	351.6

Figure 4.13 compares the resonant frequencies determined from Equ. (4.1) with those determined from the FFT method, with 512 samples. It shows good agreement between the FFT estimated and the true values of the resonant frequency for all SCRs. The maximum estimation error is 55 Hz, when SCR = 4.61, nearly 4.3% of the actual frequency. Deviations between the estimated and the actual resonant frequency values are expected, as Equ. (4.1) considers the grid resistance as negligible. The FFT estimated frequencies, on the other hand, are determined purely from the spectrum of the grid current, where grid resistance effect is not neglected.

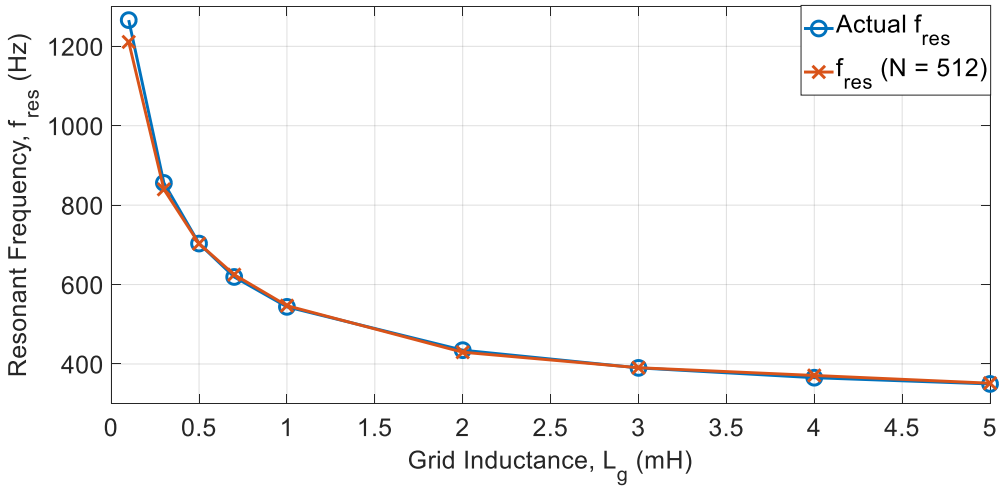

Figure 4:13: Comparison between actual and FFT determined resonant frequencies

The FFT computation time is fast, taking only *0.05 seconds*, equivalent to two and a half fundamental periods, to determine the resonant frequency. Although due to finite frequency resolution, exact estimation of resonant frequency by FFT is not possible. Thus, the width of the NF is designed to cater for a range of frequencies such that resonance attenuation is achievable.

Figure 4.14 shows the effect of varying the grid inductance on the stability of the system. The resonant frequencies and hence the SCRs differ according to the values of L_g. Without proper estimation of $f_{res,}$ the system in Fig. 4.14 (a) is unstable, with an average gain margin of –81.7 dB, while the phase margin averages at -19.7º. The effect of introducing the ANF in the control loop is seen in Fig. 4.14 (b). By cancelling the resonance caused by the LCL filter poles, the system stabilises with a gain margin averaging at 18.6 dB while the phase margin has an average value of 83.2º.

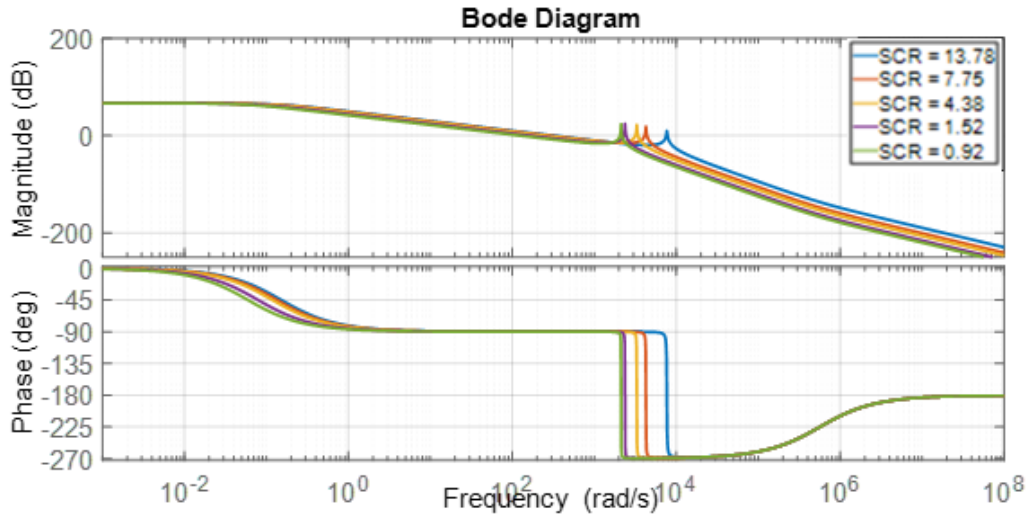

(a)

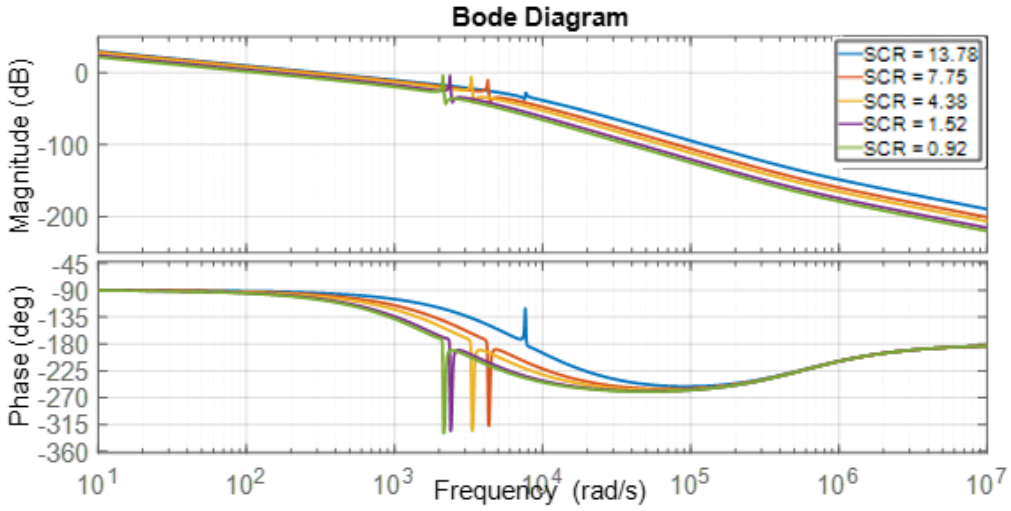

(b)

Figure 4:14: Bode plots showing the effect of varying grid inductance on LCL filter resonant frequency (a) without ANF (b) with ANF

4.5 Comparison of FFT with Goertzel Algorithm for Resonant Frequency Estimation

4.5.1 Principles of the Goertzel Algorithm

The Goertzel algorithm has been applied by some researchers for LCL resonant frequency identification and re-tuning of ANFs [107]. The Goertzel algorithm is a

specialised DFT algorithm that can calculate DFT coefficients by extracting the spectral power at a particular frequency, or a limited range of frequencies.

In terms of detail, the Goertzel algorithm resembles an FFT in that it takes a block of *N* samples at sample rate, T_S. However, it evaluates the cosine and sine coefficients of only one frequency component of interest. The algorithm treats the powers of Fourier terms in the DFT summation as the power terms in a polynomial and sampled data as a multiplier. It evaluates this polynomial in the *nested form.*

The implementation of the algorithm takes two stages: in stage one, an intermediate value, $Q[n]$ is computed from the grid current input signal, $i_2[n]$ as [107, 126]:

$$Q[n] = i_2[n] + 2\cos\left(\frac{2\pi k}{N}\right) Q[n-1] - Q[n-2], \tag{4.15}$$

where $Q[n-1]$ and $Q[n-2]$ are the intermediate values computed from the preceding two samples. This computation is repeated by using samples n =1,…, N one by one. In the second stage, the complex output current, $i_2[n]$ is computed as:

$$i_2[n] = Q[n] - Q[n-1]e^{-j\frac{2\pi k}{N}}. \tag{4.16}$$

The magnitude of $i_2[N]$ for all N samples is equivalent to the DFT output of the frequency coefficient, $I_2[k]$. Therefore, from Equ. (4.16), the magnitude of the grid current coefficient for frequency, *k* is given as:

$$|I_2[k]|^2 = Q^2[N] + Q^2[N-1] - 2\cos\left(\frac{2\pi k}{N}\right) Q[N]\, Q[N-1]. \tag{4.17}$$

The above evaluates only the magnitude for one frequency, *k* at a time. For a selected set of frequencies, it repeats the process using the same block of data, with a different frequency. Thus, the algorithm differs in its small memory requirement and in being calculated by a simple recursive procedure. These algorithms can operate on any size of data block.

The FFT algorithm, in contrast, automatically produces its output at a complete set of N frequencies simultaneously, and operates on sample blocks of size

$N = 2^n$ for some value of n. (How*e*ver, with some loss of efficiency, blocks of other sizes can be processed by augmenting them using “zero padding”, to raise the block size to a power of 2).

4.5.2 Comparisons with FFT

The FFT and Goertzel algorithms are compared in terms of three performance criteria: computational efficiency, execution speed and accuracy in the estimated resonant frequency.

1. **Computational efficiency:** For *N* samples, the Goertzel algorithm is considered more computationally efficient than the FFT, if, when evaluated for a total number, *k* of frequency components [119]:

$$k < \log_2 N. \tag{4.18}$$

According to Equ. (4.18), for a sample block of N = *512* points, the number *k* of frequency components computed must be less than 9. For estimation of f_{res}, the value of *k* based on the frequency resolution (*FR*) [107] is:

$$k = \frac{f_{res(max)} - f_{res(min)}}{FR} \tag{4.19}$$

where $f_{res(max)}$and $f_{res(min)}$ are respectively the maximum and minimum frequencies in the spectrum. With $f_{res(max)}$ corresponding to L_g= *0 mH*, k will be 105, which is 13 times larger than the required value. This clearly indicates that the FFT computation is more efficient in this particular instance of LCL resonant frequency detection.

2. **Execution speed**: for a given N, the speed of execution for the DFT algorithms are proportional to their computational complexities. The order of complexity for the Goertzel algorithm (N_{GA}) is N^2 while that of the FFT (N_{FFT}) is $N\log_2 N$. The speed ratio is therefore defined as:

$$speed\ ratio = \frac{N_{GA}}{N_{FFT}} = \frac{N}{\log_2 N}. \tag{4.20}$$

The speed ratio in Equ. (4.20) is used to compare the execution speeds for the FFT and Goertzel algorithms in LCL resonant frequency estimation as seen in Fig. 4.15.The FFT is faster by a factor of 57 when *N* is 512. This

rises significantly as *N* increases, with the FFT being over 600 times faster than the Goertzel algorithm, for *N* set to 8192.

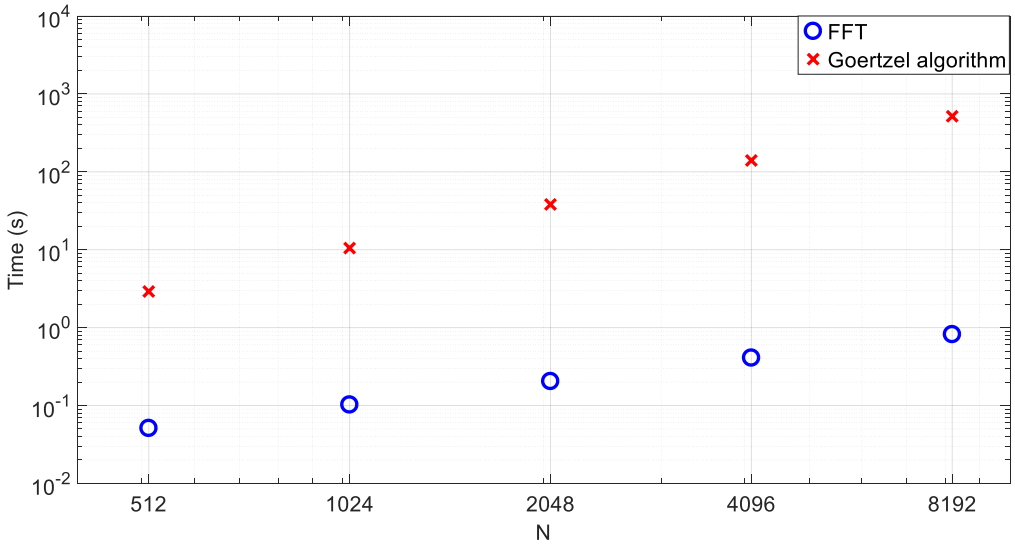

Figure 4:15: Comparison between execution speeds of the FFT and Goertzel Algorithm

For the purpose of resonant frequency estimation with the Goertzel algorithm, the frequency spectrum of interest can be narrowed through a reduction in *k* until an acceptable execution time is obtained. Reducing *k* may hinder accurate resonant frequency detection for wide variations in L_g. It is worth noting that *FR* cannot be less than the NF width , Δf_n specified in Equ. (4.13).

3. **Resonant Frequency Estimation**: Figure 4.16 shows the spectral power obtained when the Goertzel algorithm estimates f_{res} with L_g set to 1 mH. The estimate is the same for FFT in Fig. 4.11 (c). Figure 4.17 also shows that the resonant frequency estimation for the FFT and GA are entirely the same, with the GA taking a significantly larger amount of time as seen in Fig. 4.15.

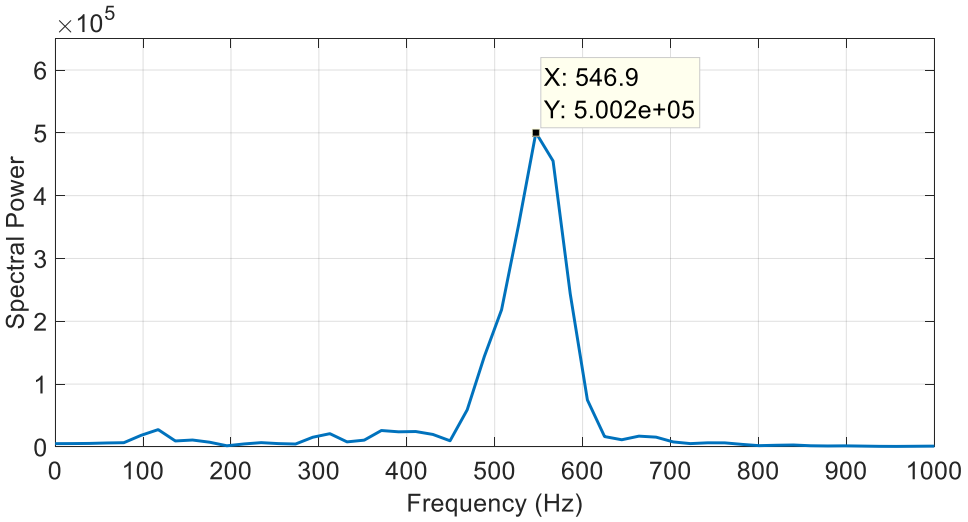

Figure 4:16: Resonant frequency estimation for Lg = 1 mH with Goertzel Algorithm

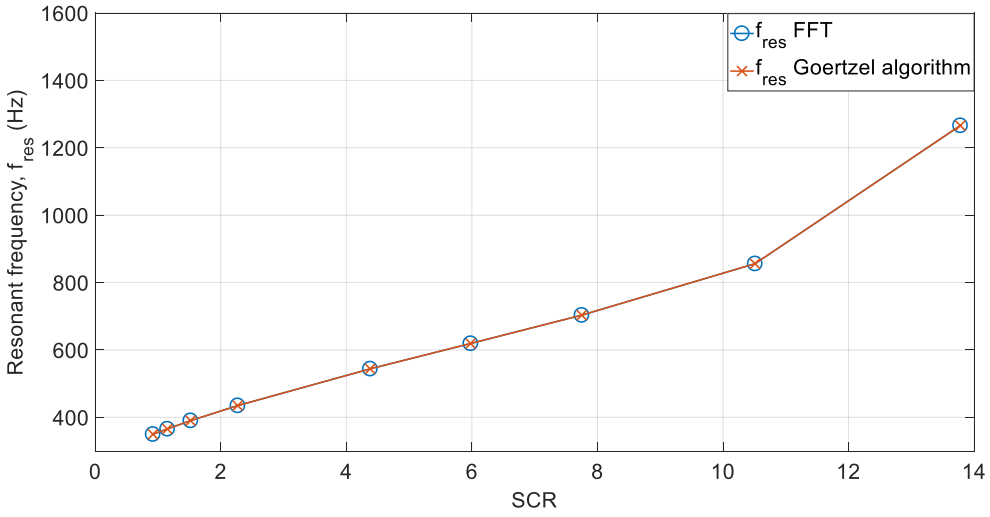

Figure 4:17: Comparing resonant frequency detection of FFT and Goertzel Algorithms

It can therefore be concluded that the only advantage the Goertzel algorithm has over the FTT in terms of resonant frequency detection lies entirely in its reduced memory requirement. As the FFT provides a faster and more efficient estimation, it is a better algorithm for online tuning of an ANF based on a varying L_g.

4.6 Conclusions

The chapter discussed the LCL filter resonance problem and the variation of the resonant frequency with the grid impedance. A solution for online tuning of the notch filter has been proposed, based on the FFT algorithm. The proposed adaptive notch filter (ANF) is capable of attenuating the resonant frequency of the

LCL filter by introducing an opposing notch at the resonant frequency. With the grid being classified based on differing levels of the short circuit ratio (SCR), the proposed algorithm is capable of adapting the notch filter to cope with varying strengths of the grid. Compared to the Goertzel algorithm, the FFT-based estimation provides a faster and more efficient algorithm, for the same frequency resolution. Additionally, it provides the following advantages over other conventional methods:

1. It is sensitive to resonant frequency variation, irrespective of the cause. This makes it applicable to both low and high voltage networks.
2. No additional sensors are required.

Chapter 5 Unbalanced Load Compensation for a Hybrid Biomass-PV Distributed Generation System

5.1 Introduction

In a three-phase power system, load current imbalance occurs often due to uneven distribution of single-phase loads, unequal line impedance, and grid faults. The recent trend of high penetration of distributed generators, particularly the single phase PV inverters, exacerbates the problem. Current imbalance may lead to unbalanced voltages at the network connection point and produces adverse effects on the power distribution network; the unbalanced voltages and currents produce a negative sequence component that degrades the performance of inverters through the production of low order harmonics [127, 128]. The occurrence of low order harmonics is due to the positive sequence synchronous reference frame of the voltages and currents rotating at grid angular speed, ω interacting with the voltages and currents in the negative sequence synchronous reference frame rotating in the reverse direction, -ω. The net result is the appearance of 2ω oscillations in the positive sequence synchronous reference frame. For rotating machines, the negative sequence currents produce a reverse rotating magnetic field, hence the torque in opposite direction to the torque generated by the positive sequence currents, causing rotor vibration. This produces additional stress on the rotating shaft of the turbine-generator set. In addition, the magnetic field due to negative sequence current induces current in the rotor windings at twice the grid frequency, leading to excessive heating of the rotor circuit. Other side effects include: transformer overheating and limiting the capacities of distribution lines, etc.

The grid connected inverters can be applied for mitigating the unbalanced load current and the control strategies can be two; the first is to defend the inverter itself such that it is immune to the effect of grid load and subsequent voltage imbalances. The second scheme is actively compensating the imbalanced current so that the inverter is dedicated to absorbing the negative sequence current. This scheme is commonly realised using FACTS devices such as a static synchronous Compensator (STATCOM) connected at the point of common coupling (PCC). The STATCOM injects the negative sequence component of the

unbalanced load current, effectively mitigating the unbalanced PCC current, hence voltage [129, 130]. For high voltage applications, multi-level converter based STATCOM is implemented [131, 132]. However, the STATCOM device is expensive and its deployment may not be viable economically for small networks. With a system having grid-connected renewable sourced generators, such as PV and wind-powered generators, it is possible to use inverters of renewable generators for load imbalance compensation, provided their power ratings are sufficiently large to cope with the additional current requirement

This chapter presents a control strategy for unbalanced load compensation in a DG system using the PV inverter within the system. The example DG system studied has both the PV-power generator presented in chapters 3 and 4 and the biomass generator presented in chapter 2: they jointly supply unbalanced loads in the system. For the PV-inverter functioning as both a compensator for load imbalance and PV power feeder, it faces two challenges; synchronisation to the grid voltage under unbalanced conditions and the control strategy when the inverter has limited power rating. For the former, since the additional negative sequence components are introduced by the asymmetrical load, the conventional synchronous reference frame PLL (SRF-PLL) cannot give precise grid angle detection [31]. Advanced techniques such as the decoupled double synchronous reference frame- PLL (DDSRF-PLL) [120] discussed in chapter 1 are required for grid synchronisation under unbalanced voltage conditions. DDSRF-PLL control is implemented through the separation of positive and negative sequence components in the SRF for grid phase angle detection. For the control scheme, it requires extracting load negative sequence currents accurately. These should be set as references for the control loop together with the PV generated real current. A compromise needs to be made between accurate load imbalance mitigation and real current supply in the case when inverter current limit may be reached, as this may impose stress on the semiconductor switches of the PV grid-tie inverter.

5.2 Hybrid Biomass-PV Distributed Generation System under Unbalanced Loading

For ease of analysis, the hybrid biomass-PV DG system may be represented by a one line diagram, where each power source is modelled according to Thevenin's theorem as an ideal voltage source in series with an open circuit impedance, as shown in Fig. 5.1. Thus, the grid is represented by a source, v_g in series with the grid impedance, $Z_g = R_g + j\omega L_g$. The PV source voltage,v_{pv}, is connected to the PCC through impedance, $Z_{pv} = R_{pv} + j\omega L_{pv}$. Since the capacitor of the inverter LCL filter for switching harmonic attenuation has negligible dynamics at the low grid frequency, it is neglected. Hence, L_{pv} represents the lump sum of the line inductance, as well as LCL filter inductances, L_1 and L_2. The biomass generator is represented by the voltage source, v_b in series with the impedance, $Z_b = R_b + j\omega L_b$, modelling generator stator winding synchronous reactance and line impedance between the stator terminal and the PCC.

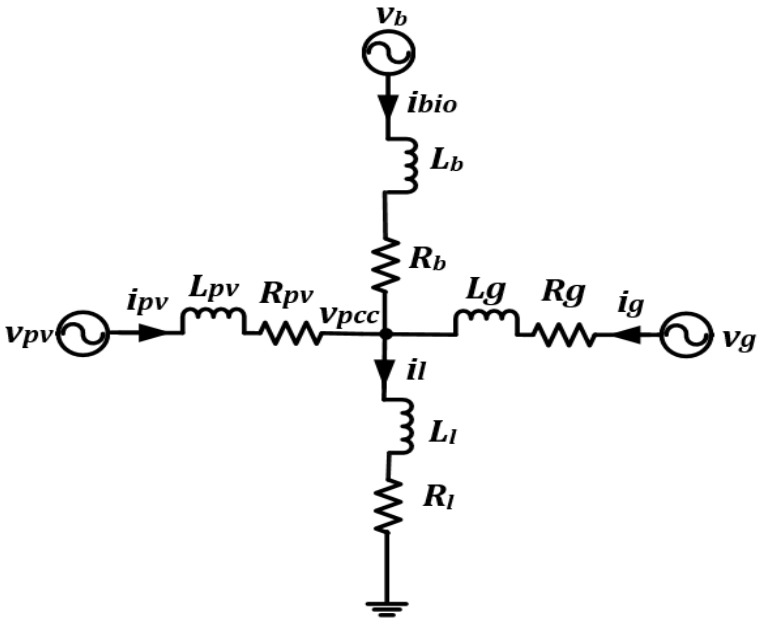

Figure 5:1: One line diagram of the grid connected hybrid biomass-PV distributed generator

An unbalanced load with impedance, $Z_l = R_l + j\omega L_l$ connected at the PCC draws both positive and negative sequence currents. The time varying AC load current, $i_l(t)$ is therefore represented as an arithmetic sum of its positive (superscript '+')

and negative (superscript '-') sequence components described in Equ. (5.1) as:

$$i_l(t) = i_l(t)^+ + i_l(t)^-. \quad (5.1)$$

Under load unbalanced conditions, the PCC voltage, $v_{pcc}(t)$ as a function of the load current and load impedance may be expressed as:

$$v_{pcc}(t) = (i_l(t)^+ + i_l(t)^-)(R_l + jX_l). \quad (5.2)$$

Equ. (5.2) shows that the interconnected unbalanced load at the PCC leads to a negative sequence in the PCC voltage. Unbalanced voltages cause undesirable effects in power systems, including damage to electrical loads due to negative sequence currents and overloading of distribution lines.

The negative sequence component of the load also affects the currents supplied by the biomass and PV generators, i_{bio} and i_{pv}. Assuming the grid impedance, Z_g is sufficiently large such that it does not supply current to the load, the current balance equation at the PCC according to Kirchhoff's current law is given by:

$$i_l(t)^+ + i_l(t)^- = i_{bio}(t) + i_{pv}(t). \quad (5.3)$$

From the point of view of the biomass generator, the negative sequence current produces a negative sequence electromagnetic torque, $T_e{}^-$ which creates an unbalance between the rotor mechanical torque and the electromagnetic torque. This leads to undue stress on the rotor and which in some cases, may lead to excessive heating.

PV inverter current limitation may exceed the rated level in the presence of unbalanced loads. This will lead to overheating of and potential damage to the PV system. Considering the PV inverter power rating as a constraint, the existing PV inverter can be controlled to produce an unbalanced load compensating negative sequence current. According to the superposition principle, the PV voltage with respect to the PCC in Fig. 5.1 is given by:

$$v_{pv}(t) = v_{pcc}(t) + L_{pv}\frac{di_{pv}(t)}{dt} + R_{pv}i_{pv}(t). \quad (5.4)$$

Converting Equ. (5.4) into synchronous reference frame using Park's transformation:

$$v_{pvdq}(t) = v_{pccdq}(t) + L_{pv}\frac{di_{pvdq}(t)}{dt} + \left(R_{pv} + j\omega L_{pv}\right)i_{pvdq}(t). \quad (5.5)$$

The Laplace transform of Equ. (5.5) for the d and q-axis components are:

$$V_{pvd} = V_{pccd} + \left(sL_{pv} + R_{pv}\right)I_{pvd} - \omega L_{pv}I_{pvq} \quad (5.6)$$

and

$$V_{pvq} = V_{pccq} + \left(sL_{pv} + R_{pv}\right)I_{pvq} + \omega L_{pv}I_{pvd}. \quad (5.7)$$

The negative sequence equivalent of Equs. (5.6) and (5.7) for the PCC voltage are:

$$V_{pccd}{}^{-} = V_{pvd}{}^{-} - \left(sL_{pv} + R_{pv}\right)I_{pvd}{}^{-} + \omega L_{pv}I_{pvq}{}^{-} \quad (5.8)$$

and

$$V_{pccq}{}^{-} = V_{pvq}{}^{-} - \left(sL_{pv} + R_{pv}\right)I_{pvq}{}^{-} - \omega L_{pv}I_{pvd}{}^{-}. \quad (5.9)$$

Equs. (5.8) and (5.9) clearly show the relationship between the negative sequence PV currents, $I_{pvd}{}^{-}$and $I_{pvq}{}^{-}$ and the PCC negative sequence voltages, $V_{pccd}{}^{-}$ and $V_{pccq}{}^{-}$. It is therefore possible to regulate the negative sequence PCC voltages to zero by controlling the negative sequence currents. As the currents and voltages are DC, the control can be implemented in the synchronous reference frame with the PI controllers designed in Chapter 3.

5.3 Performance Analysis of Biomass-PV Distributed Generation System Supplying an Unbalanced Three-phase Load

The full grid connected hybrid biomass-PV DG system is shown in Fig. 5.2 (a). The biomass generator operates at 0.8 power factor lagging to supply a current, i_{bio} to maximum active and reactive loads of 392 *kW* and 296 *kVAr* respectively. The PV current, i_{pv} corresponds to the maximum power current from the MPPT controller based on prevailing weather conditions.

The biomass generator terminal voltage is controlled by the AC5A excitation system while the rotor speed is regulated by the gas turbine speedtronics

controller as described in chapter 2. The PV controllers described in chapters 3 and 4 are: the MPP controller used to maximise power output from the PV module according to weather conditions; the DC link voltage controller for maintaining the DC bus voltage constant; the current controller for regulating the MPP current supplied to the load; the ANF for active damping of the LCL filter at different resonant frequencies; and the sine PWM for controlling the PV inverter switches. Note that the LCL resonant frequency is unaffected by inductive loads, as they are shunt connected. Hence, the ANF control can be disabled.

Two star connected loads, load a and load b are connected at the PCC with resistances, R_{la} and R_{lb} and inductances, L_{la} and L_{lb} respectively. Load a is a balanced load rated at a complex power, $S_a = 300 + j200$ *KVA,* while load b is a single-phase load with a complex power rating of $S_b = 40 + j40$ *KVA* in phase A. The PV and biomass generators are equidistant to the distribution line with impedances of: $0.1 + j0.03$ Ω.

The power grid is modelled as an ideal voltage source with a typical distribution line impedance of: $0.6 + j0.09$ Ω per km [133], equivalent to an X/R ratio of 0.15. PCC voltage synchronisation is achieved through the SRF-PLL, where the PCC voltage, v_{pcc} is measured and its phase angle, ωt detected, in addition to the dq-PCC voltage components, V_{pccd} and V_{pccq}.

The DC voltage and dq-current control loops are depicted in Fig. 5.2 (b). The d-axis controllers are a combination of an outer DC link voltage controller and an inner controller for the d-component of the PV current, I_{pvd}. The function of the DC link voltage controller is two-fold: maintaining the DC link voltage at the specified reference, ${V_{DC}}^*$ and providing the d-axis current reference, ${I_{pvd}}^*$ that will ensure transfer of PV active power to the grid. In the q-axis controller, unity power factor operation is achieved by setting the q-axis reference, ${I_{pvq}}^*$ to zero. Notch filters in both control loops eliminate the effect of LCL filter resonance. The voltage signals for the sine PWM, V_{id} and V_{iq} are obtained from the summations of the notch filter output signals with the feedforward PCC voltages, V_{pccd} and V_{pccq} and the cross-coupling terms, $-\omega L_{pv} I_{pvq}$ and $\omega L_{pv} I_{pvd}$ in the d and q-axes respectively. An inverse Park transform is performed to convert V_{id} and V_{iq} into

stationary reference frame, producing the sinusoidal reference signals for the sine PWM of the VSI.

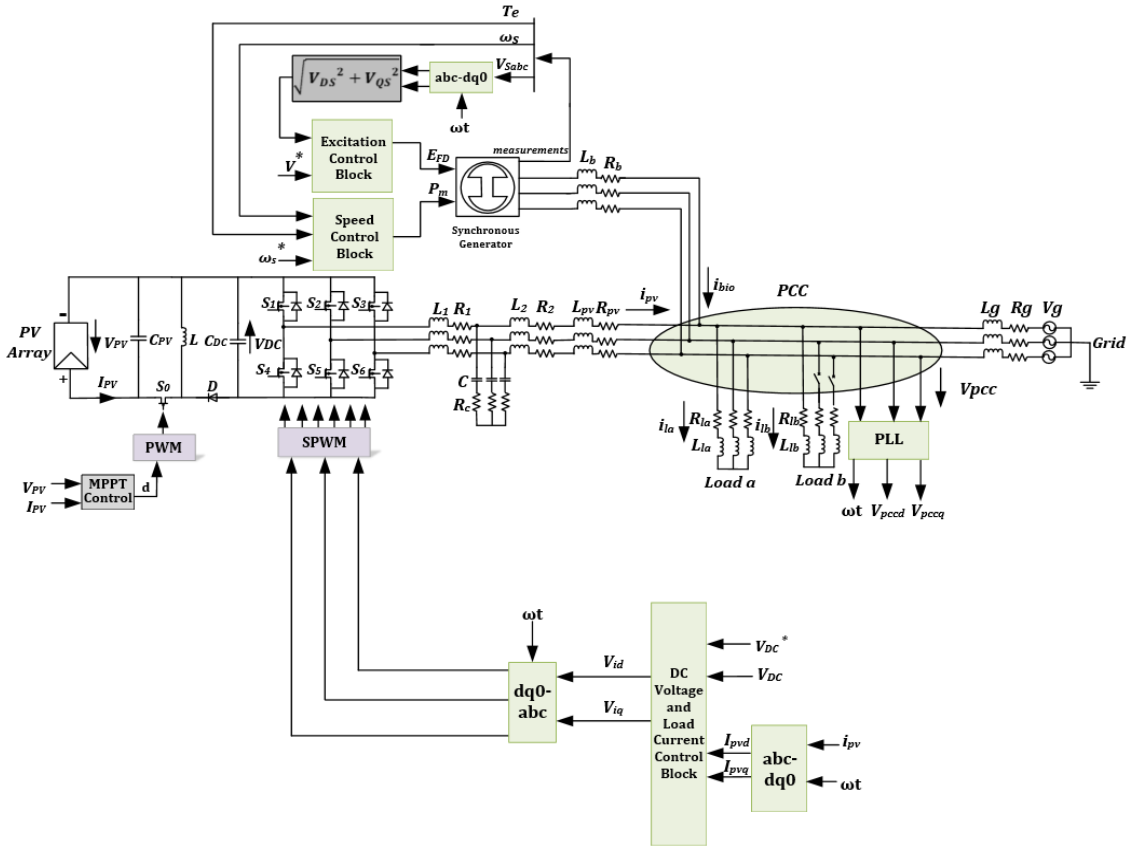

(a)

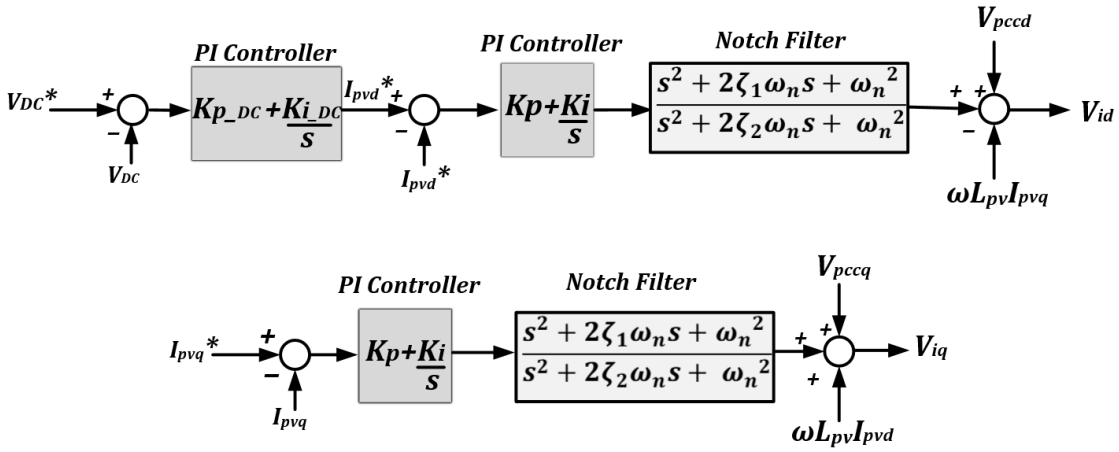

(b)

Figure 5:2: Unbalanced load connected to PCC of hybrid biomass-PV distributed generation system (a) complete DG system layout (b) DC voltage and dq-current control loops

The detrimental effects of the negative sequence component currents generated by unbalanced loads are discussed in the subsequent sections.

5.3.1 Effect on PV Generator

The active and reactive powers of a PV generator can be analysed using the instantaneous power theory [31]. According to this theory, the instantaneous real and reactive powers (p and q) generated by a three phase inverter operating under unbalanced conditions can be determined by the positive and negative sequence components of the inverter voltages and currents, ${v_d}^{\pm}$, ${v_q}^{\pm}$, ${i_d}^{\pm}$ and ${i_q}^{\pm}$, as:

$$p = \left({v_d}^{+} + {v_q}^{+} + {v_d}^{-} + {v_q}^{-}\right).\left({i_d}^{+} + {i_q}^{+} + {i_d}^{-} + {i_q}^{-}\right) \tag{5.10}$$

and

$$q = \left({v_d}^{+} + {v_q}^{+} + {v_d}^{-} + {v_q}^{-}\right) \times \left({i_d}^{+} + {i_q}^{+} + {i_d}^{-} + {i_q}^{-}\right). \tag{5.11}$$

The resultant formulae from Equs. (5.10) and (5.11) are:

$$p = P + P_c \cos(2\omega t) + P_s \sin(2\omega t) \tag{5.12}$$

and

$$q = Q + Q_c \cos(2\omega t) + Q_s \sin(2\omega t), \tag{5.13}$$

where P and Q are average values of the instantaneous active and reactive powers generated by the inverter, while P_c, P_s, Q_c and Q_s are the amplitudes of oscillating terms associated with the two powers respectively. These power terms are given as [31]:

$$P = \frac{3}{2}\left({v_d}^{+}{i_d}^{+} + {v_q}^{+}{i_q}^{+} + {v_d}^{-}{i_d}^{-} + {v_q}^{-}{i_q}^{-}\right), \tag{5.14}$$

$$P_c = \frac{3}{2}\left({v_d}^{-}{i_d}^{+} + {v_q}^{-}{i_q}^{+} + {v_d}^{+}{i_d}^{-} + {v_q}^{+}{i_q}^{-}\right), \tag{5.15}$$

$$P_s = \frac{3}{2}\left({v_q}^{-}{i_d}^{+} - {v_d}^{-}{i_q}^{+} - {v_q}^{+}{i_d}^{-} + {v_d}^{+}{i_q}^{-}\right), \tag{5.16}$$

$$Q = \frac{3}{2}\left({v_q}^{+}{i_d}^{+} - {v_d}^{+}{i_q}^{+} + {v_q}^{-}{i_d}^{-} - {v_d}^{-}{i_q}^{-}\right), \tag{5.17}$$

$$Q_c = \frac{3}{2}\left({v_q}^{-}{i_d}^{+} - {v_d}^{-}{i_q}^{+} + {v_q}^{+}{i_d}^{-} - {v_d}^{+}{i_q}^{-}\right) \tag{5.18}$$

and

$$Q_s = \frac{3}{2}\left(-v_d{}^- i_d{}^+ - v_q{}^- i_q{}^+ + v_d{}^+ i_d{}^- + v_q{}^+ i_q{}^-\right). \quad (5.19)$$

It is clear from Equs. (5.15), (5.16), (5.18) and (5.19) that the interactions of positive and negative sequence voltages and currents in a PV sourced generator lead to oscillatory terms in both active and reactive powers across the PV terminals. With asymmetrical load compensation, the PCC voltage is balanced with the negative sequence components becoming zero, hence:

$$v_d{}^- = v_q{}^- = 0. \quad (5.20)$$

The resulting oscillatory powers: P_c, P_s, Q_c and Q_s in Equs. (5.15), (5.16), (5.18) and (5.19) therefore become:

$$P_c = \frac{3}{2}\left(v_d{}^+ i_d{}^- + v_q{}^+ i_q{}^-\right), \quad (5.21)$$

$$P_s = \frac{3}{2}\left(v_q{}^+ i_d{}^- + v_d{}^+ i_q{}^-\right), \quad (5.22)$$

$$Q_c = \frac{3}{2}\left(v_q{}^+ i_d{}^- - v_d{}^+ i_q{}^-\right) \quad (5.23)$$

and

$$Q_s = \frac{3}{2}\left(v_d{}^+ i_d{}^- + v_q{}^+ i_q{}^-\right). \quad (5.24)$$

Equs. (5.21) - (5.24) verify that oscillations in the PV generated powers remain even after the unbalanced load has been compensated and the PCC voltage is balanced.

5.3.2 Effect on Biomass Generator

The dynamic equations representing the stator voltages of the generator, V_{ds} and V_{qs} in the SRF as presented in chapter 2 are:

$$V_{ds} = R_s I_{ds} + \frac{d\phi_d}{dt} - \omega_s \phi_q \quad (5.25)$$

and

$$V_{qs} = R_s I_{qs} + \frac{d\phi_q}{dt} + \omega_s \phi_d, \quad (5.26)$$

where R_s is the stator resistance,

I_{ds} is the d-axis stator current,

ϕ_d is the d-axis flux linkage,

ω_s is the synchronous speed,

ϕ_q is the q-axis flux linkage and

I_{qs} is the q-axis stator current.

The instantaneous power, P_b at the output of the biomass generator is:

$$P_b = V_{ds}I_{ds} + V_{qs}I_{qs}. \tag{5.27}$$

Substituting for V_{ds} from Equ. (5.25) and V_{qs} from Equ. (5.26) in Equ. (5.27) results in:

$$P_b = R_s\left({I_{ds}}^2 + {I_{qs}}^2\right) + \left(\frac{d\phi_d}{dt} I_{ds} + \frac{d\phi_q}{dt} I_{qs}\right) + \omega_s\left(\phi_d I_{qs} - \phi_q I_{ds}\right). \tag{5.28}$$

From Equ. (5.28), the power delivered to the air-gap, P_e is [53]:

$$P_e = \omega_s\left(\phi_d I_{qs} - \phi_q I_{ds}\right) \tag{5.29}$$

and the electromagnetic torque, T_e is related to the air-gap power via:

$$T_e = \frac{P_e}{\omega_s}. \tag{5.30}$$

Inserting Equ. (5.29) into Equ. (5.30), the expressing for T_e becomes:

$$T_e = \phi_d I_{qs} - \phi_q I_{ds}. \tag{5.31}$$

Under unbalanced conditions, the stator currents, I_{qs} and I_{ds} consist of additional negative sequence components rotating at twice the grid frequency, making:

$$T_e = \phi_d\left({I_{qs}}^+ + {I_{qs}}^-\right) - \phi_q\left({I_{ds}}^+ + {I_{ds}}^-\right). \tag{5.32}$$

In the presence of an unbalanced load, the negative sequence stator currents produce a negative sequence component in T_e according to Equ. (5.32). This prevents T_e from balancing T_m in the swing equation of chapter 2, Equ. (2.2). This causes the generator to accelerate. The torque pulsates at twice the grid

frequency, causing mechanical stress and heating in the rotor windings [134] leading to a reduction in the overall efficiency of the biomass generator.

5.3.3 Simulation Studies

Simulation studies are performed in MATLAB/Simulink software for the hybrid biomass-PV DG system in Fig. 5.2 subjected to an unbalanced load. The parameters for the DG system are listed in Table 5.1. The biomass DG and its controller parameters are identical to the values specified in Tables 2.1,2.2 and 2.3 of chapter 2.

Table 5.1: Hybrid DG system parameters

Parameter	Rating
DC Link Voltage (V_{DC})	800 V
Grid phase voltage (V_{ph})	220 V
Grid frequency (f)	50 Hz
Grid Impedance (R_g/L_g)	0.6 Ω/ 0.3 mH
LCL filter parameters: $L_1/C/L_2$	3 mH / 110 μF / 51 μH
Notch Filter damping ratios (ζ_1/ζ_2)	0.01/1
Biomass line impedance (R_{bio}/L_{bio})	0.1 Ω/ 0.1 mH
PV Impedance (R_{pv}/ L_{pv})	0.1 Ω/ 0.1 mH
Inverter switching frequency (f_{sw})	20 kHz

An important parameter in unbalanced fault analysis is the voltage unbalance factor, VUF, which is the ratio of the negative sequence component of the voltage signal to the positive sequence component:

$$VUF = \frac{|V^-|}{|V^+|} \tag{5.33}$$

A VUF of 1% may cause up to 10 times the current unbalance, which may lead to large losses within a power system [135]. It is therefore of paramount importance that the PCC voltage be maintained as minimal as possible.

The performance of the control system in Fig. 5.2 (b) is examined when subjected to an unbalanced load. Initially, only load a is connected. Load b is unconnected at time, *t > 0 seconds* to allow sufficient time for the biomass generator to settle due to machine inertia. At time, *t = 9 seconds,* the single phase load b is connected to phase A of the distribution line.

The waveform responses of the hybrid biomass-PV DG system are seen in Fig. 5.3. Prior to connection of load b, Fig. 5.3 (a) shows zero negative sequence voltage at the PCC, indicating a balance in terms of magnitude and phase angle across the three-phases of the voltage. At time, *t = 9 seconds,* the VUF in Fig. 5.3 (b) increases to 1.7%. The negative sequence current of the load is supplied by both PV and biomass, resulting in unbalanced currents in both, as seen in Fig. 5.3 (c) and (d) respectively. The biomass current has a higher degree of unbalance compared to the PV current, which may be attributed to their difference in power rating. As the biomass supplies more of the unbalanced current, minor oscillations appear in the active and reactive power output of the PV as seen in Fig. 5.3 (e).

At the biomass generator side, Fig. 5.3 (g) shows the electromagnetic torque and mechanical torque. The electromagnetic torque in Equ. (5.32) contains positive and negative sequence elements at twice the grid frequency, which causes the rotor to accelerate according to the swing equation, due to inequality between T_e and T_m. As mentioned previously, this leads to additional stress on the rotor of the generator, thereby negatively impacting its efficiency.

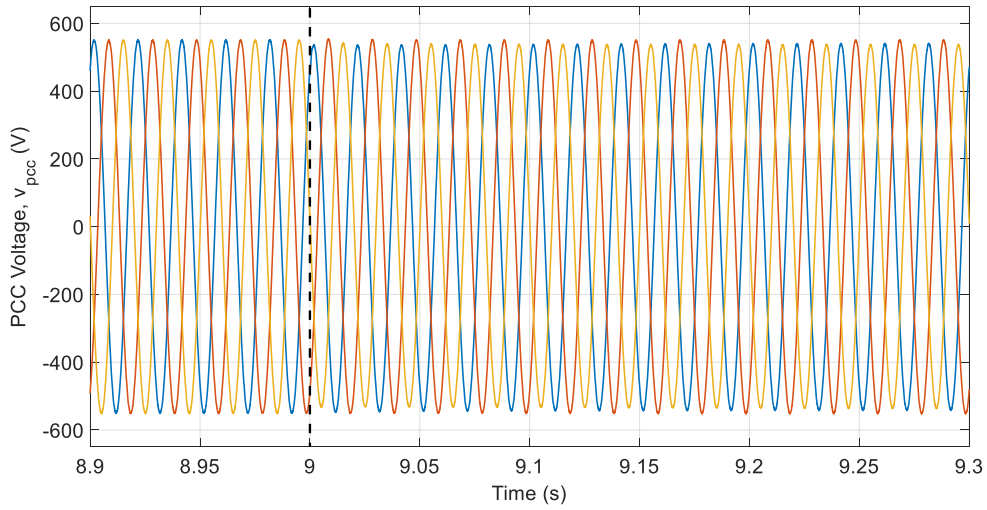
PCC Voltage, v_{pcc} (V)
600
400
200
0
-200
-400
-600
8.9
8.95
9
9.05
9.1
9.15
9.2
9.25
9.3
Time (s)

(a)

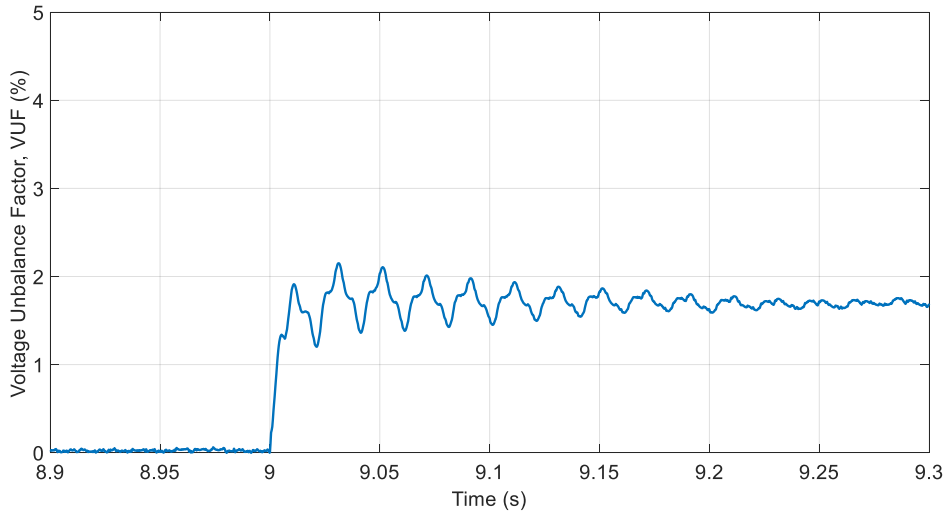
Voltage Unbalance Factor, VUF (%)
5
4
3
2
1
0
8.9
8.95
9
9.05
9.1
9.15
9.2
9.25
9.3
Time (s)

(b)

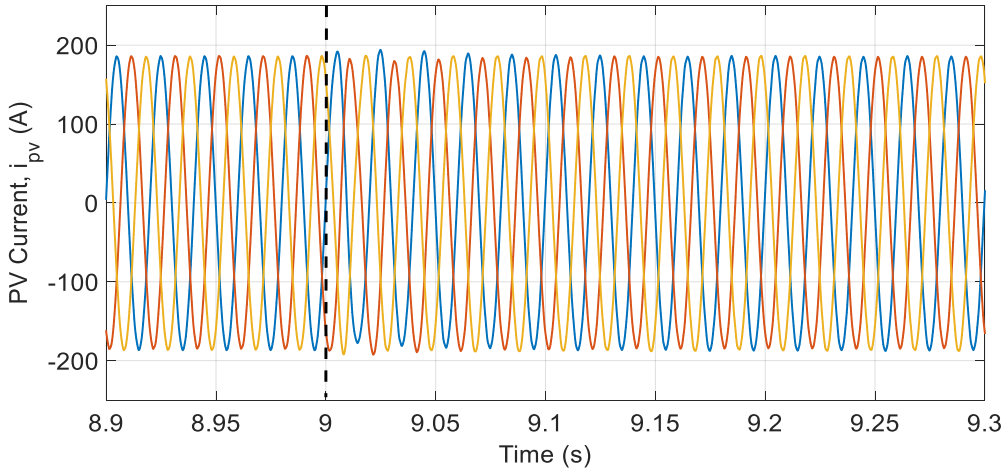
PV Current, i_{pv} (A)
200
100
0
-100
-200
8.9
8.95
9
9.05
9.1
9.15
9.2
9.25
9.3
Time (s)

(c)

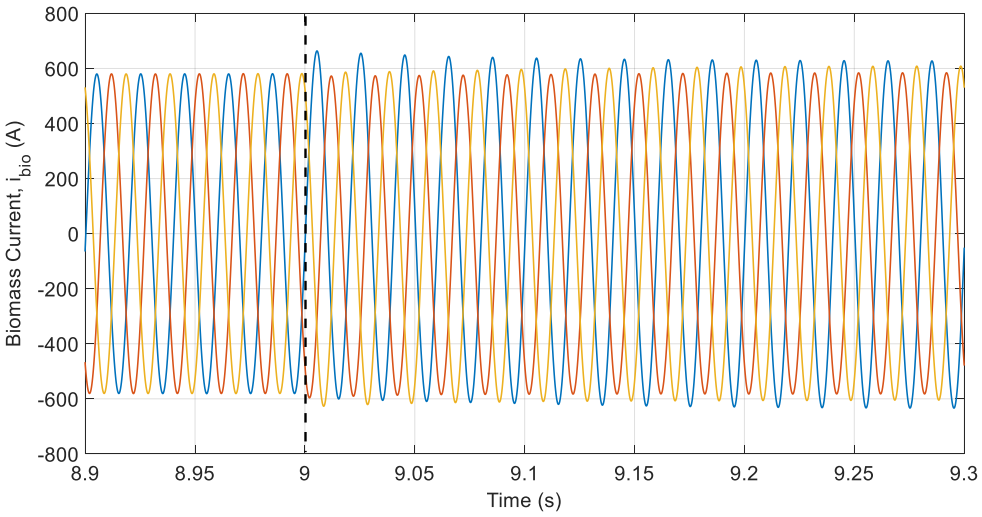
Biomass Current, i_{bio} (A)
800
600
400
200
0
-200
-400
-600
-800
8.9
8.95
9
9.05
9.1
9.15
9.2
9.25
9.3
Time (s)

(d)

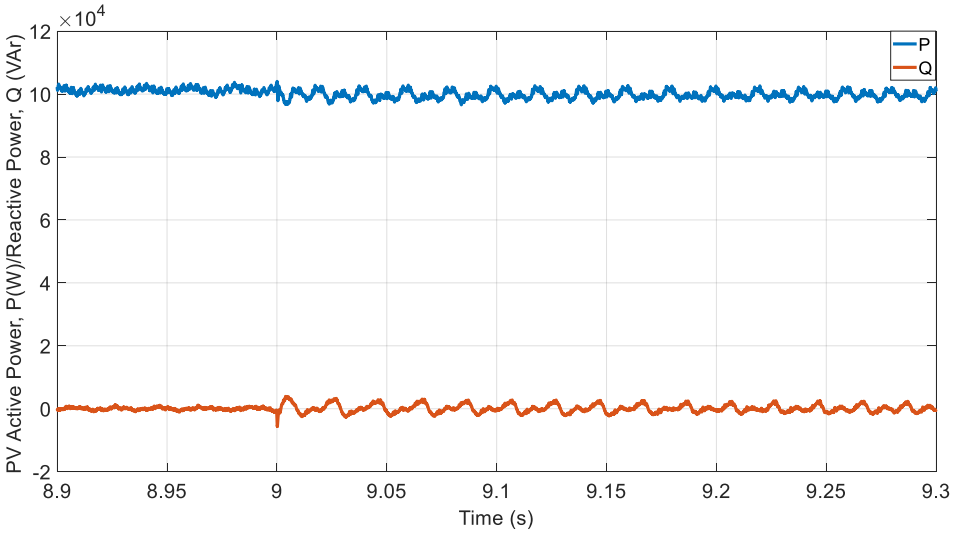
$\times 10^4$
PV Active Power, P(W)/Reactive Power, Q (VAr)
12
10
8
6
4
2
0
-2
P
Q
8.9
8.95
9
9.05
9.1
9.15
9.2
9.25
9.3
Time (s)

(e)

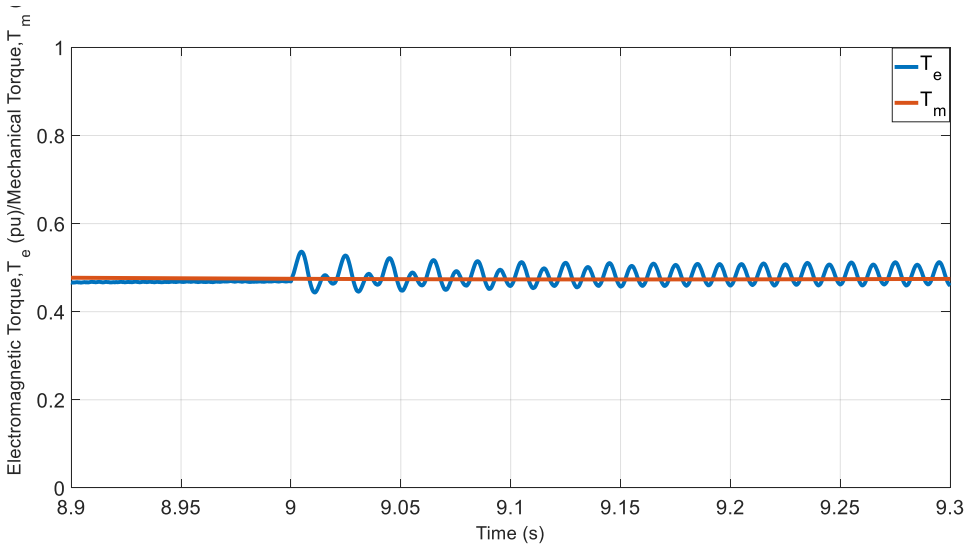

(f)

Figure 5:3: Hybrid biomass-PV DG system conventional control under unbalanced loads (a) PCC voltage (b) VUF (c) PV current (d) Biomass current (e) PV active power output (f) Machine torques

5.4 Unbalanced Load Compensation with PV Distributed Generator

The conventional controllers in section 5.3 were not able to overcome the negative effects of the unbalanced load, such as unbalanced voltages at the PCC, and imbalance in the PV and biomass currents. Additionally, oscillations at twice the grid frequency appeared in the electromagnetic torque of the biomass generator. A new control structure is therefore proposed to overcome the challenges of the previous controller by compensating the negative sequence component of the load. To this end, the existing inverter of the PV is controlled to generate negative sequence currents that compensate the unbalanced load current.

5.4.1 Control Scheme

The hybrid biomass-PV DG system and its unbalanced load compensation scheme are shown in Fig. 5.4. Due to the presence of negative sequence components in the PCC voltage, as well as the load and grid currents, additional control is required for these components which may be conveniently implemented with the DDSRF in chapter 1. In Fig. 5.4 (a), the instantaneous values of the three-phase PCC voltage, v_{pcc}, the PV inverter three-phase current, i_{pv} and the

unbalanced load current, i_{lb} are measured and converted to the synchronous reference frame using the DDSRF technique detailed in chapter 1. The positive and negative sequence synchronisation phase angles, *+ωt* and *–ωt* are determined from the DDSRF-PLL of the measured PCC voltage, v_{pcc}.

The control system consists of 4 identical PI-controllers, one for each d and q-axes component in the positive and negative SRF. The positive sequence current control is the same as the control strategy in the previous section. The unbalanced load compensation currents are determined by the negative sequence load currents, I_{ld}^{-} and I_{lq}^{-} as seen in the control loops in Fig. 5.4 (b). These currents serve as references to the amount of negative sequence currents, I_{pvd}^{-} and I_{pvq}^{-} the PV inverter must inject into the PCC to compensate the unbalanced load. Across all 4 outputs of the PI controllers are the voltage command signals for the sine PWM control. The phase angles *+ωt* and *–ωt* are used to convert the voltage command signals V_{id}^{+}, V_{iq}^{+}, V_{ld}^{-} and V_{lq}^{-} into the stationary reference frame to provide reference switching signals to the inverter.

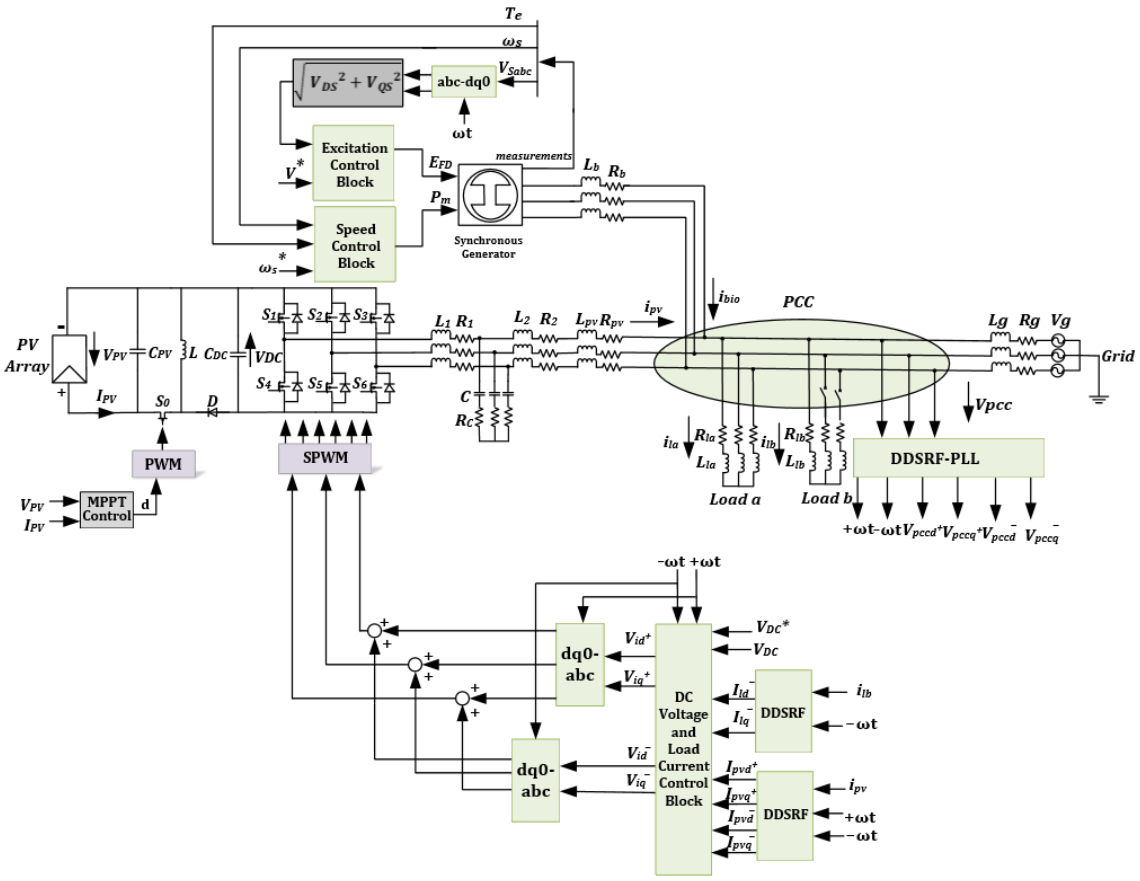

(a)

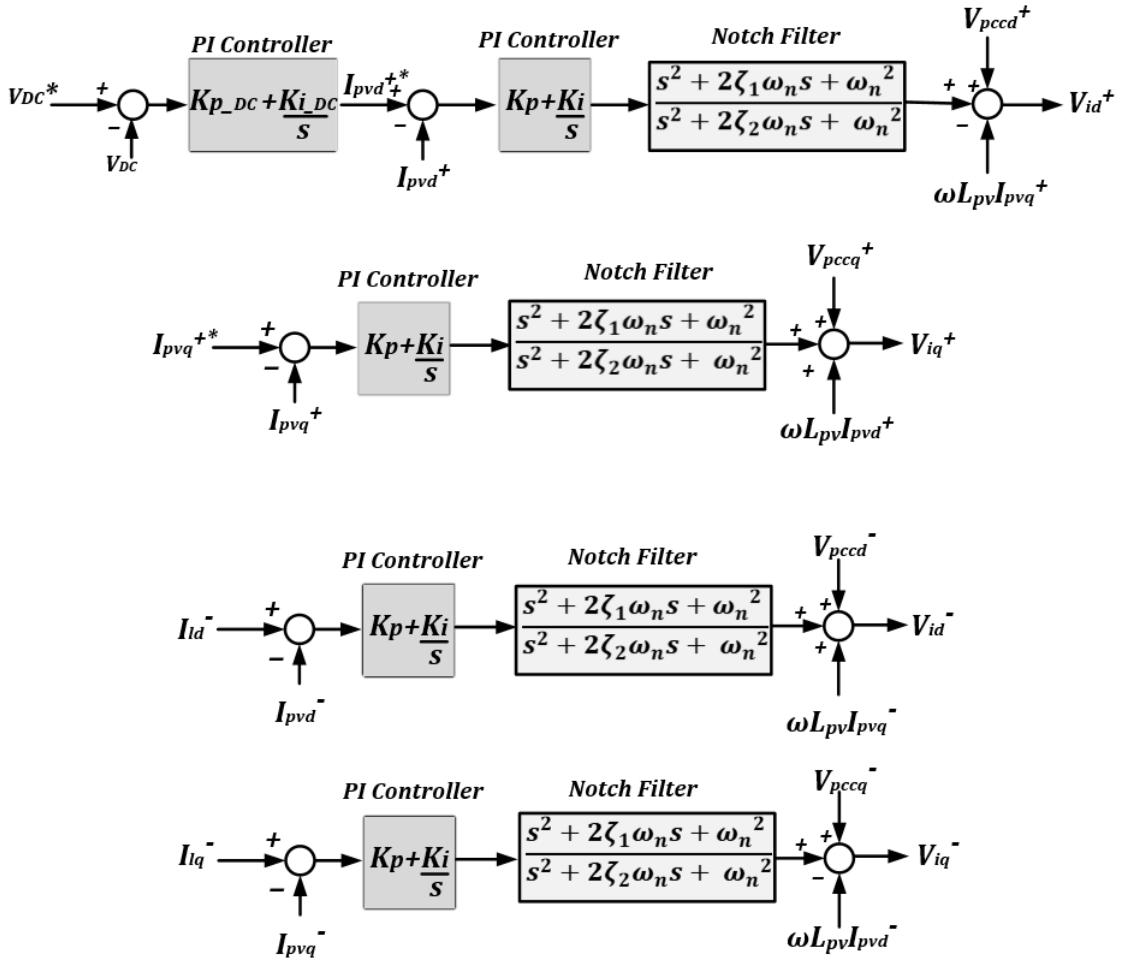

(b)

Figure 5:4: Unbalanced load compensation with PV inverter (a) complete DG system layout (b) DC voltage and dq-current control loops

5.4.2 Maximum Inverter Current

A limiting factor on the PV inverter unbalanced load compensation scheme is the rating of the inverter itself. An unbalanced load current, $i_l(t)$ consisting of both positive and negative sequence components is mathematically represented by:

$$i_l(t) = |I^+|\left(\cos\left(\omega t + \varphi^+ + q\frac{2\pi}{3}\right) + j\sin\left(\omega t + \varphi^+ + q\frac{2\pi}{3}\right)\right) +$$

$$|I^-|\left(\cos\left(-\omega t + \varphi^- + q\frac{2\pi}{3}\right) + j\sin\left(-\omega t + \varphi^- + q\frac{2\pi}{3}\right)\right), \quad (5.34)$$

where $q = 0, -1, +1$ for phases a, b and c respectively while the sums $\omega t + \varphi^+$ and $-\omega t + \varphi^-$ are the positive and negative sequence angles respectively denoted as θ^+ and θ^-.

The phase ‘a’ current through the inverter may be expressed in the stationary reference frame as:

$$i_a = \sqrt{I^{+2} + I^{-2} + 2\, I^{+} I^{-} \cos \alpha}, \tag{5.35}$$

where I^{+}, $I^{-}$are the magnitudes of the positive and negative sequence current components expressed as:

$$I^{+} = \sqrt{{I_{pvd}}^{+2} + {I_{pvq}}^{+2}} \tag{5.36}$$

and

$$I^{-} = \sqrt{{I_{pvd}}^{-2} + {I_{pvq}}^{-2}}. \tag{5.37}$$

The angle, α is given by:

$$\alpha = \theta^{+} + \theta^{-} - \varphi', \tag{5.38}$$

where

$$\varphi' = \tan^{-1} \frac{{v_q}^{+}}{{v_d}^{+}} + \tan^{-1} \frac{{v_q}^{-}}{{v_d}^{-}}. \tag{5.39}$$

The peak value for i_a occurs when:

$$\theta^{+} + \theta^{-} = \varphi'. \tag{5.40}$$

Substituting Equs. (5.36) - (5.40) into Equ. (5.35), the maximum current, I_{max} becomes:

$$I_{max} = \sqrt{{I_{pvd}}^{+2} + {I_{pvq}}^{+2} + {I_{pvd}}^{-2} + {I_{pvq}}^{-2} + 2\sqrt{{I_{pvd}}^{+2} + {I_{pvq}}^{+2}}\sqrt{{I_{pvd}}^{-2} + {I_{pvq}}^{-2}}}. \tag{5.41}$$

The maximum current limit on the inverter is uniform across the three-phases. Therefore, the phase A maximum current analysed is applicable to phases B and C. This sets a limit on the amount of negative sequence current the PV inverter is able to compensate. A safety margin of 125% is usually provided before activation of overcurrent devices [136]. Since the primary function of any PVDG is to generate active power, preference will be given to supplying active loads.

This leaves only 25% of the maximum current available for unbalanced load compensation.

5.4.3 Simulation studies

The simulation in section 5.3.3 is repeated to show the performance of the PV inverter unbalanced load compensation scheme on the DG system parameters. The maximum PV inverter current, I_{max} determined with Equ. (3.27) in chapter 3 is 215 A. A 20% increase above this value is set as the maximum inverter current limit, i.e. 258 A.

With the PV compensator activated at *t = 9 seconds*, the PCC voltage in Fig. 5.5 (a) is balanced with a VUF of 0.1% seen in Fig. 5.5 (b). The unbalance at the PCC is mitigated by the PV current, supplying an unbalanced load as seen in Fig. 5.5 (c). From the figure, it can be seen that the current is close to the boundary of the maximum value I_{max}.

The current response for the biomass generator in Fig. 5.5 (d) shows an initial supply of unbalanced current immediately load b is connected. This, however, lasts for approximately 0.1 *seconds* and the biomass returns to its initial state of positive sequence current supply.

However, the interactions of the currently balanced PCC voltage and the unbalanced PCC current form oscillating active and reactive powers shown in Fig. 5.5 (e). These oscillations have increased significantly due to the largely unbalanced PV current in Fig. 5.5 (c). Conversely, setting the PV current references to eliminate these power oscillations will cause asymmetry in the PCC voltage. As a result, careful consideration of the control objective should be made, depending on the grid code specifications.

The electromagnetic and mechanical torques of the biomass generator in Fig. 5.5 (f) reach equilibrium at time, *t = 9.1 seconds,* indicating that the machine acceleration is constant at the synchronous speed.

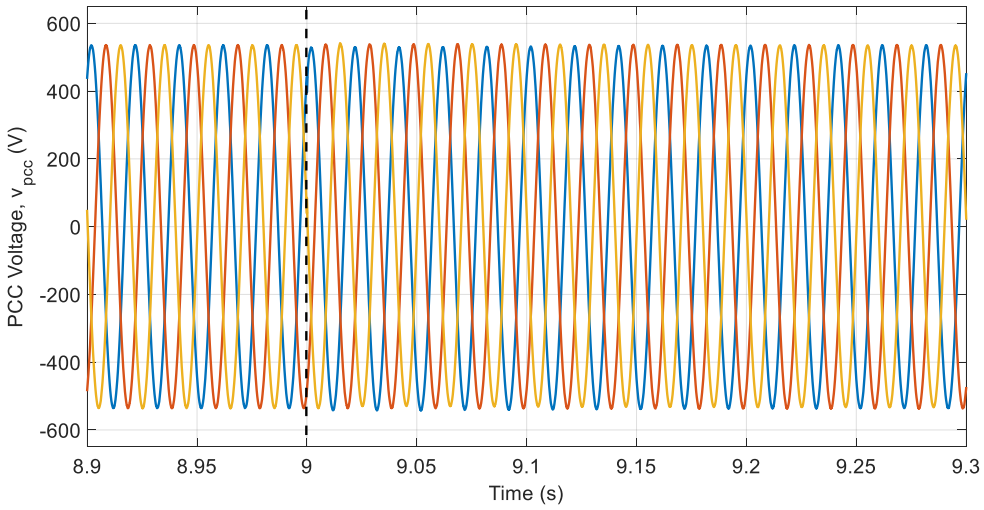
PCC Voltage, v_{pcc} (V)
600
400
200
0
-200
-400
-600
8.9
8.95
9
9.05
9.1
9.15
9.2
9.25
9.3
Time (s)

(a)

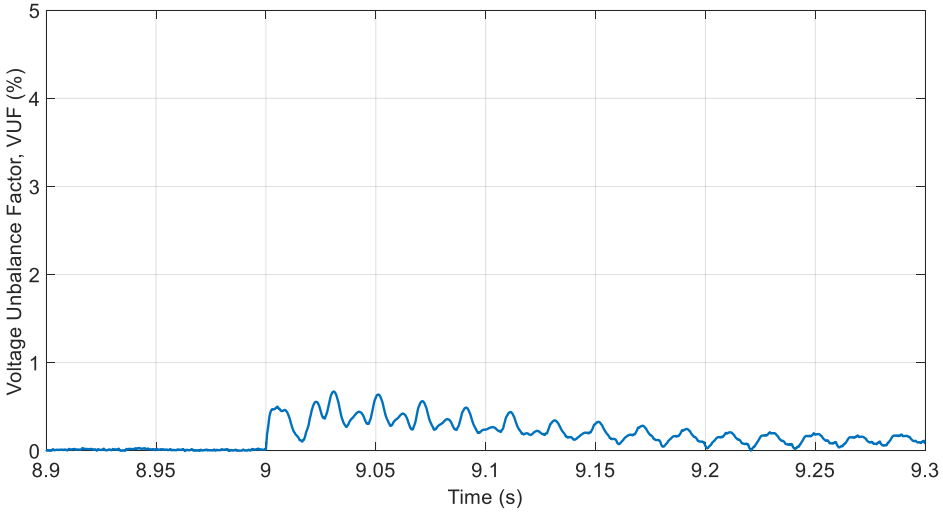
Voltage Unbalance Factor, VUF (%)
5
4
3
2
1
0
8.9
8.95
9
9.05
9.1
9.15
9.2
9.25
9.3
Time (s)

(b)

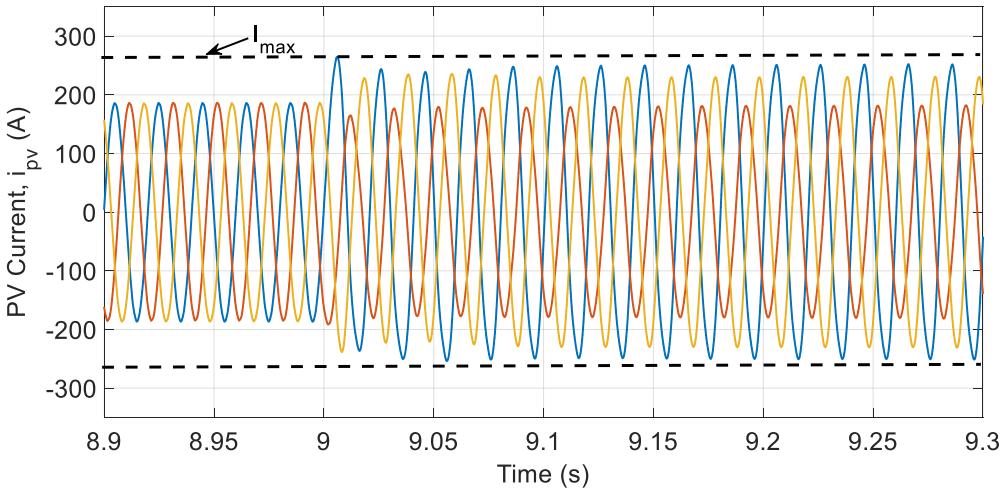
I max
300
200
100
0
-100
-200
-300
PV Current, i pv (A)
8.9
8.95
9
9.05
9.1
9.15
9.2
9.25
9.3
Time (s)

(c)

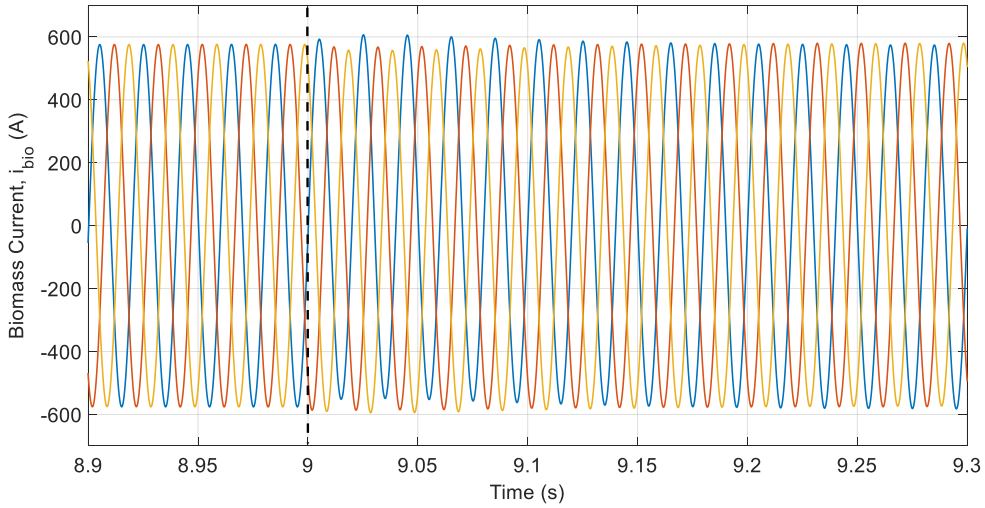
600
400
200
0
-200
-400
-600
Biomass Current, i bio (A)
8.9
8.95
9
9.05
9.1
9.15
9.2
9.25
9.3
Time (s)

(d)

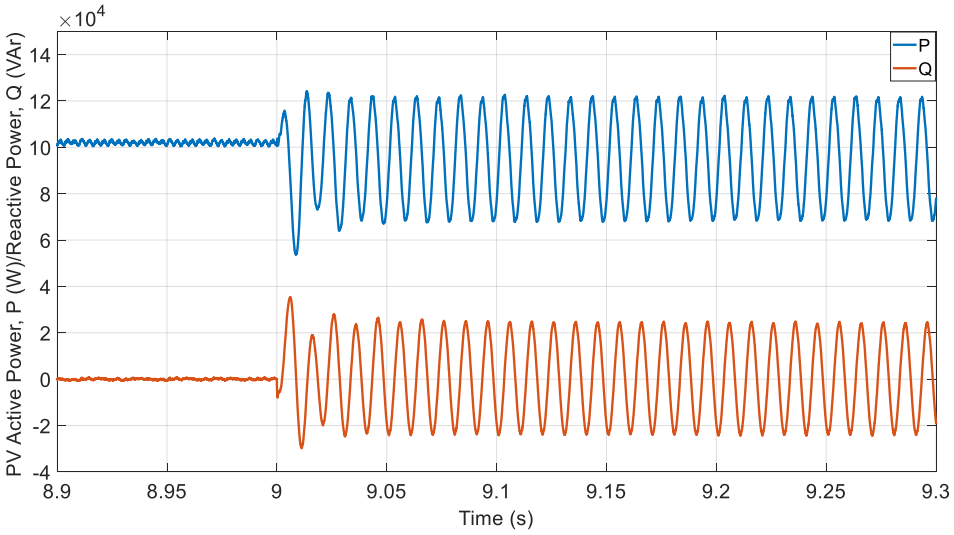

(e)

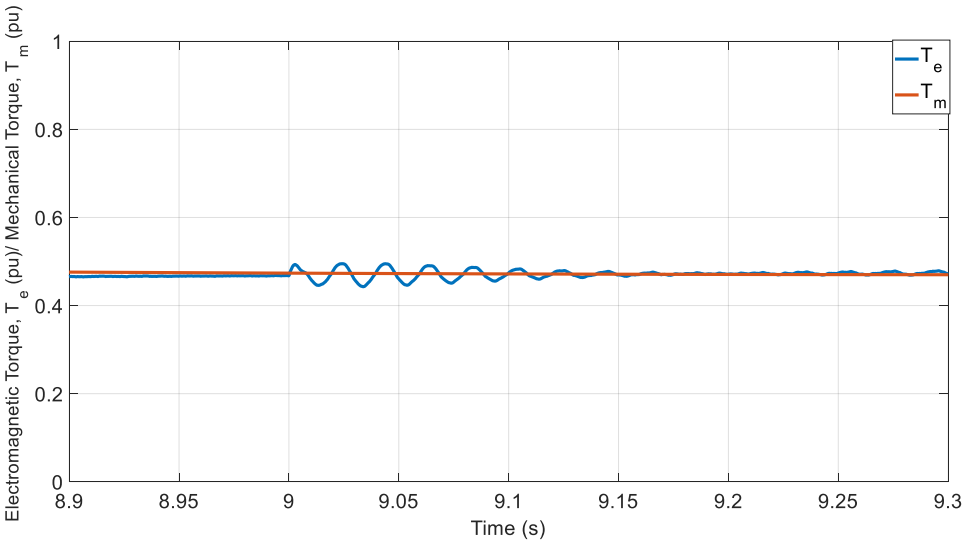

(f)

Figure 5:5: Hybrid Biomass-PV DG with proposed compensator under unbalanced loads (a) PCC voltage (b) VUF (c) PV current (d) Biomass current (e) PV active power output (f) Machine Torques

5.4.4 Limitations of the Unbalanced Load Compensation Scheme

In the preceding section, unbalanced load compensation using the PV inverter has resulted in improved responses for the PCC voltage, biomass current, as well as the generator electromagnetic torque. The unbalance, however, appears as oscillations in the PV active and reactive powers, due to the largely unbalanced PV compensating current. The unbalanced nature of the PV active power upsets the power balance at the DC link, resulting in fluctuations in the DC link voltage,

as seen in Fig. 5.6. As the ripple requirement on the DC link is generally at a maximum of 2% [100], this compensation scheme may not meet the requirement in applications where stringent rules are applied to the DC link voltage. A possible solution is to use capacitors with higher ratings, which can limit the amount of ripple at the DC link. Alternatively, other compensation schemes such as static compensators (STATCOM) could be employed if the maximum voltage ripple requirement is exceeded.

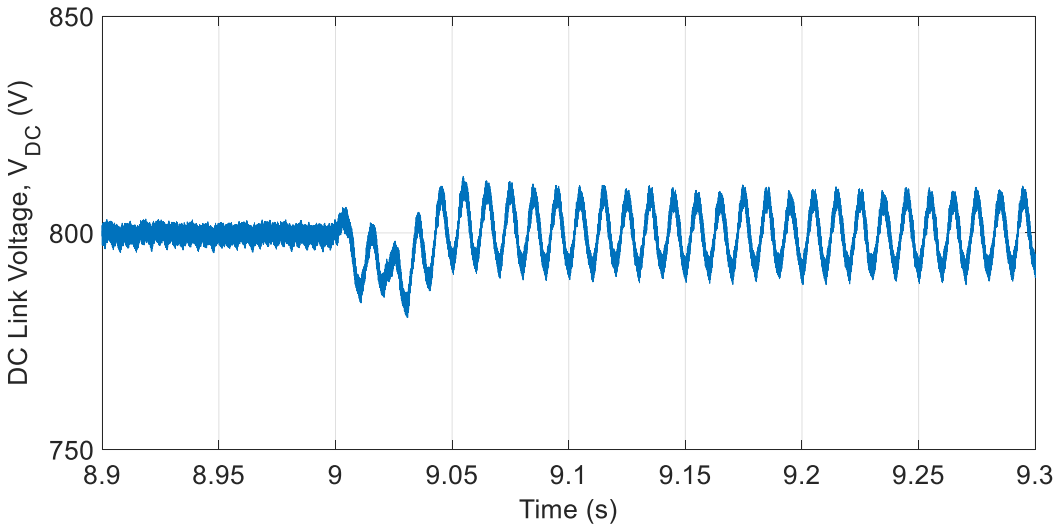

Figure 5:6: DC link voltage

5.5 Conclusion

The chapter has presented the detrimental effects of unbalanced loading on the hybrid biomass-PV distributed generation system. A solution involving modification of the PV inverter control structure has been proposed, where the PV inverter is controlled to supply a compensating negative sequence current. The result is a balanced PCC voltage, balanced biomass current and elimination of oscillations in the electromagnetic torque. Due to the elimination of pulsations in the electromagnetic torque, the rotor speed remains constant at the generator synchronous speed. However, unbalanced load compensation was achieved at the expense of PV power oscillations in both active and reactive power. The active power oscillations cause fluctuations in the DC link voltage, which may exceed the ripple requirement.

Chapter 6 Control of Grid-Connected PV Distributed Generator under Unbalanced Grid Voltage

6.1 Introduction

In Chapter 5, unbalanced loads at the PCC have been shown to affect the operational performance of the hybrid Biomass-PV DG system due to the negative sequence currents. Unbalanced loads may also cause voltage unbalance, which can be detrimental to the normal operation of grid–connected inverters. Apart from unbalanced loads, there are other causes resulting in voltage unbalance; the major one is grid faults: faults occurring in one or two phases that are shorted to ground or to each other. Under such faulty conditions, any grid-connected VSIs would inject unbalanced and distorted currents into the network, which may result in high losses and overcurrent, causing protection devices of inverters to trip. Disconnection of grid-tie inverters under such conditions may not be an option because, with an increasing proportion of power being generated by renewable sources, they have become indispensable to the power network. Grid codes now require these systems to ride through unbalanced grid faults without interruption [137].

Two objectives are set to ensure robust operation of grid-tie inverters under unbalanced conditions [31]; one is to mitigate unbalanced voltages along the distribution lines and the other is by injecting a set of unbalanced currents at the PCC. The former may rely on injection of negative sequence voltage using devices such as dynamic voltage compensators [138, 139]. The latter, however, poses more challenges. This is because, while controlling the instantaneous power exchanges with the grid, the interaction of injected current with unbalanced voltage at the PCC (three-phase three wire case) inevitably induces real and reactive power oscillations. Also, DC-link voltage fluctuations due to the instantaneous input and output power mismatch may exacerbate the situation. Properly regulating the injected unbalanced current in the grid lines can be crucial in alleviating the power oscillations. This relies on two aspects: estimating the reference current to be injected according to specific control objectives, and designing current control laws which ensure accurate tracking of the calculated reference current value by the grid connected inverter.

The control objectives can be many and some common cases are discussed in detail in [31], which include: controlling the average real or reactive power, cancellation of active power oscillations while ensuring delivery of maximum generated real power and grid required reactive power, or the cancellation of reactive power oscillations, etc. These result in different overall performance of the inverters and their interactions with the grid under unbalanced conditions may not be desirable for certain application conditions. An adequate criterion should ensure accurate control of the dominant variables, for example, the PV source generated power, while maintaining the other variables within the grid tolerated ranges. Also importantly, the inverter supplied current must be constrained to prevent overcurrent tripping. It is possible to deduce new alternative control strategies based on the existing ones by imposing certain constraints. The resultant reference currents may be more suitable to be injected into the grid by the grid-connected inverters.

This chapter, therefore, proposes a new optimised flexible power control (OFPC) scheme based on the principle of the constrained multi-objective optimisation problem (MOOP). The objective is to ensure that the PV inverter supplies all generated power to the grid, whilst simultaneously dealing with the conflicting requirements of suppressing real and reactive power oscillations. Under such a control law, the PV inverter should be able to ride through unbalanced grid faults. A single cost function with weightings and constraints will be defined. The constraints set will also limit the DC-bus voltage ripple and restrict the inverter instantaneous phase current magnitude to be below its rated level. A genetic algorithm (GA) will be used to search for the optimised solution for this cost function. The performance of the proposed method is validated through simulation studies and compared with two other major unbalanced current control schemes for the grid-connected inverters.

6.2 PV Active and Reactive Powers under Unbalanced Grid Conditions

The analysis that will be carried out in this chapter is based on the system presented in Fig.3.1 of Chapter 3, and the following assumptions are made:

- The PV generator has a slow dynamic and the weather conditions are not changed; hence, energy output to the grid remains constant during a certain period.
- The distribution network has three-phase three-wire connections, hence there is no zero sequence current flow under unbalanced conditions.

In Chapter 5, the instantaneous values of the active and reactive powers of the PV inverter, P and Q, under unbalanced PCC voltages, together with their associated oscillatory terms, P_c, P_s, Q_c and Q_s are specified in Equs. (5.14)-(5.19), and these form the basis for the reference current generation scheme presented in this chapter. The equations are revisited below:

$$P = \frac{3}{2}\left(v_d{}^{+}i_d{}^{+} + v_q{}^{+}i_q{}^{+} + v_d{}^{-}i_d{}^{-} + v_q{}^{-}i_q{}^{-}\right), \tag{6.1}$$

$$P_c = \frac{3}{2}\left(v_d{}^{-}i_d{}^{+} + v_q{}^{-}i_q{}^{+} + v_d{}^{+}i_d{}^{-} + v_q{}^{+}i_q{}^{-}\right), \tag{6.2}$$

$$P_s = \frac{3}{2}\left(v_q{}^{-}i_d{}^{+} - v_d{}^{-}i_q{}^{+} - v_q{}^{+}i_d{}^{-} + v_d{}^{+}i_q{}^{-}\right), \tag{6.3}$$

$$Q = \frac{3}{2}\left(v_q{}^{+}i_d{}^{+} - v_d{}^{+}i_q{}^{+} + v_q{}^{-}i_d{}^{-} - v_d{}^{-}i_q{}^{-}\right), \tag{6.4}$$

$$Q_c = \frac{3}{2}\left(v_q{}^{-}i_d{}^{+} - v_d{}^{-}i_q{}^{+} + v_q{}^{+}i_d{}^{-} - v_d{}^{+}i_q{}^{-}\right) \tag{6.5}$$

and

$$Q_s = \frac{3}{2}\left(-v_d{}^{-}i_d{}^{+} - v_q{}^{-}i_q{}^{+} + v_d{}^{+}i_d{}^{-} + v_q{}^{+}i_q{}^{-}\right). \tag{6.6}$$

Under unbalanced grid faults, grid codes require all the PV source generated active power, P to be delivered to the grid [140] and it should ideally be ripple-free. Depending on the types of renewable energy power generators and grid conditions, grid codes may also require a given reactive power, *Q* to be injected to the grid [31]. Such objectives rely on proper evaluations of inverter reference currents. From Equs. (6.1) to (6.6), there are only 4 current elements, $i_d{}^{\pm}$ and $i_q{}^{\pm}$, available for controlling six power terms. This gives a limited degree of freedom in the current elements which are the control variables, making it difficult to suppress both *P* and *Q* fluctuations concurrently while ensuring good performance average real and reactive power control. The choice of the power parameters to be controlled is, therefore, dependent on the set control objectives.

In low voltage distribution networks, this may be to ensure that the active power, *P* equals the PV source generated power less the inverter losses. For unity power factor operation, *Q* is set to zero, hence no reactive power flows between the inverter and the grid. Depending on the specific requirements of the grid code, the objectives may also be the injection of balanced currents, or the elimination of active/reactive power harmonics. Several unique reference current control strategies have been reported, and these are described below.

6.2.1 Reference Current Generation for Different Power Control Schemes

In the following sections, four different control schemes for generating the reference current components according to the required P and Q values are discussed. These include: the balanced positive-sequence control (BPSC) method , constant active power control (CAPC) method, constant reactive power control (CRPC) method and flexible power control (FPC) method [141-143]. Their various control criteria lead to different features, as outlined below.

6.2.1.1 Balanced Positive-Sequence Control (BPSC)

This method intends to control only real and reactive powers by injecting positive sequence component into the grid [31, 142, 144]. The reference current d-q components are determined by considering only Equs. (6.1) and (6.4), with no negative sequence current components considered. Thus by setting the reference real and reactive powers, P^* and Q^* , in these equations, the reference current vector elements are given as:

$$\begin{bmatrix} {i_d}^{+*} \\ {i_q}^{+*} \end{bmatrix} = -\frac{1}{1.5\left[\|{v_d}^+\|^2+\|{v_q}^+\|^2\right]}\begin{bmatrix} -{v_d}^+ & -{v_q}^+ \\ -{v_q}^+ & {v_d}^+ \end{bmatrix}\begin{bmatrix} P^* \\ Q^* \end{bmatrix}. \tag{6.7}$$

For unity power factor operation, Q^* is zero, so the reference currents are reduced to:

$$\begin{bmatrix} {i_d}^{+*} \\ {i_q}^{+*} \end{bmatrix} = \frac{P^*}{1.5\left[\|{v_d}^+\|^2+\|{v_q}^+\|^2\right]}\begin{bmatrix} {v_d}^+ \\ {v_q}^+ \end{bmatrix}. \tag{6.8}$$

Substituting the reference currents in Equ. (6.8) into Equs. (6.2), (6.3), (6.5) and (6.6), the oscillatory power terms for the BPSC method become:

$$P_c = \frac{P^*\left({v_d}^+{v_d}^- + {v_q}^+{v_q}^-\right)}{\|{v_d}^+\|^2+\|{v_q}^+\|^2}, \tag{6.9}$$

$$P_s = \frac{P^*(v_d{}^+ v_q{}^- - v_q{}^+ v_d{}^-)}{\|v_d{}^+\|^2 + \|v_q{}^+\|^2}, \tag{6.10}$$

$$Q_c = \frac{P^*(v_d{}^+ v_q{}^- - v_q{}^+ v_d{}^-)}{\|v_d{}^+\|^2 + \|v_q{}^+\|^2} \tag{6.11}$$

and

$$Q_s = \frac{-P^*(v_d{}^+ v_d{}^- + v_q{}^+ v_q{}^-)}{\|v_d{}^+\|^2 + \|v_q{}^+\|^2}. \tag{6.12}$$

Since in Equ. (6.8) only the positive sequence reference current elements are evaluated for power control, the oscillatory components of *P* and *Q* expressed in the above equations are not regulated.

It is clear that this method can deliver exactly the required instantaneous real and reactive powers to the grid by controlling the balanced sinusoidal reference currents. However, this power controllability is achieved at the expense of leaving oscillatory terms, P_c, P_s, Q_c and Q_s given in Equs. (6.9) - (6.12) respectively, unconstrained. Consequently, the powers exchanged between the PV inverter and grid are oscillatory, containing harmonics at twice the grid frequency. This may not be acceptable for many applications, particularly for large power inverters in the grid which may cause system operation instability.

6.2.1.2 Constant Active Power Control (CAPC)

This scheme aims to eliminate the oscillations in the active power [31, 142, 144]. The active power reference, P^* in Equ. (6.1) is set to the desired value while the reference reactive power, Q^* in Equ. (6.4) and the two real power oscillatory terms, P_c and P_s in Equs. (6.2) and (6.3) respectively are all set to zero. This scheme does not control the reactive power oscillation terms, Q_c and Q_s. Hence, the reference current components can be expressed as:

$$\begin{bmatrix} i_d{}^{+*} \\ i_q{}^{+*} \\ i_d{}^{-*} \\ i_q{}^{-*} \end{bmatrix} = \begin{bmatrix} v_d{}^+ & v_q{}^+ & v_d{}^- & v_q{}^- \\ v_q{}^+ & -v_d{}^+ & v_q{}^- & -v_d{}^- \\ v_d{}^- & v_q{}^- & v_d{}^+ & v_q{}^+ \\ v_q{}^- & -v_d{}^- & -v_q{}^+ & v_d{}^+ \end{bmatrix}^{-1} \begin{bmatrix} P^* \\ 0 \\ 0 \\ 0 \end{bmatrix}. \tag{6.13}$$

Simplifying Equ. (6.13), the reference currents can be computed as:

$$\begin{bmatrix} {i_d}^{+*} \\ {i_q}^{+*} \\ {i_d}^{-*} \\ {i_q}^{-*} \end{bmatrix} = \frac{P^*}{1.5\left[\|{v_d}^+\|^2+\|{v_q}^+\|^2-\left[\|{v_d}^-\|^2+\|{v_q}^-\|^2\right]\right]} \begin{bmatrix} {v_d}^+ \\ {v_q}^+ \\ -{v_d}^- \\ -{v_q}^- \end{bmatrix}. \quad (6.14)$$

Substituting the currents in Equ. (6.14) into Equs. (6.2), (6.3), (6.5) and (6.6), the oscillatory power components become:

$$P_c = 0, \quad (6.15)$$

$$P_s = 0, \quad (6.16)$$

$$Q_c = \frac{2P^*\left({v_d}^+{v_q}^- - {v_q}^+{v_d}^-\right)}{\|{v_d}^+\|^2+\|{v_q}^+\|^2-\left[\|{v_d}^-\|^2+\|{v_q}^-\|^2\right]} \quad (6.17)$$

and

$$Q_s = \frac{-2P^*\left({v_d}^+{v_d}^- + {v_q}^+{v_q}^-\right)}{\|{v_d}^+\|^2+\|{v_q}^+\|^2-\left[\|{v_d}^-\|^2+\|{v_q}^-\|^2\right]}. \quad (6.18)$$

It is clear from Equs. (6.15) - (6.18), that this scheme, unlike the previous BPSC method, injects unbalanced currents into the grid, to regulate the real and reactive powers and also eliminate real power oscillations. However, it leads to reactive power oscillations, even when its reference value is zero. The injection of unbalanced current is a serious drawback, as it may cause overcurrent tripping of the grid-connected inverters. Moreover, this method exclusively favours damping of real power oscillations over the reactive power oscillations, which can cause significant losses, particularly in the case of large power systems [6].

6.2.1.3 Constant Reactive Power Control (CRPC)

This control strategy is aimed at eliminating the oscillations in the reactive power [31, 142, 144]. The active power reference, P^* in Equ. (6.1) is set to the desired value while the reference reactive power, Q^* in Equ. (6.4) and the two reactive power oscillatory terms, Q_C and Q_S in Equs. (6.5) and (6.6) are set to zero. This renders the active powers, P_C and P_S uncontrolled. The corresponding current references are expressed as :

$$\begin{bmatrix} {i_d}^{+*} \\ {i_q}^{+*} \\ {i_d}^{-*} \\ {i_q}^{-*} \end{bmatrix} = \begin{bmatrix} {v_d}^+ & {v_q}^+ & {v_d}^- & {v_q}^- \\ {v_q}^+ & -{v_d}^+ & {v_q}^- & -{v_d}^- \\ {v_q}^- & -{v_d}^- & {v_q}^+ & -{v_d}^+ \\ -{v_d}^- & -{v_q}^- & {v_d}^+ & {v_q}^+ \end{bmatrix}^{-1} \begin{bmatrix} P^* \\ 0 \\ 0 \\ 0 \end{bmatrix}. \quad (6.19)$$

Upon simplification of Equ. (6.19), the reference current elements are given as:

$$\begin{bmatrix} {i_d}^{+*} \\ {i_q}^{+*} \\ {i_d}^{-*} \\ {i_q}^{-*} \end{bmatrix} = \frac{P^*}{1.5\left[\|{v_d}^+\|^2+\left\|{v_q}^+\right\|^2+\left[\|{v_d}^-\|^2+\left\|{v_q}^-\right\|^2\right]\right]} \begin{bmatrix} {v_d}^+ \\ {v_q}^+ \\ {v_d}^- \\ {v_q}^- \end{bmatrix}. \quad (6.20)$$

Substituting the reference current elements in Equ. (6.20) into Equs. (6.2), (6.3), (6.5) and (6.6), the oscillatory power components become:

$$P_c = \frac{2P^*\left({v_d}^+{v_d}^- + {v_q}^+{v_q}^-\right)}{\|{v_d}^+\|^2+\left\|{v_q}^+\right\|^2+\left[\|{v_d}^-\|^2+\left\|{v_q}^-\right\|^2\right]}, \quad (6.21)$$

$$P_s = \frac{2P^*\left({v_d}^+{v_q}^- - {v_d}^-{v_q}^+\right)}{\|{v_d}^+\|^2+\left\|{v_q}^+\right\|^2+\left[\|{v_d}^-\|^2+\left\|{v_q}^-\right\|^2\right]}, \quad (6.22)$$

$$Q_c = 0 \quad (6.23)$$

and

$$Q_s = 0. \quad (6.24)$$

Equs. (6.21) - (6.24) confirm the presence of active power ripples, P_c and P_s whilst the reactive power oscillations are removed. Similar to the previous method, this method also injects unbalanced currents to control P and Q, while supressing only the reactive power harmonics. The CRPC method gives rise to similar problems as those of the CAPC scheme. Additionally, tracking the unbalanced reference currents requires complicated control algorithms.

6.2.1.4 Flexible Power Control (FPC)

This method of current control is derived by combining the objectives of the CAPC and CRPC methods, namely to obtain both constant active power and constant reactive power controls simultaneously. Hence, the reference current d-q element expressions given by Equs. (6.14) for CAPC and (6.20) for CRPC can be combined into a single equation with the introduction of a control factor, k, in the range $-1 \leq k \leq 1$ [142, 144, 145]. This enables the suppression of both active and reactive power oscillations whilst simultaneously maintaining control of instantaneous active and reactive powers. The reference current elements are therefore expressed as:

$$\begin{bmatrix} {i_d}^{+*} \\ {i_q}^{+*} \\ {i_d}^{-*} \\ {i_q}^{-*} \end{bmatrix} = \frac{P^*}{1.5\left[\|{v_d}^+\|^2+\left\|{v_q}^+\right\|^2+k\left[\|{v_d}^-\|^2+\left\|{v_q}^-\right\|^2\right]\right]} \begin{bmatrix} {v_d}^+ \\ {v_q}^+ \\ k{v_d}^- \\ k{v_q}^- \end{bmatrix}. \tag{6.25}$$

When k is -1, the active power oscillations are eliminated, as the reference currents are identical to Equ. (6.14) in CAPC. With k set to 0, a balanced current is injected into the grid since all negative sequence components are eliminated, as in Equ. (6.8) of BPSC. Finally, setting k to 1 removes reactive power oscillations, as the reference currents are the same as Equ. (6.20) in CRPC.

Using the FPC method, the total amount of active and reactive power ripples, P_{rip} and Q_{rip} , can be computed by substituting the currents expressed in Equ. (6.25) into the oscillatory power expressions, Equ. (6.2), (6.3), (6.5) and (6.6), for a given k value as:

$$P_{rip} = \frac{P^*(1+k)({v_d}^+{v_d}^-+{v_q}^+{v_q}^-+{v_d}^+{v_q}^--{v_d}^-{v_q}^+)}{\|{v_d}^+\|^2+\left\|{v_q}^+\right\|^2+k\left[\|{v_d}^-\|^2+\left\|{v_q}^-\right\|^2\right]} \tag{6.26}$$

and

$$Q_{rip} = \frac{P^*(1-k)({v_d}^+{v_q}^--{v_d}^-{v_q}^+-{v_d}^+{v_d}^--{v_q}^+{v_q}^-)}{\|{v_d}^+\|^2+\left\|{v_q}^+\right\|^2+k\left[\|{v_d}^-\|^2+\left\|{v_q}^-\right\|^2\right]}. \tag{6.27}$$

Within the feasible range of values for k ($-1 \le k \le 1$), the real and reactive power oscillations, P_{rip} and Q_{rip} can be evaluated using Equs (6.26) and (6.27) as:

$$P_{rip} = \begin{cases} 0 & k = -1 \\ \dfrac{P^*({v_d}^+{v_d}^-+{v_q}^+{v_q}^-+{v_d}^+{v_q}^--{v_d}^-{v_q}^+)}{\|{v_d}^+\|^2+\left\|{v_q}^+\right\|^2} & k = 0 \\ \dfrac{2P^*({v_d}^+{v_d}^-+{v_q}^+{v_q}^-+{v_d}^+{v_q}^--{v_d}^-{v_q}^+)}{\|{v_d}^+\|^2+\left\|{v_q}^+\right\|^2+\left[\|{v_d}^-\|^2+\left\|{v_q}^-\right\|^2\right]} & k = +1 \end{cases} \tag{6.28}$$

and

$$Q_{rip} = \begin{cases} \dfrac{2P^*({v_d}^+{v_q}^--{v_d}^-{v_q}^+-{v_d}^+{v_d}^--{v_q}^+{v_q}^-)}{\|{v_d}^+\|^2+\left\|{v_q}^+\right\|^2-\left[\|{v_d}^-\|^2+\left\|{v_q}^-\right\|^2\right]} & k = -1 \\ \dfrac{P^*({v_d}^+{v_q}^--{v_d}^-{v_q}^+-{v_d}^+{v_d}^--{v_q}^+{v_q}^-)}{\|{v_d}^+\|^2+\left\|{v_q}^+\right\|^2}. & k = 0 \\ 0 & k = +1 \end{cases} \tag{6.29}$$

Since both Equs. (6.28) and (6.29) are functions of k, the ideal k value should minimise both P_{rip} and Q_{rip} simultaneously while confined to the range of -1 to +1. With a non-zero k value, the inverter injects unbalanced three phase currents

to the grid. The instantaneous phase current values need to be monitored and clamped if necessary to prevent overcurrent tripping of the inverter. It is therefore essential that a current constraint must be applied while searching for the optimised value for k.

6.3 Optimised Flexible Power Control (OFPC) Scheme

The strategy used in the flexible power control (FPC) scheme in section 6.2.1.4 can be defined as a constrained multi-objective optimisation problem (MOOP), since it involves two conflicting objective functions, $P_{rip}$and Q_{rip} that must be minimised simultaneously through modification of the control variable, k. The solution to this problem leads to the optimised value for k that can simultaneously satisfy the requirements for both the active and reactive powers.

There are also constraints which have not been considered by the previously described schemes but are important for grid-connected inverters under unbalanced operations. These include the percentage limit of the DC-bus voltage ripple relative to the required average voltage level and the maximum value of the reference current. Combining these constraints and applying the principle of MOOP gives rise to a new method – the optimised flexible power control (OFPC).

6.3.1 Application of Multi-Objective Optimisation Problem (MOOP)

The MOOP is a well-known technique applied widely in the fields of science, engineering and economics. It concerns an area of multiple decision making, where a problem can involve multiple objective functions that need to be optimised simultaneously. One approach involves converting the MOOP into a single problem by using a weighted sum of the multiple objective functions [146]. All possible solutions to this sum lead to a set of optimal choices for the original problem, forming the Pareto front [147]. The search for the optimal solution can be further narrowed through the introduction of constraints.

As shown in the previous section, it may not be possible to find a specific value of k which is optimal to both objective functions specified in Equs. (6.26) and (6.27).Thus, the MOOP technique can be applied, where a single objective function, $F(k)$ is defined as the sum of the two objective functions. The objective is to minimise $F(k)$, given as:

$$\min F(k) = [f_1(k), f_2(k)] \tag{6.30}$$

$$k \in X$$

subject to:

$$k \in C,$$

where:

k is the optimisation decision variable,

$f_1(k)$ is the active power ripple defined in Equ. (6.26),

$f_2(k)$ is the reactive power ripple defined in Equ. (6.27)

and C are the constraints of the optimisation.

A preference based method is employed to convert this MOOP into a single objective optimisation problem using preference factors, w_1 and w_2 assigned to each objective [147]. Thus:

$$F(k) = w_1 f_1(k) + w_2 f_2(k), \tag{6.31}$$

where, w_1 and w_2 are the assigned weights of the objective functions, $f_1(k)$ and $f_2(k)$ respectively, summing up to 1. Each set of w_1, w_2 results in an optimised k value. This k value leads to a set of reference current values optimal for the corresponding unbalanced voltage values and power requirements.

The Pareto solution to $F(k)$ in Equ. (6.31) is shown in Fig. 6.1, with $f_1(k)$ and $f_2(k)$ normalised to 1. Setting k to -1 leads to complete attenuation of the active power ripple in $f_1(k)$. Similarly, a value of +1 for k eliminates reactive power ripple in $f_2(k)$. In between the two extremes of -1 to +1 are solutions to k that can suppress both $f_1(k)$ and $f_2(k)$ simultaneously, albeit incompletely. The optimised value for k will depend on the constraints of the optimisation, as described in section 6.3.2.

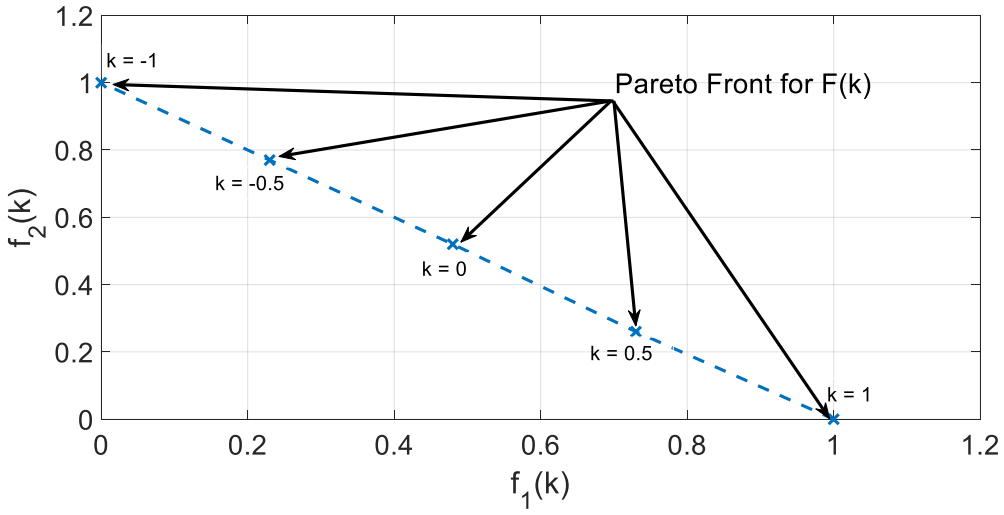

Figure 6:1: Pareto solutions for objective function, F(k)

6.3.2 Optimised Flexible Power Control (OFPC) with Constraints

There are constraints defined to ensure that the optimal value for k falls within the region of feasibility, according to a set of conditions. Therefore, two constraints are chosen based on the level of DC link voltage fluctuation and the current limitation of the inverter. Details are described as follows:

(1) DC link voltage fluctuation: Under unbalanced PCC voltage conditions, the fluctuations in the instantaneous active power cause oscillations in the DC link voltage. The level of low frequency DC link voltage fluctuation, ΔV directly relates to the maximum value of the active power ripple, $P_{rip(\max)}$ through the following [31, 141]:

$$P_{rip(max)} = 2\omega CV\Delta V, \tag{6.32}$$

where ω is the grid frequency, *C* is the capacitance of the DC link capacitor and *V* is the average DC link voltage. The choice for the value of *C* has a direct effect on the DC voltage variation; a high value reduces the magnitude of the ripple, but results in increased size and cost. The maximum voltage ripple is generally limited to 1 to 2% of the DC link voltage [100, 148, 149].

For a given value of *C*, the active power ripple can be constrained based on:

$$P_{rip} \leq P_{rip(max)}. \tag{6.33}$$

Substituting Equs. (6.26) and (6.32) into Equ. (6.33), the range for k on the basis of this constraint is:

$$k \leq \frac{\omega CV\Delta V\left[\|v_d^+\|^2+\|v_q^+\|^2\right]-P(v_d^+v_d^-+v_q^+v_q^-+v_d^+v_q^--v_d^-v_q^+)}{P(v_d^+v_d^-+v_q^+v_q^-+v_d^+v_q^--v_d^-v_q^+)-\omega CV\Delta V\left[\|v_d^-\|^2+\|v_q^-\|^2\right]}. \quad (6.34)$$

(2) Maximum inverter phase current: It is important to limit the magnitude of the inverter current to protect semiconductor devices in the inverter against excessive temperature rise. Equally important is to prevent activation of the overcurrent protection devices under conditions of transient current surge. Under the case of a phase voltage dip (any phase), the expression for per phase maximum current through the inverter, in the stationary reference frame, can be derived from Equ. (6.25) as:

$$I_{m(\max)} = \frac{P^*\sqrt{\|v_d^+\|^2+\|v_q^+\|^2+k^2\left[\|v_d^-\|^2+\|v_q^-\|^2\right]+2k\sqrt{\left[\|v_d^+\|^2+\|v_q^+\|^2\right]\left[\|v_d^-\|^2+\|v_q^-\|^2\right]}}}{1.5\left[\|v_d^+\|^2+\|v_q^+\|^2+k\left[\|v_d^-\|^2+\|v_q^-\|^2\right]\right]}, \quad (6.35)$$

where m represents the phases a, b, c. The derivation for $I_{m(\max)}$ is detailed in Appendix C.

The inverter rated current, I_{rated} is normally determined by the rated active power, P_{rated}, according to the connected PV generator under balanced conditions as:

$$I_{rated} = \frac{P_{rated}}{1.5V^+}, \quad (6.36)$$

where V^+ is the magnitude of the positive sequence voltage vector measured at the PCC and is given by:

$$V^+ = \sqrt{\|v_d^+\|^2 + \left\|v_q^+\right\|^2}. \quad (6.37)$$

To avoid tripping of protection devices due to overcurrent, the maximum current per phase in Equ. (6.35) should be set less than the rated current in Equ. (6.36), i.e:

$$I_{m(\max)} \leq I_{rated}. \quad (6.38)$$

The rated current may be increased beyond the PV maximum power point (MPP) current, as an allowance of 125% safety margin is usually implemented in sizing the inverter overcurrent level [136, 137].

For a large voltage unbalance factor expressed in Equ. (5.33), $I_{m(\max)}$ may exceed I_{rated}. Consequently, the active power reference, P^* should be reduced

to limit the inverter currents to the value of I_{rated}. The new reference for active power is determined from Equ. (6.36) as:

$$P^* = \frac{3}{2} I_{rated} V^+. \tag{6.39}$$

When there is no voltage imbalance, the negative sequence components, v_d^- and v_q^- are null. Since the quadrature positive sequence PCC voltage, v_q^+ is regulated to zero by PLL control, under normal conditions, $I_{m(\max)} = I_{rated}$ according to Equs. (6.35) and (6.36) respectively. Alternatively, when the level of voltage imbalance rises, v_d^- and v_q^-increase, causing the per phase inverter maximum current to rise, which may lead to tripping of overcurrent devices.

The DC link fluctuation and maximum inverter current constraints are both implemented in the reference current generation process, as will be described in section 6.3.5.

6.3.3 Choice of Objective Function Weights

The decision must also be made on whether w_1 and w_2 in Equ. (6.31) should be the same or different. Considering the empirical knowledge regarding the optimisation problem, differential weights are preferable [150]. The weighted sum in Equ. (6.31) uses a priori articulation of preferences, with the weights assigned directly based on their relative importance, as per the rating method [151]. The main criticism regarding this approach is its inherent difficulty in accurately determining the pareto front [147, 151]. It does, however, prove a useful tool for a single optimisation problem such as Equ. (6.31).

In terms of relative importance, the active power ripple function, $f_1(k)$ is prioritised over the reactive power ripple function, $f_2(k)$ therefore w_1 should be greater than w_2. However, the constraint based on the DC link fluctuations, ΔV already imposes a restriction on the decision variable, k which favours the minimisation of $f_1(k)$ in the objective function. For this reason, w_2 is set higher than w_1 to ensure that the contribution of $f_2(k)$ is inclusive in the minimisation problem. Figure 6.2 shows the decision variable, k obtained for different weight ratios under a PCC voltage unbalance factor of 7%. It can be observed that when $w_1 < w_2$, the decision variable, k has a value of 0.07 as imposed by the

constraints. However, when $w_1 \geq w_2$, the minimisation algorithm favours complete active ripple attenuation, with $k = -1$.

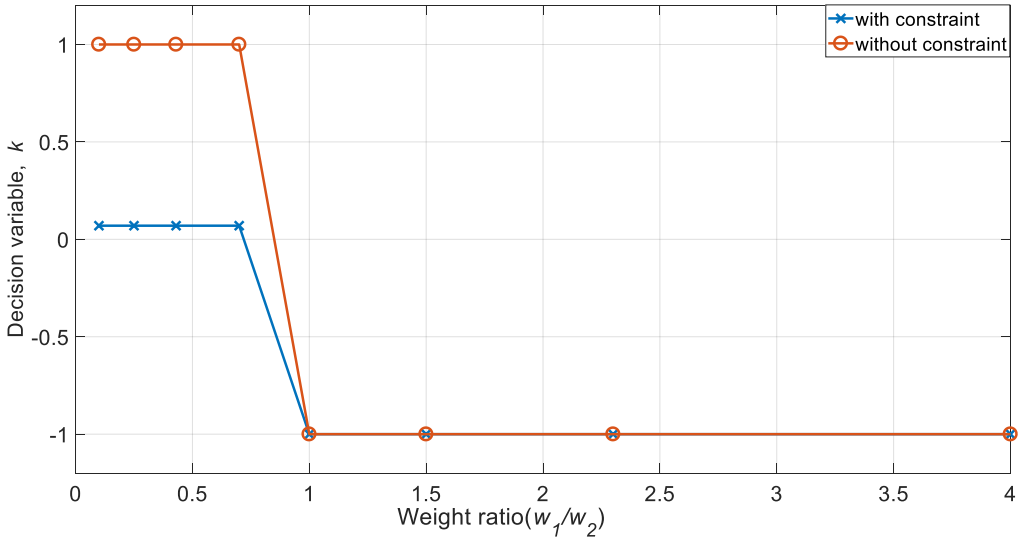

Figure 6:2: Assigned weight variation with decision variable

6.3.4 Optimised Decision Variable Searching Using Genetic Algorithm

Having finalised the objective function, its constraints and the weighting factors, the search for the optimised decision variable, k can be performed. An effective searching scheme - the genetic algorithm (GA) is chosen. GA is an optimisation technique based on Darwin's theory of natural selection [147, 152, 153]. The algorithm searches for an optimised solution for the problem studied through iteratively updating a predefined set of populations. By using certain operators at each step in the evolution process, the optimal solution can be obtained. The main operators are: selection, crossover and mutation.

In this particular application, GA searches for a single k value to minimize Equ. (6.31). The evolution process is summarised as follows [152, 153], with the flowchart shown in Fig. 6.3:

1. **Initialisation**: This generates a random initial population of k values with lower and upper bounds of -1 and +1. All elements in the population are represented as chromosomes, each encoded as an l-bit binary string comprising of "0" and "1". The length, l determines the resolution of the chromosome.

2. **Selection** : This follows the “survival-of-the–fittest” mechanism. Each of the chromosomes is decoded and applied to Equ. (6.31) - the objective function of the population. The fitter solutions are identified to form the new offspring.
3. **Crossover**: The survived chromosomes from the selection operation are put together for mating. In this process, random pairs of strings in the two mating chromosomes are interchanged to create new chromosomes which are absent in the previous generations but retain several features of their parents. The number of pairs for crossover is determined by the crossover probability, P_C.
4. **Mutation**: This operation is applied to a small number of chromosomes. The states of randomly selected bits within these chromosomes are flipped from 0 to 1 or vice versa. This is to prevent a situation in which all the bits in the parent string have the same values, so crossover operation cannot generate a new offspring. The mutation probability, P_m is set to a small value.
5. **Termination**: A new generation of population is produced by combining the newly produced strings through crossover and mutation with those generated initially. The evolution process described above can be repeated by returning to the selection process, if the convergence criteria has not been met.

The GA process may terminate if some pre-set criteria are met: the convergence criterion is the fitness function tolerance, δ, which evaluates the average change in the value of the fitness function, $\Delta F(k)$, over a number of generations known as stall generations. If $\Delta F(k)$ is less than δ, the problem has converged to an optimised solution. The final converged k value is then applied to Equ. (6.25) to evaluate the references, ${i_d}^{\pm *}, {i_q}^{\pm *}$ for the current control system. On the other hand, if $\Delta F(k)$ is not less than δ, the process needs to be renewed with a new set of chromosomes.

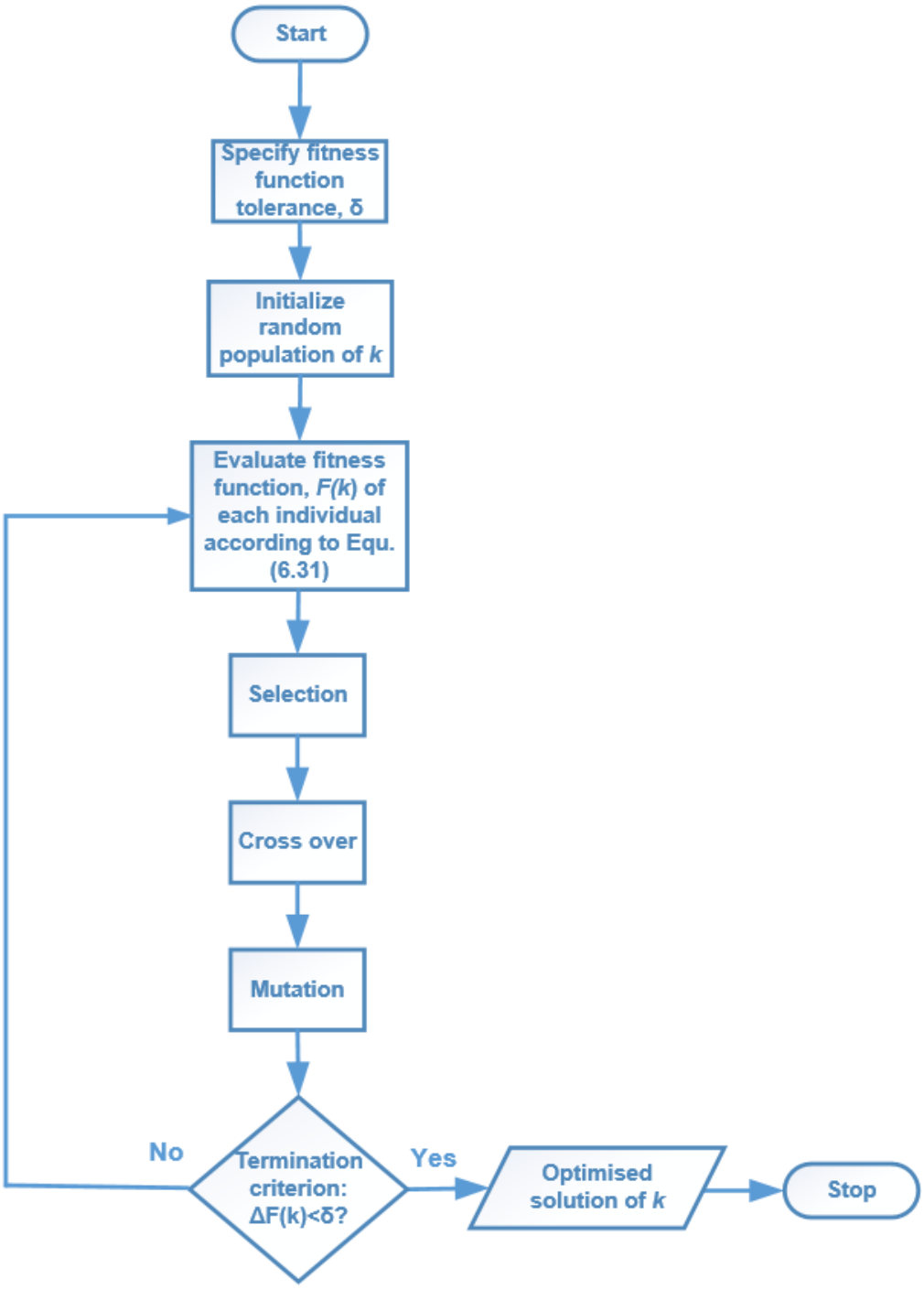

Figure 6:3: Flowchart for Genetic Algorithm process of selecting k

6.3.5 Flowchart for Reference Current Generation

Based on the above descriptions of reference current search principle, a flowchart describing the whole procedure including the application of constraints is given in Fig. 6.4. The first step, after the measurement and transformation of PCC voltages, is evaluating the range of k for the specified voltage ripple constraint, ΔV. Thereafter, the genetic algorithm (GA) is implemented to minimise the cost

function defined by Equ. (6.31) by iteratively searching for the optimal decision variable, k. The optimised k from the GA is substituted into Equ. (6.35) to assess if the maximum current constraint has been satisfied. If $I_{m(\max)}$ is less than the rated value, the reference currents for the PV inverter are computed directly using Equ. (6.25). Values of $I_{m(\max)}$ that exceed the rated boundaries of the current require a new set-point for active power, P^* determined from Equ. (6.39). With the reduced reference for active power, the inverter current references are determined from Equ. (6.25).

It is important to note that the determination of k using OFPC scheme as presented above is performed off-line, according to the PCC voltage measurement. When PCC three-phase voltages are not changed, the value of k evaluated previously is applied to the control loop for reference current estimation. Otherwise, a new k value must be generated.

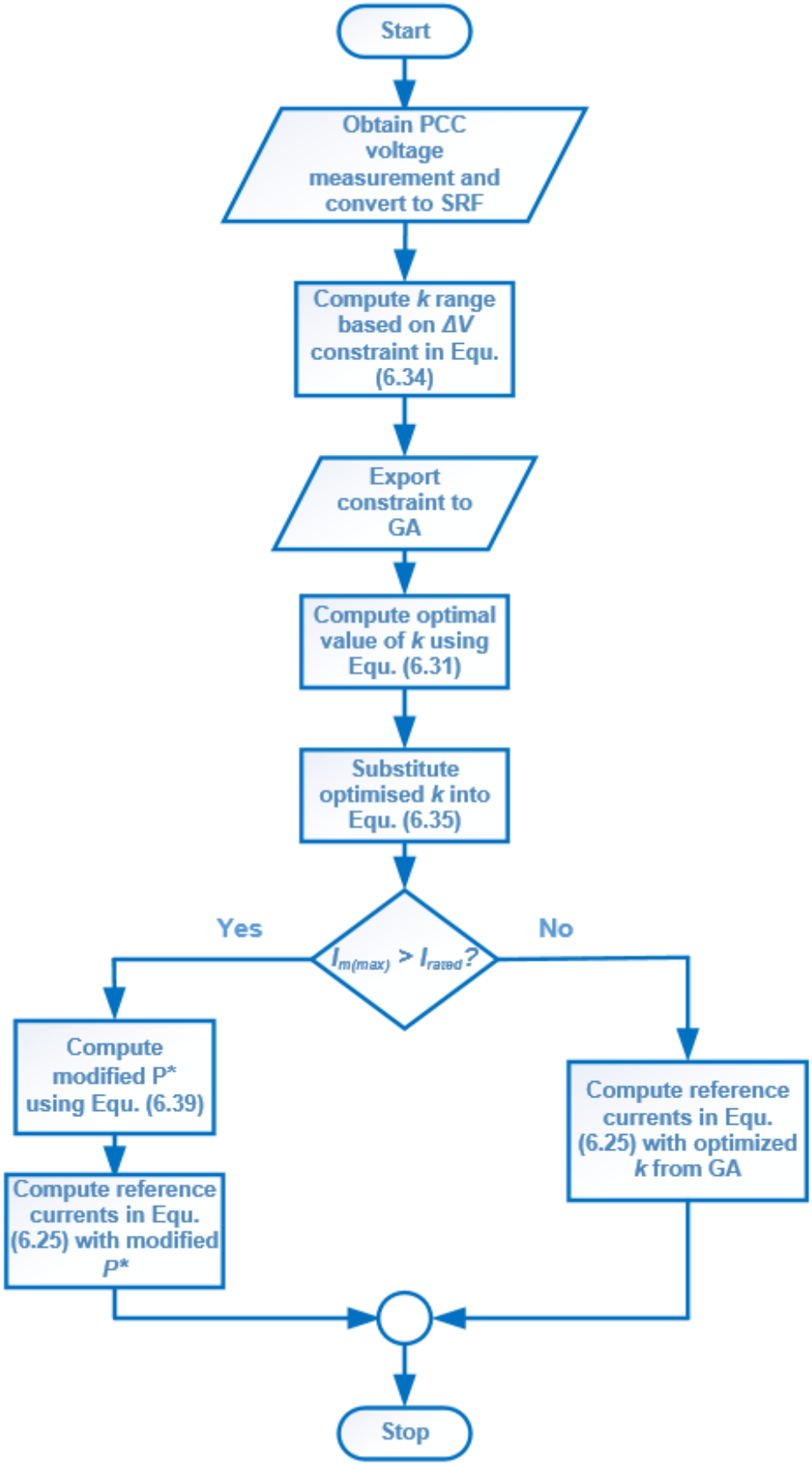

Figure 6:4: Flow chart for reference current generation using OFPC

6.4 PV Inverter Current Control Scheme For Unbalanced Grid Voltage

6.4.1 The Total Control Schematics

Accurate current control is essential for the VSI to deliver the reference current elements evaluated from the above described OFPC scheme. A crucial factor complicating the controller structure is the negative sequence component of the PCC voltage that appears when an unbalanced fault occurs. Since the conventional phase-locked loop (PLL) extracts the PCC voltage phase angle based only on the positive sequence component of the voltage, an additional controller is required to cater for the negative sequence components of both the PCC voltages and currents. This can be implemented in the decoupled double synchronous reference frame (DDSRF) described in chapter 1.

6.4.2 Proportional Resonant Current Control for Unbalanced Current

For current control under unbalanced voltage, the double synchronous reference frame PI control scheme is well-known and applied [31]. Its block diagram is shown in Fig. 6.5 with transfer function, $G_{PI}(s)_{dq}$ for PI controllers. Converting the reference frame of this control scheme to stationary reference frame leads to the proportional resonant (PR) controller, which has additional advantages compared to its synchronous reference frame counterpart. This control scheme, as detailed in sequel, is used in this work.

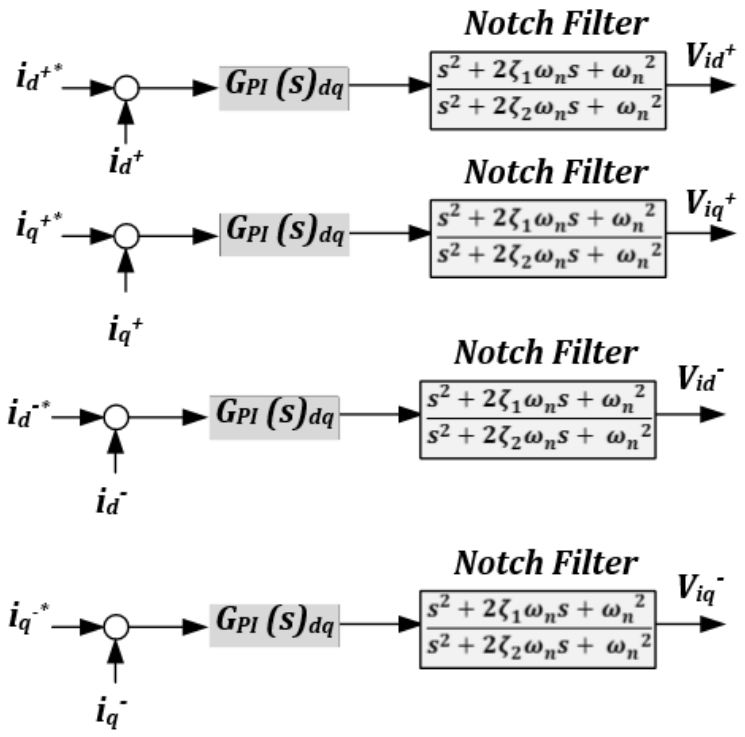

Figure 6:5: Block diagram for DDSRF current control with PI controllers

In balanced SRF control, the grid phase angle (ωt) is employed for conversion of three-phase variables to d and q-components. Under unbalanced conditions, the phase angles for the positive and negative sequence components are different as $+\omega t$ and$-\omega t$ respectively. When using PI controllers, two separate ones are required, one for the positive-sequence d-q current control, and the other the negative-sequence component. The PR controller, on the other hand, can control the positive and negative sequence components simultaneously and is thus preferred. This is due to the controller's ability to present an infinite gain at ± ω frequencies on the stationary frame. For both the positive and negative sequence components, the grid frequency is the same, so only one PR controller is required to control α and β components of both sequences. This reduces the number of required controllers by a half compared to the synchronous reference frame PI control scheme [31]. The d-q reference current components generated from Equ. (6.25) of the OFPC therefore need to be transformed into $i_\alpha{}^*$ and $i_\beta{}^*$ to regulate the PV-inverter terminal currents, $i_\alpha^\pm$ and $i_\beta^\pm$ by the PR-controllers.

Fig. 6.6 shows the proposed control system architecture for the PV-grid connected VSI under unbalanced grid voltages. It consists of the following

controllers: the MPPT, the DDSRF-PLL, the current feedback control loop consisting of the Proportional-Resonant (PR) controllers, the notch filter, the DC link voltage control and the sine PWM unit. Of these controllers, the focal point is the current control feedback loop implemented with a proportional-resonant (PR) controller.

From Fig. 6.6, the instantaneous values of the three-phase PCC voltage, v_{pcc} are measured and converted to the synchronous reference frame using the DDSRF-PLL technique as ${v_d}^{\pm}$ and ${v_q}^{\pm}$. The positive and negative sequence synchronisation phase angles, $+\omega t$ and $-\omega t$ are also determined alongside v_{pcc}.

The instantaneous value of the PV converter current, i_{pv} is measured at the inverter grid-side terminals and converted to the stationary reference frame as ${i_\alpha}^{\pm}$ and ${i_\beta}^{\pm}$ using Clarke's transform presented in chapter 1. The active power, P^* used in determining the PV-inverter reference currents is regulated by the DC link voltage control loop with the MPP power, *P* as reference. The reference currents, ${i_d}^{\pm *}$ and ${i_q}^{\pm *}$ are then determined using the OFPC scheme presented in the previous section, with the optimal *k* value determined using the genetic algorithm descried in section 6.4.3.

Cascaded notch filters are in the control loop to actively damp the resonant frequency elements present within the control signals as shown in Fig. 6.6. The output of the control loop are the voltage command signals V_α, V_β. These are converted into the stationary abc-frame to provide reference signals to the sine PWM controller of the VSI.

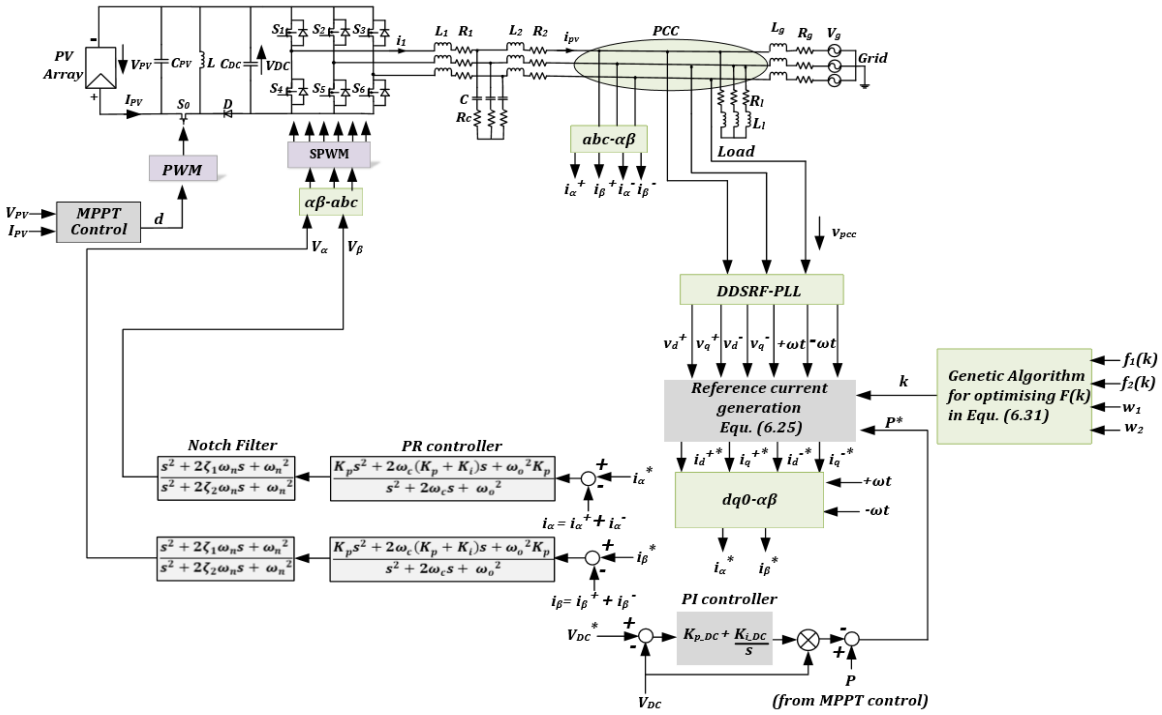

Figure 6:6: PV inverter current regulation based on the voltage oriented control in the stationary αβ-frame

As stated previously, the above described α-β dual current PR-control scheme in the stationary reference frame is equivalent to the proportional-integral (PI) controller of synchronous reference frame. The proportional gain, K_p , being time invariant, is unaffected by Clarke's transformation [154]. Consequently, K_p in the PR controller can be the same as that for the PI controller. The controller transfer function consisting of only the integral gain, K_i may therefore be represented as $G_{Ki}(s)_{dq}$.

To convert the integral gain in Fig. 6.5 from the synchronous reference frame, $G_{Ki}(s)_{dq}$ to the stationary reference frame, $G_{Ki}(s)_{\alpha\beta}$ at frequency, ω_o Clarke's transformation is used:

$$G_{Ki}(s)_{\alpha\beta} = G_{Ki}(s + j\omega_o)_{dq} + G_{Ki}(s - j\omega_o)_{dq}. \quad (6.40)$$

Evaluating Equ. (6.40):

$$G_{Ki}(s)_{\alpha\beta} = \frac{K_i}{s+j\omega_o} + \frac{K_i}{s-j\omega_o}, \quad (6.41)$$

hence:

$$G_{Ki}(s)_{\alpha\beta} = \frac{2K_i s}{s^2+{\omega_o}^2}. \quad (6.42)$$

The PR-controller transfer function, $G_{PR}(s)$ is therefore given as:

$$G_{PR}(s) = K_p + \frac{2K_i s}{s^2+{\omega_o}^2}, \quad (6.43)$$

where ω_o is the resonant frequency of the PR controller.

Assuming the closed loop bandwidth, ω_{CL} is significantly greater than ω_o, the integral gain of the PR controller in Equ. (6.42) approximates to

$$G_{Ki}(s) \cong \frac{2K_i}{s}, \quad (6.44)$$

and K_i can be designed in the same manner as that used for the synchronous frame PI controller.

Considering Equ. (6.43), the gain at any arbitrary frequency, ω will be:

$$G_{PR}(j\omega) = K_P + K_i \frac{s}{-\omega^2+{\omega_o}^2}. \quad (6.45)$$

If ω=ω_o:

$$G_{PR}(j\omega_o) = \infty. \quad (6.46)$$

From Equs. (6.45) and (6.46), it is clear that the PR controller offers an infinite gain only at its resonant frequency, ω_o, and will not introduce phase shift at any other frequencies [155]. That is why it is tuned to the grid frequency of 50 Hz in order to track the grid signals accurately. Due to stability problems associated with an infinite gain having zero bandwidth, a non-ideal PR controller with the following transfer function is considered [154]:

$$G_{PR}(s) = K_P + K_i \frac{2\omega_c s}{s^2+2\omega_c s+{\omega_o}^2} \quad (6.47)$$

where ω_c is the bandwidth around the frequency ω_o.

The Bode plot comparing the ideal and non-ideal PR controllers is shown in Fig. 6.7. K_i determines the bandwidth around the PR resonant frequency, [155] chosen as the grid frequency of 314.2 rad/s. With infinite gain as the grid frequency, the PR controller is able to track the inverter references, ${i_\alpha}^*$ and ${i_\beta}^*$ in Fig. 6.6 without steady state error.

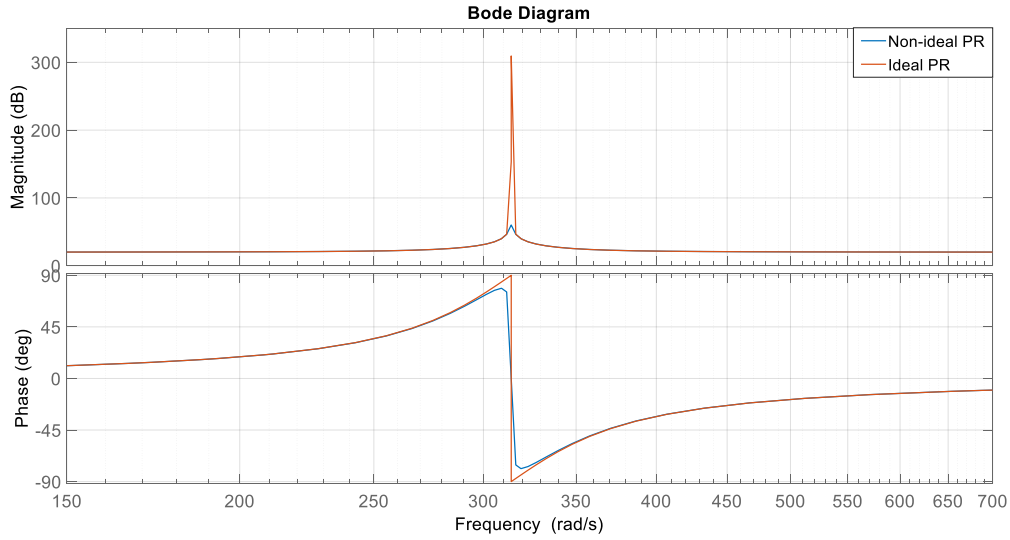

Figure 6:7: Open loop Bode plot for PR controller

6.5 Simulation Results for Current Control Methods under Unbalanced Grid Faults

The above OFPC scheme and subsequent PR current controllers are validated through simulation by controlling the power system shown in Fig. 6.6. Tables 6.1 and 6.2 specify the power system and PR controller parameters respectively.

The *Genetic Algorithm* in MATLAB optimisation toolbox (optimtool) is used to find the optimal *k* value for the single variable function of the power oscillations, $F(k)$ in Equ. (6.31) subject to the DC fluctuation and maximum inverter current constraints. The assigned weights of the simulations are: w_1 = 0.4 and w_2 = 0.6. The size of the initial population for *k* is set to 50 . The number of iterations remains unaffected by the change in population. However, increasing the population has increased the computational time without increasing the accuracy. The DC link voltage is limited to 2% maximum fluctuation.

The PR controller is the stationary reference frame equivalent of the PI controller. Hence, the design processes are the same. K_i should be large enough to eliminate steady state error, but should be bounded by the desired phase margin, since K_i introduces a phase lag at ω_o [154, 156]. The PR- controllers are similarly tuned according to the pole-assignment design technique described in Chapter 3, with a narrow bandwidth, ω_c , of 0.5 rad/s at the grid frequency.

Table 6.1: PV inverter system parameters

Parameter	Rating
PV inverter Rated Power (P)	100 kW
Grid Voltage (V)	380 V (rms)
Grid frequency (f)	50 Hz
DC link voltage (V_{DC})	620 V
Grid Impedance (R_g/ L_g)	0.1 Ω/0.1 mH
DC link capacitor (C_{DC})	2000 μF
Switching frequency (f_{sw})	20 kHz

Table 6.2: PI and PR controller parameters

Parameter	Rating
K_p	4
K_i	1200
ω_o	314.2 rad/s
ω_c	0.5 rad/s
K_{p_DC}	0.5
K_{i_DC}	10

The following control schemes relating to active power generation are considered: Balanced Positive-Sequence Control (BPSC), Constant Active Power Control (CAPC) and the proposed Optimised Flexible Power Control (OFPC). The performance of the control schemes are investigated for 3 distinct VUFs of the PCC voltage, following a corresponding single-phase grid fault in phase A at time, $t = 0.4\ s$: 7%, 11% and 18%. For time, $t < 0.4s$, balanced sinusoidal PCC voltages, PV currents, active and reactive PV powers, as well as DC link voltages are obtained in all simulation cases. For unity power factor, Q^* is set to zero.

It should be noted that the rated current value has been increased by 20% to accommodate transient surge currents under normal operation without tripping overcurrent devices [157]. With the positive sequence voltage, V^+ at 310 V, the magnitude of I_{rated} according to Equ. (6.36) is therefore 258 A.

The control schemes are activated according to the time frames shown in Table 6.3.

Table 6.3: Time frames (in seconds) for current control schemes under unbalanced grid faults

Time Frame (s)	Control Scheme
0.4 ≤ t ≤0.5	CAPC
0.5 ≤ t ≤0.6	OFPC
0.6 ≤ t ≤0.7	BPSC

The control responses at different VUF levels are described below.

6.5.1 PCC Voltage at 7% VUF

For a 7% VUF, the GA determines the value of the decision variable, k as 0.07 as shown in Fig. 6.8 (a). The corresponding amplitude of the optimally minimised fitness function, $F(k)$ as a function of the number of generations in the GA is shown in Fig. 6.8 (b). The mean value of the minimised $F(k)$ has converged to 49% of the amplitude in Equ. (6.31) after 57 iterations.

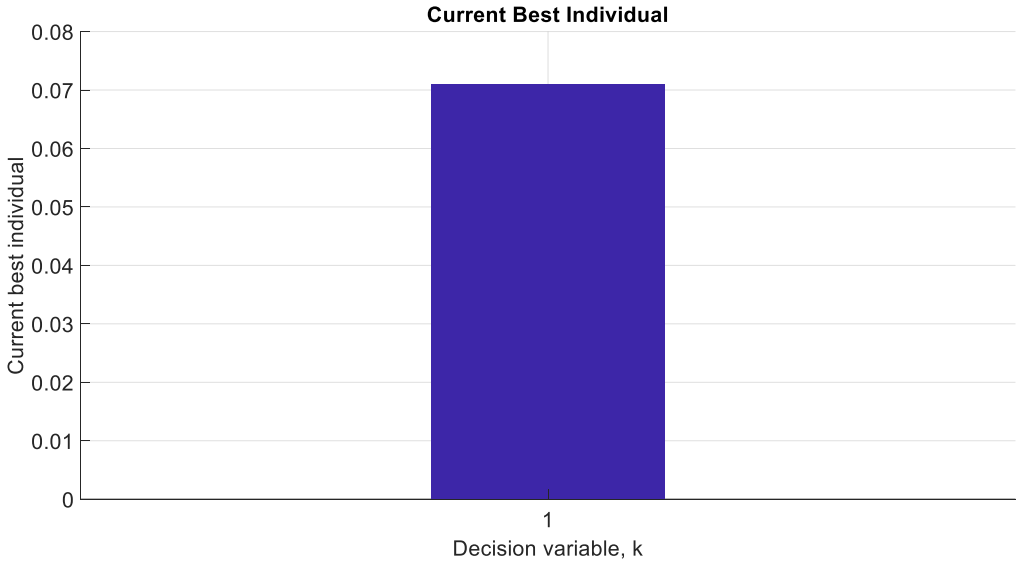

(a)

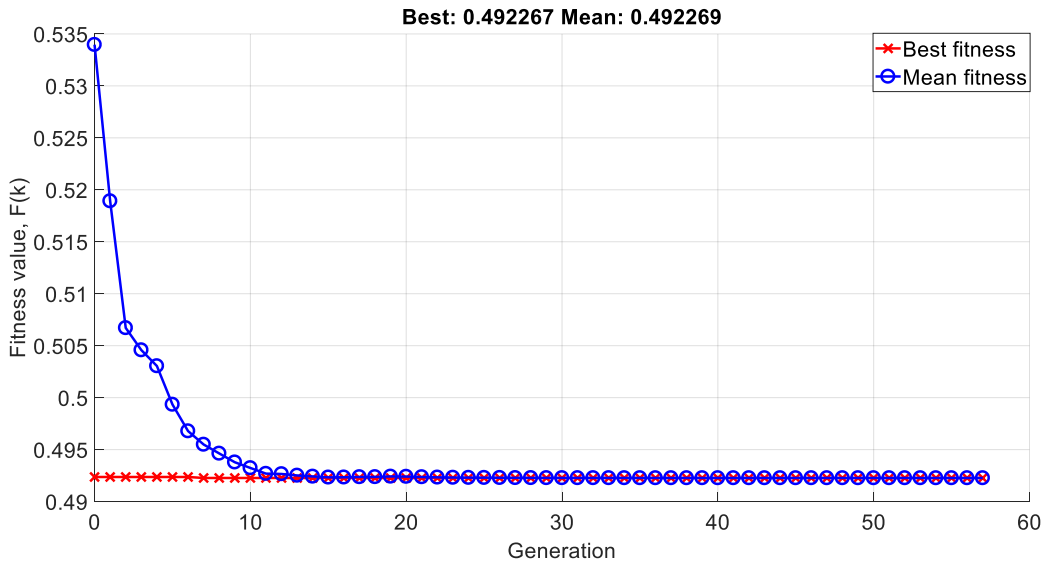

(b)

Figure 6:8: Genetic algorithm optimisation for 7% VUF (a) optimal value of k (b) minimised fitness function

Figures 6.9 (a) and (b) show the PCC voltage and the corresponding VUF respectively. At $t < 0.4s$, a balanced PCC voltage is obtained with 0% VUF. At $t > 0.4s$, a single-phase grid fault causes asymmetry in the PCC voltage, with the VUF rising to 7%.

In terms of current magnitude, the CAPC has the largest phase currents shown in Fig. 6.9 (c). Due to the relatively small amplitude of the decision variable,k Equs. (6.25) and (6.8) are approximately the same, hence the currents from the OFPC and BPSC appear equally balanced.

The power oscillations in Fig. 6.9 (d) are completely damped for the CAPC method, resulting in the oscillations entirely appearing in the reactive power. The amplitudes of the powers are similar for the OFPC and BPSC methods, owing to the small magnitude in k.

The variations in active and reactive powers can be visualised more clearly with the root mean square error (RMSE) bar charts in Fig. 6.9 (e). Compared to the OFPC, the CAPC has decreased the active power oscillation by close to a decade. Similarly, the BPSC has reduced the active power ripple by 15%, compared to the OFPC. From the point of view of the reactive power, CAPC has the largest amplitude in fluctuations, approximately twice as large as the amplitudes for either OFPC or BPSC. As previously mentioned, the reference

currents generated by the OFPC and BPSC are almost equal, owing to the optimal magnitude of k being relatively small, at 0.07.

The DC link voltage is shown in Fig. 6.9 (f) with the corresponding RMSE values in Fig. 6.9 (g). As expected, the oscillation patterns are similar to the active power oscillations in Figs. 6.9 (d) and (e). The notable exception is the OFPC, producing almost 5 times the DC oscillations in CAPC and 1.4 times the fluctuations in BPSC. However, the RMSE of the DC link voltage is still less than the required 2% constraint imposed (i.e. *12.4 V*). Thus, although the OFPC has a larger fluctuation in the DC link voltage, its operation is still deemed satisfactory, as both active and reactive powers have reduced simultaneously. With a low VUF, the BPSC method offers the highest advantages, with a balanced current and less DC link fluctuations compared to the OFPC method.

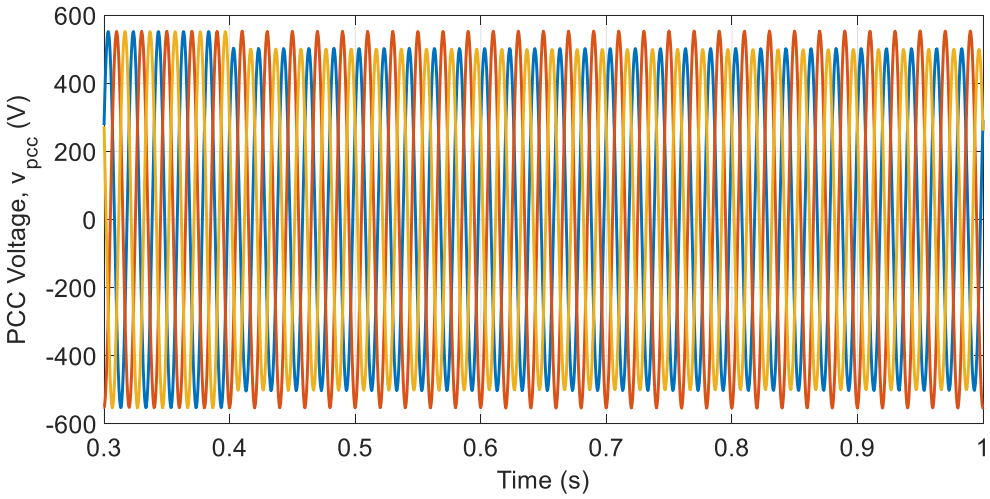

(a)

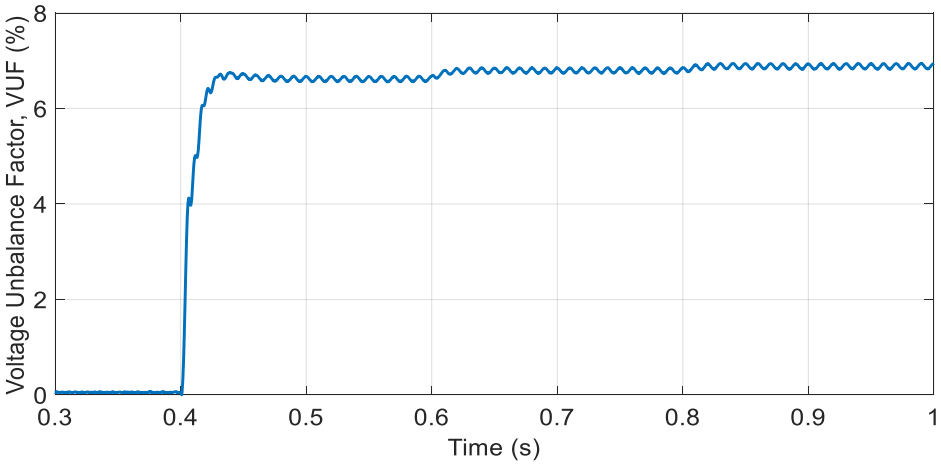

(b)

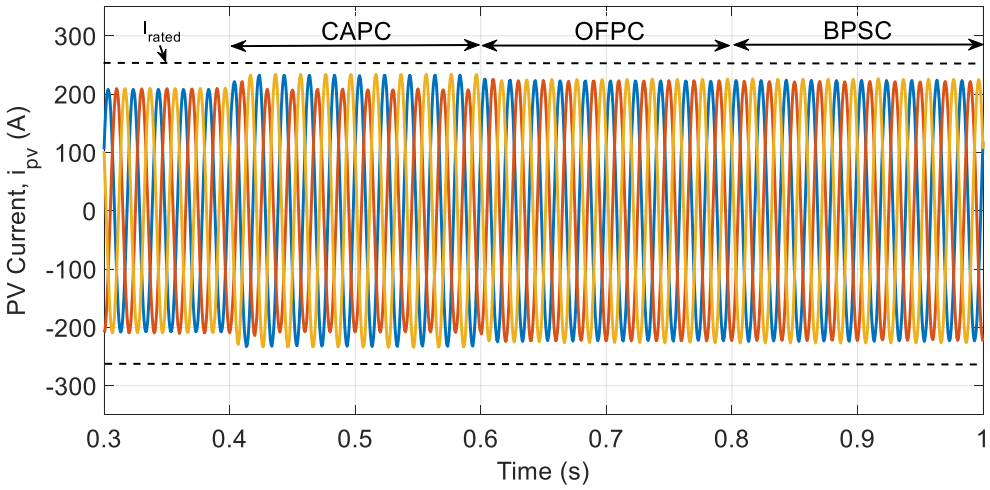
I_{rated}
CAPC
OFPC
BPSC
PV Current, i_{pv} (A)
300
200
100
0
-100
-200
-300
0.3
0.4
0.5
0.6
0.7
0.8
0.9
1
Time (s)

(c)

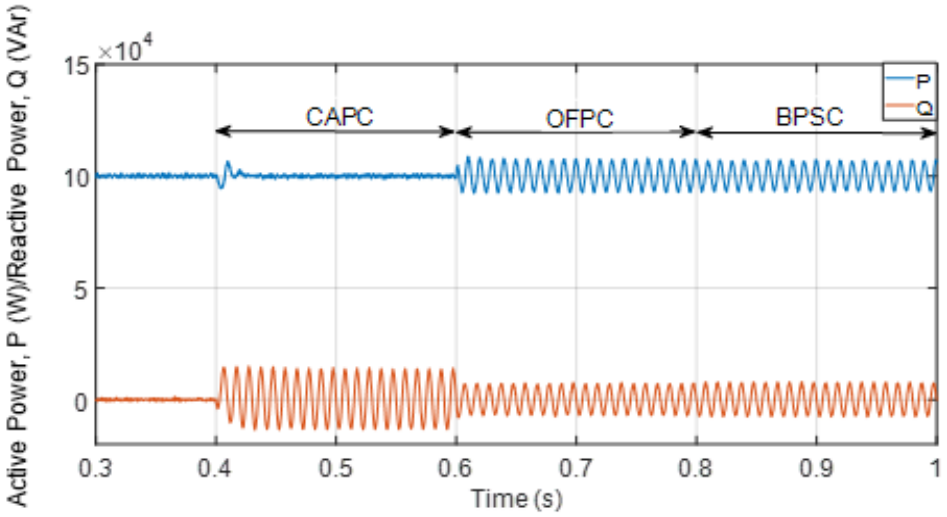
Active Power, P (W)/Reactive Power, Q (VAr)
×10^4
15
10
5
0
CAPC
OFPC
BPSC
P
Q
0.3
0.4
0.5
0.6
0.7
0.8
0.9
1
Time (s)

(d)

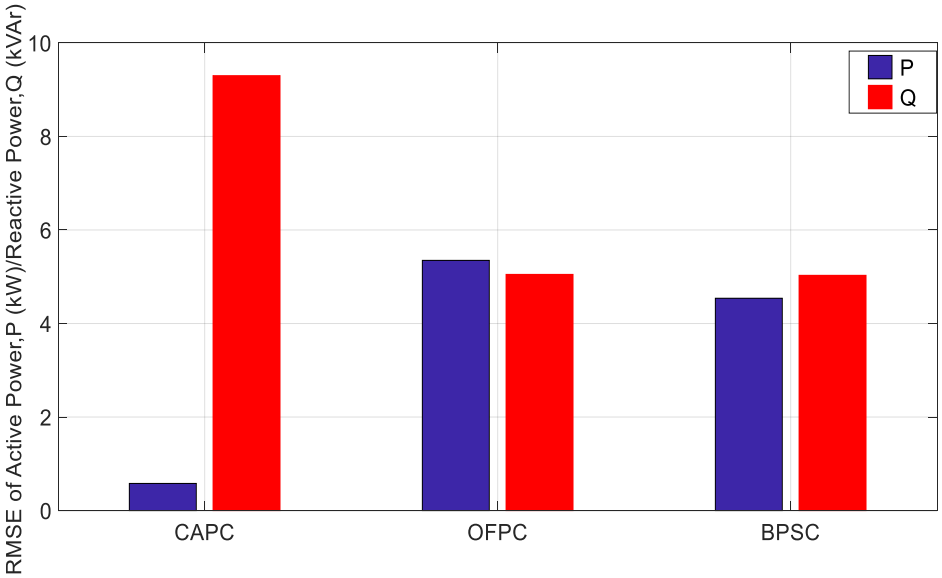
RMSE of Active Power,P (kW)/Reactive Power,Q (kVAr)
10
8
6
4
2
0
P
Q
CAPC
OFPC
BPSC

(e)

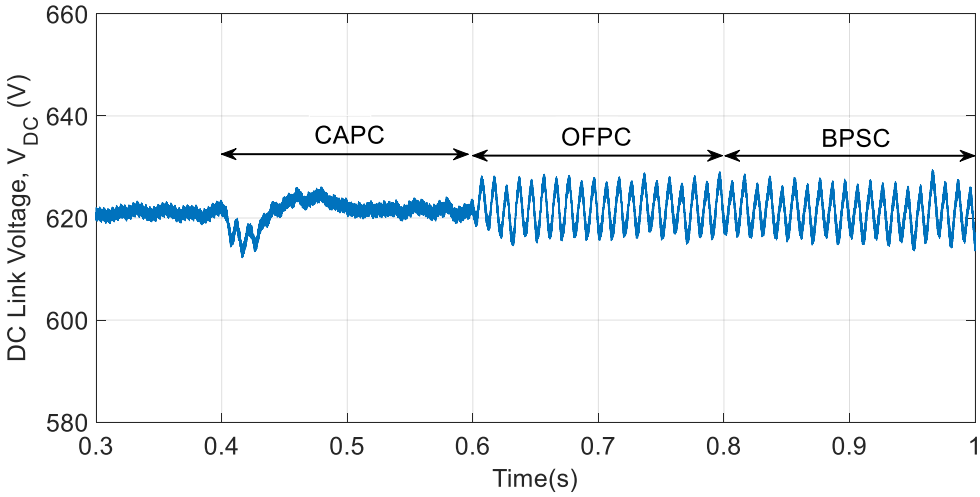
DC Link Voltage, V_{DC} (V)
660
640
620
600
580
CAPC
OFPC
BPSC
0.3
0.4
0.5
0.6
0.7
0.8
0.9
1
Time(s)

(f)

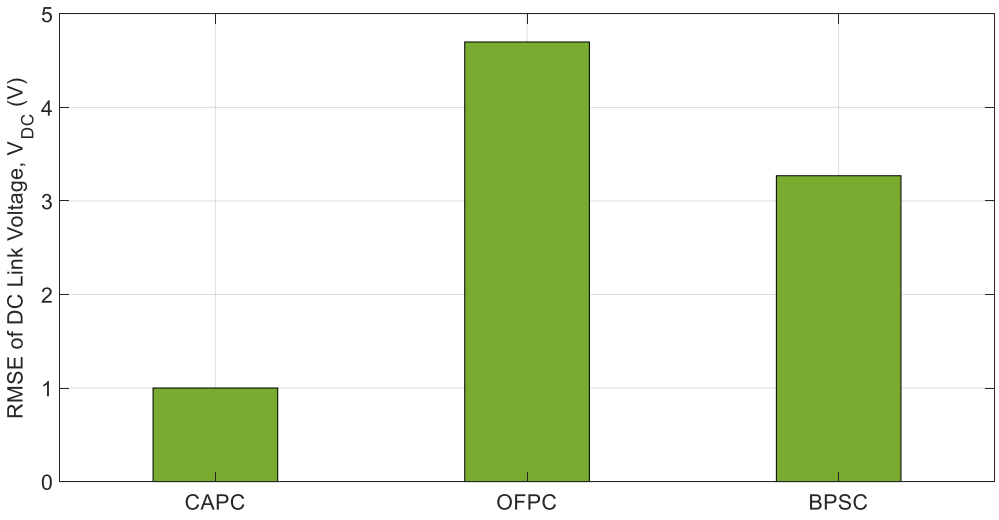

(g)

Figure 6:9: 7 % PCC voltage unbalance factor (a) PCC voltage (b) VUF (c) PV current (d) PV active and reactive powers (e) RMSE of active and reactive powers (f) DC link voltage (g) RMSE of DC link voltage

6.5.2 PCC Voltage at 11% VUF

An 11% VUF at the PCC results in an optimal value for the decision variable, k determined as -0.31 by the GA as shown in Fig. 6.10 (a). The corresponding amplitude of the minimised fitness function, $F(k)$ is shown in Fig. 6.10 (b). The mean value of the minimised $F(k)$ has converged to 53% of the magnitude described by Equ. (6.31) after the same number of iterations as 7% VUF i.e. 57 iterations.

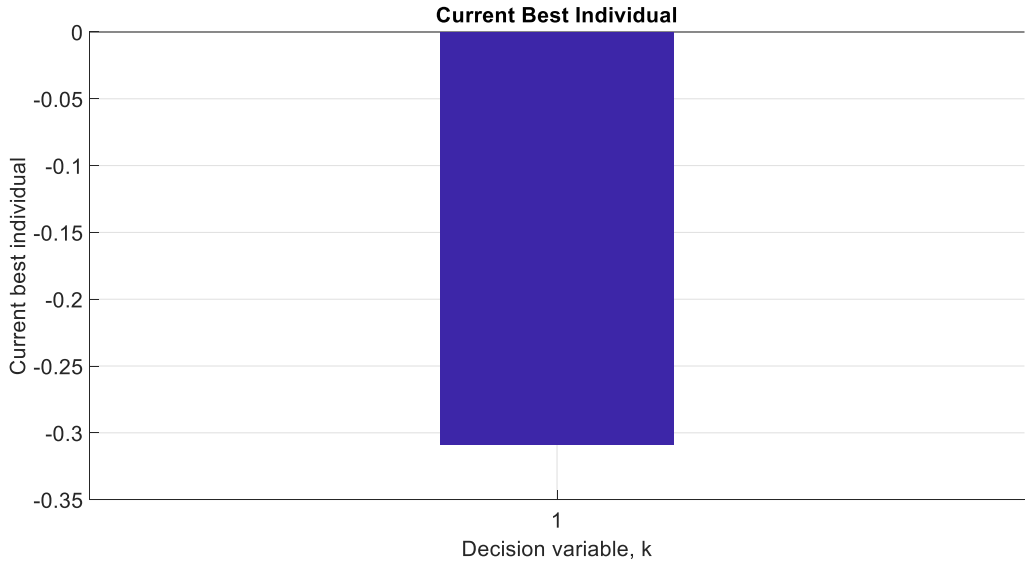

(a)

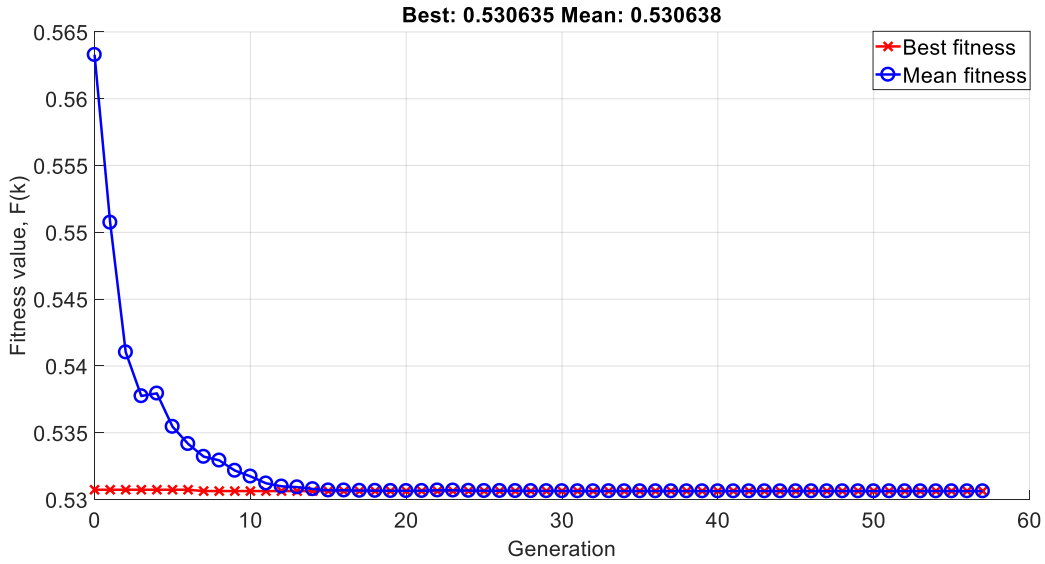

(b)

Figure 6:10: Genetic algorithm optimisation for 11% VUF (a) optimal value of k (b) minimised fitness function

Figures 6.11 (a) and (b) show the PCC voltage and the corresponding VUF respectively. At $t < 0.4s$, a balanced PCC voltage is obtained with 0% VUF. At $t > 0.4s$, a single-phase grid fault causes asymmetry in the PCC voltage, with a VUF increasing to 11%.

CAPC current amplitudes in phases A and C shown in Fig. 6.11 (c) have reached the boundary of the rated current, due to higher negative sequence voltage vectors in Equ. (6.14). An asymmetry has appeared across the OFPC currents due to a higher VUF while the BPSC currents remain balanced.

The powers in Figs. 6.11 (d) and (e) show OFPC decreasing the active power ripple by 26% compared to BPSC. On the other hand, the RMSE of the active power ripple for OFPC is 6 times larger than that for the CAPC. In terms of reactive power, OFPC has decreased the ripple by 32% compared to the CAPC method. With respect to BPSC, OFPC has increased the reactive power ripple by 25%.

The DC link voltage and its corresponding RMSE values are shown in Figs. 6.11 (f) and (g) respectively. The BPSC produces the largest ripple voltage with RMSE at 4.8 V. The OFPC reduces this by 8.3 % to 4.4 V. CAPC produces the least ripple with an RMSE of 1.2 V.

For VUF at 11%, the advantages of the OFPC have become manifested in its ability to act as a compromise solution between the extreme ends of large PV currents and reactive power ripple of the CAPC method and the large active power and DC link fluctuations of the BPSC method.

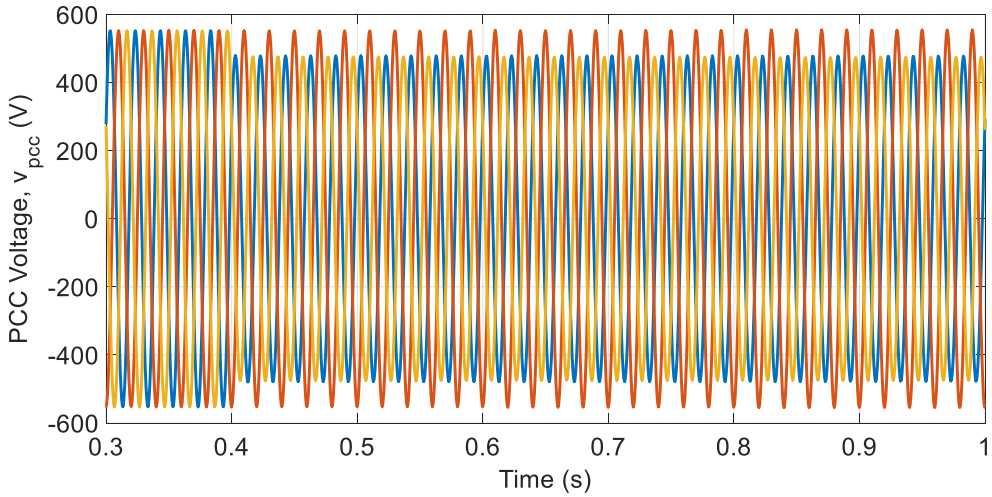

(a)

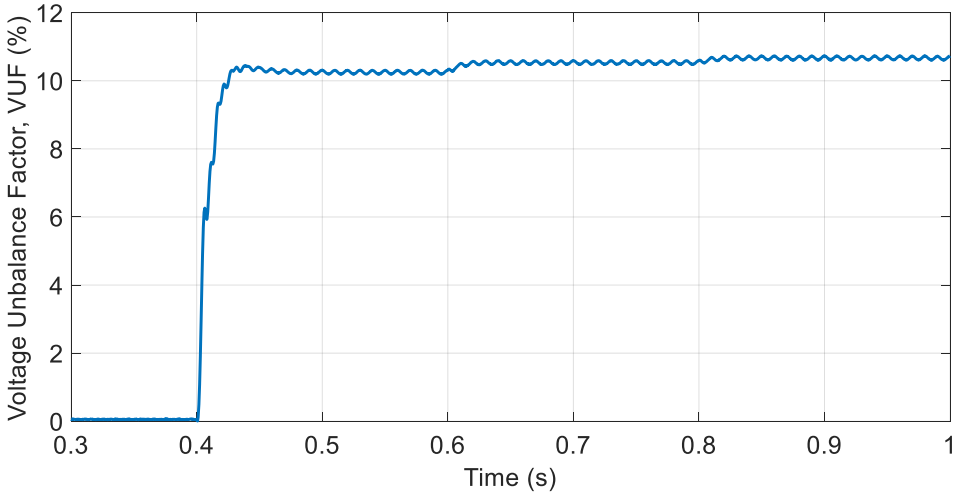

(b)

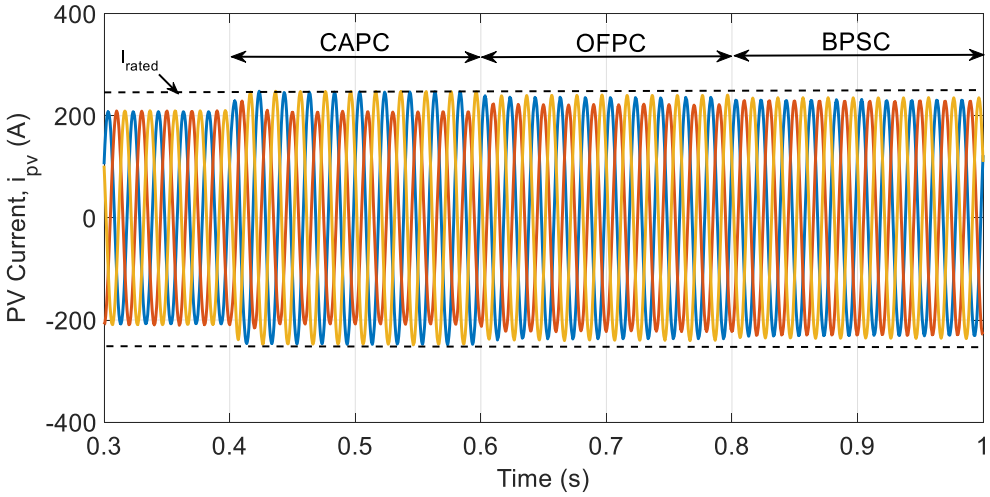
400
200
0
-200
-400
PV Current, i_{pv} (A)
I_{rated}
CAPC
OFPC
BPSC
0.3
0.4
0.5
0.6
0.7
0.8
0.9
1
Time (s)

(c)

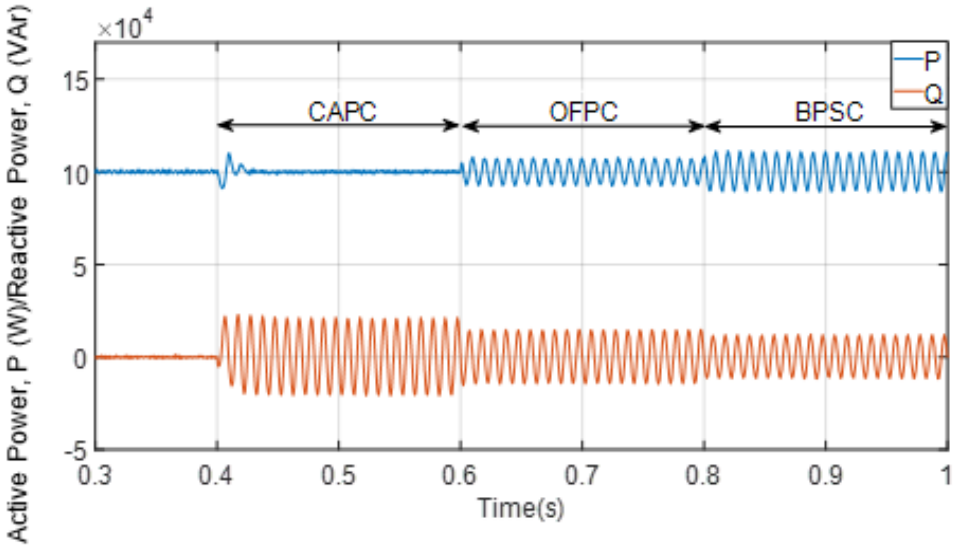
$\times 10^4$
15
10
5
0
-5
Active Power, P (W)/Reactive Power, Q (VAr)
P
Q
CAPC
OFPC
BPSC
0.3
0.4
0.5
0.6
0.7
0.8
0.9
1
Time(s)

(d)

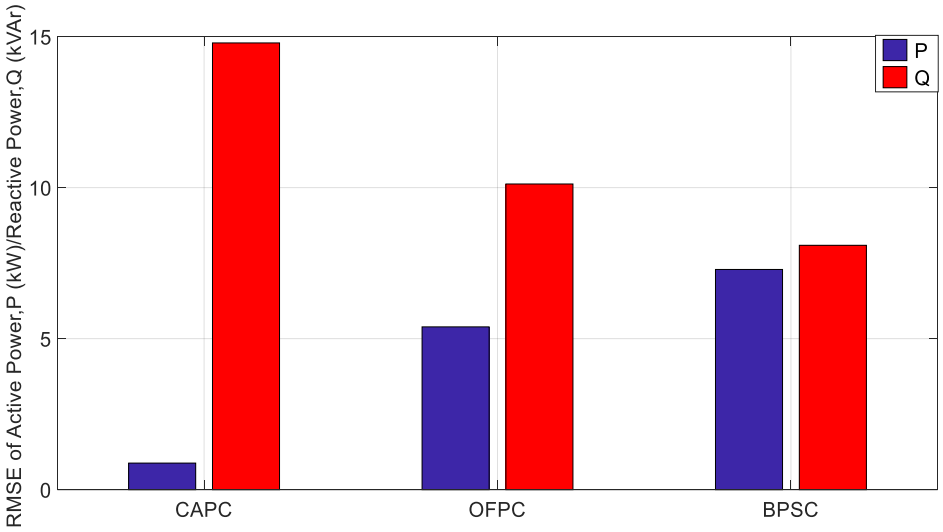
RMSE of Active Power,P (kW)/Reactive Power,Q (kVAr)
15
10
5
0
P
Q
CAPC
OFPC
BPSC

(e)

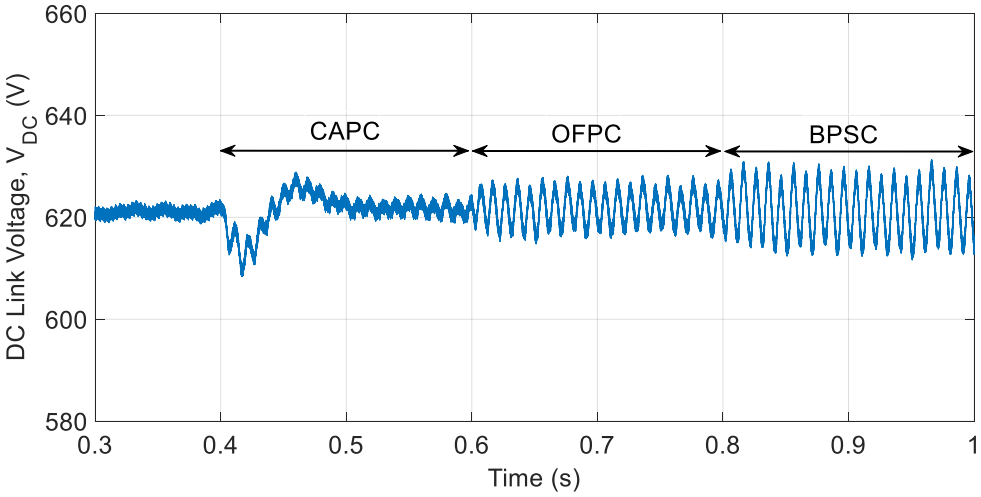
DC Link Voltage, V_{DC} (V)
660
640
620
600
580
CAPC
OFPC
BPSC
0.3
0.4
0.5
0.6
0.7
0.8
0.9
1
Time (s)

(f)

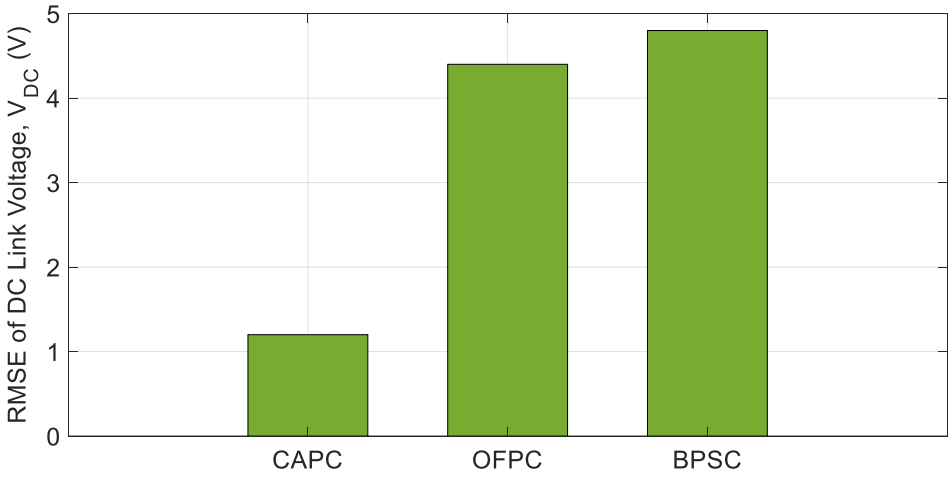

(g)

Figure 6:11: 11% PCC voltage unbalance factor (a) PCC voltage (b) VUF (c) PV current (d) PV active and reactive powers (e) RMSE of active and reactive powers (f) DC link voltage (g) RMSE of DC link voltage

6.5.3 PCC Voltage at 18% VUF

Fig. 6.12 (a) shows the optimal value of the decision variable, k obtained from the GA as -0.62, whereas Fig. 6.12 (b) shows the corresponding magnitude of the optimally minimised function, $F(k)$.The mean value of the minimised fitness function has converged to 56% of the amplitude in Equ. (6.31). The number of iterations remain unchanged at 57.

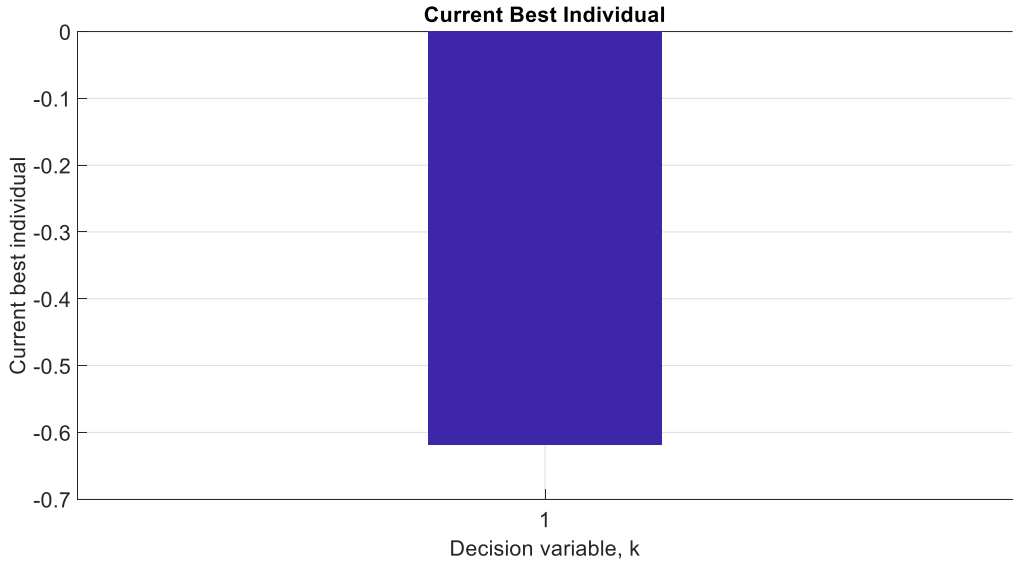

(a)

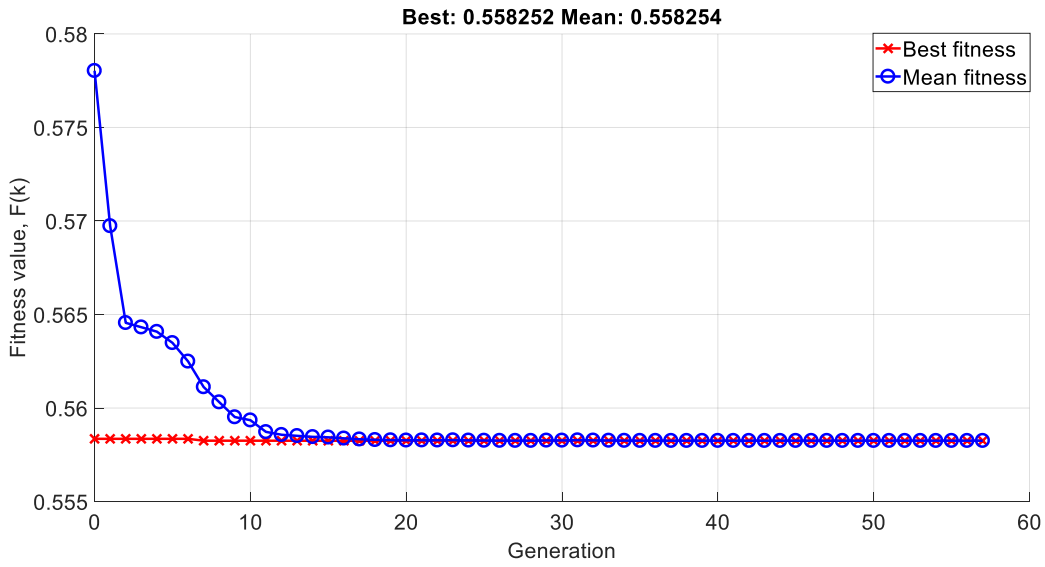

(b)

Figure 6:12: Genetic algorithm optimisation for 18% VUF (a) optimal value of k (b) minimised fitness function

Figures 6.13 (a) and (b) show the PCC voltage and the corresponding VUF respectively. At $t < 0.4\ s$, a balanced PCC voltage is obtained with 0% VUF. At $t > 0.4s$, the VUF increases to 18%, in response to a single-phase grid fault.

CAPC current amplitudes in phases A and C shown in Fig. 6.13 (c) have exceeded the rating of the PV inverter currents described by Equ. (6.36). With the increase in VUF, the OFPC method has similarly exceeded the rated current with the decision variable determined in Fig. 6.12 (a), according to Equ. (6.35). The reference power, P^* has therefore been modified according to Equ. (6.39), with the new reference determined as 90 *kW*. BPSC current magnitudes have equally increased to the boundary of the rated current with the increased VUF.

Due to a reduced active power set point, the powers in Figs. 6.13 (d) and (e) show the OFPC active and reactive power ripples decrease, as both are functions of the active power reference, as described by Equs. (6.26) and (6.27) respectively. The OFPC has decreased the active power ripple by 66% compared to the BPSC. However, its active power fluctuations are approximately 4 times larger than that produced by the CAPC. In terms of reactive power, the OFPC has reduced the ripples by 25% when compared with the CAPC method. With the BPSC method as reference point, the OFPC has increased the reactive power oscillations by 28%.

The DC link voltage and its corresponding RMSE values are shown in Figs. 6.13 (f) and (g) respectively. Due to the reduction in power set-point at the time range, 0.5<*t*< *0.6 s,* OFPC has the least DC link voltage ripple, reducing the fluctuation by 14% compared to the CAPC method and 74% compared to the BPSC method. The RMSEs for all methods were computed after the DC link voltage has settled in 4 fundamental cycles, i.e. *0.08 s*.

Although the active power delivered by the OFPC has been curtailed due to the maximum current constraint when the VUF is 18%, the active power and DC link voltage fluctuations have been significantly minimised. This can be considered a huge advantage, as the reduced ripple at the DC link makes it possible to use lower capacitor values, which is more economical.

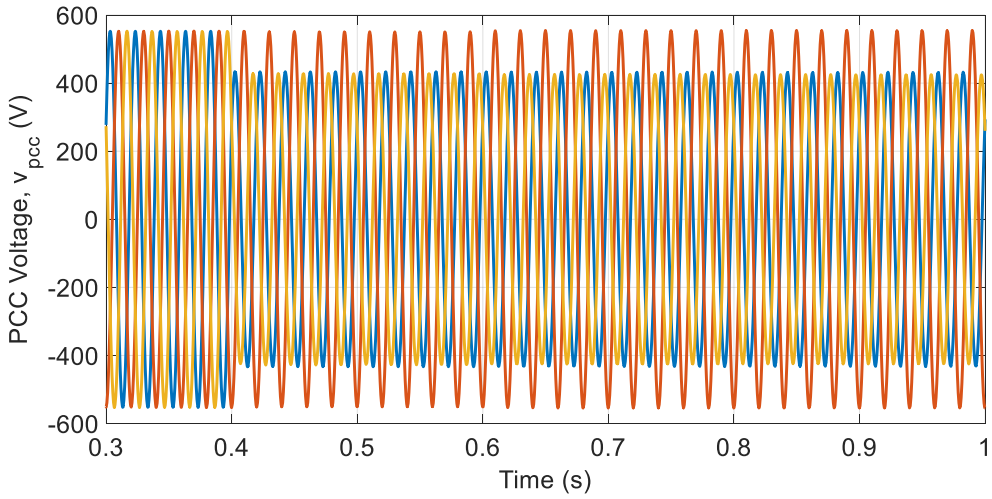

(a)

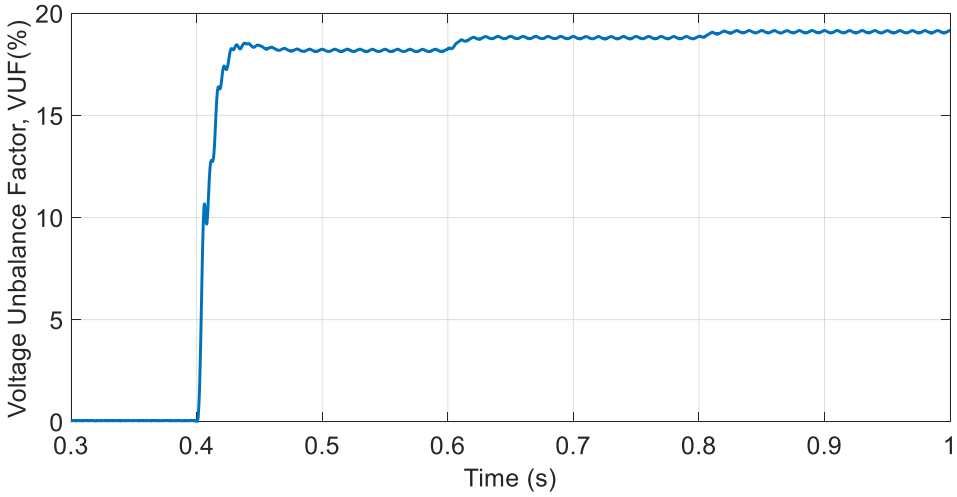

(b)

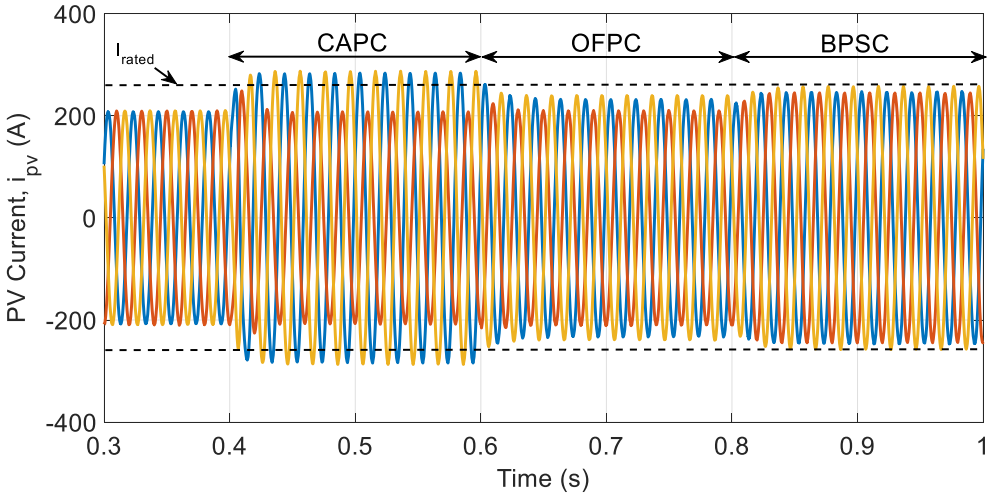
400
200
0
-200
-400
PV Current, i_pv (A)
I_rated
CAPC
OFPC
BPSC
0.3
0.4
0.5
0.6
0.7
0.8
0.9
1
Time (s)

(c)

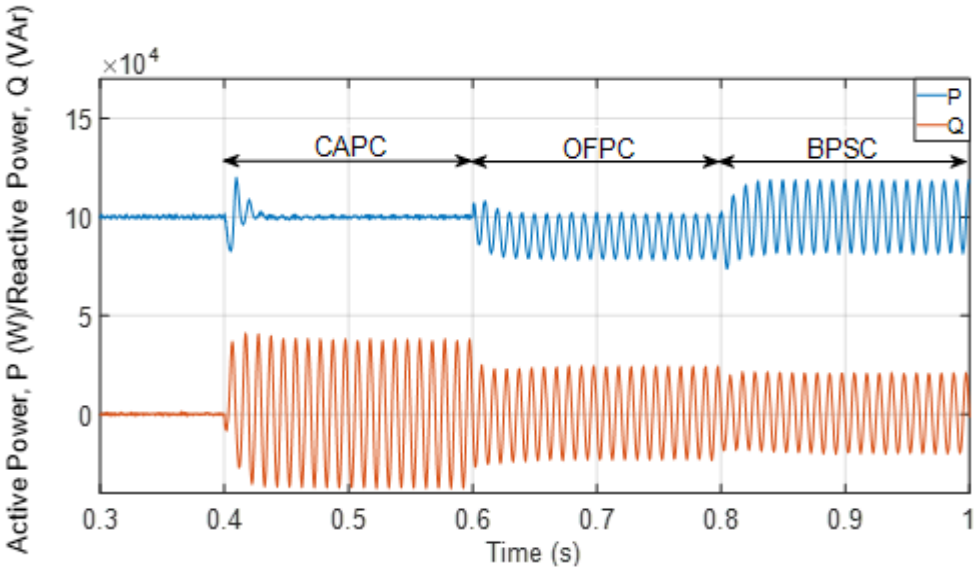
×10^4
15
10
5
0
Active Power, P (W)/Reactive Power, Q (VAr)
P
Q
CAPC
OFPC
BPSC
0.3
0.4
0.5
0.6
0.7
0.8
0.9
1
Time (s)

(d)

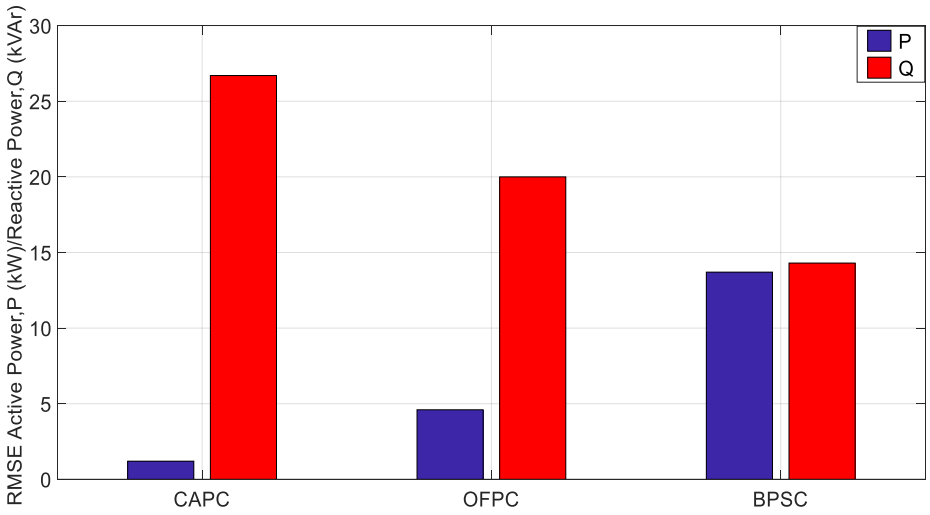
RMSE Active Power,P (kW)/Reactive Power,Q (kVAr)
30
25
20
15
10
5
0
P
Q
CAPC
OFPC
BPSC

(e)

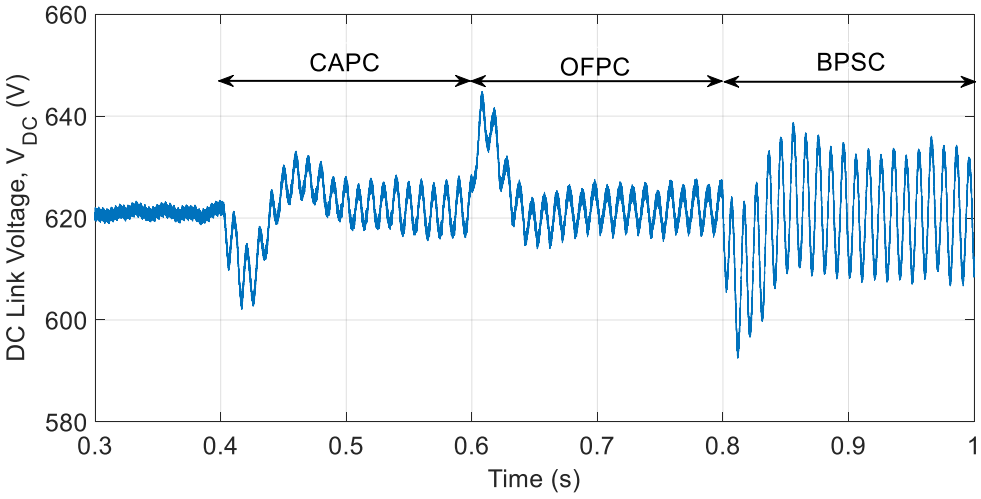
DC Link Voltage, V_{DC} (V)
660
640
620
600
580
CAPC
OFPC
BPSC
0.3
0.4
0.5
0.6
0.7
0.8
0.9
1
Time (s)

(f)

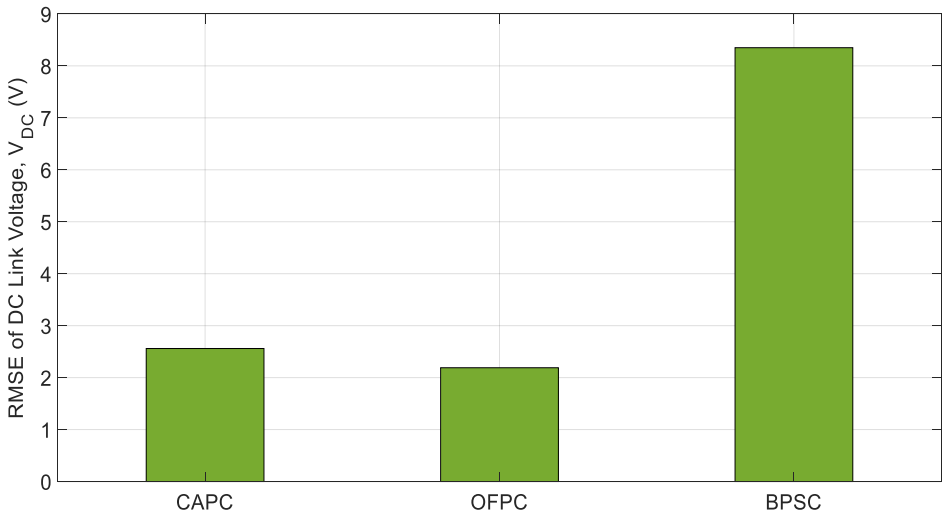

(g)

Figure 6:13: 18% PCC voltage unbalance factor (a) PCC Voltage (b) VUF (c) PV Current (d) PV Active and Reactive Powers (e) RMSE of Active and Reactive Powers (f) DC link Voltage (g) RMSE of DC link voltage

6.6 Conclusion

The chapter has proposed an optimised flexible power control (OFPC) method of controlling a PV grid connected inverter in the presence of grid voltage unbalance. It simultaneously reduces the power ripples through formulation of a multi-objective optimisation problem with decision variable, k chosen based on the genetic algorithm. The optimal coefficient, k reduces the reactive power ripple simultaneously with the active power ripple. This is considered an improvement, since the optimised value of k has resulted in a reduction of the reactive power losses while maintaining the DC link fluctuation and maximum currents within limits.

Simulation results have compared the operations of the proposed optimised flexible power control (OFPC) with two other classical methods: the constant active power control (CAPC) and the balanced positive-sequence control (BPSC). The BPSC has the advantage of injecting a balanced set of currents to the grid at the expense of large active power and DC link fluctuations. At high levels of PCC voltage unbalance, the 2% constraint on the DC link voltage may be exceeded. The CAPC method completely eliminates active power ripples, resulting in a low DC link fluctuation. However, this is at the expense of a

completely undamped reactive power ripple coupled with large currents which may exceed the semiconductor ratings with high levels of the unbalanced voltage vector at the PCC.

The proposed OFPC provides a compromised solution between the extreme ends of large PV currents and reactive power ripple of the CAPC method and the large active power and DC link fluctuations of the BPSC method. At high VUFs, it proves even better than the CAPC method is terms of reducing the DC link voltage fluctuations. Additionally, the genetic algorithm in the OFPC imposes a maximum limit on the reference currents, ensuring that regardless of VUF, the inverter current rating is never exceeded. Through the constraints of both DC link voltage ripple and maximum inverter current, the OFPC provides an advantage compared to other conventional methods of control under unbalanced grid voltage conditions.

Chapter 7 Conclusions and Recommendations for Future Research

7.1 General Conclusion

The increasing demand for electricity has resulted in a vast number of generators connected to the power grid at the distribution side of the power system. Such generators, known as distributed generators (DGs), curtail the cost of investing in power transmission equipment. An additional advantage is secured if the DGs are powered by renewable sources such as biomass and solar, as they do not increase the net atmospheric greenhouse gas (GHG) emissions. Although DGs are capable of improving power system reliability, their performance can be hindered by their poor responses to fluctuations arising within the power system.

The research has focused on investigating the challenges faced by renewably-sourced DGs, in particular synchronous generator-based biomass DGs and power electronic-based PVDGs. With the rapid infiltration of the aforementioned DGs in the traditional power system, developing advanced control schemes under abnormal grid conditions is crucial to ensuring efficient power generation and delivery to the grid and interconnected loads. The research analyses and proposes solutions to three abnormal power system conditions: a varying line impedance, unbalanced loads and unbalanced grid voltages. The main achievements and contributions of the research are outlined below:

- A detailed model for BDG interfaced with the grid via a synchronous generator was developed. Control systems for the driving gas turbine and the synchronous generator were presented. The fuel flow within the gas turbine was primarily regulated by the speed governor. In cases where the exhaust temperature reference was exceeded, the temperature control was activated to reduce fuel flow. The synchronous generator controlled the BDG system voltage through the automatic voltage regulator (AVR), which was achieved by controlling the field excitation current in the rotor windings.
- A simulation study for investigating the response of the BDG under a step change in electrical load demand was presented and the control systems responded appropriately, adapting the BDG system to accommodate the

new load. Further simulation studies on the transient stability of the BDG were performed for different inertia constants of the system in response to the same increase in load. Although the BDG with the least inertia constant offered a faster response, the temporary deviations in frequency following the load change may lead to load shedding caused by false tripping of frequency sensitive relays.

- A detailed model and design process for a PVDG system and its control was presented. The model comprised of: the PV array (for power generation), the DC-DC converter (for maximum power extraction from the PV), the voltage source inverter (for DC-AC power conversion) and finally an inductor-capacitor-inductor (LCL) filter (for harmonic filtering). The system was controlled using the voltage oriented control (VOC) method, where the d-q elements of the grid current component were aligned with the grid voltage vector, using the grid voltage phase angle obtained from the phase-locked loop (PLL) technique. The focal point of the chapter was to analyse the passive and active damping methods of the LCL filter resonance in the frequency domain. A passive resistor, virtual resistor and notch filter (NF) were analysed, and were proven to suppress the resonance adequately. Owing to the ease of implementation and high efficiency, the NF approach was analysed further. The PVDG system stability in terms of variation of the damping coefficients of the NF were studied both through frequency domain and time domain simulations. It was concluded that a small NF gain at the resonant frequency is necessary to provide adequate damping for the LCL filter.
- The variation of LCL resonant frequency was presented in the case of a varying grid impedance. It was shown through simulation studies that a varying grid inductance rendered the NF ineffective in damping. An adaptive solution was proposed for retuning the NF based on the fast Fourier transform (FFT) algorithm, an efficient form of the discrete Fourier transform (DFT). The FFT algorithm was triggered only when the grid current total harmonic distortion (THD) exceeds the 5% maximum limit. A 512-point FFT was used to analyse the frequency spectrum of the grid current, where the resonant frequency was identified as the largest frequency within the spectrum. The value for the resonant frequency was

used to update the NF centre frequency, enabling the NF to suppress the resonance adequately. The FFT algorithm was further compared with another variant of the DFT- the Goertzel algorithm. The FFT showed superior resonant frequency tracking performance in terms of both computational speed and efficiency.

- The effect of unbalanced load on a hybrid biomass-PV DG system was studied. Mathematical analysis revealed that the negative sequence component of the unbalanced load produced PCC voltage unbalance, unbalanced biomass currents and negative sequence electromagnetic torque in the BDG, which may consequently lead to rotor overheating. The proposed solution was an unbalanced load compensation scheme embedded within the VOC control structure of the PV. The control strategy relies on accurate extraction of the negative sequence components of the load current. To this end, the advanced decoupled double synchronous reference frame-PLL (DDSRF-PLL) scheme was used to extract the negative sequence load currents, which were regulated in the negative sequence control loop of the PV inverter. Simulation results proved the compensation scheme adequately eliminated the voltage unbalance at the point of common coupling (PCC). The biomass current also remained symmetrical and the negative sequence electromagnetic torque in the biomass generator was also eliminated. This proved the beneficial aspects of hybridisation of DGs, since the PV has protected the BDG from the side effects of negative sequence currents.
- A study on the effect of unbalanced grid voltages caused by faults was performed on the PVDG system. A novel reference current generation method, known as the optimised flexible power control (OFPC), was proposed to suppress both the active and reactive powers of the PVDG. It simultaneously reduced the power ripples through formulation of a multi-objective optimisation problem with a decision variable, k which was determined using the genetic algorithm, within the DC link fluctuation and maximum inverter current constraints. Simulation results under different VUFs were presented, comparing the proposed OFPC with two classical methods: the constant active power control (CAPC) and the balanced positive-sequence control (BPSC). The proposed OFPC provided the best

compromise solution amongst the three, by restricting the PV inverter current to its limits, repressing active and reactive power ripples, as well as reducing DC link fluctuations.

7.2 Recommendations for Future Research

The project has provided solutions to some of the challenges faced by DGs. Some areas in which further work is required are:

1. Incorporating the BDG with a power electronic interface to improve its controllability in the face of unbalanced loads and grid voltages.
2. Experimental validation of the adaptive notch filter in the case of a varying grid impedance.
3. Compare and analyse the proposed unbalanced load compensation scheme with other methods.
4. Provide an experimental validation for the novel OFPC method of reference current generation of the PVDG under unbalanced grid faults.

7.3 Publications from the Project

1. N. A. Rufa'I, L. Zhang, and B. Chong, "Performance analysis of adaptive notch filter active damping methods for grid-connected converters under a varying grid impedance," in *PowerTech, 2017 IEEE Manchester*, 2017.
2. N. A. Rufa'I, L. Zhang, and B. Chong, "Comparison of PI and PR Controllers with Adaptive Notch Filter for LCL Filtered Grid-Tie Converters under Weak Grid," in *PES PowerAfrica, 2019 IEEE Abuja*, 2019.
3. N. A. Rufa'I, L. Zhang, and B. Chong, "Optimised Flexible Power Control (OFPC) for Grid-Connected Converters under Unbalanced Grid Faults," in *IEEE Transactions on Control Systems Technology* (submitted).

Appendix A Classification of Biomass Gasifiers

Various types of gasifiers exist, and the choice depends on the nature of the feedstock. There are two major types of biomass gasifiers: fixed beds and fluidized beds.

Fixed Beds

As the name implies, they consist of a stationary grate on to which the feedstock is allowed to fall under gravity. These type of gasifiers utilise feedstock consisting of large solid pieces, which permit the free flow of gas. They are most suitable for small to medium scale power generation, owing to their simplicity. To avoid high costs of transportation, the syngas produced needs to be utilised on-site for heat and power generation. The low energy content of the syngas is due to a large percentage of nitrogen in air. Oxygen gasification could alleviate this problem, but the requirement for a source of pure oxygen increases the cost of gasification [21].

They are of 2 major types of fixed bed gasifiers: downdraft and updraft.

In a downdraft gasifier, the biomass feedstock, steam and oxidant are fed together in the same direction. Combustion and pyrolysis occur at the same time in the fast pyrolysis zone [27]. It is most commonly an air gasifier, where the air is supplied between the char reduction and pyrolysis zones as seen in Fig. A.1. The feedstock above is pyrolysed due to convective heat from the reduction zone. The tars and oil produced move down the hot charcoal bed and in the process, are cracked and reduced to syngas. The advantage of this gasifier is that it produces less than 10% tars and oils compared to an updraft gasifier [21].

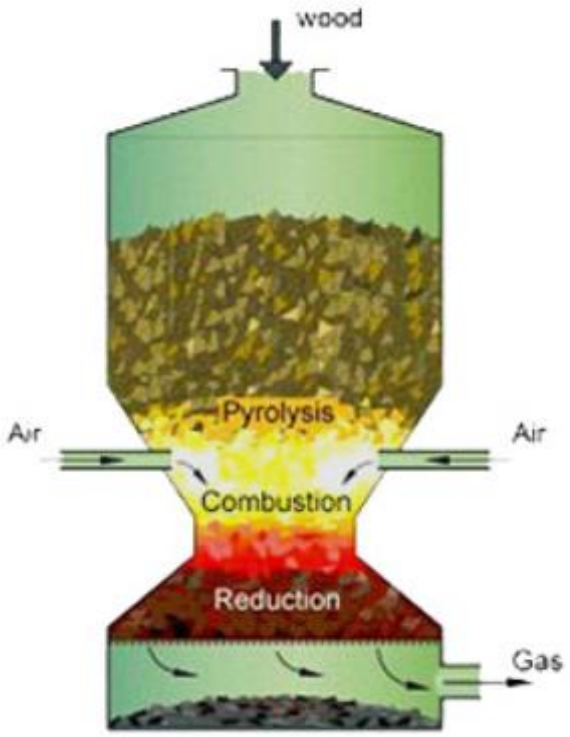

Figure A.1: Downdraft gasifier [158]

Figure A.2 shows an updraft gasifier. In this type, the biomass is fed in at the top of the gasifier with air flowing in the opposite direction. The fuel flows downwards and in the process, is dried and gasified. This type of gasifier has a high thermal efficiency. It may also be used for feedstock with moisture contents of up to 50% without an initial drying process. The updraft gasifiers, however, generate syngas with a high proportion of oil and tar [21].

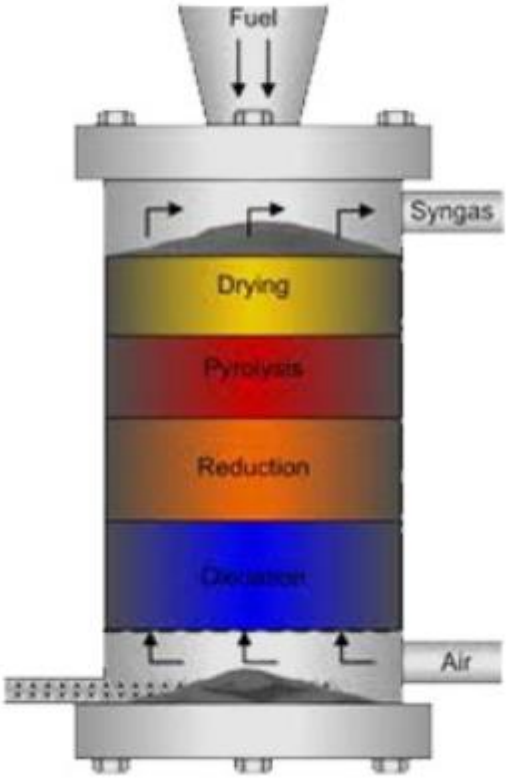

Figure A.2: Updraft gasifier [158]

Fluidised Beds

Fluidised bed gasifiers accommodate a wider range of feedstock sizes. The biomass feedstock is fed in from the bottom of the reactor where it is suspended in air in the presence of an inert material such as sand, which provides an avenue for heat transfer [18]. As the feedstock moves upward, it is converted to producer gas. Fluidised-bed reactors have uniform bed conditions and are highly efficient. Due to their flexibility regarding the nature of feedstock required, they are used with generators having capacities higher than 10 MW [18, 159]. They are generally classified into: bubbling and circulating fluidised beds. The rate of flow of the fluidising agent is greater in a circulating fluidised bed than in a bubbling fluidised bed [18].

Appendix B Thermodynamic Equilibrium Model for Determination of Synthesis Gas Composition

A thermodynamic equilibrium model is adopted to determine the heating value of wood biomass. The heating value of a fuel can be either the higher (gross) heating value (HHV) or the lower (net) heating value (LHV). The HHV refers to the quantity of heat released when a unit mass of fuel at 25^{O}C is combusted and the products have cooled to the same initial temperature of 25^{O}C [19]. The LHV is the amount of heat released in the full combustion of a fuel without considering the latent heat of vaporisation for the combustion of water.

The performance of a downdraft gasifier in the gasification of wood biomass has been presented in [6] and is represented by the following equations:

$$C + CO_2 = 2CO, \tag{B.1}$$

$$C + H_2O = H_2 + CO, \tag{B.2}$$

and

$$C + 2H_2 = CH_4. \tag{B.3}$$

Combining Equs. (B.1) and (B.2) result in the shift reaction, expressed as:

$$CO + H_2O = CO_2 + H_2. \tag{B.4}$$

The equilibrium constant for methanation in Equ. (B.3) is:

$$K_1 = \frac{P_{CH_4}}{(P_{H_2})^2}, \tag{B.5}$$

and the equilibrium constant for the shift reaction in Equ. (B.4) is:

$$K_2 = \frac{P_{CO_2}P_{H_2}}{P_{CO}P_{H_2O}} \tag{B.6}$$

The overall gasification reaction in a downdraft gasifier (with negligible amounts of char) is expressed in Equ (B.7), with $CH_{1.44}O_{0.66}$ as the chemical formula for wood biomass [6]:

$$CH_{1.44}O_{0.66} + wH_2O + mO_2 + 3.76mN_2 = x_1H_2 + x_2CO + x_3CO_2 + x_4H_2O + x_5CH_4 + 3.76mN_2, \tag{B.7}$$

where w is the amount of water ($kmol^{-1}$) with respect to wood,

m is the amount of oxygen ($kmol^{-1}$) with respect to wood,

x_1, x_2, x_3, x_4 and x_5 are the stoichiometric coefficients of the products of gasification.

The stoichiometric coefficients were determined by considering the mass balance of species and chemical equilibrium constants of the shift and methanation reactions [6]. Using Newton Raphson iteration, the concentrations of H_2 and CO in Equ. (B.7) were determined as:

$$C_{H_2} = 21.06\% \tag{B.8}$$

and

$$C_{CO} = 19.61\%. \tag{B.9}$$

From the percentage compositions of the gases, the lower heating value (LHV) of the syngas in *KJ/m³* can be determined as follows [160]:

$$LHV = 126C_{CO} + 106C_{H_2} + 359C_{CH_4} + 665C_{C_nH_m}. \tag{B.10}$$

Substituting Equs. (B.8) and (B.9) into (B.10), the syngas energy content is:

$$LHV = 126 \times 19.61 + 106 \times 21.06 \tag{B.11}$$

$$LHV = 4.7\ MJ/m^3. \tag{B.12}$$

A calorific value of $4.7\ MJ/m^3$ is much lower compared to that of natural gas, which is 34 MJ/m^3 [6]. As gas turbines are traditionally designed to accommodate natural gas, a gas turbine needs to be modified such that a higher flow rate of syngas is supplied to the combustor, if the same power output is required [161].

Appendix C Derivation of Per-Phase Maximum Inverter Current for Optimised Flexible Power Control (OFPC)

The expression for per phase maximum current through the inverter can be derived from the FPC reference current equation in chapter 6:

$$\begin{bmatrix} {i_d}^+ \\ {i_q}^+ \\ {i_d}^- \\ {i_q}^- \end{bmatrix} = \frac{P}{1.5\left[\|{v_d}^+\|^2+\|{v_q}^+\|^2+k\left[\|{v_d}^-\|^2+\|{v_q}^-\|^2\right]\right]} \begin{bmatrix} {v_d}^+ \\ {v_q}^+ \\ k{v_d}^- \\ k{v_q}^- \end{bmatrix}. \quad \text{(C.1)}$$

Applying inverse Park's transform to Equ. (C.1), the positive and negative sequence components of the current are respectively given as:

$$\begin{bmatrix} {i_a}^+ \\ {i_b}^+ \\ {i_c}^+ \end{bmatrix} = \frac{P}{1.5\left[\|{v_d}^+\|^2+\|{v_q}^+\|^2+k\left[\|{v_d}^-\|^2+\|{v_q}^-\|^2\right]\right]} \begin{bmatrix} \sin\theta^+ & \cos\theta^+ \\ \sin\left(\theta^+-\frac{2\pi}{3}\right) & \cos\left(\theta^+-\frac{2\pi}{3}\right) \\ \sin\left(\theta^++\frac{2\pi}{3}\right) & \cos\left(\theta^++\frac{2\pi}{3}\right) \end{bmatrix} \begin{bmatrix} {v_d}^+ \\ {v_q}^+ \end{bmatrix} \quad \text{(C.2)}$$

and

$$\begin{bmatrix} {i_a}^- \\ {i_b}^- \\ {i_c}^- \end{bmatrix} = \frac{P}{1.5\left[\|{v_d}^+\|^2+\|{v_q}^+\|^2+k\left[\|{v_d}^-\|^2+\|{v_q}^-\|^2\right]\right]} \begin{bmatrix} \sin\theta^- & \cos\theta^- \\ \sin\left(\theta^--\frac{2\pi}{3}\right) & \cos\left(\theta^--\frac{2\pi}{3}\right) \\ \sin\left(\theta^-+\frac{2\pi}{3}\right) & \cos\left(\theta^-+\frac{2\pi}{3}\right) \end{bmatrix} \begin{bmatrix} k{v_d}^- \\ k{v_q}^- \end{bmatrix}, \quad \text{(C.3)}$$

where θ^+ and θ^- are the positive and negative SRF angles respectively.

Combining Equs. (C.2) and (C.3), the stationary reference frame equivalent currents become:

$$\begin{bmatrix} i_a \\ i_b \\ i_c \end{bmatrix} = \frac{P}{1.5\left[\|{v_d}^+\|^2+\left\|{v_q}^+\right\|^2+k\left[\|{v_d}^-\|^2+\left\|{v_q}^-\right\|^2\right]\right]}$$

$$\left(\begin{bmatrix} \sin\theta^+ & \cos\theta^+ \\ \sin\left(\theta^+-\frac{2\pi}{3}\right) & \cos\left(\theta^+-\frac{2\pi}{3}\right) \\ \sin\left(\theta^++\frac{2\pi}{3}\right) & \cos\left(\theta^++\frac{2\pi}{3}\right) \end{bmatrix} \begin{bmatrix} {v_d}^+ \\ {v_q}^+ \end{bmatrix} + \begin{bmatrix} \sin\theta^- & \cos\theta^- \\ \sin\left(\theta^--\frac{2\pi}{3}\right) & \cos\left(\theta^--\frac{2\pi}{3}\right) \\ \sin\left(\theta^-+\frac{2\pi}{3}\right) & \cos\left(\theta^-+\frac{2\pi}{3}\right) \end{bmatrix} \begin{bmatrix} k{v_d}^- \\ k{v_q}^- \end{bmatrix} \right). \quad \text{(C.4)}$$

The phase A current, i_a from Equ. (C.4) is:

$$i_a = \frac{P\left({v_d}^+ \sin\theta^+ + {v_q}^+ \cos\theta^+ + k{v_d}^- \sin\theta^- + k{v_q}^- \cos\theta^-\right)}{1.5\left[\|{v_d}^+\|^2+\|{v_q}^+\|^2+k\left[\|{v_d}^-\|^2+\|{v_q}^-\|^2\right]\right]}. \quad \text{(C.5)}$$

Using trigonometric identities, Equ. (C.5) may be re-written as:

$$i_a = \frac{P\sqrt{\|v_d^+\|^2 + \left\|v_q^+\right\|^2 + k^2\left[\|v_d^-\|^2 + \left\|v_q^-\right\|^2\right] + 2k\sqrt{\left[\|v_d^+\|^2 + \left\|v_q^+\right\|^2\right]\left[\|v_d^-\|^2 + \left\|v_q^-\right\|^2\right]}\cos(\theta^+ + \theta^- - \varphi')}}{1.5\left[\|v_d^+\|^2 + \left\|v_q^+\right\|^2 + k\left[\|v_d^-\|^2 + \left\|v_q^-\right\|^2\right]\right]},$$

(C.6)

where

$$\varphi' = \tan^{-1}\frac{v_q^+}{v_d^+} + \tan^{-1}\frac{v_q^-}{v_d^-}. \quad \text{(C.7)}$$

At maximum value:

$$\theta^+ + \theta^- = \varphi'. \quad \text{(C.8)}$$

Hence, the maximum current through phase A, $I_{a(\max)}$ is:

$$I_{a(\max)} = \frac{P\sqrt{\|v_d^+\|^2+\|v_q^+\|^2+k^2\left[\|v_d^-\|^2+\|v_q^-\|^2\right]+2k\sqrt{\left[\|v_d^+\|^2+\|v_q^+\|^2\right]\left[\|v_d^-\|^2+\|v_q^-\|^2\right]}}}{1.5\left[\|v_d^+\|^2+\|v_q^+\|^2+k\left[\|v_d^-\|^2+\|v_q^-\|^2\right]\right]}. \quad \text{(C.9)}$$

Note that the maximum inverter current across all phases are equal, hence Equ. (C.9) applies to phases B and C.

References

[1] P. Breeze, *Power generation technologies*. Newnes, 2014.

[2] (2014). *Energy access database* Available: http://www.worldenergyoutlook.org/resources/energydevelopment/energyaccessdatabase/#d.en.8609

[3] A. Oudalov and A. Fidigatti, "Adaptive network protection in microgrids," *International Journal of Distributed Energy Resources,* vol. 5, no. 3, pp. 201-226, 2009.

[4] H. B. Puttgen, P. R. Macgregor, F. C. J. I. p. Lambert, and e. magazine, "Distributed generation: Semantic hype or the dawn of a new era?," vol. 99, no. 1, pp. 22-29, 2003.

[5] W. Shepherd and L. Zhang, *Electricity generation using wind power*. World scientific, 2011.

[6] Z. Zainal, R. Ali, C. Lean, and K. Seetharamu, "Prediction of performance of a downdraft gasifier using equilibrium modeling for different biomass materials," *Energy conversion and management,* vol. 42, no. 12, pp. 1499-1515, 2001.

[7] E. Planas, A. Gil-de-Muro, J. Andreu, I. Kortabarria, and I. M. de Alegría, "General aspects, hierarchical controls and droop methods in microgrids: A review," *Renewable and Sustainable Energy Reviews,* vol. 17, pp. 147-159, 2013.

[8] U. Nations, "Kyoto Protocol to the United Nations Framework Convention on Climate Change," 1998.

[9] P. UNION, "DIRECTIVE 2009/28/EC OF THE EUROPEAN PARLIAMENT AND OF THE COUNCIL of 23 April 2009 on the promotion of the use of energy from renewable sources and amending and subsequently repealing Directives 2001/77/EC and 2003/30/EC," 2009.

[10] (2009). *The UK renewable energy strategy*. Available: https://www.gov.uk/government/uploads/system/uploads/attachment_data/file/228866/7686.pdf

[11] O. o. E. D. a. E. R. S. G. R. D. Program, "DOE Microgrid Workshop Report," U.S. Department of Energy (DOE)August 30-31, 2011 2011, Available: http://energy.gov/sites/prod/files/Microgrid%20Workshop%20Report%20August%202011.pdf.

[12] C. Rehtanz, *Autonomous systems and intelligent agents in power system control and operation*. Springer Science & Business Media, 2003.

[13] L. Gilpin. (2014). *Microgrids: 5 things to know*. Available: http://www.techrepublic.com/article/microgrids-5-things-to-know/

[14] S. Baudoin, I. Vechiu, and H. Camblong, "A review of voltage and frequency control strategies for islanded microgrid," in *System Theory, Control and Computing (ICSTCC), 2012 16th International Conference on*, 2012, pp. 1-5: IEEE.

[15] M. G. Molina, *Dynamic modelling and control design of advanced energy storage for power system applications*. INTECH Open Access Publisher, 2010.

[16] M. Klemun. (2014). *Grid Perfection, Not Defection: A New Microgrid Landscape in the Making* Available:

http://www.greentechmedia.com/articles/read/grid-perfection-not-defection-a-new-microgrid-landscape-in-the-making
[17] P. Basak, A. Saha, S. Chowdhury, and S. Chowdhury, "Microgrid: Control techniques and modeling," in *Universities Power Engineering Conference (UPEC), 2009 Proceedings of the 44th International*, 2009, pp. 1-5: IEEE.
[18] A. Kumar, D. D. Jones, and M. A. Hanna, "Thermochemical biomass gasification: a review of the current status of the technology," *Energies,* vol. 2, no. 3, pp. 556-581, 2009.
[19] P. Basu, *Biomass gasification and pyrolysis: practical design and theory*. Academic press, 2010.
[20] V. Strezov and T. J. Evans, *Biomass processing technologies*. CRC Press, 2014.
[21] T. B. Reed, "Biomass gasification: principles and technology.[Monograph]," 1981.
[22] C. Diji, "Electricity Production from Biomass in Nigeria: Options, Prospects and Challenges," in *Advanced Materials Research*, 2013, vol. 824, pp. 444-450: Trans Tech Publ.
[23] D. G. f. Sonnenenergie and ECOFYS, *Planning and Installing Bioenergy Systems: A Guide for Installers, Architects and Engineers*. Earthscan, 2005.
[24] M. J. Prins, K. J. Ptasinski, and F. J. Janssen, "From coal to biomass gasification: Comparison of thermodynamic efficiency," *Energy,* vol. 32, no. 7, pp. 1248-1259, 2007.
[25] Y.-c. Song *et al.*, "Pathway of biomass-potassium migration in co-gasification of coal and biomass," *Fuel,* vol. 239, pp. 365-372, 2019.
[26] (2008-2011, 20-12-2014). *Biomass Energy Center*. Available: http://www.biomassenergycentre.org.uk/portal/page?_pageid=75,15179&_dad=portal&_schema=PORTAL
[27] Y. Wang and C. Kinoshita, "Kinetic model of biomass gasification," *Solar Energy,* vol. 51, no. 1, pp. 19-25, 1993.
[28] G. M. Masters, *Renewable and efficient electric power systems*. John Wiley & Sons, 2013.
[29] T. Markvart, *Solar electricity*. John Wiley & Sons, 2000.
[30] S. Shongwe and M. Hanif, "Comparative analysis of different single-diode PV modeling methods," *IEEE Journal of Photovoltaics,* vol. 5, no. 3, pp. 938-946, 2015.
[31] R. Teodorescu, M. Liserre, and P. Rodriguez, *Grid converters for photovoltaic and wind power systems*. John Wiley & Sons, 2011.
[32] L. Mariam, M. Basu, and M. F. Conlon, "A review of existing microgrid architectures," *Journal of Engineering,* vol. 2013, 2013.
[33] E. H. C. CEH, "INTRODUCTION TO MICROGRIDS," 2013.
[34] N. Hatziargyriou *et al.*, "Microgrids–large scale integration of microgeneration to low voltage grids," *CIGRE C6-309,* 2006.
[35] A. Banerji *et al.*, "Microgrid: A review," in *Global Humanitarian Technology Conference: South Asia Satellite (GHTC-SAS), 2013 IEEE*, 2013, pp. 27-35: IEEE.
[36] F. P. Sioshansi, *Distributed generation and its implications for the utility industry*. Academic Press, 2014.
[37] L. L. Lai and T. F. Chan, *Distributed generation: Induction and permanent magnet generators*. John Wiley & Sons, 2008.

[38] S. Bigerna, C. A. Bollino, and S. Micheli, *The sustainability of renewable energy in Europe*. Springer, 2015.
[39] W. D. US EIA-Energy Information Administration, "Levelized cost and levelized avoided cost of new generation resources in the annual energy outlook 2016," 2016.
[40] W. D. US EIA - Energy Information Administration, "Levelized cost and levelized avoided cost of new generation resources in the annual energy outlook 2019

" 2019.
[41] T. Hoevenaars, K. LeDoux, and M. Colosino, "Interpreting IEEE STD 519 and meeting its harmonic limits in VFD applications," in *ANNUAL PETROLEUM AND CHEMICAL INDUSTRY CONFERENCE*, 2003, vol. 50, no. 1, pp. 145-150: IEEE.
[42] N. Schäfer, T. Degner, A. Shustov, T. Keil, and J. Jäger, "Adaptive protection system for distribution networks with distributed energy resources," 2010.
[43] I. Committee, "IEEE standard for interconnecting distributed resources with electric power systems," *IEEE Std. 1547–2003,* pp. 1-28.
[44] N. K. Choudhary, S. R. Mohanty, and R. K. Singh, "A review on Microgrid protection," in *Electrical Engineering Congress (iEECON), 2014 International*, 2014, pp. 1-4: IEEE.
[45] G. Buigues, A. Dyśko, V. Valverde, I. Zamora, and E. Fernández, "Microgrid Protection: Technical challenges and existing techniques," *Renewable Energy and Power Quality Journal,* vol. 6, no. 11, pp. 1280-1292, 2013.
[46] S. Mirsaeidi, D. M. Said, M. W. Mustafa, M. H. Habibuddin, and K. Ghaffari, "Progress and problems in micro-grid protection schemes," *Renewable and Sustainable Energy Reviews,* vol. 37, pp. 834-839, 2014.
[47] Y. Han, X. Hu, and D. Zhang, "Study of adaptive fault current algorithm for microgrid dominated by inverter based distributed generators," in *Power Electronics for Distributed Generation Systems (PEDG), 2010 2nd IEEE International Symposium on*, 2010, pp. 852-854: IEEE.
[48] W. Feero, D. Dawson, and J. Stevens, "White paper on protection issues of the microgrid concept," *Consortium for Electric Reliability Technology Solutions,* 2002.
[49] M. Khederzadeh, "Adaptive setting of protective relays in microgrids in grid-connected and autonomous operation," in *Developments in Power Systems Protection, 2012. DPSP 2012. 11th International Conference on*, 2012, pp. 1-4: IET.
[50] K. Dang, X. He, D. Bi, and C. Feng, "An adaptive protection method for the inverter dominated microgrid," in *Electrical Machines and Systems (ICEMS), 2011 International Conference on*, 2011, pp. 1-5: IEEE.
[51] A.-M. Borbely and J. F. Kreider, *Distributed generation: the power paradigm for the new millennium*. CRC press, 2001.
[52] X. Xiang, G. Gong, Y. Shi, Y. Cai, and C. Wang, "Thermodynamic modeling and analysis of a serial composite process for biomass and coal co-gasification," *Renewable and Sustainable Energy Reviews,* vol. 82, pp. 2768-2778, 2018.

[53] J. Gao, L. Zhang, and X. Wang, "AC machine systems," *Mathematical Model and Parameters, Analysis, and System Performance, Tsinghua University Press, Beijing,* 2009.
[54] M. P. Boyce, *Gas turbine engineering handbook*. Elsevier, 2011.
[55] F. Jurado, A. Cano, and J. Carpio, "Biomass based micro-turbine plant and distribution network stability," *Energy Conversion and Management,* vol. 45, no. 17, pp. 2713-2727, 2004.
[56] Y. Zhu and K. Tomsovic, "Development of models for analyzing the load-following performance of microturbines and fuel cells," *Electric Power Systems Research,* vol. 62, no. 1, pp. 1-11, 2002.
[57] U. A. Bakshi and M. Bakshi, *Electrical Machines-II*. Technical Publications, 2009.
[58] C. Wadhwa, *Generation, distribution and utilization of electrical energy*. New Age International, 1989.
[59] I. Boldea, *Synchronous generators*. CRC Press, 2015.
[60] P. Kundur, N. J. Balu, and M. G. Lauby, *Power system stability and control*. McGraw-hill New York, 1994.
[61] L. L. Grigsby, *Power system stability and control*. CRC press, 2016.
[62] W. De Jong and J. R. Van Ommen, *Biomass as a Sustainable Energy Source for the Future*. Wiley Online Library, 2014.
[63] C. Baskar, S. Baskar, and R. Dhillon, *Biomass conversion: the interface of biotechnology* (Chemistry and Materials Science. Springer). 2012.
[64] J. Twidell and A. D. Weir, *Renewable energy resources*. Taylor & Francis, 2006.
[65] B. Wilson, N. Williams, B. Liss, and B. Wilson, "A Comparative Assessment of Commercial Technologies for Conversion of Solid Waste to Energy," EnviroPower Renewable, Inc.October, 2013, Accessed on: 10-12-2014.
[66] K. Braber, "Anaerobic digestion of municipal solid waste: a modern waste disposal option on the verge of breakthrough," *Biomass and bioenergy,* vol. 9, no. 1, pp. 365-376, 1995.
[67] (17-12-2014). *U.S. Energy Information Administration*. Available: http://www.eia.gov/todayinenergy/detail.cfm?id=7990
[68] A. Bridgwater, A. Toft, J. J. R. Brammer, and S. E. Reviews, "A techno-economic comparison of power production by biomass fast pyrolysis with gasification and combustion," vol. 6, no. 3, pp. 181-246, 2002.
[69] E. POWER, "HANDBOOK OF ELECTRICAL POWER SYSTEM DYNAMICS."
[70] W. I. Rowen, "Simplified mathematical representations of heavy-duty gas turbines," *Journal of Engineering for Gas Turbines and Power,* vol. 105, no. 4, pp. 865-869, 1983.
[71] W. I. Rowen, "Simplified mathematical representations of single shaft gas turbines in mechanical drive service," *Turbomachinery International,* vol. 33, no. 5, 1992.
[72] S. Guda, C. Wang, and M. Nehrir, "Modeling of microturbine power generation systems," *Electric Power Components and Systems,* vol. 34, no. 9, pp. 1027-1041, 2006.
[73] F. Jurado and A. Cano, "Use of ARX algorithms for modelling micro-turbines on the distribution feeder," *IEE Proceedings-Generation, Transmission and Distribution,* vol. 151, no. 2, pp. 232-238, 2004.

[74] A. Al-Hinai and A. Feliachi, "Dynamic model of a microturbine used as a distributed generator," in *System Theory, 2002. Proceedings of the Thirty-Fourth Southeastern Symposium on*, 2002, pp. 209-213: IEEE.

[75] H. E. Shalan, M. M. Hassan, and A. Bahgat, "Parameter estimation and dynamic simulation of gas turbine model in combined cycle power plants based on actual operational data," *Journal of American Science,* vol. 7, no. 5, pp. 303-310, 2011.

[76] G. Lalor and M. O'Malley, "Frequency control on an island power system with increasing proportions of combined cycle gas turbines," in *Power Tech Conference Proceedings, 2003 IEEE Bologna*, 2003, vol. 4, p. 7 pp. Vol. 4: IEEE.

[77] S. Massucco, A. Pitto, and F. Silvestro, "A gas turbine model for studies on distributed generation penetration into distribution networks," *Power Systems, IEEE Transactions on,* vol. 26, no. 3, pp. 992-999, 2011.

[78] Q. Zhang and P. So, "Dynamic modelling of a combined cycle plant for power system stability studies," in *Power Engineering Society Winter Meeting, 2000. IEEE*, 2000, vol. 2, pp. 1538-1543: IEEE.

[79] F. Jurado, M. Ortega, A. Cano, and J. Carpio, "Neuro-fuzzy controller for gas turbine in biomass-based electric power plant," *Electric Power Systems Research,* vol. 60, no. 3, pp. 123-135, 2002.

[80] S. R. Guda, C. Wang, and M. Nehrir, "A simulink-based microturbine model for distributed generation studies," in *Power Symposium, 2005. Proceedings of the 37th Annual North American*, 2005, pp. 269-274: IEEE.

[81] (2015). *Synchronous Machine*. Available: http://uk.mathworks.com/help/physmod/sps/powersys/ref/synchronousmachine.html

[82] D. Lee, "IEEE recommended practice for excitation system models for power system stability studies (IEEE Std 421.5-1992)," *Energy Development and Power Generating Committee of the Power Engineering Society,* 1992.

[83] G. Lalor, J. Ritchie, D. Flynn, and M. J. O'Malley, "The impact of combined-cycle gas turbine short-term dynamics on frequency control," *Power Systems, IEEE Transactions on,* vol. 20, no. 3, pp. 1456-1464, 2005.

[84] F. E. Technology, "Data Sheets Three phase Synchronous Generators," in *160 - 630 FRAME SIZES INDUSTRIAL APPLICATION*, F. E. Technology, Ed., ed, 2005.

[85] H. Cha and T.-K. Vu, "Comparative analysis of low-pass output filter for single-phase grid-connected Photovoltaic inverter," in *Applied Power Electronics Conference and Exposition (APEC), 2010 Twenty-Fifth Annual IEEE*, 2010, pp. 1659-1665: IEEE.

[86] C. Zhang, T. Dragicevic, J. C. Vasquez, and J. M. Guerrero, "Resonance damping techniques for grid-connected voltage source converters with LCL filters—A review," in *Energy Conference (ENERGYCON), 2014 IEEE International*, 2014, pp. 169-176: IEEE.

[87] M. Büyük, A. Tan, M. Tümay, and K. Ç. Bayındır, "Topologies, generalized designs, passive and active damping methods of switching ripple filters for voltage source inverter: A comprehensive review," *Renewable and Sustainable Energy Reviews,* vol. 62, pp. 46-69, 2016.

[88] W. Zhao and G. Chen, "Comparison of active and passive damping methods for application in high power active power filter with LCL-filter," in

Sustainable Power Generation and Supply, 2009. SUPERGEN'09. International Conference on, 2009, pp. 1-6: IEEE.

[89] C. Wessels, J. Dannehl, and F. W. Fuchs, "Active damping of LCL-filter resonance based on virtual resistor for PWM rectifiers—Stability analysis with different filter parameters," in *2008 IEEE Power Electronics Specialists Conference*, 2008, pp. 3532-3538: IEEE.

[90] X. Yan, J. Tang, W. Zhang, and Y. Zhang, "Multi-objective optimization design for active damping LCL grid-connected," 2015.

[91] M. B. Saïd-Romdhane, M. W. Naouar, I. Slama-Belkhodja, and E. Monmasson, "Robust Active Damping Methods for LCL Filter-Based Grid-Connected Converters," *IEEE Transactions on Power Electronics,* vol. 32, no. 9, pp. 6739-6750, 2017.

[92] J. Xu, S. Xie, and T. Tang, "Improved control strategy with grid-voltage feedforward for LCL-filter-based inverter connected to weak grid," *IET Power Electronics,* vol. 7, no. 10, pp. 2660-2671, 2014.

[93] M. H. Durgante, H. F. B. Plotzki, and M. Stefanello, "Combined active damping with adaptive current control for converters with LCL filters," in *Industrial Electronics Society, IECON 2013-39th Annual Conference of the IEEE*, 2013, pp. 520-525: IEEE.

[94] J. Dannehl, M. Liserre, and F. W. Fuchs, "Filter-based active damping of voltage source converters with filter," *IEEE Transactions on Industrial Electronics,* vol. 58, no. 8, pp. 3623-3633, 2011.

[95] M. Liserre, F. Blaabjerg, and S. Hansen, "Design and control of an LCL-filter-based three-phase active rectifier," *Industry Applications, IEEE Transactions on,* vol. 41, no. 5, pp. 1281-1291, 2005.

[96] M. Zarif and M. Monfared, "Step-by-step design and tuning of VOC control loops for grid connected rectifiers," *International Journal of Electrical Power & Energy Systems,* vol. 64, pp. 708-713, 2015.

[97] X. Ruan, X. Wang, D. Pan, D. Yang, W. Li, and C. Bao, *Control techniques for LCL-type grid-connected inverters*. Springer, 2018.

[98] H. Rahbarimagham, E. M. AMIRI, B. Vahidi, G. B. GHAREHPETIAN, and M. Abedi, "Superior decoupled control of active and reactive power for three-phase voltage source converters," *Turkish Journal of Electrical Engineering & Computer Sciences,* vol. 23, no. 4, pp. 1025-1039, 2015.

[99] S. Anwar, *Handbook of research on solar energy systems and Technologies*. IGI Global, 2012.

[100] J. D. Irwin and B. M. Wilamowski, *The Industrial Electronics Handbook, - Five Volume Set*. CRC Press, 2011.

[101] C. RICHARDSON, "Designing an Inverting Buck-boost Converter with MagI³C Power Module WPMDH1302401 / 171032401 (6 - 42 VIN / 3A / 5 - 24 VOUT)," 2015-07-09 2015.

[102] N. P. Iyer, *Power Electronic Converters: Interactive Modelling Using Simulink*. CRC Press, 2018.

[103] A. Reznik, M. G. Simoes, A. Al-Durra, and S. Muyeen, "Filter Design and Performance Analysis for Grid-Interconnected Systems," *Industry Applications, IEEE Transactions on,* vol. 50, no. 2, pp. 1225-1232, 2014.

[104] H. C. Luong and G. C. T. Leung, *Low-voltage CMOS RF frequency synthesizers*. Cambridge University Press, 2004.

[105] F. Ellinger, *Radio frequency integrated circuits and technologies*. Springer Science & Business Media, 2008.

[106] L. Wang, S. Chai, D. Yoo, L. Gan, and K. Ng, *PID and predictive control of electrical drives and power converters using MATLAB/Simulink*. John Wiley & Sons, 2015.
[107] R. Pena-Alzola, M. Liserre, F. Blaabjerg, M. Ordonez, and T. Kerekes, "A self-commissioning notch filter for active damping in a three-phase LCL-filter-based grid-tie converter," *IEEE Trans. Power Electron.,* vol. 29, no. 12, pp. 6754-6761, 2014.
[108] M. Büyük, A. Tan, and M. Tümay, "Improved adaptive notch filter-based active damping method for shunt active power filter with LCL-filter," *Electrical Engineering,* pp. 1-13, 2018.
[109] F. Bronchart, Y. Mollet, and J. Gyselinck, "LCL Filters for a grid emulator application-Comparative study of active damping techniques," in *Industrial Electronics Society, IECON 2013-39th Annual Conference of the IEEE*, 2013, pp. 2087-2092: IEEE.
[110] Y.-C. Cho, K.-Y. Choi, and R.-Y. Kim, "Adaptive damping scheme of LCL filter resonance under inductance variation for a single-phase grid-connected inverter," in *2015 9th International Conference on Power Electronics and ECCE Asia (ICPE-ECCE Asia)*, 2015, pp. 978-983: IEEE.
[111] M. Ciobotaru, A. Rossé, L. Bede, B. Karanayil, and V. G. Agelidis, "Adaptive Notch filter based active damping for power converters using LCL filters," in *Power Electronics for Distributed Generation Systems (PEDG), 2016 IEEE 7th International Symposium on*, 2016, pp. 1-7: IEEE.
[112] S. Chattopadhyay, M. Mitra, and S. Sengupta, "Electric power quality," in *Electric Power Quality*: Springer, 2011, pp. 5-12.
[113] M. V. Mane and M. A. Agashe, "An Adaptive Notch Filter For Noise Reduction and Signal Decomposition," *IJCSI,* 2011.
[114] R. P. Vieira, L. T. Martins, J. R. Massing, and M. Stefanello, "Sliding Mode Controller in a Multi-Loop Framework for a Grid-Connected VSI with LCL Filter," *IEEE Transactions on Industrial Electronics,* 2017.
[115] W. Yao, Y. Yang, X. Zhang, F. Blaabjerg, and P. C. Loh, "Design and analysis of robust active damping for LCL filters using digital notch filters," *IEEE Transactions on Power Electronics,* vol. 32, no. 3, pp. 2360-2375, 2017.
[116] D. Pan, X. Ruan, C. Bao, W. Li, and X. Wang, "Optimized controller design for LCL-type grid-connected inverter to achieve high robustness against grid-impedance variation," *IEEE Transactions on Industrial Electronics,* vol. 62, no. 3, pp. 1537-1547, 2015.
[117] R. Pena-Alzola *et al.*, "Robust active damping in LCL-filter based medium-voltage parallel grid-inverters for wind turbines," *IEEE Transactions on Power Electronics,* 2018.
[118] W. Yao, Y. Yang, X. Zhang, and F. Blaabjerg, "Digital notch filter based active damping for LCL filters," in *Applied Power Electronics Conference and Exposition (APEC), 2015 IEEE*, 2015, pp. 2399-2406: IEEE.
[119] P. Sysel and P. Rajmic, "Goertzel algorithm generalized to non-integer multiples of fundamental frequency," *EURASIP Journal on Advances in Signal Processing,* vol. 2012, no. 1, p. 56, 2012.
[120] M. Liserre, F. Blaabjerg, and R. Teodorescu, "Grid impedance estimation via excitation of LCL-filter resonance," *IEEE Transactions on Industry Applications,* vol. 43, no. 5, pp. 1401-1407, 2007.

[121] C. Bajracharya, M. Molinas, J. A. Suul, and T. M. Undeland, "Understanding of tuning techniques of converter controllers for VSC-HVDC," in *Nordic Workshop on Power and Industrial Electronics (NORPIE/2008), June 9-11, 2008, Espoo, Finland*, 2008: Helsinki University of Technology.
[122] D. Jovcic and K. Ahmed, *High voltage direct current transmission: converters, systems and DC grids*. John Wiley & Sons, 2015.
[123] M. Rahman, *Applications of Fourier transforms to generalized functions*. WIT Press, 2011.
[124] P. R. Nicolas, *Scala for machine learning*. Packt Publishing Ltd, 2015.
[125] M. Frigo and S. G. Johnson, "FFTW: An adaptive software architecture for the FFT," in *Acoustics, Speech and Signal Processing, 1998. Proceedings of the 1998 IEEE International Conference on*, 1998, vol. 3, pp. 1381-1384: IEEE.
[126] J.-H. Kim, J.-G. Kim, Y.-H. Ji, Y.-C. Jung, and C.-Y. Won, "An islanding detection method for a grid-connected system based on the goertzel algorithm," *IEEE Transactions on Power Electronics,* vol. 26, no. 4, pp. 1049-1055, 2011.
[127] M. Castilla, J. Miret, A. Camacho, J. Matas, and L. G. de Vicuña, "Voltage support control strategies for static synchronous compensators under unbalanced voltage sags," *IEEE transactions on industrial electronics,* vol. 61, no. 2, pp. 808-820, 2014.
[128] A. Rodríguez, E. J. Bueno, Á. Mayor, F. J. Rodríguez, and A. García-Cerrada, "Voltage support provided by STATCOM in unbalanced power systems," *Energies,* vol. 7, no. 2, pp. 1003-1026, 2014.
[129] Y. Xu, L. M. Tolbert, J. D. Kueck, and D. T. Rizy, "Voltage and current unbalance compensation using a static var compensator," *IET Power Electronics,* vol. 3, no. 6, pp. 977-988, 2010.
[130] G.-H. Kim, C. Hwang, J.-H. Jeon, J.-B. Ahn, and E.-S. Kim, "A novel three-phase four-leg inverter based load unbalance compensator for stand-alone microgrid," *International Journal of Electrical Power & Energy Systems,* vol. 65, pp. 70-75, 2015.
[131] O. Oghorada and L. Zhang, "Analysis of star and delta connected modular multilevel cascaded converter-based STATCOM for load unbalanced compensation," *International Journal of Electrical Power & Energy Systems,* vol. 95, pp. 341-352, 2018.
[132] W.-N. Chang, C.-H. Liao, and P.-L. Wang, "UNBALANCED LOAD COMPENSATION IN THREE-PHASE POWER SYSTEM WITH A CURRENT-REGULATED DSTATCOM BASED ON MULTILEVEL CONVERTER," *Journal of Marine Science and Technology,* vol. 24, no. 3, pp. 484-492, 2016.
[133] A. Engler, "Applicability of droops in low voltage grids," *International Journal of Distributed Energy Resources,* vol. 1, no. 1, pp. 1-6, 2005.
[134] R. G. Harley, E. B. Makram, and E. G. Duran, "The effects of unbalanced networks on synchronous and asynchronous machine transient stability," *Electric power systems research,* vol. 13, no. 2, pp. 119-127, 1987.
[135] A. Ahmad, *Smart Grid as a Solution for Renewable and Efficient Energy*. IGI Global, 2016.
[136] G. W. Fletcher, *The Guide to Photovoltaic System Installation*. Cengage Learning, 2013.

[137] C. Ng, L. Ran, and J. Bumby, "Unbalanced grid fault ride-through control for a wind turbine inverter," in *2007 IEEE Industry Applications Annual Meeting*, 2007, pp. 154-164: IEEE.
[138] K. Bhumkittipich and N. J. E. P. Mithulananthan, "Performance enhancement of DVR for mitigating voltage sag/swell using vector control strategy," vol. 9, pp. 366-379, 2011.
[139] N. Salgado-Herrera, A. Medina-Rios, R. Tapia-Sánchez, O. Anaya-Lara, J. J. I. i. e. m. Rodríguez-Rodríguez, and drives, "Voltage compensation and power factor correction in distribution networks with DVR," 2015.
[140] J. L. Sosa, M. Castilla, J. Miret, J. Matas, and Y. Al-Turki, "Control strategy to maximize the power capability of PV three-phase inverters during voltage sags," *IEEE Transactions on Power Electronics,* vol. 31, no. 4, pp. 3314-3323, 2016.
[141] F. Wang, J. Duarte, and M. Hendrix, "Design and analysis of active power control strategies for distributed generation inverters under unbalanced grid faults," *IET generation, transmission & distribution,* vol. 4, no. 8, pp. 905-916, 2010.
[142] R. Kabiri, D. G. Holmes, and B. P. McGrath, "Control of active and reactive power ripple to mitigate unbalanced grid voltages," *IEEE Trans. Ind. Appl,* vol. 52, no. 2, pp. 1660-1668, 2016.
[143] E. Afshari, G. R. Moradi, Y. Yang, B. Farhangi, and S. Farhangi, "A review on current reference calculation of three-phase grid-connected PV converters under grid faults," in *Power and Energy Conference at Illinois (PECI), 2017 IEEE*, 2017, pp. 1-7: IEEE.
[144] J. Jia, G. Yang, and A. H. Nielsen, "A Review on Grid-Connected Converter Control for Short-Circuit Power Provision Under Grid Unbalanced Faults," *IEEE Transactions on Power Delivery,* vol. 33, no. 2, pp. 649-661, 2018.
[145] F. Wang, J. L. Duarte, and M. A. Hendrix, "Active power control strategies for inverter-based distributed power generation adapted to grid-fault ride-through requirements," in *Power Electronics and Applications, 2009. EPE'09. 13th European Conference on*, 2009, pp. 1-10: IEEE.
[146] P. Ngatchou, A. Zarei, and A. El-Sharkawi, "Pareto multi objective optimization," in *Intelligent systems application to power systems, 2005. Proceedings of the 13th international conference on*, 2005, pp. 84-91: IEEE.
[147] A. Konak, D. W. Coit, and A. E. Smith, "Multi-objective optimization using genetic algorithms: A tutorial," *Reliability Engineering & System Safety,* vol. 91, no. 9, pp. 992-1007, 2006.
[148] G. Abad, *Power electronics and electric drives for traction applications*. John Wiley & Sons, 2016.
[149] T. Thomas, K. Haddad, G. Joós, and A. Jaafari, "Design and performance of active power filters," *IEEE Industry Applications Magazine,* vol. 4, no. 5, pp. 38-46, 1998.
[150] F. Maggino and E. Ruviglioni, "Obtaining weights: from objective to subjective approaches in view of more participative methods in the construction of composite indicators," *Proceedings NTTS: New Techniques and Technologies for Statistics,* pp. 37-46, 2009.

[151] R. T. Marler and J. S. Arora, "The weighted sum method for multi-objective optimization: new insights," *Structural and multidisciplinary optimization,* vol. 41, no. 6, pp. 853-862, 2010.
[152] M. Mitchell, *An introduction to genetic algorithms*. MIT press, 1998.
[153] D. A. Coley, *An introduction to genetic algorithms for scientists and engineers*. World Scientific Publishing Company, 1999.
[154] S. Buso and P. Mattavelli, "Digital control in power electronics," *Lectures on power electronics,* vol. 1, no. 1, pp. 1-158, 2006.
[155] R. Teodorescu, F. Blaabjerg, and M. Liserre, "Proportional-resonant controllers. A new breed of controllers suitable for grid-connected voltage-source converters," *Proc. Optim,* vol. 3, pp. 9-14, 2004.
[156] S. Bacha, I. Munteanu, and A. I. Bratcu, "Linear Control Approaches for DC-AC and AC-DC Power Converters," in *Power Electronic Converters Modeling and Control*: Springer, 2014, pp. 237-296.
[157] M. Singh, *Power electronics*. Tata McGraw-Hill Education, 2008.
[158] (2011). *BIOMASS GASIFIERS*. Available: http://www.infiniteenergyindia.com/biomass-gasifiers.html
[159] (1996-2013, 16-12-2014). *The Alternative Energy eMagazine*. Available: http://www.altenergymag.com/emagazine.php?issue_number=09.06.01&article=zafar
[160] D.-Z. Li and J.-y. Ma, "Wood biomass gasification process modeling and optimization of the parameters of control," in *Control and Decision Conference, 2009. CCDC'09. Chinese*, 2009, pp. 5152-5157: IEEE.
[161] *Syngas Composition for IGCC*. Available: http://www.netl.doe.gov/research/coal/energy-systems/gasification/gasifipedia/syngas-composition-igcc